DIVERTOR EXPERIMENTS IN A TOROIDAL PLASMA, WITH ExB DRIFT DUE TO AN APPLIED RADIAL ELECTRIC FIELD

BY

EDWARD JONATHAN STRAIT

A thesis submitted in partial fulfillment of the requirements for the degree of

DOCTOR OF PHILOSOPHY

(Physics)

at the

UNIVERSITY OF WISCONSIN - MADISON

1979

ABSTRACT

DIVERTOR EXPERIMENTS IN A TOROIDAL PLASMA, WITH
E×B DRIFT DUE TO AN APPLIED RADIAL ELECTRIC FIELD

Edward Jonathan Strait

Under the supervision of Professor J.C. Sprott.

It is proposed that the E×B drift arising from an externally applied electric field could be used in a tokamak or other toroidal magnetic plasma confinement device to remove plasma and impurities from the region near the wall and reduce the amount of plasma striking the wall. This could either augment or replace a conventional magnetic field divertor. Among the possible advantages of this scheme are easy external control over the rate of removal of plasma, more rapid removal than the naturally ocurring rate in a magnetic divertor, and simplification of construction if the magnetic divertor is eliminated. Results of several related experiments performed in the Wisconsin Levitated Octupole are presented.

A model based on the plasma's perpendicular dielectric constant and perpendicular conductivity suggests that such an electric field applied perpendicular to the magnetic field will be inversely proportional to plasma density, allowing the electric field to penetrate the plasma on the scale length of the density profile. Experimental measurements agreed well in spatial dependence with the model, assuming

that collisions with neutral particles are responsible for the perpendicular conductivity. The numerical value of the measured conductivity was about two orders of magnitude too large, however, implying the existence of some anomalous process.

In the first of two divertor experiments, E×B drifts were used alone, in the absence of any magnetic divertor, to remove the outer layer of plasma. The existence of a separatrix dividing diverted and undiverted E×B drift surfaces was demonstrated. Despite the localized nature of this divertor, plasma flux to the wall was reduced by 30% to 50% everywhere in the machine, with no deleterious effect on confinement of the central plasma.

For the second divertor experiment, a poloidal divertor (without pumping chamber) was added to the octupole. To simulate a tokamak, the octupole was then operated with a relatively large ratio of toroidal to poloidal magnetic field ($q = .7$). When operated conventionally, without applied E×B drift, the divertor reduced plasma flux to the wall by an order of magnitude or more, consistent with simple divertor theory. Central confinement time was also reduced as expected, due to narrowing of the available volume. Plasma flow to the divertor was measured at .6 of the ion acoustic speed.

Addition of an E×B drift by biasing a divertor ring improved the divertor action, reducing the plasma flux to the wall by a further factor of 5, and also reducing the density profile's scale length near the wall, with little adverse effect on the confinement of the central plasma. At low electric field this effect was in reasonable agreement

with a modification of simple divertor theory which takes into account the E×B drift. At larger electric field the divertor effect saturated, which is predicted qualitatively by the model if the electric field is inversely proportional to density. Measured plasma flow velocity in the scrape-off zone far from the divertor was consistent with E×B drift up to at least half the ion acoustic speed, but near the divertor parallel flow was dominant, evidently due to parallel electric fields. Application of the electric field did not give rise to any new instabilities.

ACKNOWLEDGEMENTS

I would like to thank the entire Wisconsin Plasma Group, all of whom have contributed to this work in some way. In particular, I would like to express my appreciation for the support and encouragement of Dr. J.C. Sprott. The ideas and suggestions of Dr. D.W. Kerst, which inspired and guided this project, were also essential.

This thesis, particularly the chapter on applied radial electric fields, also owes much to many discussions with Dr. C.J. Armentrout. Helpful discussions and technical assistance were also provided by Dr. R.S. Post, Dr. G.A. Emmert, Evan Rose, Jim Halle, Skip Garner, Dr. T.L.Owens, and Cliff Strawitch. Data acquisition would have been much more difficult without the PDP-11 system and software developed and maintained by Dr. J.R. Greenwood, Mike Zarnstorff, and Jon Twichell.

I am grateful to Glenn Henderson and the Physical Sciences Laboratory staff for assistance in the construction of the divertor hoops. Paul Nonn's expertise was also invaluable in the design and construction of the divertor and the retractable fin. Special thanks are due to John Laufenberg for his assistance not only in the projects just mentioned, but in the often frustrating job of day-to-day maintenance and operation of the octupole.

This work would have been impossible without the encouragement, love, and great patience of my wife Terri.

TABLE OF CONTENTS

INTRODUCTION

It is the purpose of this thesis to discuss a proposed new method for reducing impurity concentrations in a tokamak (or other toroidal magnetic plasma confinement device), and to present results of experiments performed in the Wisconsin Levitated Octupole to test this idea. Briefly, the $\vec{E}\times\vec{B}/B^2$ drift due to an externally applied electric field is used to remove a layer of plasma near the wall of the confinement chamber, thus isolating the wall and the centrally confined plasma from each other. This flow across magnetic field lines may either be used by itself or combined with a conventional magnetic divertor, which performs the same function utilizing flow along field lines.

Chapter 1 supplies the context by describing the need for divertors, and reviewing experiments and theories for magnetic divertors. The E×B divertor is then introduced in Chapter 2, and some theoretical aspects are discussed, including the modification of the simple divertor theory of Chapter 1, which predicts the effect on plasma density near the wall and plasma flux striking the wall. Some possible limitations of the scheme are also considered.

Chapter 3 describes the hardware of the experiments, including the octupole and the diagnostics used in it. Also included is a description of the poloidal magnetic divertor installed in the octupole for this project.

Chapter 4 is a slight digression to examine the question of

whether the electric field required for the E×B divertor can be applied in the presence of a plasma, and just what the resulting distribution of electric field is. A theoretical model based on perpendicular conductivity is developed, and compared to the results of an experiment in which the electric field is applied by biasing one of the octupole's internal rings.

Divertor action by E×B drift alone is the simplest case to consider, and two such experiments are discussed in Chapter 5. The first consists simply of the observation of the electric field induced by the time-changing magnetic field in the octupole and its divertor-like effect on plasma loss to the wall. For the second experiment, the electric fields are applied externally by biasing one of the octupole's internal rings and a retractable, limiter-like metal plate installed for this purpose. The divertor action of this arrangement is shown in both local and distant measurements of plasma flux to the wall, plasma density distribution, and other quantities.

Chapter 6 concerns experiments with the poloidal magnetic divertor. This can be operated either as a purely magnetic divertor or with the addition of an E×B drift due to the electric field produced by applying a bias potential to one of the divertor rings. The effects of these two modes of operation on the plasma's confinement time, density profile, distribution of wall losses, flow velocity, and other quantities are compared with each other and with theory.

Finally, Chapter 7 summarizes the results and the conclusions to be drawn, and indicates directions for possible further investigation.

CHAPTER 1

REVIEW OF DIVERTORS

1.A. Tokamaks and the Impurity Problem

The harnessing of thermonuclear fusion for cheap, clean electrical power generation has been a dream of physicists almost since the fusion reaction was first understood. Although this goal has proved more elusive than originally anticipated, it has become more desirable than ever. Resources of fossil fuels and fissionable uranium are limited, and the hazards of radiation and weapons proliferation associated with the breeder reactor make it essential to explore the alternative of controlled fusion. The radiation hazards of the deuterium-tritium fuel cycle are smaller, and it is hoped that this will be only a stepping stone on the way to the low-neutron "advanced" fuel cycles such as $D-{}^{3}He$, $p-{}^{6}Li$, or $p-{}^{11}B$.

The most promising scheme for the first demonstration of fusion power production, if not for the long term, is the magnetic plasma confinement device known as the tokamak.[1] This is a toroidal device with a strong toroidal magnetic field, B_t, provided by external coils, and a weaker poloidal field, B_p, provided by a toroidal plasma current. (See Figure 1.1.) The fuel is ionized, the resulting plasma is confined away from the walls by the magnetic field, and is heated to fusion temperatures by the plasma current and various auxiliary heating

methods. Tokamak terminology which will occasionally be used in this paper includes the inverse aspect ratio $\varepsilon = a/R$, where a is the minor radius and R the major radius of the toroid, and the "safety factor" $q = aB_t/RB_p$, which must be greater than unity for gross magnetohydrodynamic stability of the plasma.

Control of impurities is likely to be of vital importance for fusion reactors. Impurity ions, particularly heavy ones, can greatly enhance loss of plasma energy by electron bremsstrahlung (proportional to the square of the ion charge) and by atomic line radiation (if the impurity's atomic number is sufficiently high that it is not completely ionized). For example, a concentration of as little as .2% of tungsten at the center of a DT fusion reactor would increase the Lawson $n_e\tau$ "breakeven" value by a factor of 2.5, raise the required ion temperature by a factor of 2, and make actual ignition impossible under any circumstances.[2] The problem is reduced for light impurities, which have lower Z and will be completely ionized, but still only a few percent of carbon is tolerable.

Neutral impurity atoms entering the plasma are not affected by the confining magnetic field and may travel partway to the center of the plasma before being ionized and confined. After being ionized, if their concentration is small and their charge state large, they will diffuse in the direction of <u>increasing</u> plasma density, accumulating at the center, where they will do the most harm. This can be seen from the expression[3] for the flux of species i (e.g., an impurity) due to collisions with species j (e.g., fuel ions), assuming $T_i = T_j = T$ and $\nabla T = 0$:

$$\Gamma_{ij} = \alpha_{ij} q_i n_i \left[\frac{\nabla n_j}{q_j n_j} - \frac{\nabla n_i}{q_i n_i}\right] \tag{1.1}$$

where the classical coefficient is

$$\alpha_{ij} = \frac{4}{3}\left(\frac{2\pi m}{kT}\right)^{\frac{1}{2}} \frac{q_j^2}{n_j \epsilon_o B^2} \ell n\Lambda \tag{1.2}$$

with q and n the charge and density of each species, B the magnetic field, m the reduced mass, and $\ell n\Lambda$ the Coulomb logarithm. In an axisymmetric toroidal system α_{ij} is multiplied by the usual neoclassical factor.[4]

Many schemes have been proposed to keep tokamak plasmas free of impurities; one class of such schemes is that of the magnetic divertor, in which the outermost magnetic field lines are led out through an opening in the wall of the main confinement chamber. Field lines are divided into two classes: those that stay in the confinement region, and those that leave it; the line or surface which divides them is called the separatrix. The region filled by field lines which lead out of the confinement chamber to the divertor is often referred to as the "divertor zone" or "scrape-off zone." Plasma near the wall flows along the diverted field lines to a differentially pumped external chamber, thus isolating the plasma and the wall from each other. The diverted field lines intersect a conducting plate which neutralizes the plasma striking it; the plate may be gettered or cooled to cryogenic temperatures to keep neutralized particles from re-entering the plasma.

Divertors are seen as having two functions, which may be difficult

to accomplish simultaneously. An "unload" divertor is supposed to remove plasma diffusing out of the confinement region, which would otherwise strike the wall, causing sputtering of impurities and erosion of the wall. In this case rapid removal of plasma, and consequently a short e-folding length for plasma density in the scrape-off region, are desired. A "screening" divertor is supposed to remove impurities that do leave the wall, before they can reach the center of the plasma. In this case a denser plasma in the scrape-off zone is desired to ensure ionization of the entering impurities.

Divertors rely on thermal flow along field lines to take plasma out of the main chamber, and this does not lend itself to easy external control. If an electric field were applied by external means in the divertor zone, such that the resulting $\frac{\vec{E}\times\vec{B}}{B^2}$ drift of the plasma had a component in the direction of the pumping chamber, then this would provide external control over the rate of removal of plasma, and permit adjustment of plasma density near the wall. This scheme, with its advantages and limitations, will be discussed in Chapter 2.

1.B. Magnetic Divertors

Although not the main subject of this thesis, a brief summary of conventional divertor experiments and theories is in order. A much more comprehensive review can be found in the thesis of A.T. Mense.[5]

1.B.1. Experiments

The first divertor was proposed by Spitzer[6] for use in the B-65 stellarator. This was a toroidal field divertor, in which the toroidal component of magnetic field is perturbed to accomplish the diversion (see Figure 1.2). Use of this divertor reduced central impurity concentrations by an order of magnitude and raised the ion temperature by 50%.[7]

The toroidal field divertor has the disadvantages of destroying axisymmetry and producing a large perturbation of the magnetic field at the magnetic axis, both of which can enhance plasma loss. These problems do not arise in the poloidal field divertor (see Figure 1.2), which has axisymmetry and a smaller perturbing field at the axis, especially in the double-null type. Single-null poloidal divertor experiments have been carried out in the FM-1 spherator[8] and the JFT-2 tokamak (DIVA),[9] and a double-null divertor experiment in the T-12 tokamak.[10] Large tokamaks with poloidal divertors just beginning operation or still under construction are PDX,[11] ASDEX,[12] and JT-4.[13]

The FM-1 divertor received about 80% of the particle loss from the plasma. In DIVA, the divertor receives 1/3 of the particle number loss and 3/4 of the particle energy loss, and radiation loss from the plasma is reduced by a factor of 2 or more.[14] The divertor reduces the central concentration of artificially injected impurities by a factor of 2 to 4.[15] In T-12 the radiation loss was again reduced by a factor of 2.

A third type of divertor is the bundle divertor, in which a small bundle of field lines is brought out of the confinement region[16,17]

(see Figure 1.2). This has the advantage of being more compact to construct than a poloidal divertor, while causing little perturbation of the central magnetic field. It destroys the closed flux surface topology, but in such a way that the consequences for confinement may not be too serious. Since it does not divert all field lines, its scrape-off layer is inherently thicker than that of a poloidal divertor, which may or may not be desirable, depending on the relative importance of the screening and unload functions. In the DITE tokamak experiment,[18] a bundle divertor receives 60% of the energy loss, reduces radiated power by a factor of 5 to 8, and appears to prevent artificially injected impurities from reaching the center of the plasma.

Due to its axisymmetry, the poloidal divertor is probably the best understood and most often proposed type. The discussion below of theoretical models, and the rest of this chapter, will be restricted to the poloidal divertor when a specific geometry is required, even though the adjective "poloidal" may not be mentioned.

1.B.2. Theoretical Models

The most fundamental quantities to ask from a theoretical model of a divertor are the distributions of plasma density and plasma flux found near the wall under the influence of the divertor. Even these are not trivial to estimate, because a divertor is inherently two-dimensional, with very different processes dominating the transport in the two directions. However, some insight can be gained from one-dimensional models.

First, consider the flow along field lines to the divertor. A model based on fluid theory, though grossly simplified, provides some justification for other assumptions to be made later. Take the plasma to be a single fluid; in fact, this will be an almost purely hydrodynamic model. The divertor's scrape-off region is to be thought of as a channel extending for a distance L in the y-direction, with a fixed width w in the x-direction and symmetry in the z-direction (see Figure 1.3). The y-direction corresponds to the direction of the magnetic field, with y=0 representing a symmetry plane, such as the midplane of a tokamak with double-null poloidal divertor, and y=L at the divertor throat, in which case

$$L \approx \frac{\pi}{2} a \frac{B}{B_p} \approx \frac{\pi}{2} qR \tag{1.3}$$

with q the tokamak's safety factor. The x-direction corresponds to minor radius, with w being the distance from the separatrix to the wall. The fluid is assumed to be uniform across this width. The equation of motion for flow in the y-direction is

$$nm_i v_y \frac{dv_y}{dy} = -\nabla p = -kT_e \frac{dn}{dy} \tag{1.4}$$

if $T_i < T_e$ and $dT_e/dy = 0$. The assumption of isothermal electrons is likely to be valid since the electron thermal speed is much larger than the ion acoustic speed, which will turn out to be the maximum flow speed. If the divertor has to take whatever diffuses out of the

confinement region then there is a flux into the channel of Γ_o everywhere on the side x=0, representing the separatrix. By symmetry the flux across the other sides is 0, except for the end y=L which is the exhaust to the pumping chamber, and the side x=w where it is assumed also to be 0 since most plasma particles are expected to go to the divertor. Then continuity requires

$$0 = \nabla \cdot \Gamma = -\frac{\Gamma_o}{w} + \frac{d}{dy}(nv_y)$$

$$nv_y = \Gamma_o \frac{y}{w} \tag{1.5}$$

Integrating Eq. (1.4),

$$\frac{1}{2} v_y^2 = -c_s^2 \ell n \frac{n}{n_o} \tag{1.6}$$

where $c_s = (kT_e/m_i)^{\frac{1}{2}}$ is the ion acoustic speed, and n_o is the density at y=0. Substituting from Eq. (1.5),

$$y = w \frac{c_s}{\Gamma_o} n\sqrt{2\ell n \frac{n_o}{n}} \tag{1.7}$$

As y increases from 0, n decreases from n_o, until dy/dn = 0. This occurs when $n = n_o e^{-\frac{1}{2}}$, $y = wc_s\Gamma_o^{-1}n_o e^{-\frac{1}{2}}$, and $v_y = c_s$. This is analogous to fluid flow in a converging channel or nozzle, except here the addition of material takes the place of narrowing the channel. The flow velocity is limited to the sound speed, and can exceed it only if

the nozzle's cross-sectional area has a minimum where the velocity reaches the sound speed.[19] Supersonic flow requires the nozzle to diverge after this point, but the analogous removal of fluid does not occur in the present model, so $v_y \leq c_s$ throughout. But the Bohm sheath criterion[20] requires the fluid velocity at an absorbing obstacle such as the divertor's neutralizer plate to be equal to c_s, so the above solution just covers the length of the divertor. Setting $L = wc_s\Gamma_o^{-1}n_o e^{-\frac{1}{2}}$ gives a characteristic density in the scrape-off zone of

$$n_o = \frac{\Gamma_o}{c_s}\frac{L}{w}e^{\frac{1}{2}} \tag{1.8}$$

Another important conclusion is that the density varies by only a factor of $e^{-\frac{1}{2}} = .61$ over the length of the scrape-off zone. If the flow had been assumed adiabatic rather than isothermal a very similar solution would result, with only small changes in density and temperature along the length of the divertor. Therefore it may not be too bad an approximation, when examining variations across the width of the scrape-off zone, to assume that density and temperature are constant along any field line.

Turning next to such a model, the same geometry (Figure 1.3) is used, with different assumptions. Now the plasma is assumed uniform in y and z and variable in x. Transport in the x-direction is by Fick's law diffusion:

$$\Gamma_x = -D_\perp \frac{dn}{dx} \tag{1.9}$$

Plasma is lost to the divertor at y=L, with a flux $\Gamma_d(x)$. This process can be characterized by a parallel confinement time τ_{11}, so that

$$\Gamma_d(x) = n(x)L/\tau_{11} \tag{1.10}$$

Two natural possibilities for τ_{11} are the following: First, if the velocity at y=L can be specified as c_s, as discussed above, then $\Gamma_d(x) = n(x)c_s$, so $\tau_{11} = L/c_s$. Second, a particle approaching the divertor may encounter an increasing magnetic field, due either to the 1/R dependence of the main field or to the perturbation required to create the divertor, and thus be prevented from reaching the divertor by mirror-trapping. If most particles are mirror-trapped then τ_{11} will be the time required for particles to scatter into the loss cone, or the ion collision time τ_{ii}. However, it has been suggested[21] that since the loss cone is not filled with untrapped particles (they are immediately lost to the divertor) the scrape-off region would be subject to velocity-space instabilities, which can scatter particles into the loss cone much faster than classical collisions. In this case $\tau_{11} = L/c_s$ would still be valid. Experimental measurements from FM-1[22] and DIVA[23] tend to confirm this, showing the flow velocity into the divertor to be .3 to .5 of c_s.

The continuity equation, in this case applied to slabs of infinitesimal thickness in the x-direction, gives

$$0 = \nabla \cdot \Gamma = \frac{d\Gamma_x}{dx} + \frac{\Gamma_d(x)}{L}$$

$$\frac{d}{dx}\left(D_{\perp}\frac{dn}{dx}\right) = \frac{n}{\tau_{11}} \tag{1.11}$$

Various forms for $D_{\perp}$ and τ_{11} can be inserted to obtain the x-dependence of the density. If $D_{\perp}$ and τ_{11} are assumed constant (for instance, Bohm diffusion with no temperature gradients) then the general solution is

$$n(x) = A_1 e^{-x/\lambda} + A_2 e^{x/\lambda} \tag{1.12}$$

where $\lambda = \sqrt{D_{\perp}\tau_{11}}$ (1.13)

A_1 and A_2 are determined by boundary conditions. One reasonable condition is to assume the plasma flux crossing the separatrix is a constant determined by processes in the confined plasma, rather than by what happens in the divertor:

$$\Gamma_x(o) = \Gamma_o \tag{1.14}$$

For the second condition, we may set $A_2=0$. This amounts to assuming $n\to 0$ as $x\to\infty$, which is a reasonable approximation everywhere except near $x = w$ as long as w is greater than several times λ. This gives

$$n(x) = n_o e^{-x/\lambda} \tag{1.15}$$

where $$n_o = \frac{\Gamma_o \lambda}{D_\perp} = \Gamma_o \sqrt{\frac{\tau_{11}}{D_\perp}} \tag{1.16}$$

Also, $$\Gamma_x(w) = \Gamma_o e^{-w/\lambda} \tag{1.17}$$

Note that the same n_o results if λ is substituted for w in Eq. (1.8). A better boundary condition is n(w)=0. Then

$$n(x) = n_o \frac{\sinh \frac{w-x}{\lambda}}{\cosh \frac{w}{\lambda}} \tag{1.18}$$

and $$\Gamma_x(w) = \frac{\Gamma_o}{\cosh \frac{w}{\lambda}} \tag{1.19}$$

with n_o as defined above. The two solutions for n(x) are nearly equal up to a distance λ from the wall at w, and the values for flux reaching the wall, $\Gamma_x(w)$, agree within a factor of 2, which is unimportant compared to $e^{-w/\lambda}$. A density source term due to ionization of neutrals can be added, in which case[24]

$$\lambda = \sqrt{D_\perp \tau_{11} (1 - n_{neut} \langle \sigma v_e \rangle \tau_{11})^{-1}} \tag{1.20}$$

where n_{neut} is the neutral density and $\langle \sigma v_e \rangle$ the electron ionization rate. Mense[5] solves Eq. (1.11) for various forms of $D_\perp$ and τ_{11}; the resulting density profiles, while not always exponential, have scale lengths still roughly given by Eq. (1.20).

Some two-dimensional theories of divertors have been developed.

Hinton and Hazeltine[25] start by assuming collisional electrons but collisionless ions in the scrape-off region, and neoclassical diffusion. Then most ions are kept from reaching the divertor by mirror-trapping, and τ_{ll} becomes τ_{ii}, the time required for ions to scatter into the loss cone and go to the divertor. They find

$$\lambda \approx 3.9 \frac{\rho_{pi} a}{R} \tag{1.21}$$

where ρ_{pi} is the ion gyroradius evaluated with the poloidal magnetic field, or the banana width. This can be approximately obtained from Eq. (1.13), with the banana regime ion diffusion coefficient $D_{\perp} \sim \rho_{pi}^2 \nu_i$ and $\tau_{ll} \sim \nu_i^{-1}$. However, as pointed out before, $\tau_{ll} = \tau_{ii}$ is not likely to be true due to microinstabilities.

Boozer[26] points out that, although most theories such as the preceding ones assume equal fluxes of ions and electrons everywhere, electrons and ions may leave the divertor in different places while still maintaining charge neutrality, since the diverted field lines intersect a conducting obstacle. Allowing this, and using two-fluid theory with collisional electrons and cold ions, he finds that ions leave the divertor over a width

$$\lambda_i = \rho_i(T_e) \tag{1.22}$$

the ion gyroradius evaluated at the electron temperature, and this defines the scrape-off distance. Due to their more rapid thermal

speed, most electrons leave the divertor over the much narrower width

$$\lambda_e = \rho_e \frac{L}{\ell_e} \tag{1.23}$$

where ℓ_e is the electron mean free path. There is evidence for this behavior in several experiments,[7,27] including the present one (see Chapters 4.B and 6.B). However, in a tokamak, Boozer's assumption of cold ions is not likely to be valid; $T_i \geq T_e$ is expected in the divertor scrape-off zone.

Mense and Emmert[5,28] have carried out a numerical model which, while only one-dimensional, is much more detailed than any of the above. The model includes particle and energy transport in the core of the tokamak as well as in the divertor region. Diffusion in the central plasma is assumed due to trapped particle instabilities, while the diffusion coefficient in the scrape-off region is taken as Bohm diffusion multiplied by a numerical factor (~ .1) to match the two diffusion coefficients at the separatrix. Parallel transport to the divertor is by thermal flow at c_s, with electron and ion fluxes equal everywhere. The model is applied to the operating parameters of the conceptual reactors UWMAK-II[29] and UWMAK-III.[30]

While a complete description of the results is neither possible nor appropriate here, some of the more important conclusions are these: n, T_e, and T_i all drop rapidly in the scrape-off region, with scale lengths of about 5 cm for n and T_e, and 10 cm for T_i (to be compared to the distance of 50 cm from separatrix to wall). The more rapid cooling

of electrons is due to the electrostatic sheath required to equalize fluxes of ions and electrons at the neutralizer plate, which allows only the most energetic electrons to reach it. This rapid removal of particles and energy by the divertor causes n to decrease by a factor of 100, and T_e and T_i by 10, from the center of the plasma to the separatrix.

The plasma flux reaching the wall is 10^{-3} of that leaving the plasma core, and consequently the greatest source of impurities is sputtering from the wall by fast charge-exchange neutrals, originating near the separatrix. The slow neutrals responsible for this are those returning from the divertor, due to an assumption of only 90% efficient capture of the diverted plasma. Impurity effects on the plasma are not included in the model; based on the profiles calculated without impurities it is estimated that 90% of carbon atoms released from the wall would be ionized before reaching the separatrix, and most of these would go to the divertor before diffusing across the separatrix.

The question of impurity transport is an important one, however, since the diffusion up the density gradient mentioned earlier can lead to a large steady-state concentration at the center of the plasma, even for a small flux of impurities entering across the separatrix. In steady state, with impurity diffusion given by Eq. (1.1), the density profile of impurity ions of charge Ze is proportional to the density profile of hydrogen ions raised to the power Z, so that the impurity profile is sharply peaked at the center of the plasma.[31] Using this result, and a divertor model like that of Eqs. (1.11) to (1.17), the

steady-state impurity concentration averaged over the density profile inside the separatrix is estimated as[32]

$$I \approx \frac{2\gamma}{Z+1} \frac{\tau_Z}{\tau_H} \left(\frac{N_H}{n_H}\right)^{Z-1} \tag{1.24}$$

Here γ is the number of impurity atoms released into the scrape-off layer from the wall or divertor for each hydrogen ion leaving the central plasma, so that γ depends on sputtering processes at the wall and in the divertor and on how much plasma reaches each. τ_Z and τ_H are the parallel confinement times for impurity and hydrogen ions, respectively in the divertor, and N_H/n_H is the ratio of central plasma density to density at the separatrix. For Mense's density profiles, even assuming $\tau_Z=\tau_H$, when the impurity is carbon,

$$I \approx \frac{2\gamma}{Z+1} 10^{2(Z-1)} \tag{1.25}$$

Requiring $I < 3\%$ for carbon gives $\gamma < 6\times10^{-6}$ for C^{+3}, and $\gamma < 1\times10^{-11}$ for fully stripped carbon. Even the first value of γ is quite stringent, and the second is probably impossible. Mense's values of 10^{-3} of outgoing plasma reaching the wall, and a sputtering coefficient of 10^{-2}, already give $\gamma \sim 10^{-5}$ without even considering other sources of impruities. However, if diffusion is due to turbulence rather than classical collisions between particles, the impurities and hydrogen ions may have the same diffusion coefficient, in which case the problem is much less severe.

All of the models described above provide useful insights, but all contain assumptions and simplifications which prevent their being considered as accurate predictions of the behavior of an actual divertor in a reactor. There is much work still to be done, both theoretical and experimental, toward the understanding of transport and other processes in a divertor.

REFERENCES - CHAPTER 1

1. Review articles on the tokamak include:

   L.A. Artsimovich, Nuclear Fusion 12, 215 (1972).
   H.P. Furth, Nuclear Fusion 15, 487 (1975).

   while more popular articles include:

   B. Coppi, J. Rem, Sci. Am. 227:1, 65 (1972).
   H.P. Furth, Sci. Am. 241:2, 50 (1979).
   M. Murakami, H.P. Eubank, Physics Today 32:5, 25 (1979).

2. D.M. Meade, Nuclear Fusion 14, 289 (1974).

3. C.L. Longmire and M.N. Rosenbluth, Phys. Rev. 103, 507 (1956).

4. P.H. Rutherford, Phys. Fluids 17, 1782 (1974).

5. A.T. Mense, University of Wisconsin Ph.D. Thesis (1977).

6. L. Spitzer, Jr., Phys. Fluids 1, 253 (1958).

7. C.R. Burnett, et al., Phys. Fluids 1, 483 (1958).

8. K. Ando, et al., in Plasma Physics and Controlled Nuclear Fusion Research (Proc. 5th Conf., Tokyo, 1974), (IAEA, Vienna, 1975), Vol. II, p. 103.

9. Y. Shimomura, Phys. Fluids 19, 1635 (1976).

10. G.A. Bobrovskii and V.E. Golant, Fiz. Plazmy 4, 969 (1978), (Sov. J. Plasma Phys. 4, 540 (1978))

11. D.M. Meade and J.C. Sinnis in Plasma Wall Interaction (Proc. Int. Symp., Jülich, 1976), (Pergamon Press, Oxford, 1977), p. 683.

12. G. Haas and M. Keilhacker, Ibid., p. 691.

13. A. Kitsunezaki, et al., Ibid., p. 697.

14. DIVA Group, Nuclear Fusion 18, 1619 (1978).

15. M. Nagami, et al., Nuclear Fusion 18, 1347 (1978).

16. P.E. Stott, et al., Nuclear Fusion 17, 481 (1977).

17. P.E. Stott, et al., Nuclear Fusion 18, 475 (1978).

18. J.W.M. Paul, et al., in Plasma Physics and Controlled Nuclear Fusion Research (Proc. 6th Conf., Berchtesgaden, 1976), (IAEA, Vienna, 1977), Vol. II, p. 269.

19. P.A. Thompson, Compressible-Fluid Dynamics (McGraw-Hill, N.Y., 1972), p. 276.

20. D. Bohm in Characteristics of Electrical Discharges in Magnetic Fields, A. Guthrie, R.K. Wakerling, eds., (McGraw-Hill, N.Y., 1949), p. 77. (See also the discussion of Langmuir probes in chapter 3.C.1.)

21. A.T. Mense, G.A. Emmert, and J.D. Callen, Nuclear Fusion 15, 703 (1975).

22. H. Hsuan, M. Okabayaski, and S. Ejima, Nuclear Fusion 15, 191 (1975).

23. H. Ohtsuka, et al., Plasma Phys. 20, 749 (1978).

24. D.M. Meade, et al., in Plasma Physics and Controlled Nuclear Fusion Research (Proc. 5th Conf., Tokyo, 1974), (IAEA, Vienna, 1975), Vol. 1, p. 605.

25. F.L. Hinton and R.D. Hazeltine, Phys. Fluids 17, 2236 (1974).

26. A.H. Boozer, Phys. Fluids 19, 1210 (1976).

27. C.M. Strawitch and G.A. Emmert, Bull. Am. Phys. Soc. 23, 896 (1978), also University of Wisconsin PLP 795 (1979).

28. A.T. Mense and G.A. Emmert, Nuclear Fusion 19, 361 (1979).

29. R.W. Conn, et al., in Plasma Physics and Controlled Nuclear Fusion Research (Proc. 5th Conf., Tokyo, 1974), (IAEA, Vienna, 1975), Vol. III, p. 497. See also B. Badger, et al., University of Wisconsin FDM-112 (1975).

30. R.W. Conn, et al., in Plasma Physics and Controlled Nuclear Fusion Research (Proc. 6th Conf., Berchtesgaden, 1977), (IAEA, Vienna, 1977), Vol. III, p. 203. See also B. Badger, et al., University of Wisconsin FDM-150 (1976).

31. J.B. Taylor, Phys. Fluids 4, 1142 (1961).

32. J.B. Taylor in Nuclear Fusion Suppl. on Fusion Reactor Design Problems (IAEA, Vienna, 1974), p. 403.

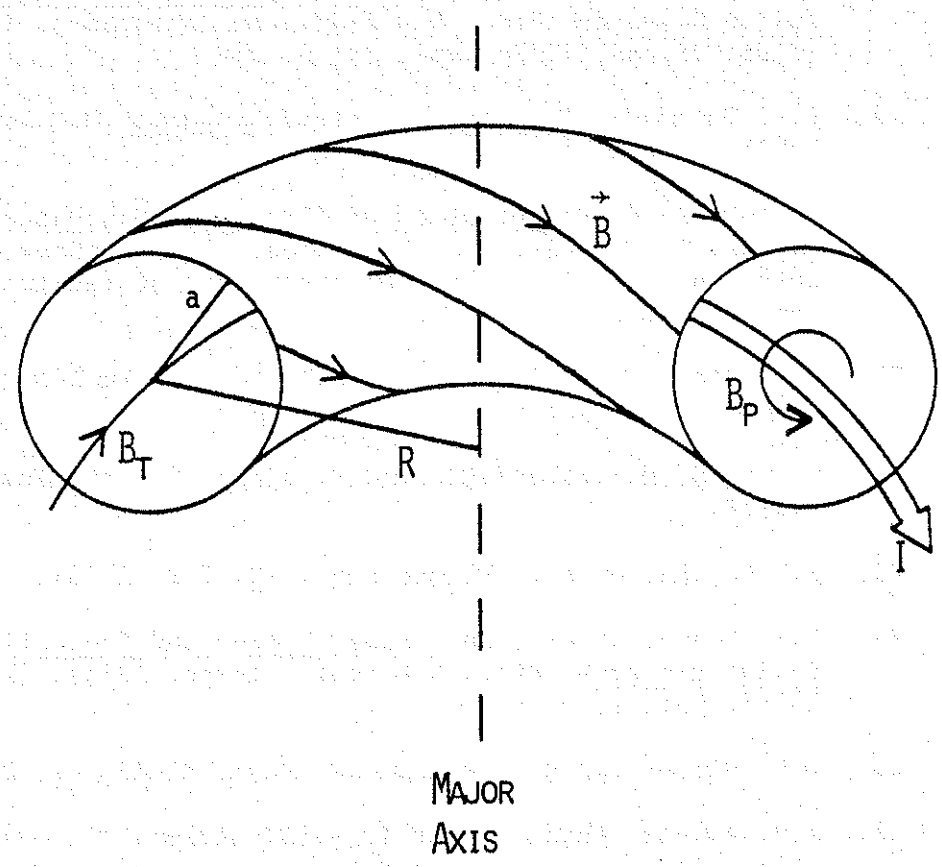

Fig. 1.1 - Tokamak plasma (schematic) showing plasma current I, toroidal and poloidal magnetic fields B_t and B_p, total magnetic field $\vec{B}$, and major and minor radii R and a.

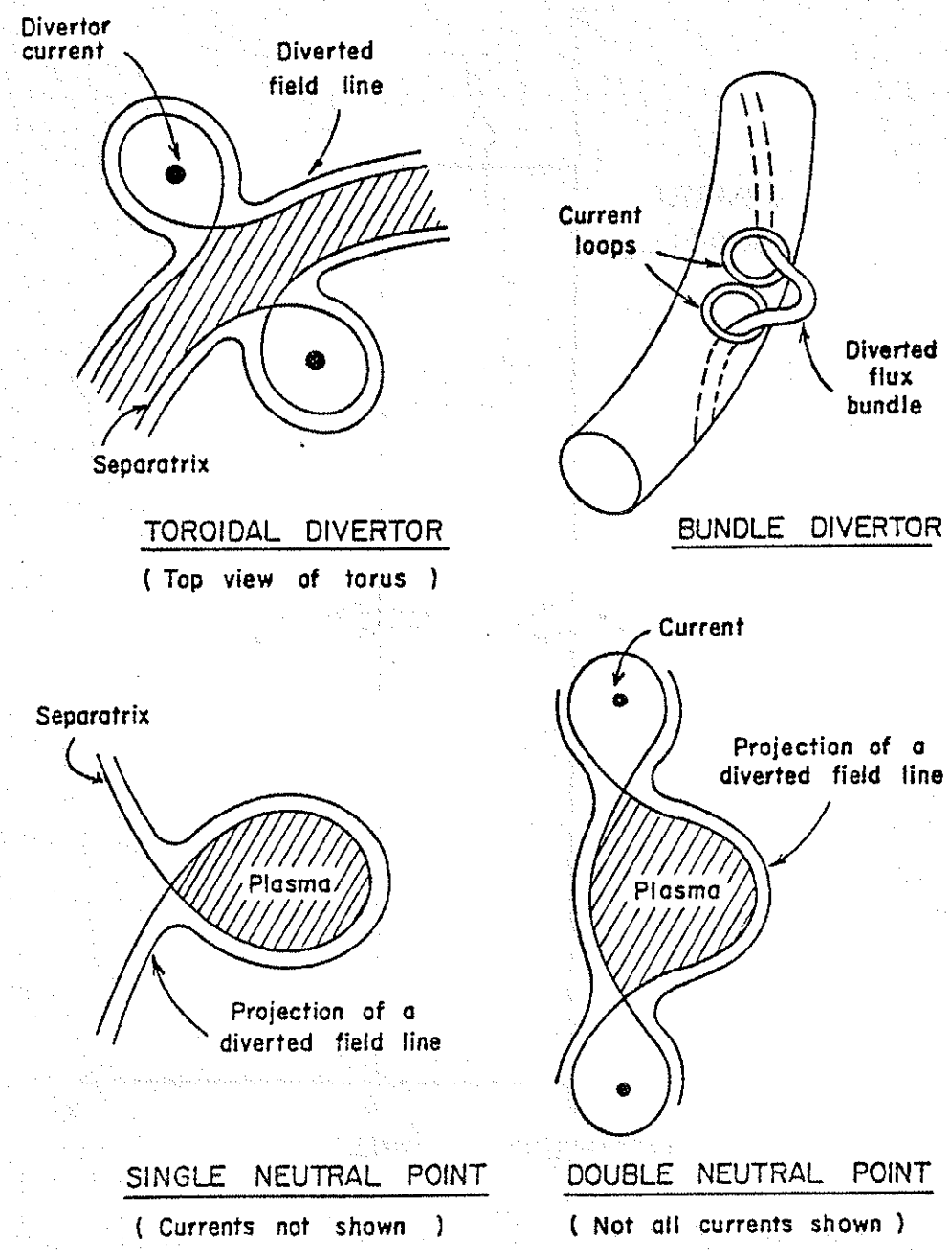

Fig. 1.2 - Divertors for toroidal devices. Magnetic field lines are shown projected into a toroidal plane (toroidal divertor) or poloidal plane (poloidal divertors). (from ref. 29)

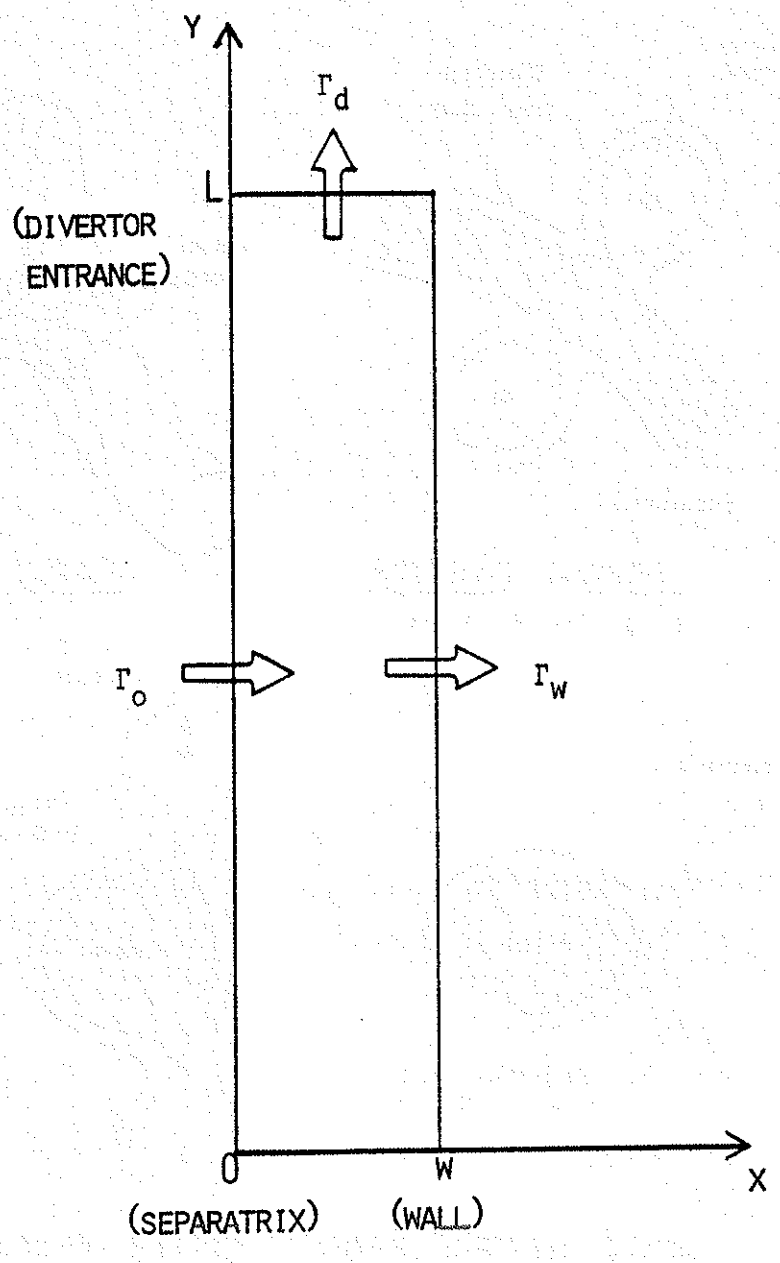

Fig. 1.3 - Slab model of divertor scrape-off region. Γ_o is plasma flux leaving confinement region, Γ_d is plasma flux to pumping chamber, Γ_w is plasma flux reaching wall.

CHAPTER 2

THEORY OF E×B DRIFT DIVERTOR

2.A. Introduction

In the preceding chapter it was seen that the behavior of a divertor in a tokamak reactor cannot yet be predicted theoretically with great confidence. Present divertor experiments show both reduction of wall loading and screening of incoming impurities, but probably not to the extent required to meet the stringent requirements for a steady-state or long-pulse reactor. We turn now to the subject of the present work, the suggestion that the E×B drift due to an externally applied electric field could be used, either alone or in conjunction with the thermal flow of a conventional divertor, to take plasma from the scrape-off layer to a remote pumping chamber for disposal.[1]

Figure 2.1 shows, schematically, the physical layout envisioned for an E×B divertor in a tokamak. The figure shows the minor cross-section of a tokamak, such as UWMAK-III, with a double-null poloidal divertor. Added to the picture are radial electric fields in the region between the separatrix and the wall, with the proper sign so that $E \times B_t$ is toward the divertor. The $E \times B_p$ component of the drift is in the symmetry (toroidal) direction and can be ignored; in a typical tokamak $B_t >> B_p$, so the E×B drift is mainly in the poloidal direction.

One way to apply such an electric field might be to divide the wall into four segments electrically insulated from each other, as shown, and to give them alternately positive and negative DC bias potentials with respect to the central plasma. The diverted field lines lead to an external pumping chamber and terminate on a plate where the plasma is neutralized; the neutralizer plate is in good electrical contact with the plasma, and may be used to provide a reference potential for biasing the segmented walls. Alternatively, the neutralizer plate may be divided into strips extending in the toroidal direction, which could be held at graded potentials. Due to the good conduction along magnetic field lines, the desired electric field could be applied in this manner.

One could also imagine omitting the magnetic field divertor, while retaining the slots in the wall, and using only E×B drifts to remove the outer part of the plasma through the slots. In this case the slots would probably have to spiral with the field lines in order to avoid short-circuiting parallel to field lines across the slots (Figure 2.2). The coils required to shape the poloidal magnetic field for a poloidal divertor increase the cost and complicate the maintainance of a tokamak reactor. If it were possible to perform the functions of a divertor with E×B drifts alone, this might simplify the construction of a reactor.

If the "unload" function of the divertor, that is, reduction of plasma flux to the wall, is most important, then the E×B drift can be made large enough to remove plasma more rapidly than thermal flow, and

thus prove advantageous.

On the other hand, if, as Mense suggests, the major contribution to impurity sputtering is due to neutrals rather than plasma particles bombarding the wall, then the emphasis will likely be on the "screening" function, ionizing and removing impurities before they can reach the plasma core. It has even been suggested that in a poloidal magnetic divertor it may be necessary to inject cold plasma onto the diverted field lines if the naturally occurring density is not high enough.[2] If E×B drifts alone were used to remove the outer layer of plasma, as in Figure 2.2, then the speed of removal could be adjusted through the magnitude of the electric field to maintain the desired density for ionization of impurities.

The ratio of the thermal speed of impurity ions (Z) to that of hydrogen ions (H) is $(T_Z/T_H)^{\frac{1}{2}}\ (m_H/m_Z)^{\frac{1}{2}}$. The mass ratio is always less than unity, and Mense's model suggests that the temperature ratio is likely to be .1 or less, so impurity ions will go to the divertor considerably slower than fuel ions. The E×B drift speed, however, is the same to first order for all charged species, so it is proportionately more effective at removing impurities, as is desirable for a screening divertor.

If the plasma goes to the divertor by thermal flow, each ion lost to the divertor carries an average energy of $2\ kT_i$. If an electrostatic sheath retards the electrons to make the fluxes of electrons and ions equal, then each electron lost to the divertor carries an average energy of[3] $(\frac{1}{2}\ln(T_e m_i/T_i m_e)+2)kT_e$, or about $6\ kT_e$ if $T_e = T_i$.

This causes the rapid cooling in the scrape-off region seen in Mense's model. Particles of all energies have the same E×B drift speed (to first order) and thus particles taken to the divertor by E×B drift would each carry an average energy of only 1.5 kT. If the particle fluxes are the same for the magnetic field divertor and E×B divertor cases, the E×B divertor causes less surface cooling of the plasma.

Fluid theory predicts the rather surprising result that all plasma diffusing across a separatrix such as the divertor separatrix in Figure 2.1 is channeled through the poloidal field nulls, or "X-points," seen near the entrances to the pumping chambers.[4] This raises the speculation that the density in the scrape-off zone could be controlled by more localized E×B drifts applied at the X-points. However, surfaces of constant poloidal magnetic flux ψ (see Appendix) tend to be equipotentials, and if this property is maintained near the X-point then the electric field is

$$E = -\nabla\phi = -\frac{d\phi}{d\psi}\nabla\psi = -\frac{d\phi}{d\psi}2\pi RB_p \qquad (2.1)$$

This goes to zero at the X-point, which would indicate that it is not possible to apply a perpendicular electric field at the X-point. However, the poloidal connection length along field lines becomes infinite at the separatrix, so near the separatrix magnetic flux surfaces need not be equipotentials. The DC electric field distribution is determined by $\nabla \cdot J = 0$ (see Chapter 4), and in some neighborhood of the X-point the poloidal component of magnetic field becomes small

enough that the poloidal component of electric field is determined by perpendicular rather than parallel conduction. In such a region equipotential surfaces deviate from magnetic flux surfaces, allowing a perpendicular electric field at the X-point. The size of the neighborhood, and of the electric field, depend on the ratio of perpendicular to parallel conductivities, as well as on the details of the geometry.

These are some of the possible advantages of an E×B divertor. There may, however, be limits on the drift velocity and electric field which can be sustained. These will be discussed later.

The magnitude of electric field required for this scheme can be estimated as follows: if the speed of parallel flow in a poloidal divertor is v_o (where probably $v_o \lesssim c_s$), then the poloidal component of this flow is $v_o B_p/B$. The poloidal component of E×B drift is EB_t/B^2, so the condition for the E×B drift to make an appreciable contribution to the flow toward the divertor is

$$\frac{EB_t}{B^2} \gtrsim v_o \frac{B_p}{B} \tag{2.2}$$

or, since $B_t \gg B_p$, approximately

$$E \gtrsim v_o B_p \tag{2.3}$$

For $B_p = 5$ kG and deuterium at 1 keV this gives $E \gtrsim 10^3$ V/cm, but for carbon at 100 eV it gives $E \gtrsim 140$ V/cm, a not unreasonable magnitude.

2.B. Comparison to Similar Proposals

Somewhat similar ideas have been proposed by others. Braginskii[5] suggests using a segmented limiter biased at graded potentials, similar to the segmented neutralizer plate mentioned above, to apply an E×B drift, which could cause the outer edge of the plasma to rotate fast enough to expel impurities by centrifugal force, reversing their tendency to diffuse toward larger plasma density. Expulsion of impurities by centrifugal force is also suggested by Lehnert[6] and Consoli.[7] The latter paper also suggests using E×B drifts to guide the outer layer of plasma away from the confinement region, somewhat in the manner of Figure 2.2.

A brief digression seems worthwhile to discuss the expulsion of impurities by centrifugal force. Qualitatively, if the plasma rotates due to an E×B drift (in the present case, in the poloidal direction) then the centrifugal force causes an apparent additional radial force outward on the ions, proportional to their mass. This in turn modifies their poloidal drift speed, so that species of different mass drift at different speeds. In the fluid picture, a frictional force between species results, with the proper sign, when crossed with B, to give the heavier species an outward drift. Kinetic theory gives the modification of Eq. (1.1):[6]

$$\Gamma_{ij} = \alpha_{ij} \left\{ \left[\frac{\nabla n_j}{q_j n_j} - \frac{\nabla n_i}{q_i n_i} \right] - \left(\frac{m_j}{q_j} - \frac{m_i}{q_i} \right) \frac{1}{r} \left(\frac{E}{B} \right)^2 \frac{1}{kT} \right\} \qquad (2.4)$$

where r is the radius of rotation, the minor radius in this case. The centrifugal force term makes a significant contribution toward expelling impurities if

$$\frac{m_i}{q_i}\frac{1}{r}\left(\frac{E}{B}\right)^2\frac{1}{kT} \gtrsim \frac{\nabla n_j}{q_j n_j}$$

or (2.5)

$$E \gtrsim \sqrt{Z}\, v_o B$$

where v_o is the thermal speed of the impurity. This is greater than the condition of Eq. (2.3) by a factor of $Z^{\frac{1}{2}}B/B_p \sim 10Z^{\frac{1}{2}}$ for typical tokamak parameters. Hence the expulsion of impurities requires electric fields at least an order of magnitude larger than the E×B divertor, a possible disadvantage. Also, therefore, centrifugal force will not play an important part in the E×B divertor schemes.

2.C. Single particle Orbits

We now examine in a little more detail the motion of a single particle under the influence of such a radial electric field. The combined curvature and ∇B drifts due to the 1/R dependence of the magnetic field are, for an average particle,

$$\vec{V}_B = \frac{m}{q}\left(V_\perp^2 + 2v_{11}^2\right)\frac{\vec{B}\times\vec{\nabla B}}{B^3} \sim \sqrt{\frac{2kT}{m}}\,\frac{\rho}{R} \qquad (2.6)$$

where ρ is the gyroradius. Using Eq. (2.3) above, the ratio of E×B drift speed to curvature and ∇B drift speed is

$$\frac{v_E}{v_B} \sim \frac{v_o B_p/B}{v_o \rho/R} = \frac{R}{\rho}\frac{B_p}{B} = \frac{1}{q}\frac{a}{\rho} \tag{2.7}$$

where, in this equation only, q denotes the tokamak safety factor. The ratio of minor radius to ion gyroradius for a tokamak reactor is in the range 10^2 to 10^3, so the applied E×B drift will be much larger than the drift due to inhomogeneity of the magnetic field, which can consequently be ignored hereafter.

If a particle moves from a region of no electric field (such as the midplane in Figure 2.1) to a region of electric field, it will undergo a polarization drift given by

$$\vec{v}_r = \frac{m}{q}\frac{1}{B^2}\frac{d\vec{E}}{dt} \tag{2.8}$$

If E is given by Eq. (2.3), then the radial displacment of the particle's guiding center is

$$\Delta r = \int v_r \, dt = \frac{mE}{qB^2} \sim \rho \frac{B_p}{B} \tag{2.9}$$

The radial displacement is smaller then a gyroradius and much smaller than a banana width, and consequently can be neglected.

The E×B drift will have the effect of taking some particles to the divertor which would otherwise be prevented from reaching it by

mirror trapping. If a particle starts out (say, near the midplane) with parallel velocity $v_{\parallel o}$ and perpendicular velocity $v_{\perp o}$ at a magnetic field B_o, then its (adiabatically invariant) magnetic moment is $\mu = mv_{\perp}^2/2B$. The equations of motion parallel and perpendicular to field lines are

$$m\frac{dv_{\parallel}}{dt} = -\mu\nabla_{\parallel}B \tag{2.10a}$$

and

$$v_{\perp} = v_E = \frac{E}{B} \tag{2.10b}$$

A tokamak can be roughly approximated by assuming that ∇B is constant but makes an angle $\frac{1}{2}\pi-\alpha$ with the field lines. This corresponds to ∇B pointing in the poloidal direction, with $\tan\alpha = B_p/B_t$. Curvature of field lines is ignored. Integrating Eqs. (2.10), the net poloidal drift velocity is found to be

$$v_p = \pm[(v_E\cos\alpha+v_{\parallel o}\sin\alpha)^2 - \frac{2\mu}{m}(B-B_o)\sin^2\alpha]^{\frac{1}{2}} \tag{2.11}$$

If M is the mirror ratio, or maximum value of B/B_o, then the particle is not trapped if

$$(v_E\cot\alpha+v_{\parallel o})^2 > v_{\perp o}^2(M-1) \tag{2.12}$$

The loss cone has been shifted by an amount $v_E \cot\alpha = E/B_p$, and if E/B_p is an appreciable fraction of the thermal speed, as suggested by Eq. (2.3), then a large fraction of the particles that previously fell outside the loss cone now fall inside and can reach the divertor (Figure 2.3). The E×B drift may in addition shift the center of the distribution function in the $v_\perp$ direction by v_E, but this is less important than the shift of the loss cone by the factor $\cot\alpha$. Ignoring this small correction, the fraction of trapped particles for a Maxwellian distribution is reduced from $f_t = ((M-1)/M)^{\frac{1}{2}}$ to

$$f_t = \left(\frac{M-1}{M}\right)^{\frac{1}{2}} \exp\left(-\frac{m}{2kT}\frac{v_E^2 \cot^2\alpha}{M}\right) \tag{2.13}$$

If $v_E \cot\alpha = E/B_p = (2kT/m)^{\frac{1}{2}}$, then $f_t = ((M-1)/M)^{\frac{1}{2}}\, e^{-1/M}$.

At first glance this conclusion may appear to violate conservation of energy. The kinetic energy of the particle is $\mu B + \frac{1}{2}mv_{11}^2$, and now the particle is found at larger values of μB than at its turning point ($v_{11}=0$) in the absence of E×B drift. Yet $\vec{B}$ can do no work on the particle, and $\vec{E}$ is perpendicular to both the parallel motion and the E×B drift motion, and thus apparently can do no work on the particle (averaged over a cyclotron period). However, note that the magnetic field gradient also induces a drift

$$\vec{v}_{\nabla B} = \frac{\mu}{q}\frac{\vec{B}\times\nabla B}{B^2} \tag{2.14}$$

This has a component parallel to $\vec{E}$, so the electric field does work on

the particle at a rate

$$q\vec{E} \cdot \vec{v}_{\nabla B} = \mu\vec{E} \cdot \frac{B\times\nabla B}{B^2} = \mu\nabla B \cdot \frac{\vec{E}\times\vec{B}}{B^2} \tag{2.15}$$

which is just the rate at which the particle gains extra μB kinetic energy due to the component of E×B drift parallel to ∇B. Therefore energy is conserved.

2.D. Density Profiles

Next, we consider the effect of the E×B drift on the density profile. The model of Eq. (1.11) must be modified by the addition of the poloidal component of the E×B drift:

$$\frac{d}{dx}\left(D_\perp \frac{dn}{dx}\right) = \frac{n}{\tau_{11}} + \frac{n}{\tau_E} \tag{2.16}$$

where $\tau_E = L_\perp/v_E = \frac{1}{2}\pi aB/E$, and $\tau_{11} = L_{11}/v_{11} = \frac{1}{2}\pi aB/v_{11}B_p$. Assuming $D_\perp$ and τ_{11} to be constant, there are two cases which are natural to examine: E constant and E inversely proportional to n. The second form for E is expected to be more realistic, being derivable from either the low-frequency dielectric constant or perpendicular conductivity, as will be discussed in Chapter 4.

i) E constant

The solution is exactly the same as that given by Eqs. (1.12) to (1.19), making everywhere the substitution

$$\lambda \to \lambda' = \sqrt{D_\perp \left(\frac{1}{\tau_{11}} + \frac{1}{\tau_E}\right)^{-1}} = \lambda \Big/ \sqrt{1 + \frac{\tau_{11}}{\tau_E}} \tag{2.17}$$

The fraction of plasma flux reaching the wall is

$$\frac{\Gamma(w)}{\Gamma_o} = e^{-w/\lambda'} = e^{-\frac{w}{\lambda}\sqrt{1 + \frac{\tau_{11}}{\tau_E}}} \tag{2.18}$$

which can be controlled through τ_E by altering E.

ii) $E = E_o n_o / n$

Letting

$$\tau_E = \frac{\pi a B}{2E} = \frac{\pi a B}{2E_o n_o} n = \frac{n}{n_o} \tau_{Eo} \tag{2.19}$$

Eq. (1.11) becomes

$$D_\perp \frac{d^2 n}{dx^2} = \frac{n}{\tau_{11}} + \frac{n_o}{\tau_{Eo}} \tag{2.20}$$

which has the general solution

$$n(x) = A_1 e^{-x/\lambda} + A_2 e^{x/\lambda} - n_o \frac{\tau_{11}}{\tau_{Eo}} \tag{2.21}$$

with λ the same as before. A_1 and A_2 are again determined from the boundary conditions. For the first boundary condition we can again use Eq. (1.14). The second boundary condition is much more important than before, and less straightforward. $n(w) = 0$ will no longer do,

since this leads to an infinite electric field at the wall, and an infinite potential drop between the wall and any point in the plasma. The density could be held constant at some small but non-zero value at the wall, but since this is where the electric field is largest the solution will depend strongly on the particular value chosen. A better answer may be to assume that the plasma strikes the wall at a fixed velocity v_w, giving the boundary condition

$$n(w) = \frac{\Gamma(w)}{v_w} \tag{2.22}$$

The solution will still depend strongly on the value of v_w, but there may be better physical reasons for picking a particular value. For instance, ions whose guiding centers diffuse to within a gyroradius of the wall may then strike the wall at the thermal speed, rather than at a speed determined by diffusion. The resulting solution is complex enough to make it worthwhile to introduce the following scaling:

$$\xi = \frac{x}{\lambda}$$

$$\eta = \frac{w}{\lambda}$$

$$\varepsilon = \frac{\tau_{11}}{\tau_{Eo}} \qquad (\tau_{Eo} \text{ as defined in Eq. (2.19)}$$

$$\omega = \frac{\Gamma_o}{n_o v_w} \qquad (n_o \text{ as defined in Eq. (1.16))}$$

$$\nu(\xi) = \frac{n(x)}{n_o}$$

$$\gamma(\xi) = -\frac{d\nu}{d\xi} = \frac{\Gamma(x)}{\Gamma_o}$$

Then Eq. 2.20 becomes

$$\frac{d^2\nu}{d\xi^2} = \nu + \varepsilon \tag{2.23}$$

with boundary conditions $\gamma(0) = 1$ and $\nu(\eta) = \gamma(\eta)\omega$. The solution for the density profile is

$$\nu(\xi) = \frac{\omega\cosh(\eta-\xi) + \sinh(\eta-\xi) + \varepsilon\cosh\xi}{\omega\sinh\eta + \cosh\eta} - \varepsilon \tag{2.24}$$

and the values at the boundaries are

$$\begin{aligned} \nu(o) &= \frac{(\omega-\varepsilon)\cosh\eta + (1-\varepsilon\omega)\sinh\eta + \varepsilon}{\omega\sinh\eta + \cosh\eta} \\ \gamma(\eta) &= \frac{\nu(\eta)}{\omega} = \frac{1 - \varepsilon\sinh\eta}{\omega\sinh\eta + \cosh\eta} \end{aligned} \tag{2.25}$$

When $\varepsilon=0$ (no E×B drift) the earlier solutions given in Eqs. (1.15) and (1.18) for $n(x \to \infty) = 0$ and $n(w)=0$ are recovered for $\omega=1$ and $\omega=0$, respectively.

The relation of the electric field to ε and τ_{Eo} is not as simple as Eq.(2.19)might make it appear. If the electric field is applied by biasing wall segments or other electrodes, then the externally controllable quantity will be ϕ, the potential difference between the separatrix and the wall. But for a given ε or E , $\phi = -\int_o^w E\,dx$ also

depends on the shape of the density profile. Therefore the procedure to be followed must be to pick a value of ε, calculate the density profile and any other quantities of interest, and then perform the integration to find the corresponding value of ϕ. To do this in terms of the scaled variables, define

$$\chi = \frac{\phi}{wBL_{\perp}} \tau_{11} = \frac{\tau_{11}}{\bar{\tau}_E} \tag{2.26}$$

where $\bar{\tau}_E$ is the constant value τ_E would have for a uniform electric field with the same potential difference. Then χ is calculated by

$$\chi = \frac{\varepsilon}{\eta} \int_0^{\eta} \frac{d\xi}{\nu(\xi)} \tag{2.27}$$

The integral can be performed numerically.

It now remains only to choose some values for η, ω, and ε, and calculate some representative results. In the UWMAK studies η is typically 5 to 10; we will use $\eta = 5$. If $\tau_{11} = L/c_s$, then $\omega = (\lambda/L)(c_s/v_w)$. If $v_w = c_s$, then for UWMAK-III values $\omega \sim 10^{-3}$. However, c_s represents the sound speed near the separatrix where most particles reaching the divertor by thermal flow originate, but v_w is at most the thermal speed at the wall, which may be lower by an order of magnitude or more, giving $\omega \gtrsim 10^{-2}$.

Figure 2.4 shows $\gamma(\eta)$, the fraction of flux reaching the wall, as a function of χ, the normalized potential difference between the

separatrix and the wall, for various values of ω. For comparison, two cases with uniform electric field are also plotted. The unload performance is worse for the cases where $E \propto n^{-1}$, and among these is worse for decreasing ω which corresponds to decreasing density at the wall, because the E×B drift is more localized at the wall, where there is less plasma for it to remove.

As the electric field is increased, the density is lowered proportionately more near the wall than near the separatrix, which in turn causes the electric field to be even more concentrated near the wall; the electric field "digs a hole" for itself at the wall. This is the reason the curves in Figure 2.4 become flatter at large χ, and can be seen explicitly in Figure 2.5, where density profiles are plotted for several values of χ. The case of $\omega = 1$ was chosen for ease of viewing; for smaller ω the effect is similar but more localized at the wall. A uniform electric field case is again plotted for comparison.

The solution above cannot be taken to the limit $\tau_{11} \to \infty$ (divertor action by E×B drift only) since the differential equation changes form and the scaling by λ can no longer be defined. The solution for $n(x)$ becomes a parabola, and the integration to find ϕ can be performed analytically. The solutions are easy to obtain but will not be given here; the behavior with respect to the electric field is qualitatively the same as described above.

The extreme concentration of the electric field near the wall is a drawback in that it requires much larger potential differences than

the uniform electric field case for the same reduction of wall flux. It also means that impurity atoms sputtered from the wall are more likely to pass the region of greatest E×B drift before they are ionized. However, for a comparable reduction of wall flux, the E×B drift makes a much smaller change in the total number of particles between the separatrix and the wall than does the uniform electric field case (or any other method of reducing λ uniformly). For example, even in the $\omega = 1$ case, a factor of 10 decrease in the wall flux is accompanied by a 5% decrease in integrated density from separatrix to wall for the $E \propto n^{-1}$ case, and a decrease of over 50% for the uniform electric field case. Thus the E×B drift, in the more realistic case, has the advantage of reducing the wall loading with little degradation of the screening action of the divertor.

However, the extreme concentration of the electric field at the wall if $E \propto n^{-1}$ may limit the effectiveness of the E×B divertor for other reasons. It results in very high electric fields and drift speeds near the wall, and also large shears in the drift speed. The reasons for expecting this dependence of the electric field, and a possible upper limit on the magnitude of the electric field, will be discussed in Chapter 4. The limitations on the drift speed and its shear will be discussed next.

2.E. Shock Limitation of Drift Speed

It was mentioned earlier, when considering single-particle orbits,

that if the magnetic field increases along the path to the divertor some particles will be mirror confined and prevented from reaching the divertor, a situation which could be helped by the application of an E×B drift. However, when the collective effects of a plasma are considered the situation is quite different, as shown in a paper by Hazeltine, Lee, and Rosenbluth.[8] Applying single-fluid equations to a tokamak plasma with poloidal rotation, they show that as the plasma moves toward smaller major radius, and encounters a larger magnetic field not accompanied by a proportional increase in radial electric field, its poloidal velocity actually increases and density decreases, due to pressure effects. This disturbance can propagate along field lines at the sound speed, but due to axisymmetry only the poloidal component is important; the disturbance can propagate in the poloidal direction at a speed $c_s B_p/B$. They find that when the largest fluid velocity in the plasma reaches this "effective sound speed" a weak shock forms, and dissipative processes in the shock tend to keep the fluid velocity from increasing further.

A similar effect may occur in a divertor. If the exits to the divertor are located toward the major axis of the toroid for the sake of the favorable "D" shape, as in Figure 2.1, then plasma headed for the divertor from much of the scrapeoff region will encounter increasing magnetic field, and the poloidal component of the flow may be limited to $c_s B_p/B$. This is, in fact, the velocity already predicted for thermal flow limited by an electrostatic sheath at the neutralizer plate. If the actual velocity of thermal flow is some fraction of

this, as indicated in the FM-1 and DIVA experiments, then an applied E×B drift may provide some improvement while still being limited to the effective sound speed. Possibly this problem could be minimized by careful shaping of the divertor's magnetic field to reduce the size of the magnetic hill.

2.F. Instabilities

A question which must be asked is whether the addition of an externally applied E×B drift gives rise to any new instabilities in the plasma, which might enhance the radial transport in the divertor region, thus defeating the purpose. A plasma with a uniform E×B drift is clearly not subject to any new instability, since in the frame of reference moving with the plasma the electric field vanishes and everything looks the same as with no E×B drift. Nevertheless, there are at least two ways for the drift to cause instabilities.

The first is known as the "neutral drag" instability. Any neutrals which are present do not move with the E×B drift. In the typical high magnetic field limit where

$$\omega_{ce}\tau_e >> \omega_{ci}\tau_i >> 1 \tag{2.28}$$

with $\tau_{e,i}$ being the neutral collision times and $\omega_{ce,i}$ the cyclotron frequencies, the ions will drift slightly slower than the electrons due to the drag force of neutral collisions, the net drift speed in

the E×B direction being given by[9]

$$v_E \approx \frac{E}{B}(1 - (\omega_c \tau)^{-2}) \tag{2.29}$$

In the presence of a density gradient, when the equilibrium density is perturbed this differential drift leads to a separation of charge; if the charge separation has the proper sign the resulting perturbed E×B drift will increase the perturbation, leading to an instability. To obtain the proper sign for instability, $\vec{E} \cdot \vec{\nabla} n$ must be positive. This is very similar to the flute modes caused by charge separation due to curvature drift in a magnetic field with "bad curvature;" in fact, the most unstable modes of the neutral drag instability are flute modes with $k_{11} = 0$, where k_{11} is the component of the wave vector parallel to B.[10] If the electric field has the right sign for instability, and if $k_{11} = 0$, then a mode with wave number $k_\perp$ in the E×B direction is unstable if[10]

$$E \gtrsim k_\perp^2 \frac{n}{\nabla n} \frac{kT_i + kT_e}{e} \frac{\omega_{ci}\tau_i}{\omega_{ce}\tau_e} \tag{2.30}$$

The least stable modes are those with small $k_\perp$. Even if $\nabla n/n$ is taken as a lower limit to $k_\perp$, the electric field which can produce an instability may be quite small due to assumption Eq. (2.28). This process could be important in a divertor if there are large numbers of neutrals entering the plasma from the wall or backstreaming from the pumping chamber. It is interesting to note that if the cross-field

diffusion is due to neutral collisions as well, the ambipolar electric field points in the stable direction; instability can only result from an externally applied electric field.

The second type of instability which can be caused by an E×B drift occurs when the drift is not uniform but has a shear, due to a non-uniform electric field, for example. This is called the "Kelvin-Helmholtz" instability, by analogy with the well-known hydrodynamic instability in a fluid with velocity shear and a density gradient. The usual example of this is a fluid stabilized by gravity, such as the ocean. An energy criterion often quoted for stability of such fluid is[11,12]

$$J = -\frac{g}{\rho}\frac{dp}{dz}/\left(\frac{dU}{dz}\right)^2 > \frac{1}{4} \qquad (2.31)$$

where g is the gravitational acceleration, ρ is the mass density, U is the horizontal velocity, z is the vertical co-ordinate, and J is known as the Richardson number. In a plasma, however, gravitation is usually negligible compared with other forces, and velocities are so large that $J \approx 0$ in any event, so the behavior of the instability must be examined in more detail.

The density gradient in Eq. (2.31) was to provide a restoring force through gravity; in the absence of gravity the density gradient can be omitted from the discussion, and the unperturbed plasma will be assumed uniform except for the drift velocity.

First, consider the case where the fluid velocity jumps from 0 to

$\vec{v}_o$ across a sharp boundary. In the absence of a magnetic field, all modes are unstable for any non-zero value of $\vec{v}_o$.[12] If the plasma is in a magnetic field B, then stretching of field lines furnishes a restoring force, and the mode is stable if[13]

$$|\vec{k} \cdot \vec{v}_o| < 2|\vec{k} \cdot \vec{v}_A| \tag{2.32}$$

where $\vec{v}_A = (\mu_o m_i n_o)^{\frac{1}{2}} \vec{B}$ is the Alfvén velocity. Stability depends only on the direction of $\vec{k}$, and not on its magnitude, though in the unstable case the growth rate is proportional to k.[14] When $\vec{k}$ is perpendicular to $\vec{B}$, all wavelengths are unstable unless $\vec{v}_o$ is parallel to $\vec{B}$; this is just an interchange mode, with the same properties as if there were no B. In fact, if $\vec{v}_o$ is perpendicular to $\vec{B}$, it is identical to the hydrodynamic mode.

Next, consider the more realistic case where the fluid velocity changes linearly from $-\vec{v}_o$ to $+\vec{v}_o$ through a layer of thickness 2d, and is constant outside the layer. For the least stable modes where $\vec{k}$ and $\vec{v}_o$ are both perpendicular to $\vec{B}$, the dispersion relation is[13]

$$(2\,\frac{\omega}{\omega_o})^2 = (\,1 - 2\,kd)^2 - e^{-4kd} \tag{2.33}$$

where $\omega_o = v_o/d$. Although the dispersion relation above was derived using E×B drifts, since it is an interchange mode the identical dispersion relation is found in the hydrodynamic case.[12] Modes with kd > .64 are stable; the most unstable mode occurs at kd = .40 with a

growth rate of .20 ω_o. If $\vec{v}_o$ is allowed to have a component parallel to $\vec{B}$, the minimum k for stability increases but the growth rates of the unstable modes decrease.[14]

So far, only the case of incompressible plasma has been considered. If the plasma is allowed to be compressible, in the absence of B both the minimum k for stability and the growth rates of the unstable modes are reduced. But now the case with a perpendicular B is different from the hydrodynamic case, and tends to return to the incompressible case, since E×B flow is incompressible.[14]

The Kelvin-Helmholtz instability is probably not a serious problem for an E×B divertor. The drift velocities involved are so much less than the Alfvén velocity that any mode with a component of $\vec{k}$ in the direction of $\vec{B}$ will be stable. The modes with $\vec{k}$ perpendicular to B are unstable only for wavelengths of the order of the thickness of the shear layer or greater, and long wavelengths are more easily stabilized by other effects such as magnetic field shear, line-tying at the divertor's neutralizer plate, or the presence of a nearby vacuum tank wall. In fact, if the derivation of Eq. (2.33) given in reference (13) is modified to include a conducting boundary parallel to the shear layer and a distance b outside the surface of the layer, the dispersion relation becomes

$$\left(2\frac{\omega}{\omega_o}\right)^2 + \left(2\frac{\omega}{\omega_o}\right)\left(1 - e^{-4kd}\right)e^{-kb} = (1 - 2kd)^2 - e^{-4kd} - \left(1 - 4kd - e^{-4kd}\right)e^{-2kb} \tag{2.34}$$

If the discriminant is evaluated numerically, it is found that all k are stable for $b \lesssim 2d$, which could easily hold in a divertor scrape-off layer.

REFERENCES - CHAPTER 2

1. D.W. Kerst, Bull. Am. Phys. Soc. 20, 1334 (1975). Also University of Wisconsin PLP 613 (1975).

2. D.M. Meade, et.al., in Plasma Physics and Controlled Nuclear Fusion Research (Proc. 5th Conf., Tokyo, 1974), (IAEA, Vienna, 1975), Vol. I, p. 605.

3. R.S. Lovberg in Plasma Diagnostic Techniques, R.H. Huddlestone, S.L. Leonard, eds., (Academic Press, N.Y., 1965) p. 95.

4. A.H. Boozer and S.P. Auerbach, PPPL-EPRI-7 (1978).

5. S.I. Braginskii, Fiz. Plazmy 1, 370 (1975) (Sov. J. Plasma Phys. 1, 202 (1975)).

6. B. Lehnert, Nuclear Fusion 11, 485 (1971).

7. T. Consoli, et.al., in Plasma Physics and Controlled Nuclear Fusion Research (Proc. 5th Conf., Tokyo, 1975), (IAEA, Vienna, 1975), Vol. I, p. 571.

8. R.D. Hazeltine, E.P. Lee, M.N. Rosenbluth, Phys. Fluids 14, 361 (1971).

9. A. Hasegawa, Plasma Instabilities and Nonlinear Effects (Springer-Verlag, N.Y., 1975), p. 99.

10. A. Simon, Phys. Fluids 6, 382 (1963).

11. O.M. Phillips, Dynamics of the Upper Ocean (Cambridge University Press, 1969), p. 186.

12. S. Chandrasekhar, Hydrodynamic and Hydromagnetic Stability (Clarendon Press, Oxford, 1961), Chap. 11.

13. A. Hasegawa, p. 125.

14. R.S.B. Ong and N. Roderick, Planet. Space Sci., 20, 1 (1972).

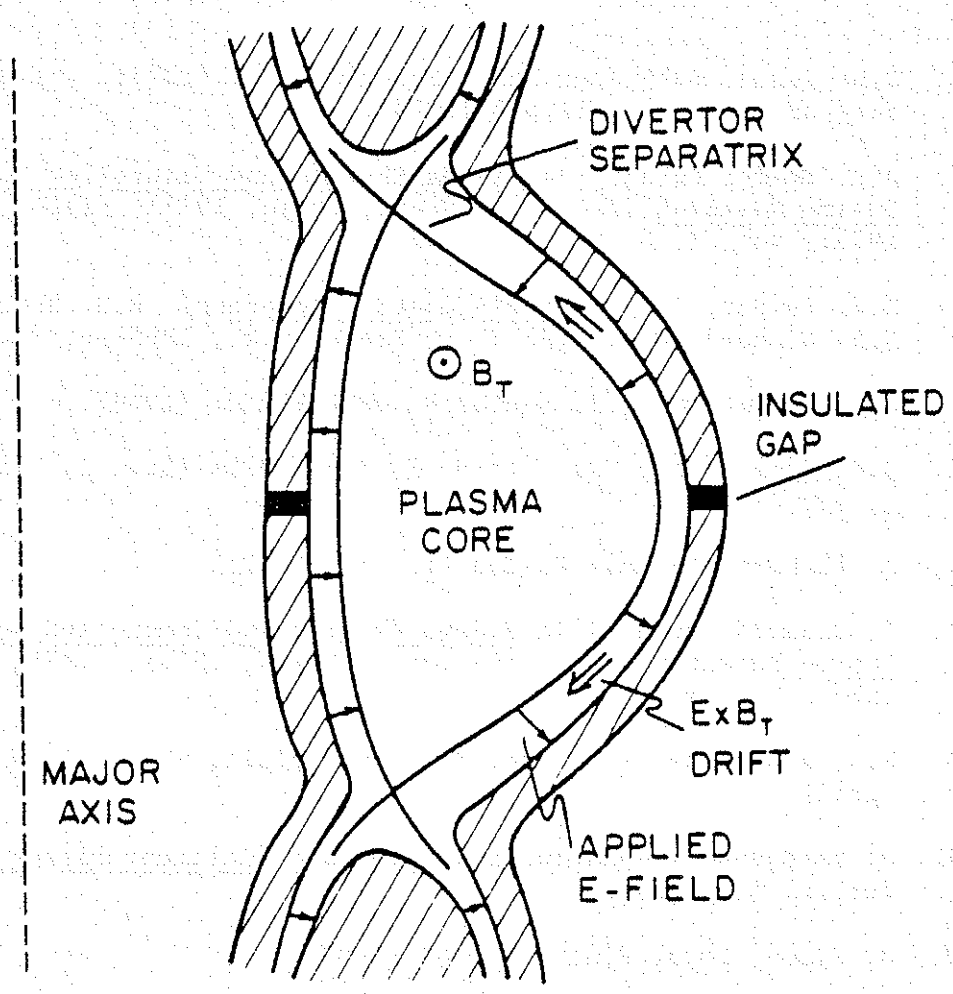

Fig. 2.1 - ExB divertor with magnetic divertor: shown is minor cross-section of tokamak with double poloidal null divertor. Radial electric field (arrows) applied by biased wall segments results in ExB_t drift (double arrows) toward pumping chambers.

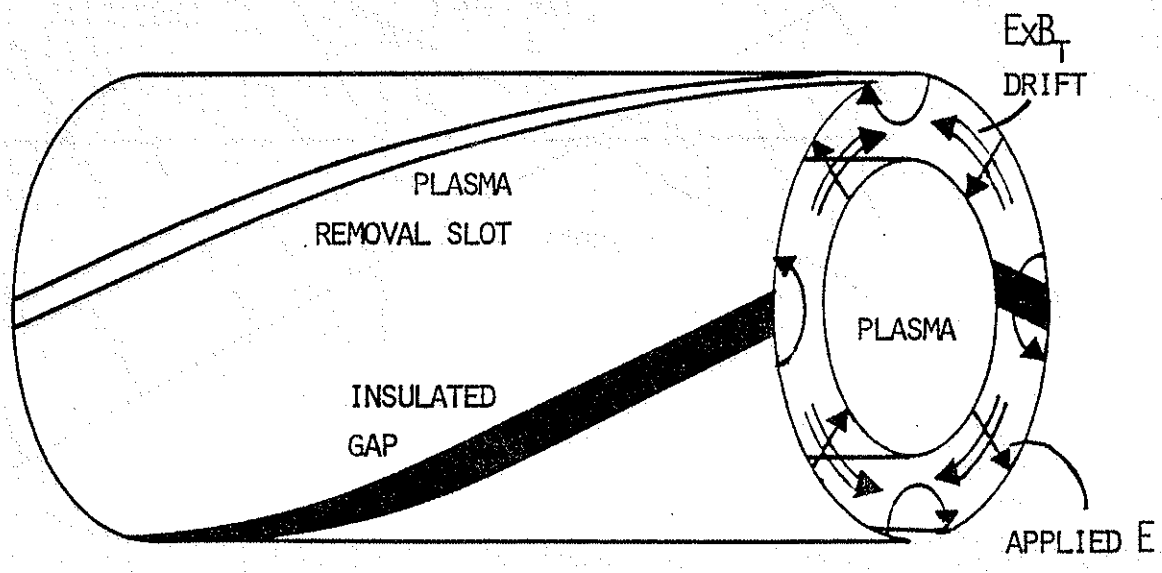

Fig. 2.2 - ExB divertor without magnetic divertor: shown is section of tokamak with wall segments spiraling to follow $\vec{B}$ field lines. Radial electric field (arrows) applied by biased wall segments results in ExB$_t$ drift (double arrows) toward pumping chambers.

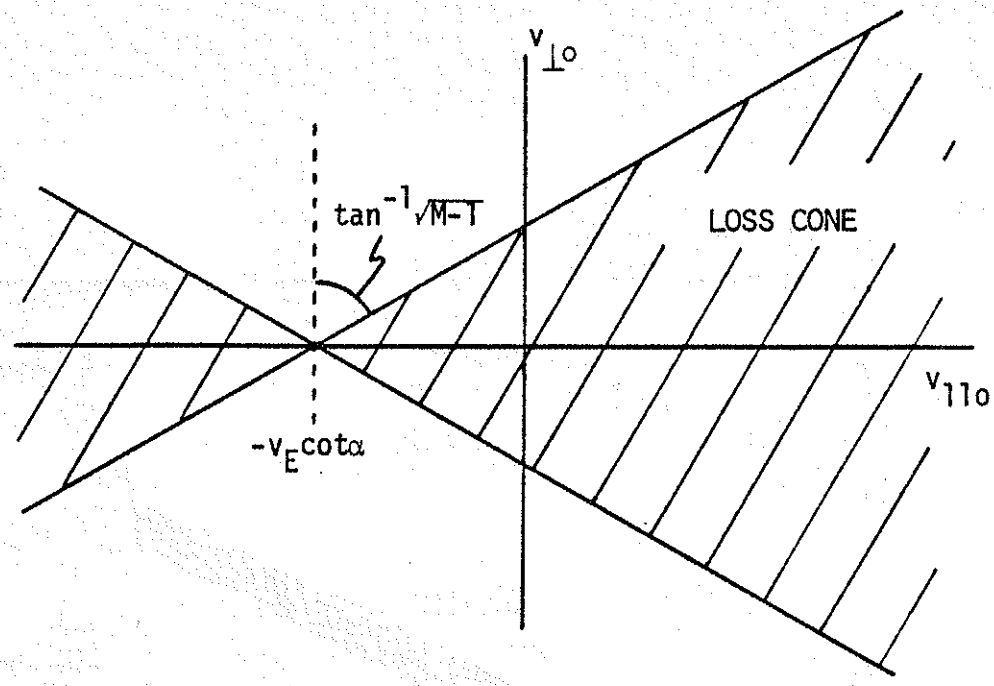

Fig. 2.3 - Loss cone shifted by ExB drift: M is mirror ratio, v_E is ExB drift speed, and $\tan\alpha = B_p/B_t$.

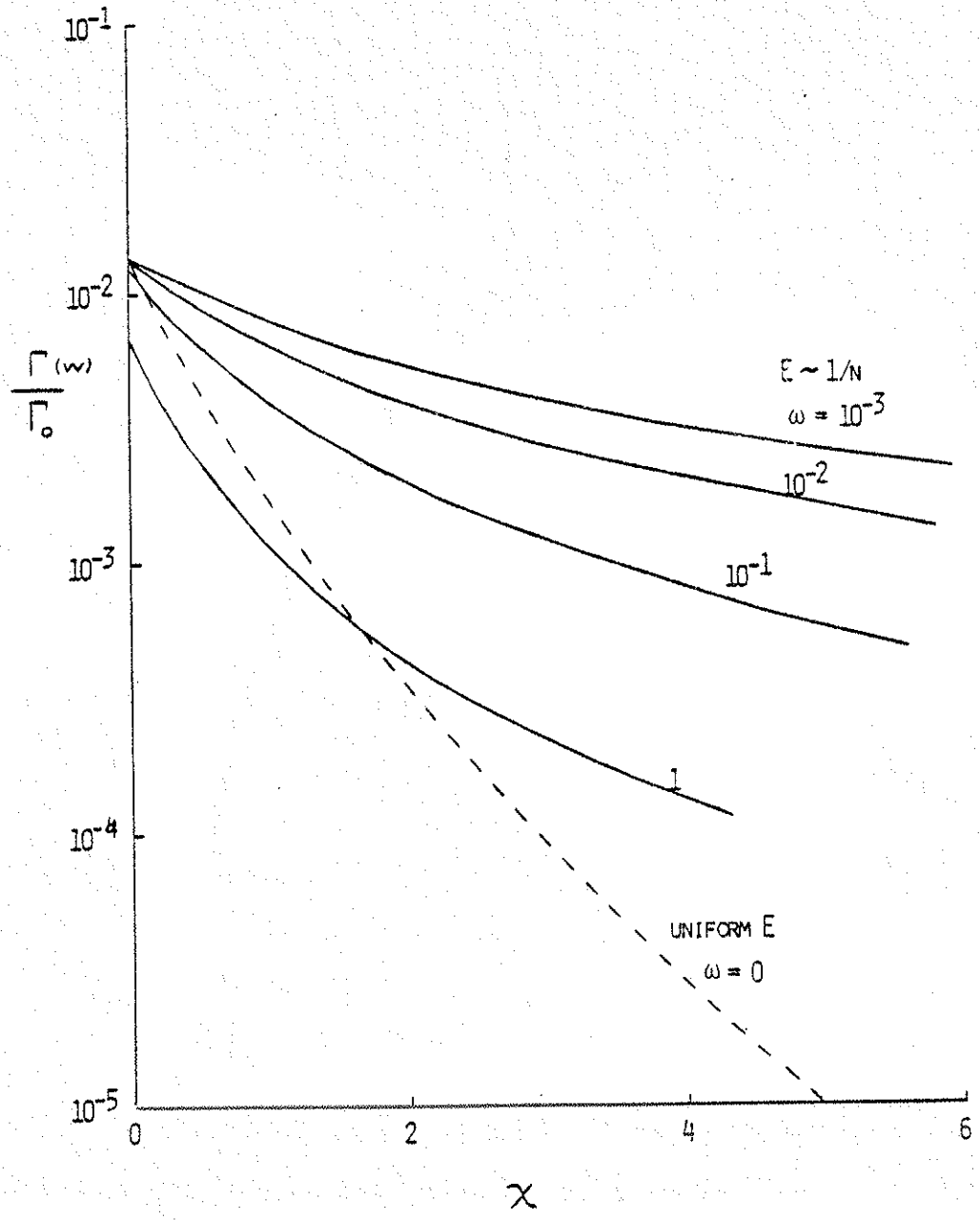

Fig. 2.4 - Normalized plasma flux to wall ($\gamma = \Gamma(w)/\Gamma_o$) vs. normalized electric field (χ) for various boundary conditions at wall (characterized by ω). Uniform E-field case is also shown for comparison.

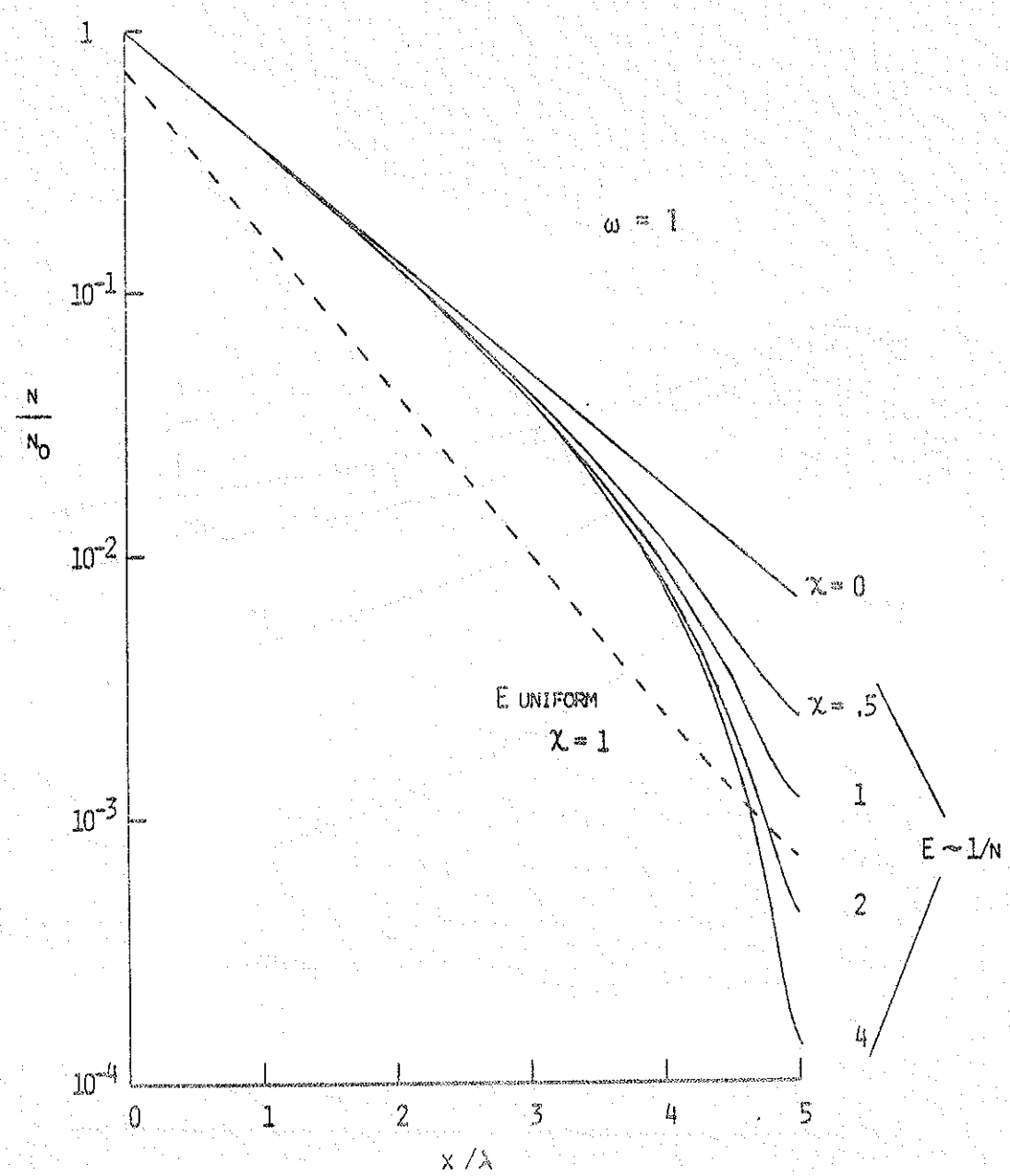

Fig. 2.5 - Spatial profiles of normalized plasma density (ν) for various values of normalized electric field (χ). Only ω = 1 case is shown. Uniform E-field case is also shown for comparison.

CHAPTER 3

EXPERIMENTAL APPARATUS

3.A. Octupole

Multipoles[1] provide stable plasma confinement in a closed, axisymmetric geometry, without the need for a plasma current and the instabilities which may accompany it. They have a large region of low magnetic field, which can greatly reduce the energy loss due to synchrotron radiation from the plasma, as emphasized by J. Tuck in the early days of cusps.[2] This makes them attractive for reactors using the high-temperature "advanced" fuel cycles.[3-6] These advantages are offset by the drawback of having conductors embedded in the plasma, with the attendant problems of levitation and cooling; and the neutron damage problem is severe enough that multipoles are probably feasible as reactors only for neutron-free advanced fuel cycles. Nevertheless, due to their good confinement properties, multipoles have been valuable for a wide range of plasma experiments.

The Wisconsin Levitated Toroidal Octupole[7,8] and its confinement properties[9] have been discussed elsewhere,[10] and only a brief description of the machine will be given here. The machine itself is shown in Figure 3.1, and Table 3.1 gives some of its important parameters. The poloidal magnetic field is produced by four internal rings, which are inductively driven, and the toroidal field is due to a poloidal

current in the vacuum tank wall. The two field strengths are independently variable. When the machine is pulsed they rise sinusoidally to peak value in about 21 msec, and are then crowbarred, with a decay time of about 70 msec. The hoop supports, which act as obstacles for the plasma, can be withdrawn pneumatically during the machine pulse, momentarily levitating the hoops.[11] The supports take about 20 msec to withdraw, remain out for 20 msec and take another 20 msec to return. Titanium gettering and a liquid helium cryopanel maintain the base pressure at 2×10^{-8} Torr or better.

Figure 3.2 is a minor cross-section of the toroid, showing computer-calculated poloidal magnetic field lines,[12] plotted for 25 msec after the beginning of the pulse. These lines are contours of constant magnetic flux ψ, labeled in units of Dories (see Appendix). The dashed lines (ψ = 5.62 and 5.66) are the separatrices, dividing field lines into three classes: private field lines which link a single hoop, a small class of semi-private field lines which link two hoops, and common field lines which link all four hoops. (Since the separatrices are so close together they are often spoken of in the singular, as if there were a completely degenerate octupole field null at the minor axis and hence a single separatrix.) $\oint B^{-1}dl$ has a maximum at a separatrix (in fact, it becomes infinite), so density profiles peaked at the separatrix are stable against interchange instabilities.[13] Under the definition of ψ in the Appendix, it can be shown that $\oint B^{-1}dl = V'(\psi)$, where $V'(\psi)d\psi$ is the volume enclosed between surfaces ψ and $\psi + d\psi$. Therefore the great majority of the

particles in the machine are confined near the separatrix. The dot-dash line (ψ = 7.80) is a minimum of $\oint B^{-1} dl$, known as the critical field line, outside of which the plasma is unstable.

Figure 3.3 shows the corresponding countours of magnetic field strength $|B|$. The units are kilogauss at the design value of .63 Webers in the transformer core at peak field. (It should be noted that the measured value for maximum core flux is .72 Webers.[14])

3.B. Poloidal Divertor

In November, 1977, three small hoops were added to the octupole, to give the capabilities of creating a divertor-like magnetic field configuration near the wall (although without an external chamber and differential pumping), and of applying radial electric fields near the divertor. They are driven directly by their own capacitor bank, and some of the important parameters of the hoops and bank are shown in Table 3.2. In order to restrict to manageable levels the mechanical and thermal stresses on the hoops, and the size of the capacitor bank, the divertor was designed to operate only at poloidal fields corresponding to 1 kV or less on the main capacitor bank.

The location and dimensions of the hoops are shown in Figure 3.4. They are located almost exactly midway between the radii of the inner main hoops and the midcylinder, in order to be as close as possible to the midcylinder, where the main field is low and ψ_{crit} is far from the wall, but without interfering with the microwave interferometer

mirrors or other features on the midcylinder. When not energized, they are designed to just touch ψ_{crit}. Also shown are the path taken by a probe inserted in a port drilled for the divertor, and a simplified outline of a support structure, of which there are twelve, evenly spaced.

Each hoop consists of type 316 stainless steel tubing, 7/8" O.D. and 1/16" wall, containing seven turns of #6 copper wire. Each hoop has two sidearms projecting through the vacuum wall: one to admit cooling air, and one for current leads and air exhaust. The exhaust temperature is monitored with a thermocouple to avoid melting of the insulation inside.

Due to their small minor diameters, the L/R time of the hoops is short and they act mainly as a resistive load on the capacitor bank. The three hoops can be connected in a number of ways, the most interesting of which consist of simply driving a current in the middle hoop in the same direction as that of the main hoops, (referred to hereafter as the 1-hoop or single hoop configuration), or also allowing half the current to return in the opposite direction in each of the other two hoops (3-hoop or triplet configuration). The 3-hoop configuration can easily be achieved by a series-parallel connection of the windings:

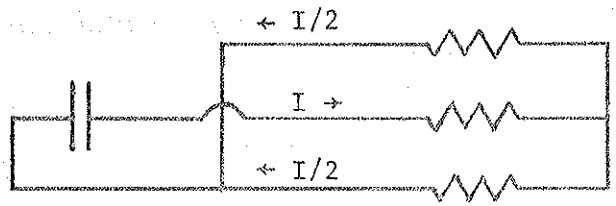

For the flux plots (discussed later) and inductance calculations, several approximations were made. Since the current is distributed through seven turns of wire, it was assumed that the current density was uniform throughout the interior of the hoop, giving the same field outside the conductor as a filament current at the hoop's minor axis. The stainless shells do link the transformer core, but their small cross-section and large resistivity combine to give them large resistances and L/R times of less than 1 msec, so currents in them can be ignored. On the other hand, for the risetime of the divertor current, the skin depth in the nearby aluminum lid is on the order of 1 cm or less, so the lid has been assumed to be superconducting, which permits the magnetic fields to be easily calculated using image currents in the lid. Toroidal effects were ignored and the fields were calculated as if for straight rods. Two factors contribute to the validity of this: First, toroidal effects in the field of a single hoop are of order r/R, where R is the major radius of the hoop and r is the distance from its minor axis, and $r/R \lesssim .1$ for the flux plots to be shown below. Second, note that the far field from a rod with an image in a superconducting wall falls off inversely as the square, rather than the first power, of the distance. Therefore the incremental contribution to the field at a distance r from a circular hoop separated by a distance d from a superconducting wall, due to a point far away on the hoop where the curvature begins to become noticeable, will be reduced in a similar way as long as $r \ll R$ and $d \ll R$, making toroidal effects even less important. (In the triplet

configuration, the far field falls off even faster.) Image currents in other wall surfaces and in the octupole hoops have been neglected since their far field will be small for the same reason. These approximations result in a very simple expression for the poloidal flux due to one of the hoops (with its image):

$$\psi = (2\pi R)\,\frac{\mu_o I}{2\pi}\,\ell n\left(\frac{r'}{r}\right) \qquad (3.1)$$

where R is the major radius of the hoop, and r and r' are the distances of the point under consideration from the minor axes of the hoop and its image. Calculated under these assumptions, the theoretical electrical characteristics of the hoops are shown in Table 3.2, and the measured values agree quite closely.

Eq. (3.1) was also used to calculate flux plots for the immediate vicinity of the divertor hoops (the area indicated in Figure 3.4). These were multiplied by appropriate numerical factors and superposed on the unperturbed octupole flux plot (Figure 3.2) to give the net field. Figures 3.5 and 3.6 show ψ and $|B|$ plots for two particular cases, and Figures 3.7 and 3.8 show two series of flux plots for varying divertor currents. For comparable ψ values of the divertor separatrix, the triplet case gives a "harder" field null, with a smaller region of low field, than the single hoop case. The triplet case tends to force diverted field lines to pass between the hoops rather than through them. Due to the partial cancellation of the fields from the three hoops, the triplet case requires larger hoop

currents and creates a larger magnetic "hill."

Magnetic probes (see section 3.C.6), inserted along the path shown in Figure 3.4 were used to verify the theoretical flux plots. Figure 3.9 shows measured unit vectors in the direction of $\vec{B}$, superposed on the appropriate flux plot. (The vectors are not plotted with length proportional to $|B|$ due to the large variation from near the hoops to near the field null.) The agreement is quite good, with only some disagreement near the lid due to neglect of field soak-in. Perhaps more significant are the direct measurements of ψ shown in Figure 3.10. The probe was first calibrated against the standard flux plot with no divertor current, also shown in Figure 3.10. Again the agreement is quite good, including the ψ value of the divertor separatrix (seen as a local minimum of ψ). There are some small deviations near the lid, due to neglect of soak-in, and at the left-hand edge of the plot, probably due to image currents in the upper inner octupole hoop, which have been neglected. These results give credence to the theoretical flux plots.

3.C. Diagnostics

The diagnostic methods used in these experiments have been discussed elsewhere, and will not be dealt with in great detail here. Brief descriptions of each will be given, with an indication of their use in this particular experiment. The actual location in the machine of the various devices will be shown when the experimental

measurements are discussed.

3.C.1. Langmuir Probes

One of the oldest and simplest, yet most versatile, plasma diagnostic methods is the Langmuir probe;[15] several review papers are available on the subject.[16-19] A Langmuir probe consists simply of a small electrode immersed in the plasma, which can be biased to different potentials and the current which it draws from the plasma measured, and which can be moved through the plasma to determine the spatial variation of the measured quantities.

Figure 3.11 shows schematically a simple circuit for making such measurements, and an idealized current vs. voltage characteristic. When the bias potential is much more positive than the plasma space potential ($V >> V_p$) ions are repelled from the probe. The resulting electron sheath around the probe shields its potential from the rest of the plasma, and the current to the probe saturates at a value determined by the random flux of electrons entering the sheath:

$$I_{oe} = \tfrac{1}{4} enA \sqrt{\frac{8kT_e}{\pi m_e}} \qquad (3.2)$$

if the electron velocity distribution is Maxwellian, where n is the plasma density and A is the probe's surface area. When $V << V_p$, electrons are repelled and ions are collected. However, in order for the potential to decrease monotonically through the sheath, the ions

must enter with a velocity of at least the ion acoustic speed[20,21] ($c_s = \sqrt{(kT_e + kT_i)/m_i}$); this requirement is known as the Bohm sheath criterion. If $T_i > T_e$ then the expression for ion saturation current is analogous to that for electrons, but if $T_i < T_e$ then there must exist outside the sheath a "pre-sheath" with a potential drop comparable to kT_e/e, accelerating the ions to the ion acoustic speed. Therefore the ion saturation current is

$$I_{oi} = \begin{cases} \frac{1}{4}enA\sqrt{\frac{8kT_i}{\pi m_i}} & (T_i > T_e) \\ \frac{1}{2}enA\sqrt{\frac{kT_e}{m_i}} & (T_i < T_e) \end{cases} \tag{3.3}$$

If no temperature gradients exist in the plasma, profiles of I_{oi} at a given time are proportional to density profiles, and if the temperature is known, density can be calculated. For $V < V_p$, but not so far negative that the electron current is negligible, the probe current is given by

$$I(V) = I_{oe} \exp \frac{e(V-V_p)}{kT_e} - I_{oi} \tag{3.4}$$

if the electrons are Maxwellian. This portion of the curve can be used to find T_e.

At the floating potential ($V = V_f$) the probe current is zero, so the floating potential is given by

$$V_f - V_p = \frac{kT_e}{e} \ell n \left(\frac{I_{oi}}{I_{oe}}\right) = \begin{cases} \left[\frac{1}{2}\ell n \left(\frac{T_i}{T_e}\right) - 3.6\right] \frac{kT_e}{e} & (T_i > T_e) \\ -3.6 \frac{kT_e}{e} & (T_i < T_e) \end{cases} \tag{3.5}$$

If no temperature gradients exist in the plasma, V_f differs from the space potential only by a constant, and gives a measure of electric fields in the plasma. Floating potential can be measured directly if the input impedance of the amplifier connected to the probe is much larger than the sheath impedance (e.g., by using a Tektronix 10 MΩ, 10x attenuating probe).

A variation on the Langmuir probe is the floating double probe,[22] in which the bias potential is applied between two nearby probe tips, and the entire biasing circuit is allowed to float. The current can be measured either with a differential amplifier connected across a resistor in the biasing circuit, or with an optically isolated ammeter circuit.[23] If one tip is biased to collect ion saturation current, the other remains within $\sim kT_e/e$ of the floating potential, guaranteeing that I_{oi} is always measured at the same point on the I-V curve, even if there are large variations in plasma potential.

More realistic theories take into account particle orbits within a finite thickness sheath,[24] and the presence of a magnetic field.[25] In the latter case, which is important for the octupole, it appears that under most circumstances the probe acts the same as in the field-free case, but with an effective area for electron collection

limited to its projection normal to $\vec{B}$.

Surface contaminants can alter the response of a probe,[26-28] so probes were degreased with acetone and alcohol, and then abraded to expose an oxide-free surface, immediately before insertion.

In practice, the ion saturation branch of the I-V characteristic is not horizontal. When analyzing probe curves by hand, the usual procedure is to estimate a line through the ion saturation branch, and subtract this line from the entire curve. The electron repulsion part of the curve, near V_f, is then plotted on semi-log paper and a line estimated through the points to obtain T_e. V_p is estimated as the point where the data begin to deviate from the line at large V. If the estimated line for ion saturation current is not correct, the resulting error can be large in the region where the electron current is small ($V < V_f$). For this reason, and because of the tedium of the above procedure when many T_e measurements are desired, a computer program was written to analyze probe characteristics.

The probe characteristic for $V < V_p$ is modeled by

$$f(V) = a_1 + a_2 V + a_3 \exp(a_4 V) \tag{3.6}$$

where $a_4^{-1} = kT_e/e$. If theory or empirical evidence dictates, a different form for the ion saturation current could easily be substituted. The values of a_j are desired which minimize the variance Q:

$$Q = \sum_i (f(V_i) - I_i)^2 \tag{3.7}$$

where I_i is the measured current at a bias of V_i. Since f is not linear in all the a_j, a version of Newton's method[29] is used. V_p and initial estimates a_j^o are obtained by methods similar to the hand analysis described above, giving the first estimate for the fitted curve:

$$f^o(V) = f(V;a_j^o) \tag{3.8}$$

The problem is linearized by letting the next estimates be small corrections to the $a_j^o (a_j^1 = a_j^o + \delta_j)$ and expanding f to the first order in δ_j:

$$f^1(V) = f(V;a_j^1) = f^o(V) + \sum_j \delta_j \left.\frac{\partial f}{\partial a_j}\right|_{(V;a_j^o)} \tag{3.9}$$

Then $f^1(V)$ is substituted in Eq. (3.7) and the variance is minimized with respect to the δ_j by setting $\partial Q/\partial \delta_j = 0$; this gives a set of linear equations in the δ_j which can be solved by the usual means. The δ_j corrections are applied to the a_j^o, giving a_j^1; these then become the new estimates a_j^o, and the procedure is repeated until it converges to the desired accuracy. This method has the great advantage of optimizing the fit to the entire curve at once, rather than the piecewise fit of the hand analysis.

3.C.2. Paddle Probe

Another variation on the Langmuir probe is the paddle probe, a

two-sided probe consisting of two plane parallel electrodes with an insulating layer sandwiched between them. If the plasma is not isotropic but has a drift velocity with a component normal to the plane of the electrodes, more particles will strike one side than the other, so this can be used to measure plasma current or flow velocity.

If the probe is biased into saturation so that all particles of one species entering the probe sheath are collected and none of the other species, and if the collected species enters the sheath with a velocity distribution given by a Maxwellian shifted by the drift velocity $\vec{v}_o$ (electrons, or ions with $T_i > T_e$):

$$f(\vec{v}) = n\left(\frac{m}{2\pi kT}\right)^{3/2} \exp\left[-\frac{m(\vec{v}-\vec{v}_o)^2}{2kT}\right] \tag{3.10}$$

then the net particle flux reaching one electrode is

$$\Gamma(u_o) = \tfrac{1}{4}n\bar{v}e^{-g^2} + \tfrac{1}{2}nu_o(1 + \mathrm{erf}(g)) \tag{3.11}$$

where $\bar{v} = (8kT/\pi m)^{\frac{1}{2}}$, $g = (mu_o^2/2kT)^{\frac{1}{2}}$, and u_o is the component of $\vec{v}_o$ normal to the electode. The second term of Eq. (3.11) is odd in u_o, while the first and third are even, so the difference between the fluxes to the two sides of the probe is

$$\Gamma(u_o) - \Gamma(-u_o) = nu_o \tag{3.12}$$

which is just the net flux in the plasma of the species being

collected. If the velocity is desired, however, further calculation is necessary. The sum of the fluxes to the two sides of the probe is

$$\Gamma(u_o) + \Gamma(-u_o) = \tfrac{1}{2}n\bar{v}e^{-g^2} + nu_o\,\mathrm{erf}(g) \tag{3.13}$$

$$\longrightarrow \begin{cases} \tfrac{1}{2}n\bar{v} & \text{if } g \ll 1 \\ nu_o & \text{if } g \gg 1 \end{cases}$$

If $g \ll 1$, then to first order in g the ratio of drift speed to thermal speed $c = (kT/m)^{\frac{1}{2}}$ (which is also the ion acoustic speed if ions are being collected and $T_i \geq T_e$) can be found simply from

$$g = \frac{1}{\sqrt{2}}\frac{u_o}{c} \approx \tfrac{1}{2}M \tag{3.14}$$

where $$M = \frac{2}{\sqrt{\pi}}\frac{\Gamma(u_o) - \Gamma(-u_o)}{\Gamma(u_o) + \Gamma(-u_o)}$$

For larger values of $g < 1$, a third order expansion gives

$$\Gamma(u_o) + \Gamma(-u_o) \approx \tfrac{1}{2}n\bar{v}(1 + g^2) \tag{3.15}$$

This can be used to solve for the ratio of drift speed to thermal speed:

$$g = \frac{1}{\sqrt{2}}\frac{u_o}{c} \approx \frac{1}{M}\left[1 - \sqrt{1 - M^2}\right] \tag{3.16}$$

This expression has a solution only for $M \leq 1$, but the error in the value it gives for g is less than 10% for $M \lesssim .96$ or $g \lesssim .7$, making it a reasonable approximation under most circumstances.

3.C.3. Skimmer Probe

Although some methods have been suggested,[30] ion temperature is very difficult to obtain from a Langmuir probe characteristic, due to the overwhelmingly large electron current in the ion repulsion regime. T_i measurements can be made with a skimmer probe,[31] which has its electrode recessed inside a shield. The opening of the shield is oriented parallel to B, and due to their small gyroradius electrons cannot enter and reach the collecting electrode. The collector bias can then be varied to repel ions, while measuring only ion current.

3.C.4. Fabry-Perot Interferometer

A measurement of plasma density independent of temperature is given by the microwave Fabry-Perot interferometer.[32] Two confocal mirrors provide a resonant cavity for 35 GHz microwaves, most of which is filled by the low field region at the minor axis of the machine, near ψ_{sep}. The frequency is swept repetetively over a small range, and the resonant frequency, which depends on the density of plasma in the cavity, is measured.

3.C.5. Striped Collectors

Plasma flux to the wall of the machine is measured with striped collectors.[33-35] These consist of two sets of interdigitated conducting stripes, biased alternatively positive and negative. (See Figure 3.12.) The width and spacing of the stripes are less than the Debye shielding length of the plasma, so that the plasma does not electrically shield the stripes from each other, and due to the large number of stripes the electric field falls off rapidly away from the collector. They are then expected to collect, as measured saturation current, a large fraction of the plasma particles striking them, without perturbing the transport processes in the nearby plasma.[36]

A case can be made that the measurement is less perturbing when the average potential of the two sets of stripes is held at the potential of the surface they are mounted on.[37] However, in most of the present experiments the circuit was allowed to float, similar to a floating double probe, and in some instances this has been seen to be the less perturbing mode.[38] In particular, when the stripes are biased positive and negative by the same amount with respect to ground, and the magnitude of the bias voltage is varied, it is generally observed that the ion current saturates while the electron current does not, showing that the electric field of the collector is not completely non-perturbing. Consequently, the only way to make a truly non-perturbing measurement would be to first make a low-impedance measurement of the net current to the collector with both

sets of stripes at ground potential, this presumably being the current drawn from the plasma to the same patch of wall in the absence of the collector. Then when the collector is biased to obtain charge separation of the plasma striking it, the bias must be carefully chosen to make the net current drawn from the plasma the same as before. An arbitrary bias voltage with the center of the circuit grounded might well be at least as perturbing as letting the circuit float. In practice, very little difference is usually seen between the ion currents measured in the two cases, floating or center-grounded.

3.C.6. Magnetic Probes

The magnetic field of the divertor was verified using magnetic probes,[39] consisting of small coils of wire inside stainless steel tubing much thinner than a skin depth. Such a coil measures the change of magnetic flux through it ($\dot{\phi} = A\dot{B}$) which can be integrated electronically to obtain B. One such probe had two small coils at right angles in order to measure locally both radial and vertical components of the poloidal magnetic field (see Figure 3.13(a)). Another probe had a long, narrow coil, closed outside the magnetic field region, in order to perform the spatial integration necessary to obtain the poloidal flux ψ (see Figure 3.13(b)).

3.D. Plasma Sources

A variety of methods for producing and heating a plasma are available on the octupole, of which three were used for the data to be presented here. These sources and the plasmas they produce will be briefly characterized below:

3.D.1. Electron Cyclotron Resonant Heating (ECRH) Plasma

The field strengths in the octupole are such that microwave frequencies can be conveniently chosen to resonate with the cyclotron frequency of the electrons, thus heating them. A fast valve is used to puff neutral hydrogen gas into the toroid about 100 msec before the start of the magnetic field pulse, filling it typically to 5×10^{-6} Torr. A 50 W, 2.45 GHz magnetron is run CW to pre-ionize the gas, producing a plasma with a density of about $10^{8} cm^{-3}$. Near peak field, a 1 kW, 2.86 GHz magnetron is pulsed for several milliseconds, ionizing a significant fraction of the filling gas, and heating the electrons. Figure 3.14 shows typical values for density and electron temperature at the separatrix, obtained from analysis of Langmuir probe I-V characteristics. Despite the fact that electron heating occurs only at localized resonance zones (defined by B = 1020 Gauss at 2.86 GHz), T_e is uniform throughout the machine within a few milliseconds after the end of the heating pulse.[40] The ions are heated only by collisions with electrons, and at these parameters the temperature equilibration

time between electrons and ions is $\gtrsim$ 10 msec,[41] while charge exchange and elastic collisions with neutral gas cool the ions.[42,43] The computer model SIMULT[44] predicts $T_i \lesssim$ 1 eV.

3.D.2. Small Gun Plasma

A small coaxial Marshall-type[45] plasma gun (labeled "injector" in Figure 3.1) is located at the top of a 3 m long drift tank. A fast valve admits gas to the region between the inner and outer electrodes; after the gas has filled this region a voltage is applied between the electrodes, breaking down the gas and accelerating the plasma out the end of the gun. The cloud of plasma passes rapidly into the toroid, while the large volume and small aperture of the drift tank keep most unionized, thermal atoms from reaching the toroid for at least 10 msec. The energy density of the plasma is too small to allow it to push magnetic field lines aside by diamagnetic currents; rather, it is able to enter the magnetic field region by becoming electrically polarized.[46,47] This causes an E×B drift which carries it into the toroid, where it is captured, becoming azimuthally symmetric in a few tenths of a millisecond.[48]

This plasma has been extensively studied under a wide range of operating conditions.[10] Figure 3.15 shows measurements of density at the separatrix from the Fabry-Perot microwave interferometer, electron temperature from Langmuir probe characteristics, and ion temperature from skimmer probe measurements, for the conditions of

the present experiment. The ions and electrons enter the toroid with comparable velocities, hence the ions have larger kinetic energy. The low neutral background pressure made possible by use of the drift tank results in a relatively long lifetime for the ion temperature, and both ions and electrons are collisionless in the sense that their collision times are longer than their transit times along a magnetic field line, as is expected to be the case in fusion-regime tokamaks.

3.D.3. Large Gun Plasma

A larger Marshall gun is mounted on the lower lid, opening directly into the toroid.[49] It produces a cold, collisional plasma with a density of about 10^{12} cm^{-3}, about an equal number of neutrals, $T_i \sim 1$ eV, and $T_e < 1$ eV.

3.E. Experimental Sequence

Figure 3.16 shows typical timing sequences for a machine pulse, including the events discussed in the preceding three sections. Data acquisition equipment may be triggered at any time during the pulse, but for these experiments was usually triggered simultaneously with the plasma source.

REFERENCES - CHAPTER 3

1. T. Ohkawa and D.W. Kerst, Phys. Rev. Lett. 7, 41 (1961); Nuovo Cimento 22, 784 (1961).

2. J.L. Tuck, Nature 187, 863 (1960).

3. J.M. Dawson, UCLA Plasma Group Report PPG-273 (1976).

4. D. Arnush, R. Conn, J.M. Dawson, B. Fried, D. Kerst, T. Samec, V. Vanek, A.Y. Wong in Review Meeting on Advanced-Fuel Fusion, EPRI-ER-536-SR (1977), p. 103.

5. R.T. Taussig, EPRI ER-544 (1977).

6. R.W. Conn and G. Shuy, University of Wisconsin FDM-262 (1978).

7. H.K. Forsen, D.W. Kerst, R.A. Breun, A.J. Cavallo, J.R. Drake, J.C. Sprott in Fourth European Conference on Controlled Fusion and Plasma Physics (CNEN, Rome, 1970), p. 24.

8. J.D. Steben, J. Appl. Phys. 43, 1211 (1972).

9. G.A. Navratil and R.S. Post, University of Wisconsin PLP 790 (1979), and references therein.

10. See University of Wisconsin Ph.D. Theses by J.R. Drake (1973), J.W. Rudmin (1974), R.A. Breun (1975), A.J. Cavallo (1975), J.R. Greenwood (1975), G.A. Navratil (1976), C.J. Armentrout (1977), A. Butcher Ehrhardt (1978).

11. I.N. Sviatoslovsky and N.C. Lien, Hydraulics and Pneumatics 24:9, 86 (1971), also University of Wisconsin PLP 275 (1969).

12. R.L. Willig, University of Wisconsin PLP 418 (1971).

13. M.N. Rosenbluth and C.L. Longmire, Ann. Phys. 1, 120 (1957).

14. J.R. Drake, University of Wisconsin Ph.D. Thesis (1973), p. 5.

15. I. Langmuir and H. Mott-Smith, General Electric Review 27, 449, 538, 616, 762, 810 (1924).

16. F.F. Chen in Plasma Diagnostic Techniques, R.H. Huddlestone and S.L. Leonard, eds., (Academic Press, N.Y., 1965), ch. 4.

17. L. Schott in Plasma Diagnostics, W. Lochte-Holtgreven, ed., (Wiley Interscience, N.Y., 1968), ch. 11.

18. P.M. Chung, L. Talbot, K.J. Touryan, Electric Probes in Stationary and Flowing Plasma: Theory and Application, (Springer-Verlag, N.Y., 1975).

19. J.C. Sprott, University of Wisconsin PLP 88 (1966).

20. S.A. Self, Phys. Fluids 6, 1762 (1963).

21. A.H. Boozer, MATT-1148 (1975).

22. E.O. Johnson and L. Malter, Phys. Rev. 80, 58 (1950).

23. C.J. Armentrout, University of Wisconsin Ph.D. Thesis (1977), p. 37.

24. J.G. Laframboise, UTIAS Report No. 100 (1966).

25. J.R. Sanmartin, Phys. Fluids 13, 103 (1970).

26. E.P. Szuszczewicz and J.C. Holmes, J. Appl. Phys. 46, 5134 (1975).

27. C.J. Armentrout, Thesis, p. 44.

28. J.W. Rudmin, University of Wisconsin Ph.D. Thesis (1974), p. 82.

29. D. Greenspan, Introduction to Numerical Analysis and Applications, (Markham Publ. Co., Chicago, 1970), p. 32.

30. M. Sato, Phys. Fluids 15, 2427 (1972).

31. D.A. Brouchous, University of Wisconsin PLP 624 (1975).

32. J.W. Rudmin, Thesis, p. 42.

33. E.R. Mosburg, J. Appl. Phys. 40, 5290 (1969).

34. D.E. Lencioni and D.W. Kerst, Bull. Am. Phys. Soc. 15, 1466 (1970).

35. A.J. Cavallo, Phys Fluids 19, 394 (1976).

36. S.I. Mak, University of Wisconsin Ph.D. Thesis (1975).

37. G.A. Navratil, University of Wisconsin Ph.D. Thesis (1976), p. 38.

38. A.J. Cavallo, University of Wisconsin Ph.D. Thesis (1975), p. 22.

39. R.S. Lovberg in Plasma Diagnostic Techniques, R.H. Huddlestone, S.L. Leonard, eds., (Academic Press, N.Y., 1965), ch. 3.

40. E.J. Strait, University of Wisconsin PLP 566 (1974).

41. L. Spitzer, Physics of Fully Ionized Gases, (Wiley Interscience, N.Y., 1962), p. 135.

42. E.J. Strait, University of Wisconsin PLP 592 (1974).

43. E.J. Strait, University of Wisconsin PLP 670 (1976).

44. J.C. Sprott and E.J. Strait, IEEE Transactions on Plasma Sci. 4, 6 (1976).

45. J. Marshall, Phys. Fluids 3, 134 (1960).

46. G. Schmidt, et.al., Phys. Fluids 3, 961 (1963).

47. D.M. Meade, University of Wisconsin Ph.D. Thesis (1965).

48. R.A. Dory, D.W. Kerst, D.M. Meade, W.E. Wilson, C.W. Erickson, Phys. Fluids 9, 997 (1966).

49. G.A. Navratil, Thesis, p. 13.

Table 3.1 - LEVITATED OCTUPOLE PARAMETERS

Physical

Major Radius
- Vacuum Tank: 139.5 cm
- Inner Hoop: 99.5 cm
- Outer Hoop: 179.2 cm

Minor Radius of Hoops: 8.9 cm

Surface Area
- Wall: 42.2 m^2
- Inner Hoop: 3.5 m^2 (×2)
- Outer Hoop: 6.3 m^2 (×2)
- Hoop Support: 42 cm^2 (×16)

Volume
- Vacuum Tank: 8.6 m^3
- Within ψ_{crit}: 7.7 m^3

Electrical (Maximum Field)

B_p

Capacitor Bank
- Capacitance: .048 F
- Voltage: 5 kV
- Energy: .60 MJ

Maximum B at Surface*
- Wall: 6 kG
- Inner Hoop: 12 kG
- Outer Hoop: 5.5 kG

Current*
- Wall: 1.42 MA
- Inner Hoop: .46 MA
- Outer Hoop: .25 MA

B_t

Capacitor Bank
- Capacitance: .37 F
- Voltage: 450 V
- Energy: 37 kJ

B (midcylinder)*: 400 G

*Approximate Values

Table 3.2 - POLOIDAL DIVERTOR PARAMETERS

Physical

Major Radius
- Inner Hoop 115.4 cm
- Middle Hoop: 119.4 cm
- Outer Hoop: 123.0 cm

Minor Radius of Hoops: 1.1 cm

Electrical

Capacitor Bank
- Capacitance: .47 F
- Voltage: 450 V
- Energy: 48 kJ

Hoops	Single	Triplet
Resistance	.068 Ω	.104 Ω
Inductance	220 μH	160 μH
Peak current (Amp-turns, Middle Hoop)	39 kA	28 kA
Time to peak current	8.6 ms	5.6 ms
Current decay time	32 ms	49 ms

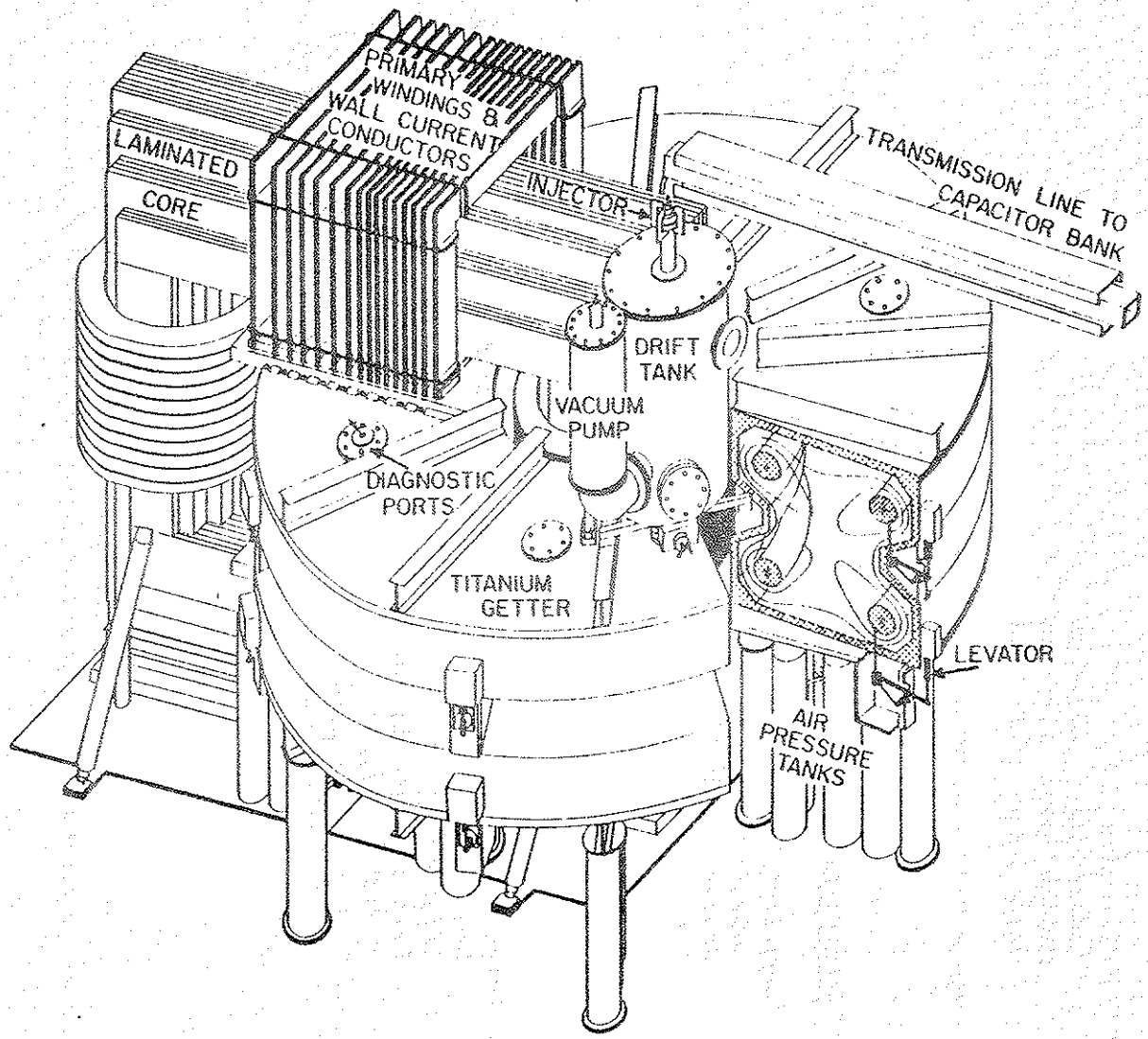

Fig. 3.1 - WISCONSIN LEVITATED OCTUPOLE

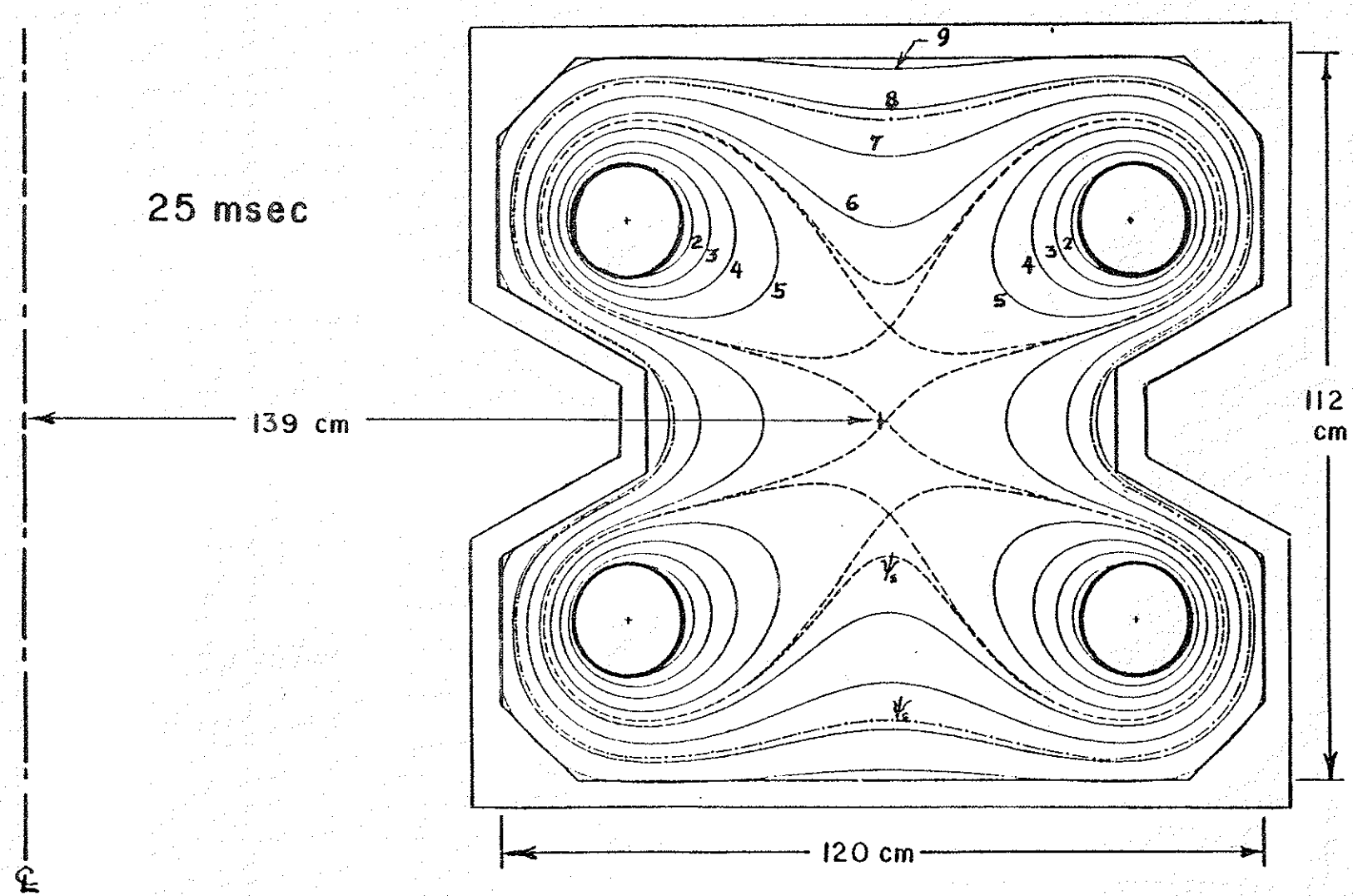

Fig. 3.2 - Minor cross-section of octupole with contours of poloidal flux Ψ (labeled in Dories). Ψ_s is separatrix, Ψ_c is critical field line.

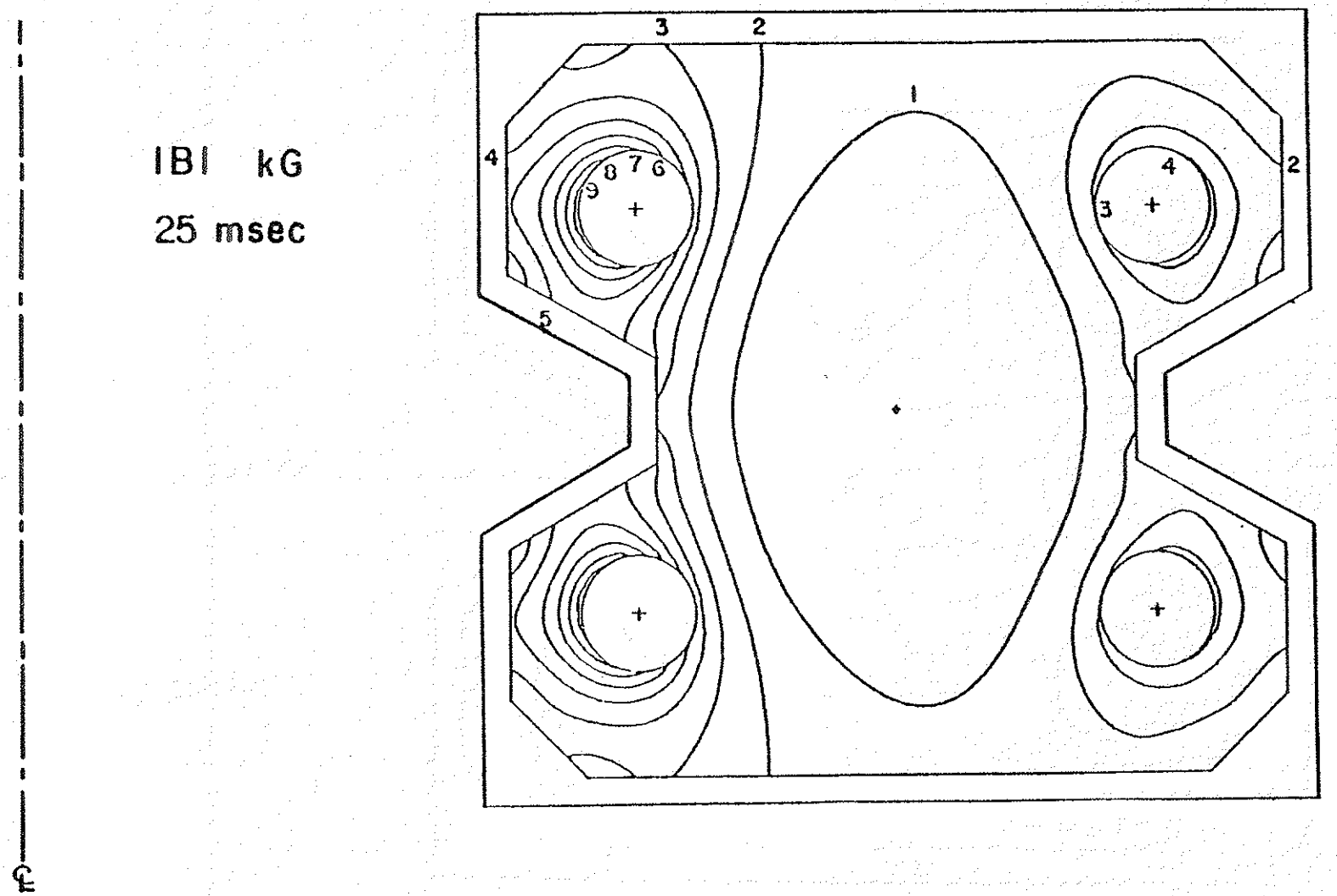

Fig. 3.3 - Minor cross-section of octupole with contours of poloidal magnetic field strength $|B_p|$. Units are kG at .63 Webers in the core.

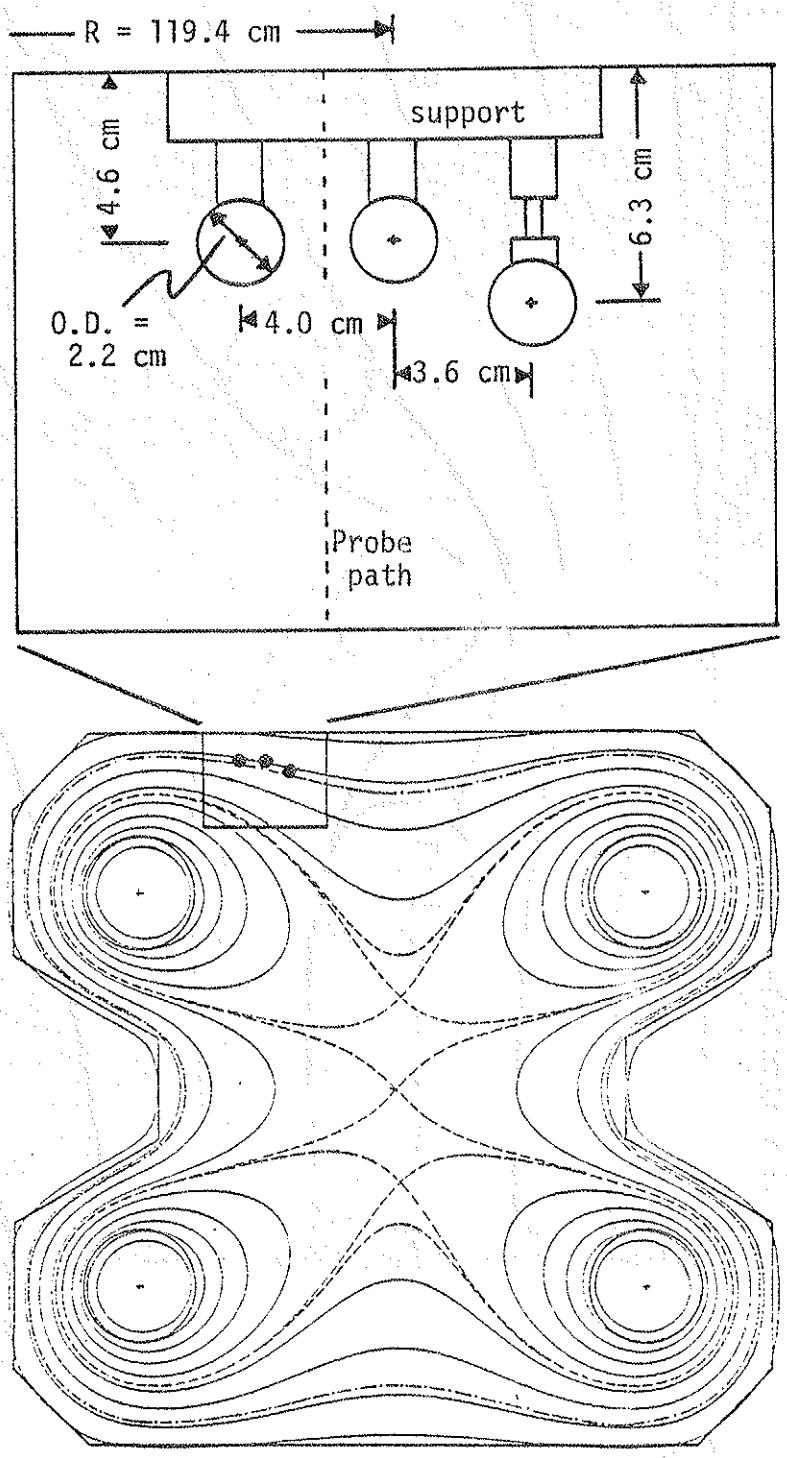

Fig. 3.4 - Location and dimensions of divertor hoop assembly, with simplified outline of support structure.

Fig. 3.5(a)

Single hoop configuration.

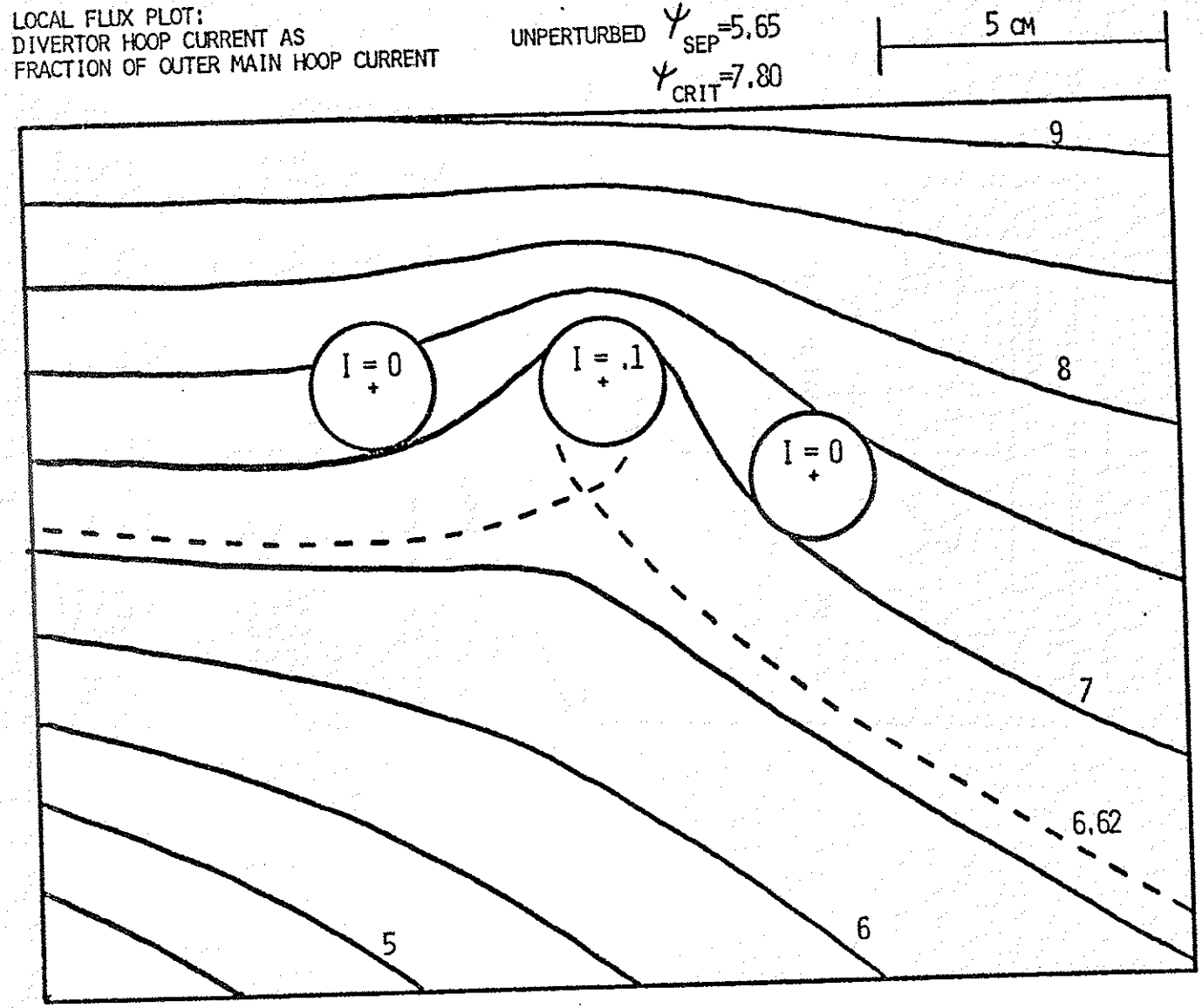

Fig. 3.5(b)

Single hoop configuration.

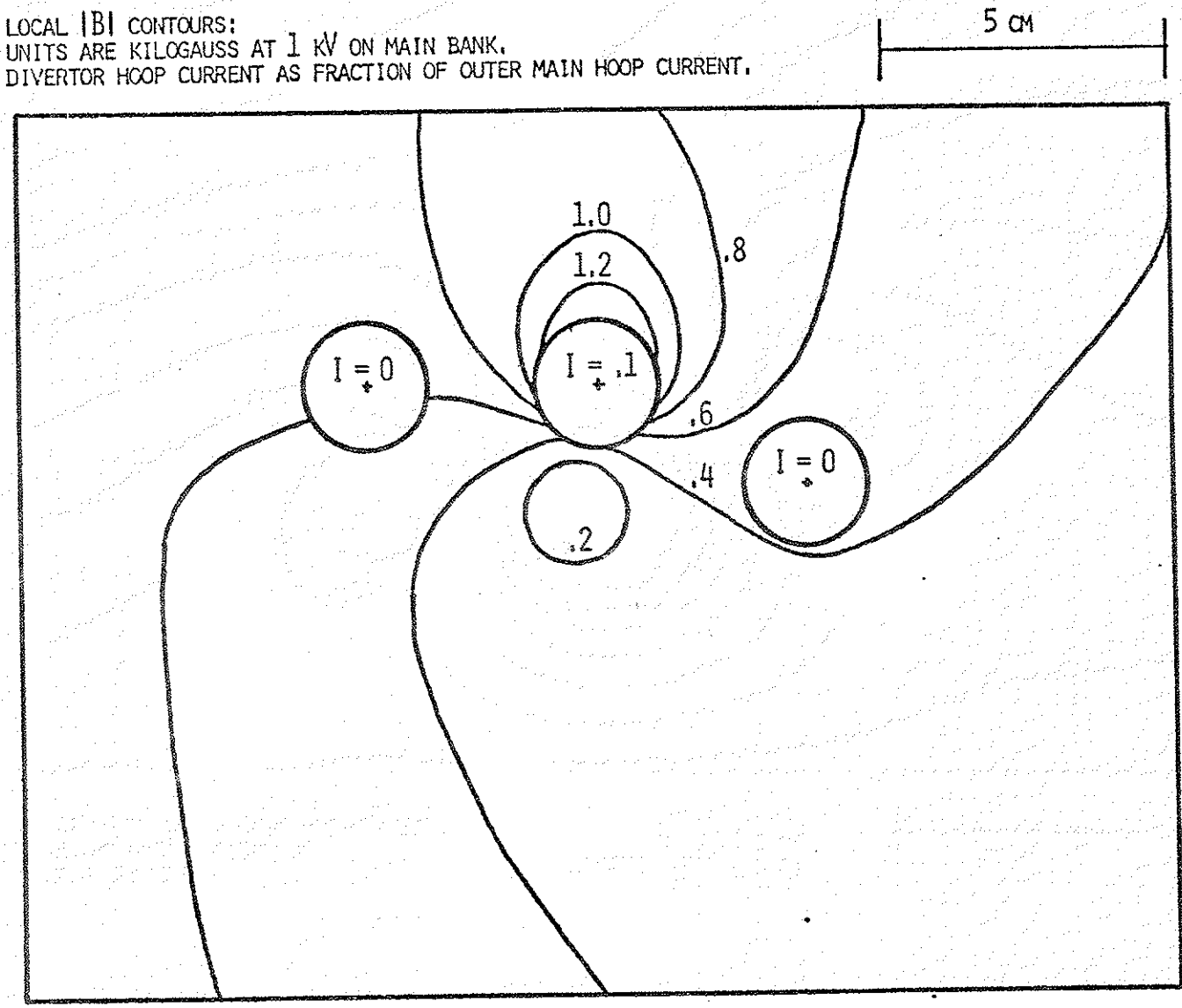

Fig. 3.6(a)

Triplet configuration.

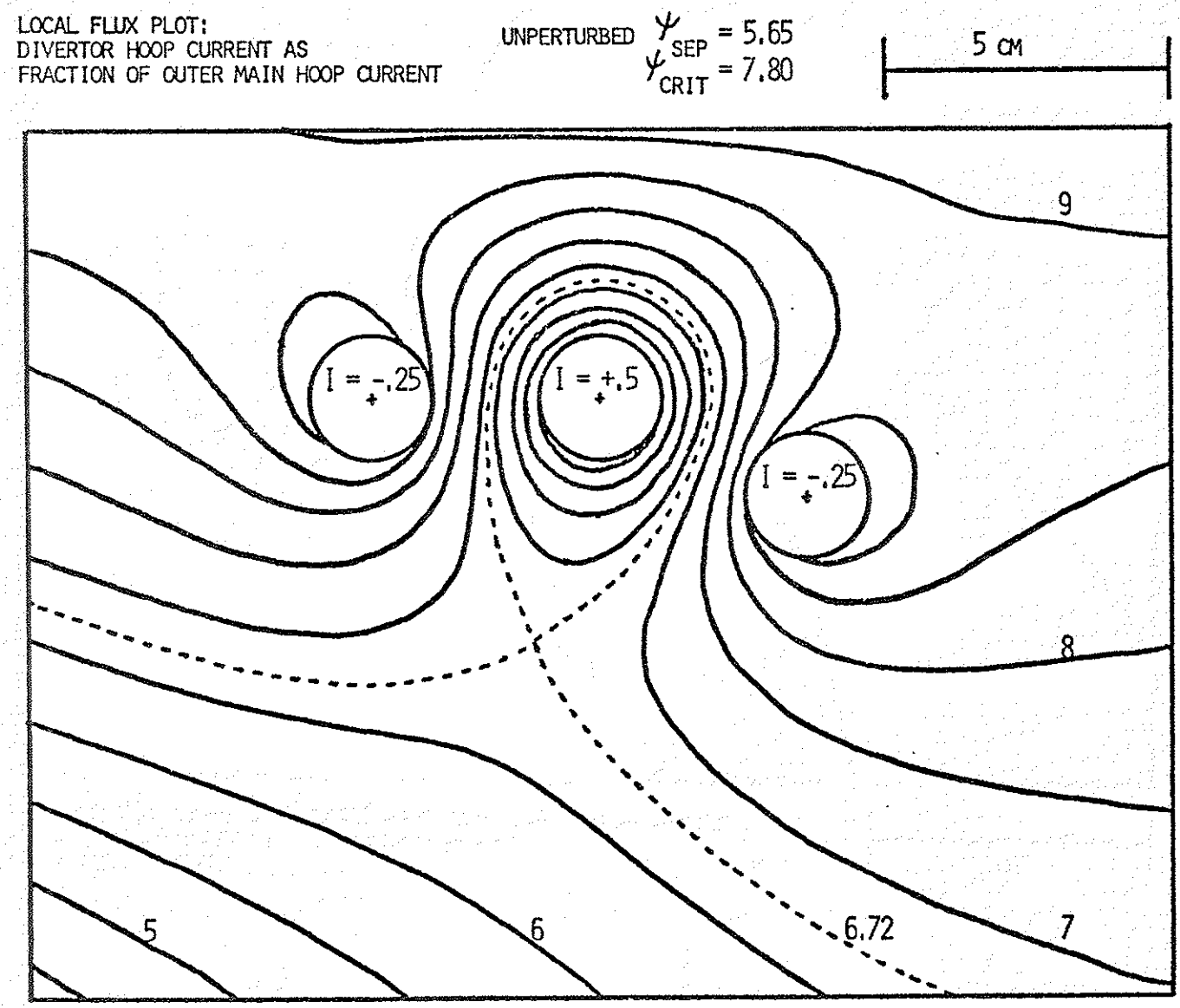

Fig. 3.6(b)

Triplet configuration.

LOCAL |B| CONTOURS:
UNITS ARE KILOGAUSS AT 1 kV ON MAIN BANK.*
DIVERTOR HOOP CURRENTS AS FRACTION OF OUTER MAIN HOOP CURRENT.

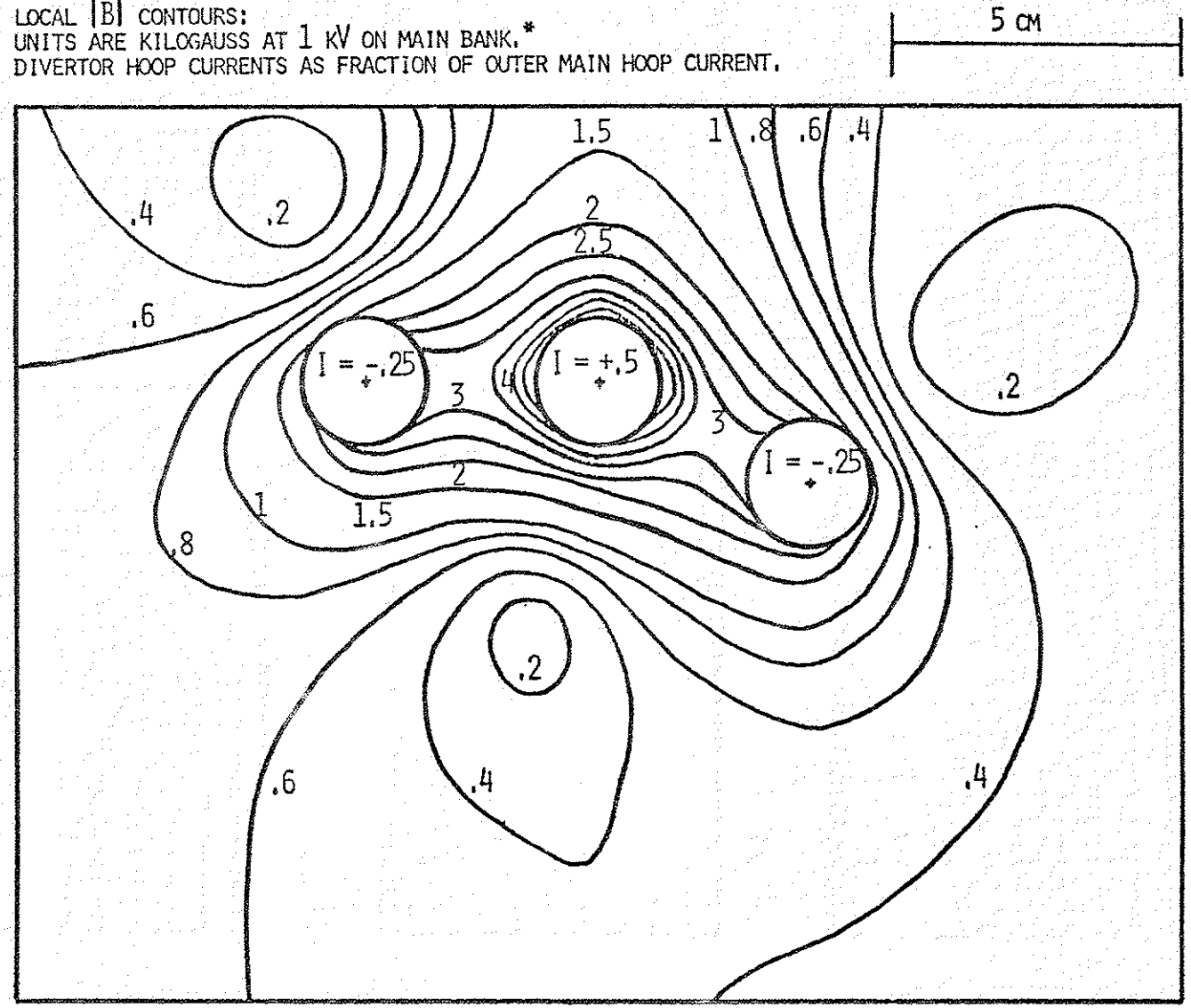

*NOTE CHANGE IN CONTOUR SPACING AT |B| = 1.

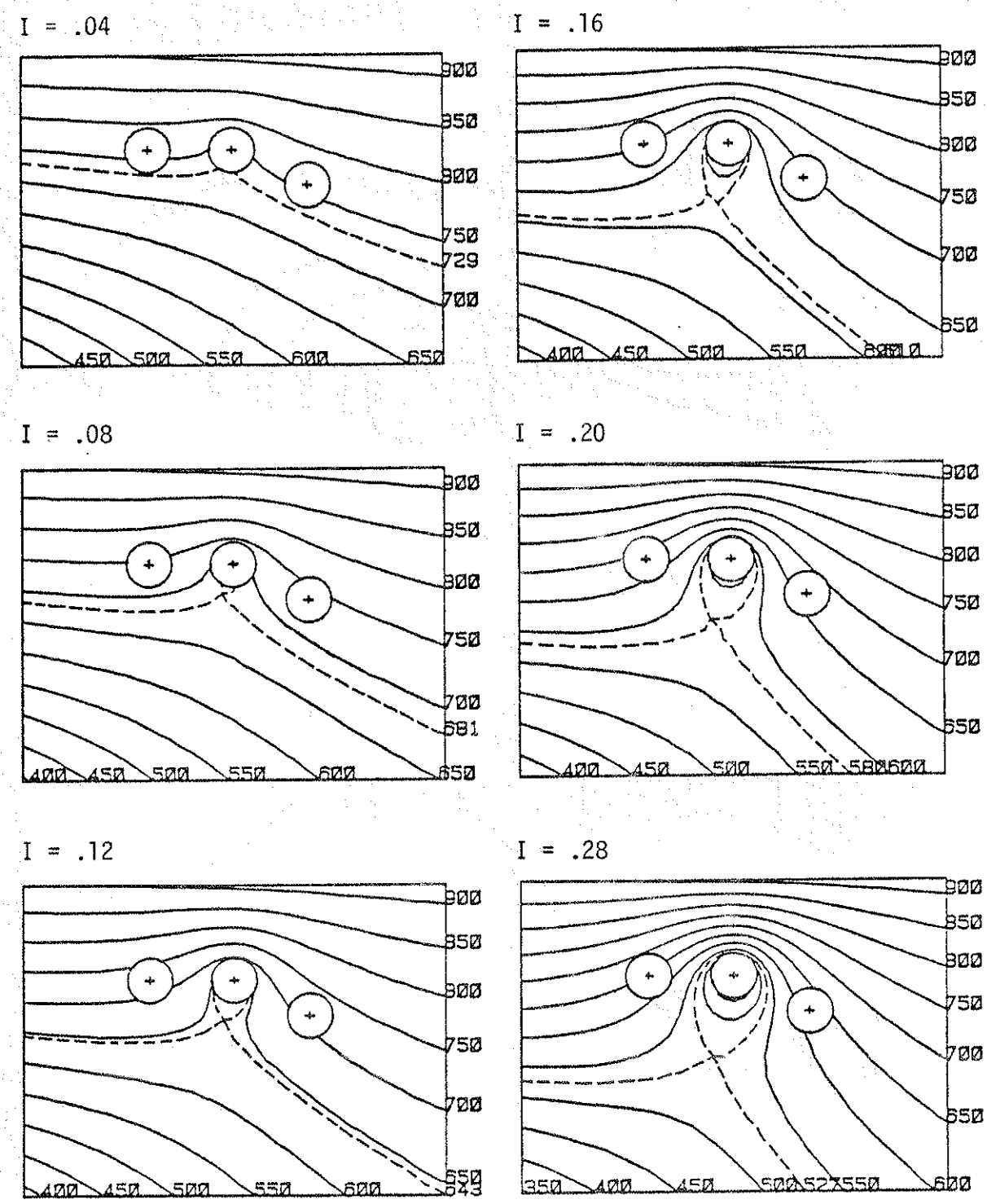

Fig. 3.7 - Single hoop configuration: poloidal flux plots for varying current (shown as ratio of divertor current to outer main hoop current). Dotted line is divertor separatrix.

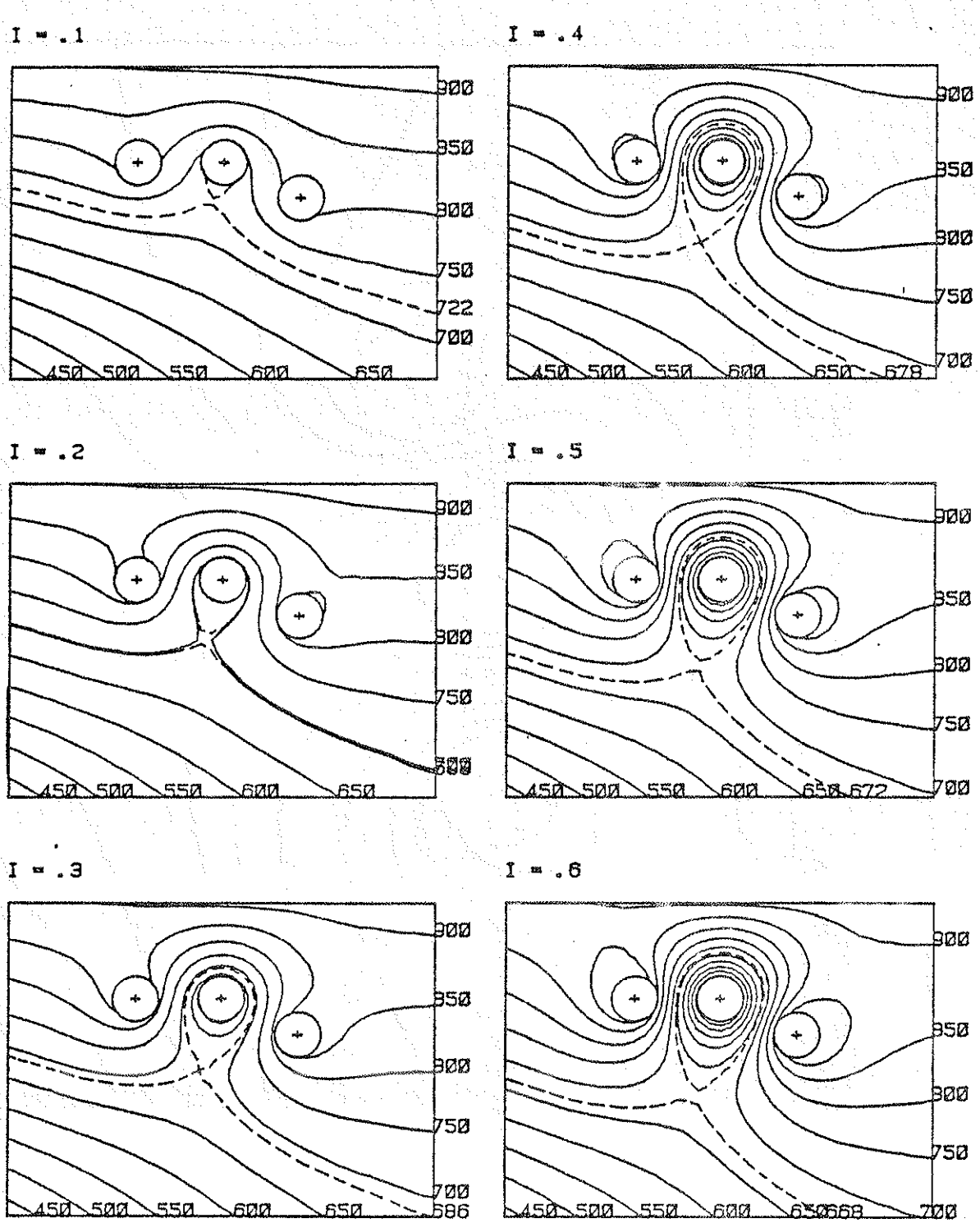

Fig. 3.8 - Triplet configuration: poloidal flux plots for varying current (shown as ratio of middle divertor hoop current to outer main hoop current). Dotted line is divertor separatrix.

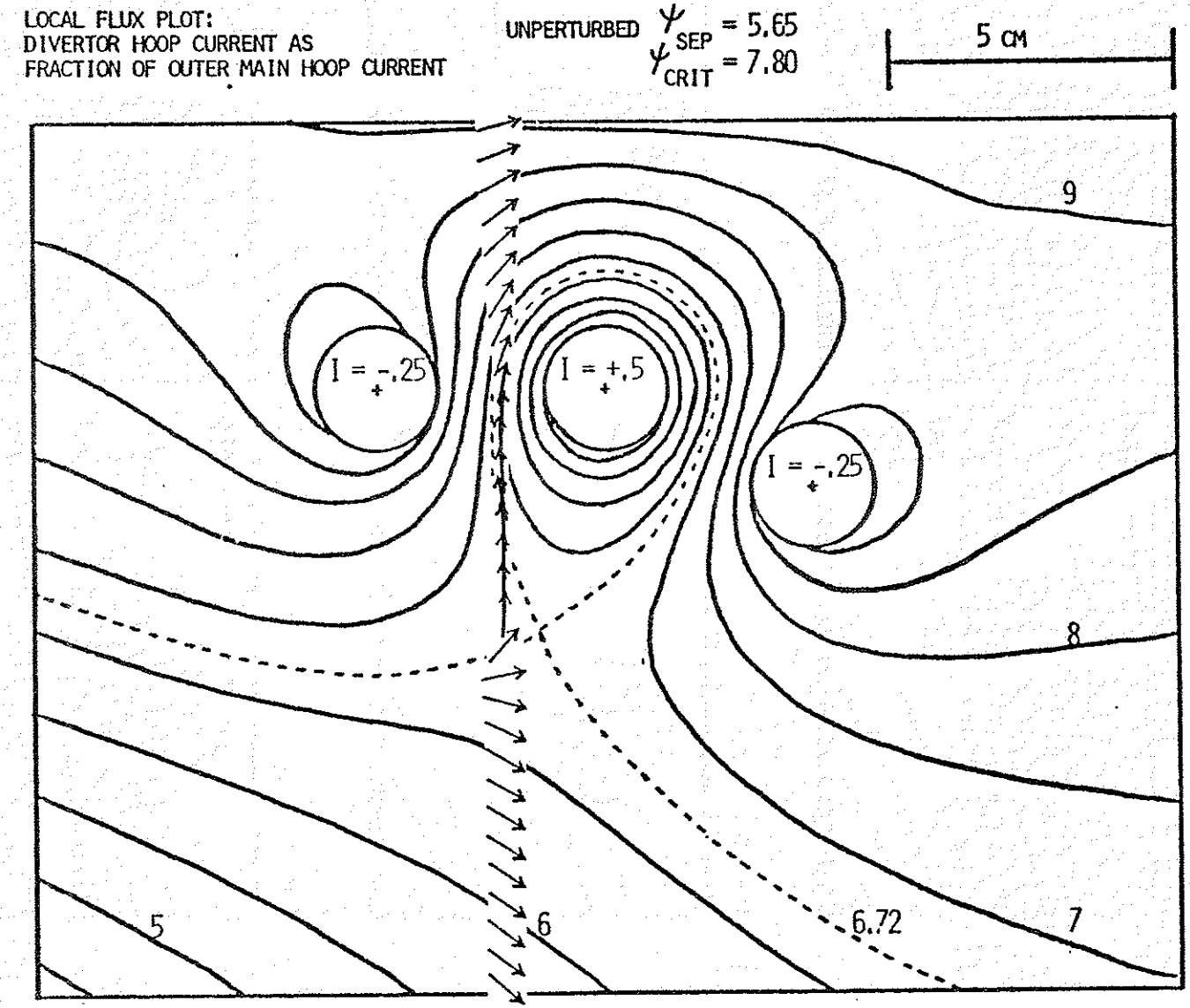

Fig. 3.9 - Unit $\vec{B}/|B|$ vectors (measured) on calculated flux plot. Triplet configuration.

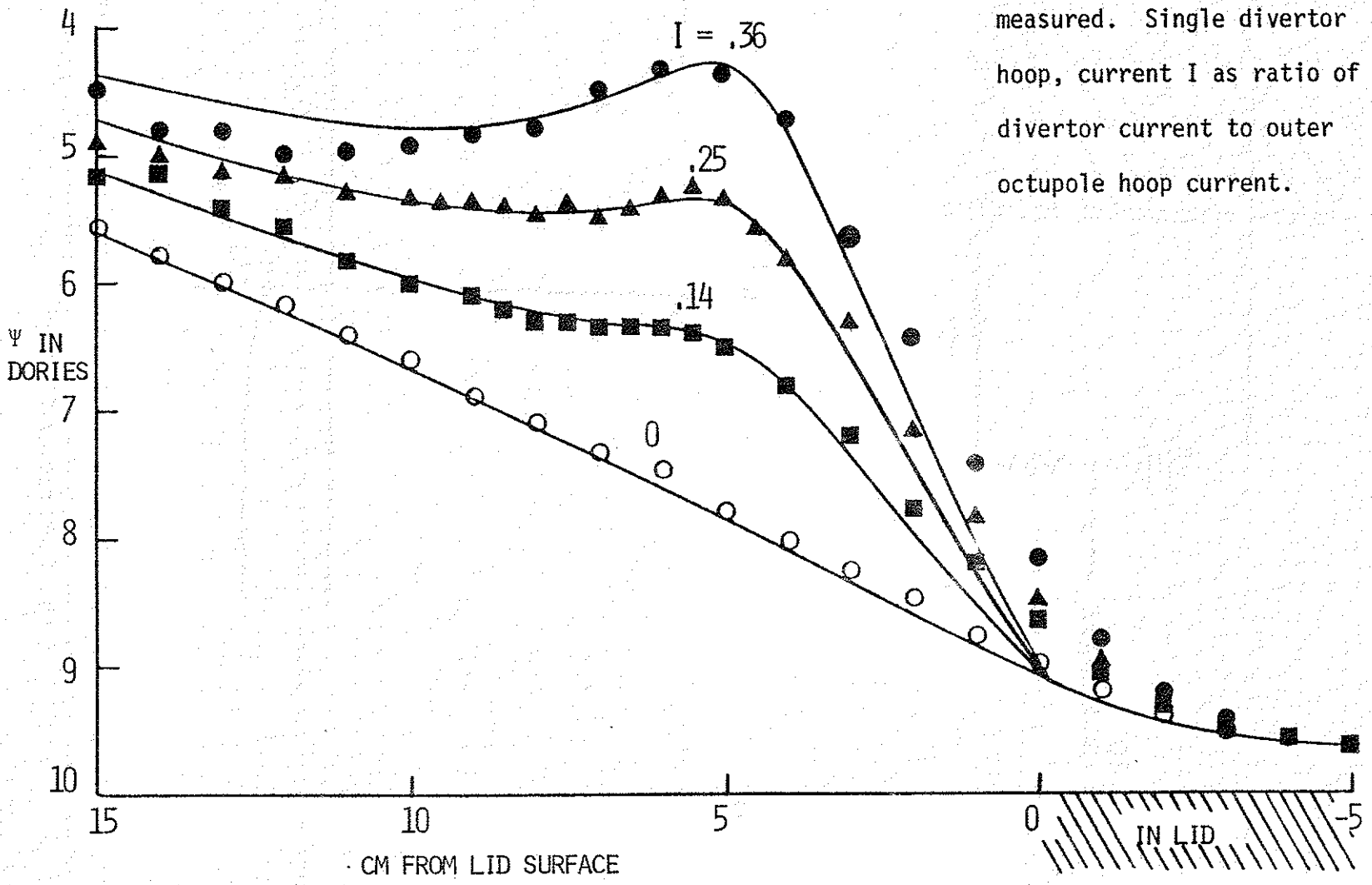

Fig. 3.10 - Ψ profiles, calculated and measured. Single divertor hoop, current I as ratio of divertor current to outer octupole hoop current.

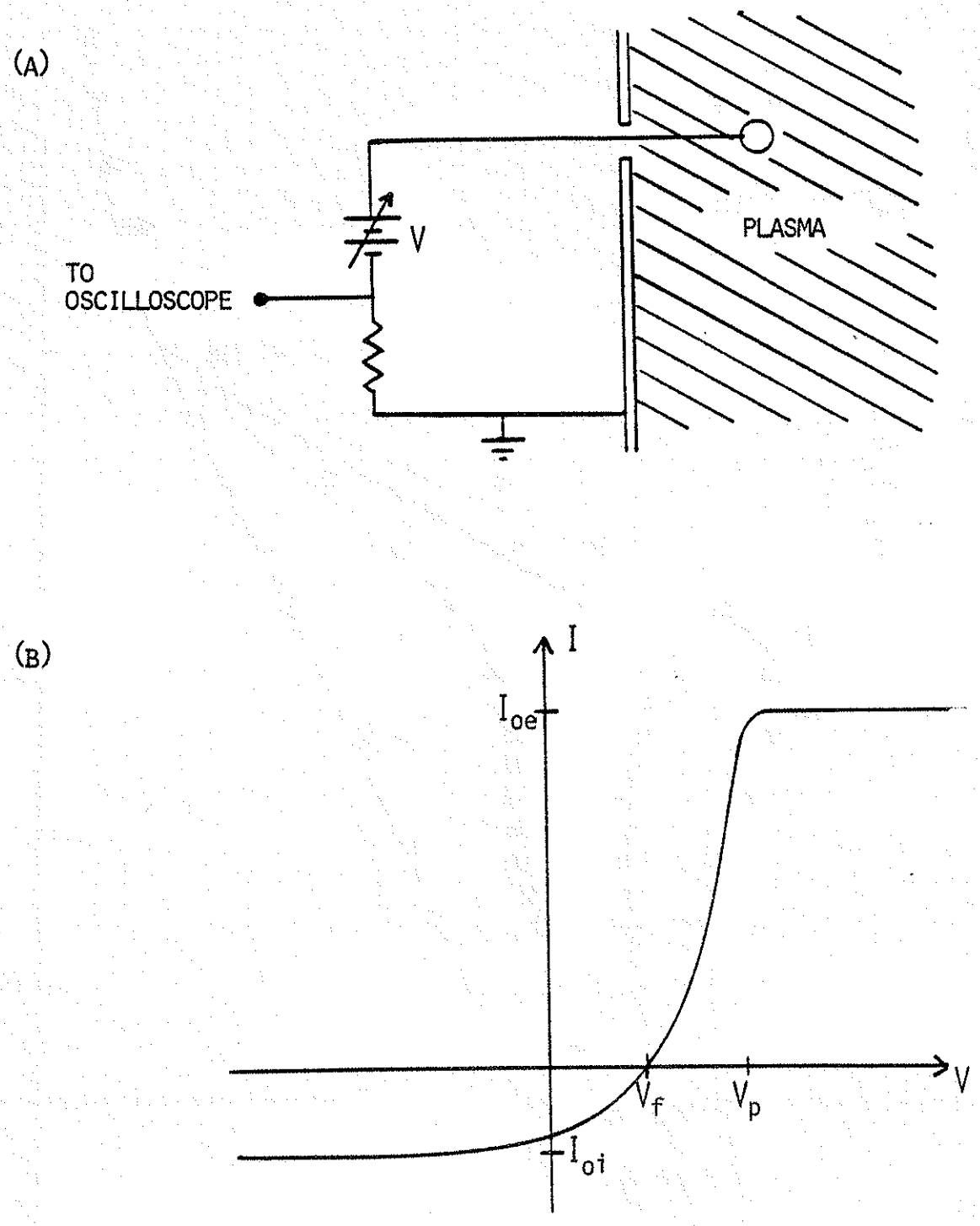

Fig. 3.11 - Langmuir probe (a) biasing circuit, (b) idealized I vs. V characteristic.

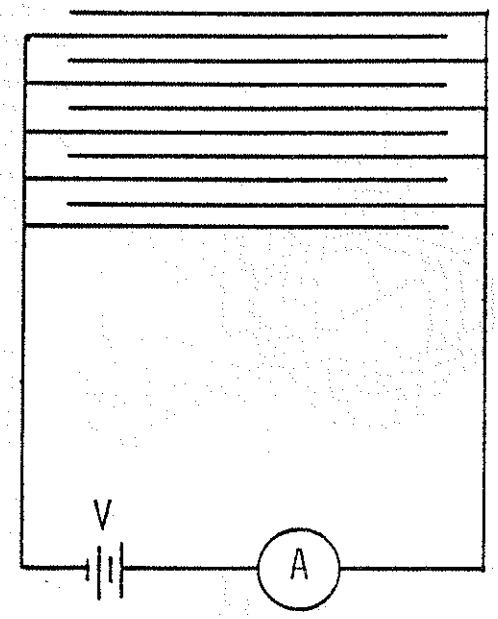

Fig. 3.12 - Striped collector: 16 lines/cm, 6 cm x 6 cm (typically).

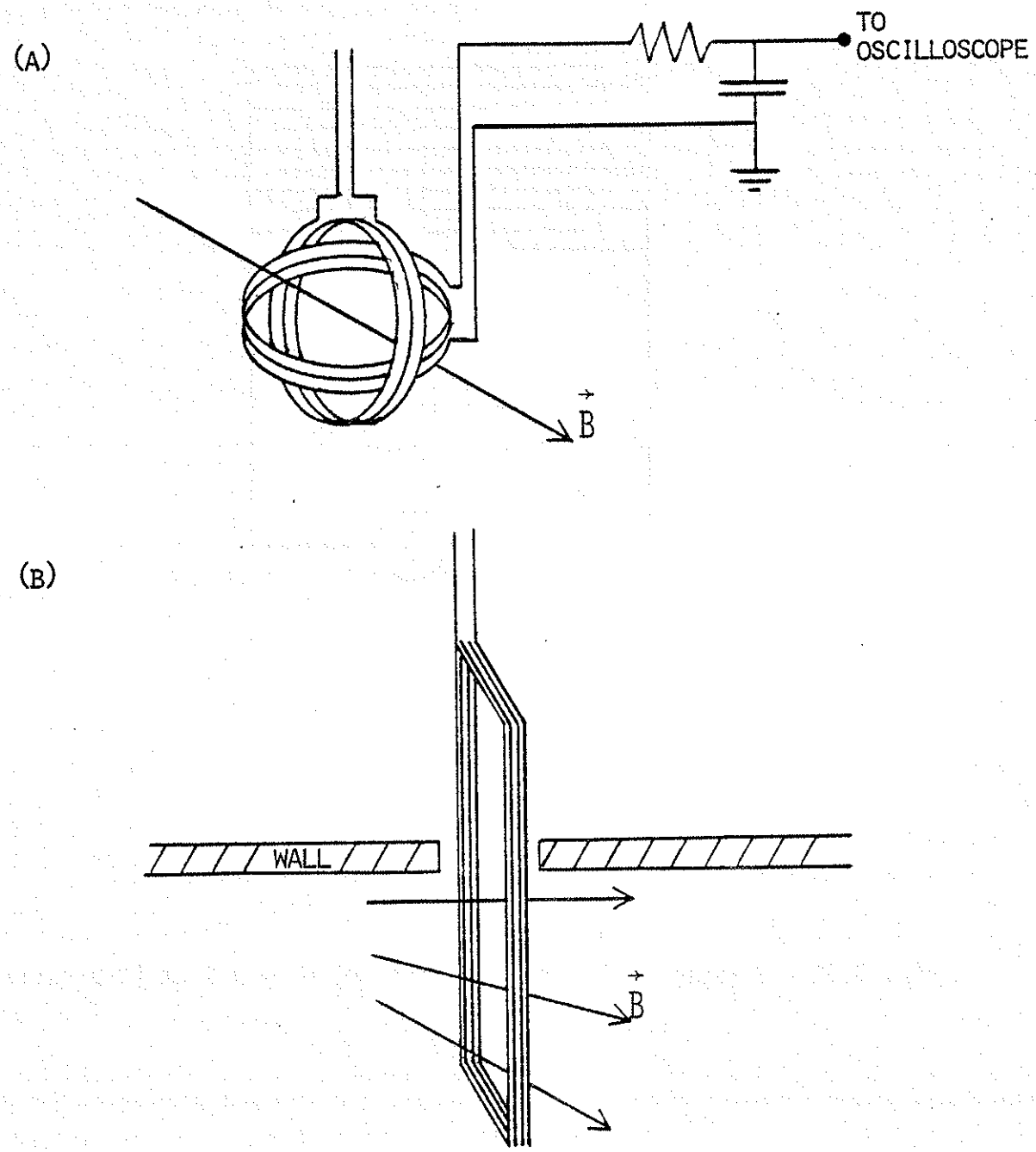

Fig. 3.13 - $\dot{\vec{B}}$ probes: (a) local $\vec{B}$, (b) total flux Ψ.

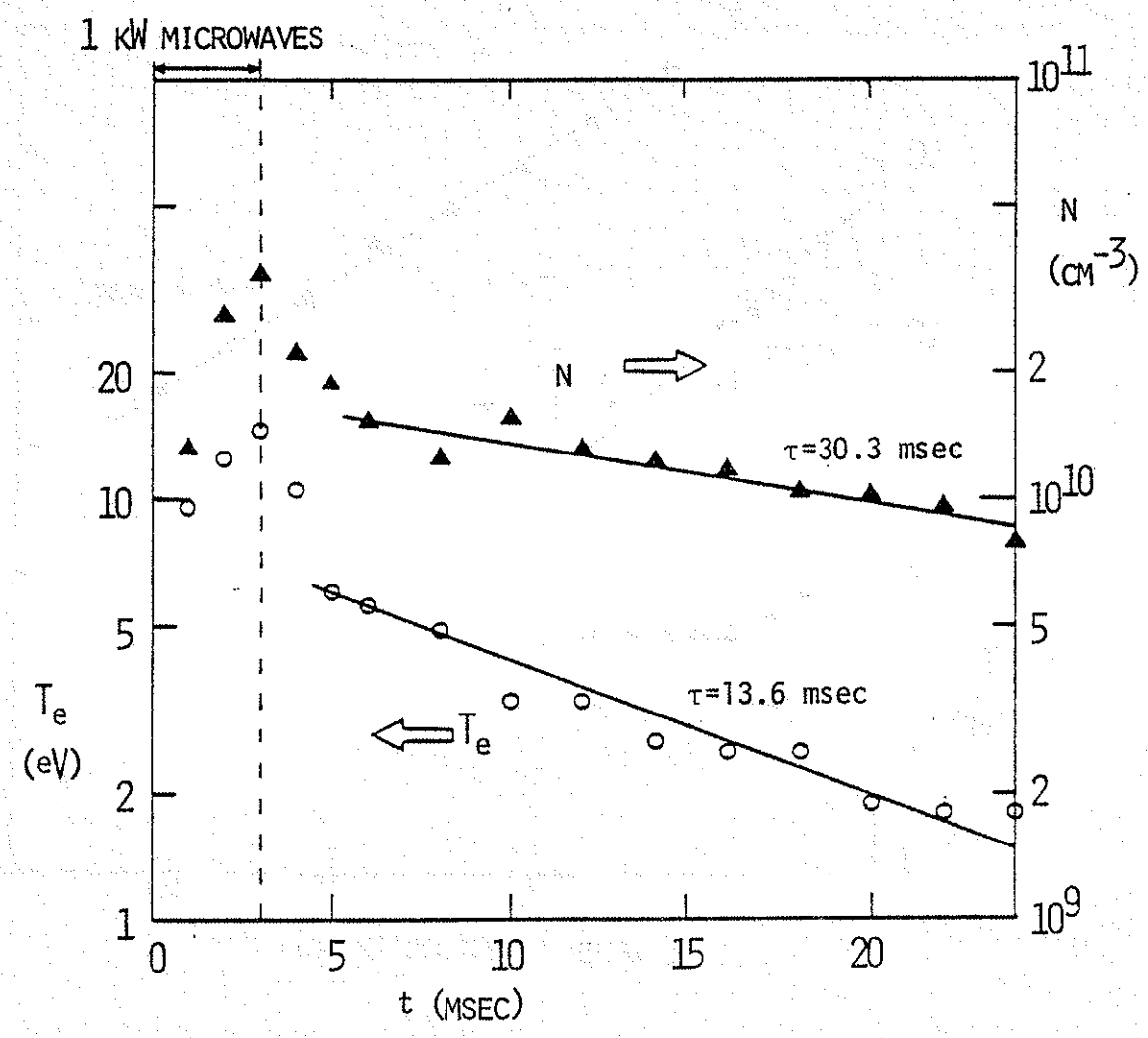

Fig. 3.14 - ECRH plasma: time evolution of n and T_e (from Langmuir probe).

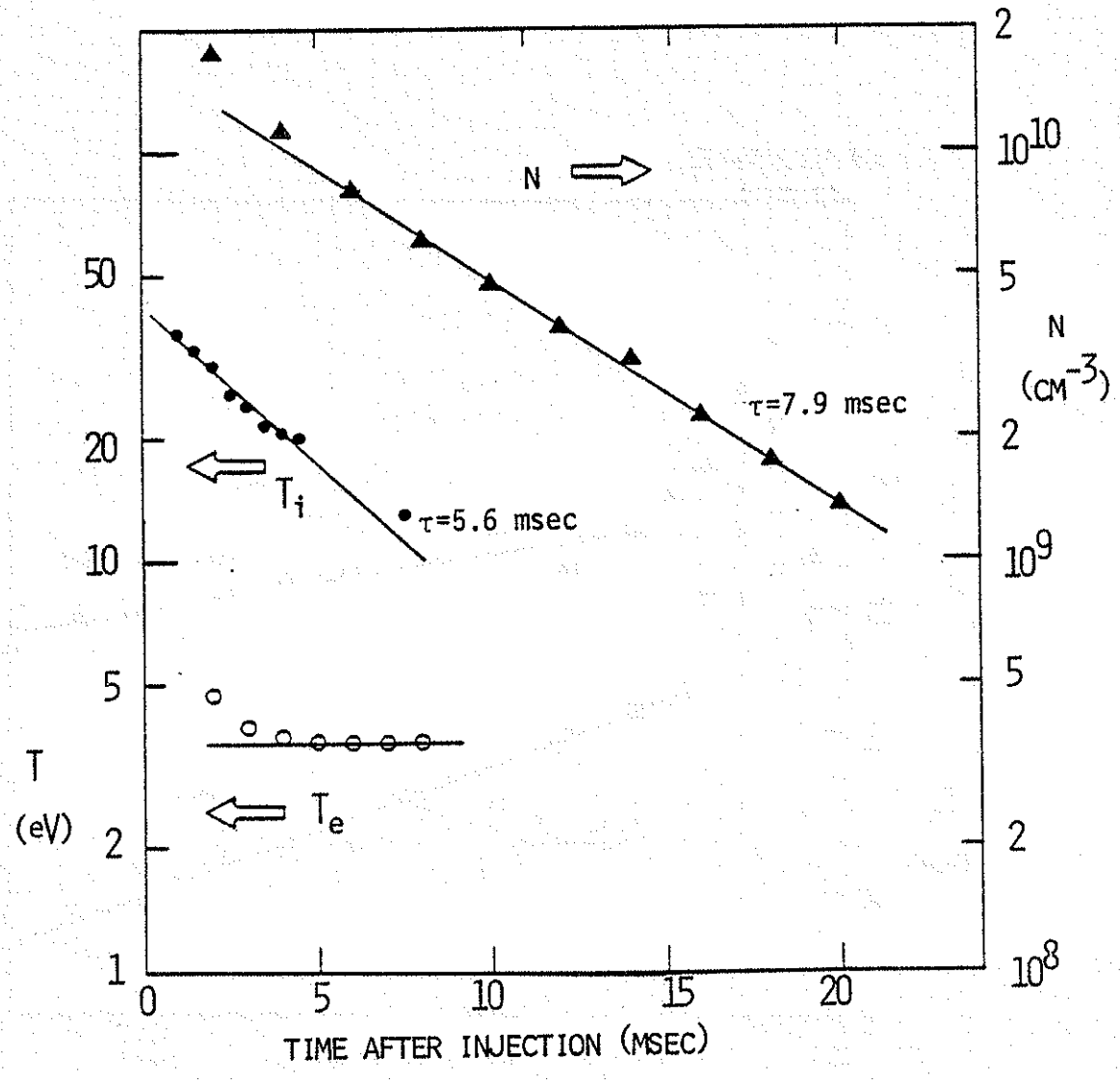

Fig. 3.15 - Small gun plasma: time evolution of n (from microwave Fabry-Perot interferometer), T_i (from skimmer probe), and T_e (from Langmuir probe). B_p bank = 700 volts, B_t bank = 400 volts.

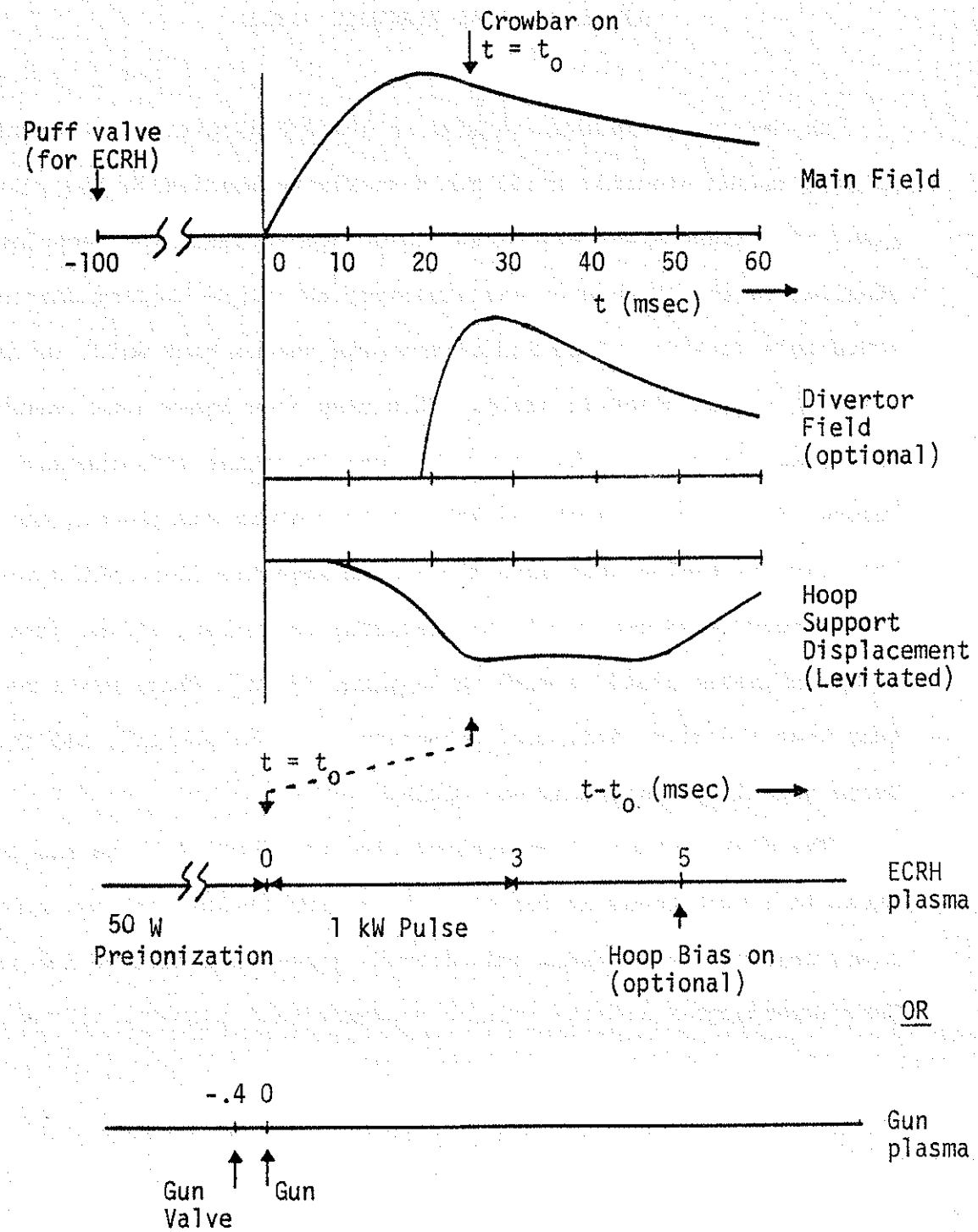

Fig. 3.16 - Timing of experimental sequence (typical). Note the change of time scale near the middle of the figure.

CHAPTER 4

APPLIED RADIAL ELECTRIC FIELD

An important question related to the E×B divertor is whether the desired radial electric field can actually be applied in the plasma, given the plasma's well-known shielding properties. The question was studied, in the absence of any divertor, by simply biasing one of the octupole's internal rings relative to the vacuum tank wall, in order to create a radial electric field. This ring then bears some resemblance to a giant Langmuir probe, but with some important differences: the "probe" is no longer small enough not to perturb the plasma, and in this case particles must move across the magnetic field while most probe theories assume freely accelerating particles, either parallel to the magnetic field or with no magnetic field. These facts mean that some electric field must penetrate into the plasma[1], and the usual Debye shielding length may not apply.

The distribution of an applied electric field will be discussed first in a slab geometry for the sake of simplicity, and the modifications required for tokamak and octupole geometries will be described. Then experimental results will be presented and compared to the models.

4.A. Theoretical Models

4.A.1. Slab Geometry

Consider a plasma which varies only in the x-direction (analogous to the minor radius of a toroid), confined by a uniform magnetic field perpendicular to x. In order to apply a low-frequency or dc electric field parallel to x there are conducting boundaries at x=0 and x=L, which can be given an arbitrary potential difference. In the guiding center approximation such an electric field causes plasma particles to have two types of motion parallel to the electric field. (We are not concerned with the transverse E×B drift for the time being since, due to symmetry, it does not alter the spatial distribution of particles.)

First, there is the polarization drift due to a time-varying electric field. This causes the plasma to act as a dielectric, with dielectric constant at low frequency given by[2]

$$\varepsilon = (1 + \frac{n(m_i + m_e)}{\varepsilon_o B^2})\varepsilon_o \qquad (4.1)$$

Assuming for the moment that this is the plasma's only response to the electric field, that is, it behaves as an ideal dielectric, then the resulting distribution of the electric field can be found simply from

$$\nabla \cdot \vec{D} = \nabla \cdot (\epsilon \vec{E}) = 0$$

$$E = \frac{\text{const.}}{\left(1 + \frac{n(m_i + m_e)}{\epsilon_o B^2}\right)\epsilon_o} \tag{4.2}$$

The constant can be found by integrating E between the boundaries and equating the result to the applied potential difference. If $\epsilon >> \epsilon_o$, which is usually the case for plasmas of interest, then E is inversely proportional to n, so E will be largest near the boundaries, where the density is lowest, but depending on the shape of the density profile there may be an appreciable electric field inside the plasma.

If the plasma particles make collisions, with neutral particles for example, at frequency ν_o, then their guiding centers will have a resulting conduction drift

$$\vec{V}_c = \frac{q}{m} \frac{\nu_o}{\nu_o^2 + \omega_c^2} \vec{E} \tag{4.3}$$

If $\nu_o << \omega_c$, then the $(E \times B)/B^2$ drift is unchanged to first order, and

$$\vec{V}_c \approx \frac{m\nu_o}{qB^2} \vec{E} \tag{4.4}$$

which gives rise to a net current density in the plasma of[3]

$$\vec{J} = n(m_i \nu_{oi} + m_e \nu_{oe}) \frac{1}{B^2} \vec{E} = \sigma_\perp \vec{E} \tag{4.5}$$

where $\sigma_\perp$ is the conductivity. In steady state,

$$\nabla \cdot \vec{J} = \nabla \cdot (\sigma_\perp \vec{E}) = 0$$

$$J = \text{const.}$$

$$E = \frac{J}{\sigma_\perp} = \frac{J}{n(m_i \nu_{oi} + m_e \nu_{oe})/B^2} \tag{4.6}$$

If the collision frequencies $\nu_{oi,e}$ are constants then this is essentially the same electric field distribution as in Eq. (4.2); however, this need not be true in general. If not, and if a potential difference is applied rapidly (in a time less than ν_o^{-1}) the electric field will first take the form of Eq. (4.2), then relax to that of Eq. (4.6). If the ratio of σ and ε is not spatially constant within the plasma, the relaxation will be more complicated than a simple exponential decay, but a characteristic local "RC" time for the relaxation is

$$\tau = \frac{\varepsilon}{\sigma} \approx \frac{1}{\nu_{oi} + \frac{m_e}{m_i} \nu_{oe}} \tag{4.7}$$

The physical justification for this is that in the dielectric model, in an electric field E, the ions have been displaced a distance $E/\omega_{ci}B = m_i E/qB^2$ from their initial positions. A single collision by an ion will cause a displacement of the same size, so the ion collision time provides a time scale for the decay due to ion collisions of the initial dielectric model field. However, if the decay is due to electron collisions, because of their smaller gyroradius they must undergo m_i/m_e collisions for the same displacement.

Both the dielectric model and the perpendicular conduction model (assuming collision frequencies do not depend on n) suggest that the scale length for the perpendicular electric field is that of the density profile's scale length, rather than the Debye length.

A true steady state is not possible in the conduction model, in the absence of particle sources, since the current of Eq. (4.5) draws particles out of the plasma, and if there are density gradients the same collisions which are repsonsible for the current will also give rise to diffusion. A somewhat more general solution can be obtained by writing down transport equations for the electrons and ions:

$$\vec{\Gamma}_e = -D_e \nabla n - \mu_e n \vec{E} \tag{4.8a}$$

$$\vec{\Gamma}_i = -D_i \nabla n + \mu_i n \vec{E} \tag{4.8b}$$

where $\vec{\Gamma}_\alpha$ is the flux of species α, and D_α and μ_α are diffusion and mobility coefficients of unspecified form, with μ_e taken to be positive. The usual quasineutrality assumption is made in order to avoid unrealistically large charge densities and electric fields: $n_e \approx n_i = n$. Ambipolar diffusion is discussed in most plasma texts,[4] and has been thoroughly discussed by Armentrout,[5] but these all eventually make the assumption, in order to preserve quasineutrality, that $\vec{\Gamma}_i = \vec{\Gamma}_e$. This is reasonable in many cases, but actually a weaker condition is sufficient to maintain quasineutrality:

$$\frac{\partial}{\partial t}(n_e - n_i) = \nabla \cdot (\vec{\Gamma}_i - \vec{\Gamma}_e) = 0 \tag{4.9}$$

In the present slab geometry, then

$$\Gamma_i - \Gamma_e = \frac{J}{e} \tag{4.10}$$

where J is constant in space as before. Subtracting Eq. (4.8a) from Eq. (4.8b),

$$\frac{J}{e} = -(D_i - D_e)\, n + (\mu_i + \mu_e) nE$$

$$E = \frac{D_i - D_e}{\mu_i + \mu_e} \frac{\nabla n}{n} + \frac{J}{ne(\mu_i + \mu_e)} = E_{amb} + \frac{J}{\sigma_\perp} \tag{4.11}$$

The net electric field is a superposition of E_{amb}, the usual ambipolar electric field for the case of zero current, and a contribution proportional to the current due to the applied potential. The second term is essentially the same as the electric field of Eq. (4.6), where diffusion was omitted.

To find the net fluxes of the two species, Eq. (4.11) is substituted into the transport equations (4.8) to obtain

$$\Gamma_i = -\frac{\mu_i D_e + \mu_e D_i}{\mu_i + \mu_e} \nabla n + \frac{\mu_i}{\mu_i + \mu_e} \frac{J}{e} = -D_{amb} \nabla n + \frac{\mu_i}{\mu_i + \mu_e} \frac{J}{e} \tag{4.12a}$$

$$\Gamma_e = -\frac{\mu_i D_e + \mu_e D_i}{\mu_i + \mu_e} \nabla n - \frac{\mu_e}{\mu_i + \mu_e} \frac{J}{e} = -D_{amb} \nabla n - \frac{\mu_e}{\mu_i + \mu_e} \frac{J}{e} \tag{4.12b}$$

The particle fluxes respond to the density gradient with the usual ambipolar diffusion coefficient D_{amb}, and have an additional term due to the externally applied electric field. Note that due to the assumption $\nabla \cdot J = 0$,

$$\frac{\partial n}{\partial t} = -\nabla \cdot \Gamma_i = \nabla \cdot (D_{amb} \nabla n) - \frac{J}{e} \nabla \left(\frac{\mu_i}{\mu_i + \mu_e} \right) \tag{4.13}$$

The time evolution of the density is affected by the externally applied electric field only through the term $\nabla \left(\frac{\mu_i}{\mu_i + \mu_e} \right)$; if μ_e / μ_i is spatially constant (as in Eqs. (4.3) to (4.5) above) then there is no effect at all on the density evolution.

The net electric field given in Eq. (4.11) is a superposition of the ambipolar field and the field due to the external source. In all the discussion following, E will be taken to mean only the external contribution.

The contribution from the external source is the same as for the simplified derivation resulting in Eq. (4.6), varying inversely with density if the mobilities are spatially constant. The magnitude of electric field appearing in the plasma for a given potential difference between the boundaries, then, depends on the shape of the density profile. In fact, it depends strongly on the density profile close to the boundaries, where the density is most difficult to measure experimentally and where the assumptions made above are most likely to be invalid.

One of the most obvious ways in which the assumptions may fail is

the following: if the applied potential difference is large enough, the flux of one species predicted by Eqs. (4.12) may go to zero at the boundary from which the applied potential repels it. That is, the flux of this species due to the electric field becomes equal and opposite to the flux due to the density gradient. Since under ordinary circumstances the boundary cannot act as a source of particles, the net flux at the boundary cannot change sign. Therefore the electric field cannot increase beyond this point, nor can the current, without violating the assumptions made earlier. The upper limit on the current density obtained by applying this condition to the ions is

$$\left.\frac{\mu_i}{\mu_i + \mu_e}\right|_{o+} \left.\frac{J}{e} \leq D_{amb}\nabla n\right|_{o+}$$

$$J \leq e(D_e + \frac{\mu_e}{\mu_i}D_i)\nabla n\Big|_{o+} \qquad (4.14a)$$

and the corresponding condition for electrons is

$$J \leq e\,(D_i + \frac{\mu_i}{\mu_e}D_e)\nabla n\Big|_{o-} \qquad (4.14b)$$

where the right-hand sides are evaluated at the boundary which repels the species in question. The smaller of the two limits on J then applies. If the potential difference between the boundaries is increased further, in the present idealized model, the species which is limiting the current must become depleted at the boundary, thus forming

a non-quasineutral sheath, the details of which will not be discussed here. Presumably, any additional applied potential difference will appear in the sheath and the current will saturate at the smaller of the limits. This saturation current is equal to $\lambda e D_{amb} \nabla n$ evaluated at the boundary where the sheath forms, with $\lambda > 1$ a numerical factor depending on μ_i/μ_e. In fact, if either $\mu_i >> \mu_e$ or $\mu_i << \mu_e$ then $\lambda \approx 1$, and the saturation current is equal to the unperturbed plasma flux to the boundary (multiplied by e). Then if the applied potential is reversed a similar sheath will form at the other boundary, and the saturation current will equal the unperturbed flux to that boundary. For example, if $\mu_i >> \mu_e$, then a large enough potential difference will prevent any ions from reaching the more positive boundary, while having very little effect on electron transport to that boundary. Therefore the saturation current will equal the unperturbed electron flux to the positive boundary.

The corresponding limits on E in the neutral plasma at the edge of the sheath are

$$E\Big|_{o+} = \frac{J}{\sigma} < \frac{D_{amb}}{\mu_i} \frac{\nabla n}{n}\Big|_{o+} \tag{4.15a}$$

$$E\Big|_{o-} < \frac{D_{amb}}{\mu_e} \frac{\nabla n}{n}\Big|_{o-} \tag{4.15b}$$

If σ increases with n, and the density is lowest at the boundaries, as is usually the case, then the more stringent of these conditions

provides an upper limit for the electric field everywhere outside the sheath.

If the assumptions are made that $D_\alpha = \frac{kT}{e}\mu_\alpha$ (the Einstein relation) and $T_i = T_e$, then

$$E \lesssim \left(\frac{2D_<}{D_>}\frac{kT}{e}\frac{\nabla n}{n}\right)\Bigg|_o \tag{4.16}$$

where $D_<$ is the smaller of D_i and D_e, and $D_>$ is the larger. This is a rather pessimistic result, since the limit on the external contribution to E is less than E_{amb} by the factor $2D_</D_>$. However, the latest assumptions may not be true.

In particular, the Einstein relation may not hold in the simple form given above. Nonequilibrium thermodynamics predicts a relationship between the coefficients of diffusion and mobility, but the details of the relationship are not clear for a magnetized plasma.[6] In fact, in the fluid picture used above, different mechanisms may be responsible for diffusion and mobility. For instance, to first order, classical collisions between unlike charged particles can cause diffusion but not mobility. This is easily seen by arguing from the effect to the cause: If, due to perpendicular mobility, there is a current density $\vec{J}$ parallel to $\vec{E}$ in the plasma, then there is a resulting $\vec{J}\times\vec{B}$ force density in the plasma in the $\vec{E}\times\vec{B}$ direction. The plasma is not accelerating, but has a constant $\vec{E}\times\vec{B}/B^2$ drift, so there must be some drag force balancing the $\vec{J}\times\vec{B}$; this drag is the mechanism repsonsible for the mobility. To first order, all charged particles

in a small volume of plasma drift at the same speed and thus cannot produce the drag force.[7] On the other hand, collisions with stationary neutral particles can cause drag. The net force is then

$$\vec{F} = \vec{J}\times\vec{B} - n(m_i\nu_{io} + m_e\nu_{eo})\vec{v} = 0 \qquad (4.17)$$

which gives Eq. (4.5) again. Charged particle collisions can result in a drag force through viscosity effects if the drift is not spatially uniform, but then the drag depends on the second spatial derivative of the drift speed and hence of the electric field; therefore the simple linear relation of Eq. (4.8) no longer holds.

It has also been found in a numerical simulation of a two-dimensional guiding center plasma that perpendicular conductivity can arise from fluctuating electric fields in the plasma.[8] The corresponding mobility satisfies the Einstein relation with the Bohm-like diffusion coefficient of Taylor and McNamara.[9] This calculation was done in a finite-size box, and the fluctuations were assumed isotropic with respect to the box, which makes them anisotropic in the E×B drift frame, playing a role somewhat analogous to neutral particle collisions. However, one might expect that in a plasma with a uniform E×B drift, unless the fluctuations are caused by some stationary feature on the wall, they might as likely be isotropic in the rest frame of the plasma (the E×B drift frame), resulting in no conductivity.

4.A.2. Tokamak Geometry

The preceding arguments illustrate some of the basic principles involved in perpendicular electric fields, and may be useful (with modifications to account for geometry) in other situations where the E×B drift is in a symmetry direction, such as in the octupole with poloidal field only. In a tokamak, however, the results are more complicated. A number of theoretical papers have been written concerning the damping of an initial rotation and its accompanying electric field, and they are directly applicable to the case where the rotation is maintained in steady state by an external voltage source.

As an element of plasma moves with the E×B drift in a tokamak, the poloidal component of its motion carries it toward smaller major radius. This tends to compress it in the toroidal direction, and to maintain divergenceless flow (a valid assumption if the drift speed does not approach the sound speed) it will expand parallel to B. This additional, non-uniform flow leads to "neo-classical" corrections to the perpendicular conductivity.

Using fluid theory, Boozer[10] has identified three regimes according to the relative importance of viscosity:

$$\sigma_\perp = \begin{cases} \dfrac{\rho}{B^2}\dfrac{1}{\tau_t}\,(1+2q^2)\,, & \alpha \ll 1 \\ \dfrac{\rho}{B^2}\dfrac{1}{\tau_p}\,(1+2q^2)\,, & 1 \ll \alpha \ll \dfrac{1}{\epsilon^2} \\ \dfrac{\rho}{B_p{}^2}\dfrac{1}{\tau_t}\,, & \dfrac{1}{\epsilon^2} \ll \alpha \end{cases} \tag{4.18}$$

τ_t is the damping time for toroidal angular momentum, which like the damping of linear momentum in the slab model, must be due to collisions with neutral particles or other stationary structures. τ_p is the damping time for poloidal angular momentum due to ion viscosity, and $\alpha = (2 + q^{-2})\tau_t/\tau_p$. ρ is the plasma mass density, q is the tokamak "safety factor," and ε is the inverse aspect ratio.

Similar considerations apply to the polarization current, and Boozer obtains for the low-frequency perpendicular dielectric constant[11]

$$\kappa = \begin{cases} 1 + \dfrac{\rho}{B^2} & \omega >> \dfrac{1}{\tau_s} \\ 1 + \dfrac{\rho}{B^2}\,(1 + 2q^2) & \dfrac{1}{\tau_p} << \omega << \dfrac{1}{\tau_s} \\ 1 + \dfrac{\rho}{B_p^{\,2}} & \dfrac{1}{\tau_t} << \omega << \dfrac{\varepsilon^2}{\tau_p} \end{cases} \tag{4.19}$$

The classical value of $1 + \rho/B^2$ applies only for times shorter than $\tau_s = qR_o/c_s$, the sound transit time, when there is not enough time for the pressure to equalize on a flux surface. When $\omega \leq \tau_p^{-1}$ the dielectric constant also has a large imaginary part corresponding to the conductivity given above: $\mathrm{Im}(\kappa) = \sigma/\omega\varepsilon_o$.

Boozer's results were obtained for the collisional ($\tau_i << \tau_s$) regime, and this is reflected in his expression for the poloidal damping time:

$$\tau_p = \frac{4}{3}(1 + 2q^2)\,\frac{R^2 m_i}{T_i \tau_i} \tag{4.20}$$

where R is the major radius and τ_i the classical ion-ion collision time. This appears directly only in the parameter α and in the conductivity expression for intermediate viscosity, so in other collisionality regimes it should be valid to use the conductivity expressions at least for high and low viscosities, and all the dielectric constant expressions, using the new value of τ_p to choose the appropriate one.

Stix[12] uses the drift kinetic equation to obtain poloidal damping times for the collisionless (banana) and plateau regimes of neoclassical theory:

$$\tau_p = \begin{cases} \frac{\varepsilon^{\frac{1}{2}}}{q^2}\tau_i \ , & \varepsilon^{-3/2}\tau_s \ll \tau_i \\ \\ \frac{1}{q^2}\tau_s \ , & \tau_s \ll \tau_i \ll \varepsilon^{-3/2}\tau_s \end{cases} \tag{4.21}$$

Hirshman[13] takes viscosities obtained from the drift kinetic equation and uses fluid theory to obtain

$$\tau_p = (2 + \frac{1}{q^2}) \times \begin{cases} 1.29\varepsilon^{3/2}\tau_i \ , & \varepsilon^{-3/2}\tau_s \ll \tau_i \\ \frac{2}{\sqrt{\pi}}\tau_s \ , & \tau_s \ll \tau_i \ll \varepsilon^{-3/2}\tau_s \\ \\ \frac{\tau_s}{\tau_i}\tau_s \ , & \tau_i \ll \tau_s \end{cases} \tag{4.22}$$

which agree with those of Stix and Boozer except for numerical factors and a factor of ε in the collisionless regime. All of the above derivations of τ_p use only parallel viscosity (transport parallel to $\vec{B}$

parallel momentum) since perpendicular viscosity (parallel transport of perpendicular momentum or perpendicular transport of parallel momentum) is smaller by $(\omega_{ci}\tau_i)^{-2}$ where ω_{ci} is the ion cyclotron frequency.[14]

As mentioned before, due to conservation of angular momentum, the toroidal damping expressed by τ_t must be caused by neutral collisions, toroidal field ripple, or some other interaction with a stationary structure, rather than charged-particle collisions. However, if the toroidal rotation has shear, perpendicular viscosity can cause it to relax toward rotation as a solid body, in a time[15]

$$\tau_{ts} \sim 10 \frac{1}{q^2} \frac{a^2}{\rho_i^2} \tau_i \qquad (4.23)$$

where ρ_i is the ion gyroradius.

4.A.3. Octupole Geometry

In an octupole with purely poloidal field, the E×B drift due to a radial electric field is in the toroidal direction only, and the complications seen in the tokamak case due to magnetic pumping do not arise. However, the peculiarities of its magnetic field shape do affect the distribution of the electric field. The following discussion will be in terms of the magnetic co-ordinates ψ, χ, and θ (see Appendix) and much of it will not be unique to the octupole.

First, it is interesting to note that if magnetic field lines are

equipotentials and azimuthal symmetry holds, so that the electrostatic potential depends only on ψ, then the frequency of toroidal E×B rotation is given by

$$f = \frac{E}{B}\frac{1}{2\pi R} = \frac{\nabla\phi}{\nabla\psi} = \frac{d\phi}{d\psi} \tag{4.24}$$

which depends only on ψ. Surfaces of constant ψ rotate as rigid bodies, and any viscous effects must occur between surfaces, not within them.

As in the slab geometry, the contribution to the steady-state electric field due to an applied potential difference is determined from the continuity equation for electric charge. The following is a physical argument, but a rigorous transformation of $\nabla \cdot (\sigma\vec{E}) = 0$ into magnetic co-ordinates gives the same result. Assume plasma potential ϕ and density n are constant along field lines, while other quantities ($\sigma_\perp$, $J_\perp$, and charge density ρ) may vary along field lines. The charge crossing flux surface ψ per unit time is

$$I(\psi) = \int_0^{2\pi}\int_0^{\ell} J_\perp R d\ell d\theta = 2\pi\oint J_\perp R d\ell \tag{4.25}$$

where R is major radius. If no charge is to accumulate at any ψ surface then $dI/d\psi = 0$ everywhere, that is, I is a constant. Then

$$I = 2\pi\oint J_\perp R d\ell$$

$$= 2\pi\oint \sigma_\perp E R d\ell$$

$$= -2\pi\oint \sigma_\perp \frac{d\phi}{d\psi}\nabla\psi R d\ell$$

$$= -4\pi^2 \frac{d\phi}{d\psi}\oint \sigma_\perp R^2 B d\ell \tag{4.26}$$

$$\frac{d\phi}{d\psi} = -\frac{I}{4\pi^2\oint \sigma_\perp R^2 B d\ell} \tag{4.27}$$

As an example, suppose $\sigma_\perp$ is due to neutral collisions, as in Eq. (4.5) and assume the collision frequency ν does not vary along a field line. Then

$$\frac{d\phi}{d\psi} = -\frac{I}{4\pi^2(m_i\nu_i + m_e\nu_e)n\oint R^2 B^{-1} d\ell} \tag{4.28}$$

The electric field is inversely proportional to n, and now also to the geometrical factor $\oint R^2 B^{-1} d\ell$. This function behaves similarly to $R^2\oint B^{-1} d\ell$, which it approaches in the large aspect ratio limit. It becomes infinite at the separatrix, and thus enhances the exclusion of electric field from the center of the plasma.

In the absence of cross-field mobility, or on very short time scales, the plasma behaves as a dielectric, and the electric field is determined by Eqs. (4.1) and (4.2), with a similar modification for geometrical effects:

$$\frac{d\phi}{d\psi} = \frac{A}{4\pi^2 \oint \varepsilon R^2 B d\ell} = \frac{A'}{\frac{\varepsilon_o}{m_i}\oint R^2 B d\ell + n\oint R^2 B^{-1} d\ell} \tag{4.29}$$

where $A = 4\pi^2 m_i A'$ is a constant determined by the boundary conditions. If $\varepsilon/\varepsilon_o \approx (\omega_{pi}/\omega_{ci})^2 >> 1$, as is often the case, then

$$\frac{d\phi}{d\psi} \approx \frac{A'}{n\oint R^2 B^{-1} d\ell} \tag{4.30}$$

The electric field is essentially the same as in the neutral collision case.

4.A.4. Summary

To summarize the preceding discussion, if a potential difference is applied across a magnetized plasma, perpendicular to the magnetic field, the plasma will first respond as a dielectric. The electric field distribution will be determined by

$$\nabla \cdot \vec{D} = \nabla \cdot (\varepsilon \vec{E}) = 0 \tag{4.31}$$

where ε is given by Eq.(4.1),or in the case of a tokamak, by Eq. (4.19). Due to perpendicular conductivity, this will relax to an electric field determined by

$$\nabla \cdot \vec{J} = \nabla \cdot (\sigma \vec{E}) = 0 \tag{4.32}$$

where σ is given by Eqs. (4.7) or (4.11), or in the case of a tokamak by Eqs. (4.18). Corrections for a non-uniform magnetic field geometry, as in the octupole, are given by Eqs. (4.29) and (4.27). The relaxation time is ε/σ, corresponding to τ_t in the tokamak discussion. The conductivity σ is determined by the damping of the momentum of the E×B drift, which must be due to interaction with some stationary structure, such as neutral particles or magnetic field variations.

Since ε and σ are both proportional to n, the electric field will be concentrated at the edges of the plasma where the density is low, but if collision frequencies are spatially constant the scale length of the electric field will be that of the density profile, rather than the Debye length, up to some maximum electric field. If σ is due to neutral collisions and the neutral density is low in the center, this will help the electric field penetrate into the plasma. Perpendicular viscosity can also make a contribution to σ, and will tend to transport perpendicular momentum, and thus electric field, toward the center of the plasma.

The magnitude of the current, and thus of the electric field, existing in the plasma, is limited by Eqs. (4.14) to (4.16), at least if there is to be no serious perturbation of the plasma.

These relationships, then, give the distribution and maximum magnitude of the velocity field available for an E×B divertor.

4.B. Experiment

In order to test some of the ideas of the preceding section, an

experiment was performed in the octupole in which one of the hoops was given an electrostatic potential relative to the wall, creating a radial electric field. This was done in the absence of any divertor, and the resulting floating potential profile across the plasma was measured. In the absence of temperature gradients the floating potential measured by a probe differs from the plasma potential only by an additive constant, and thus can be compared directly to theoretical predictions for the electric field.

4.B.1. Observations

Figure 4.1 shows such floating potential profiles for three different plasmas, all with poloidal field only and 2.5 kV on the capacitor bank, for both polarities of hoop potential. For these profiles the DC potential was applied to the upper outer hoop by means of a wire leading from a hoop support through the vacuum tank wall. The profiles are qualitatively quite similar, and only the case of the ECRH plasma was studied in detail.

In order to remove extraneous effect, two things were done for the measurements to be discussed below. First, instead of a truly DC potential, the hoop bias was switched on with an SCR-controlled relay circuit following the ECRH microwave pulse, precluding any effect of the electric field on the formation of the plasma. When this is done, the current drawn to the hoop starts out large and decays to its steady-state value in a time on the order of 10 μsec (see Figure 4.2). Since

the dielectric response of the plasma occurs on the time scale of the ion cyclotron period ($\lesssim$ 1 μsec), this must represent the relaxation time ε/σ discussed in section A; its relation to the ion collision time will be discussed later. However, small adjustments of the floating potential profile are seen to continue for a millisecond or more, so data to be shown below are typically for 5 msec after the potential was switched on, to allow transient effects to die out.

Second, data were taken with the hoops levitated, the bias then being applied by means of a springy, insulated wire inserted through a probe port to touch the hoops. When the hoops are supported, charge can easily flow along magnetic field lines to the conducting supports and short out, or at least alter, the electric field. This is particularly important for the biased hoop, where the supports, which are insulated from the wall but in electrical contact with the hoop, can draw a net current from the plasma. This is illustrated in Figure 4.3, which shows oscilloscope traces of floating potential at the separatrix with the hoops levitated one at a time. The most significant difference is seen when the biased hoop is levitated. Not surprisingly, for both polarities the presence of biased supports extending through the plasma brings the center of the plasma closer to the bias potential.

Figure 4.4 shows the separatrix floating potential, and Figure 4.5 the current drawn by the biased hoop, as a function of hoop potential, for the cases of hoops supported and of three hoops levitated (the lower inner hoop could not be levitated at the time). Evidently, in the levitated case the plasma potential tends to stay near that of the

more positive of the two boundaries. When the hoop is positive the plasma is already near the bias potential, but when the hoop is negative, inserting the supports brings the plasma closer to the bias potential, drawing a large current in the process. It was predicted in Eqs. (4.14) and (4.15) that as the electric field is increased, at some point the perpendicular current will saturate, and this is seen to occur at about ± 10 V on the hoop. The apparent symmetry of the current characteristic in the levitated case may be accidental, since the sheath forms at the hoop for one polarity and at the wall for the other, and the two need not be the same.

For reference, Figures 4.6 and 4.7 show ion saturation current and floating potential profiles for the case where all hoops are electrically floating, and three hoops are levitated. The flat spot in the V_f profile near ψ_{crit} is due to the presence of the divertor hoops which, while carrying no current and electrically floating for this experiment, hold the plasma potential of field lines intersecting them at a constant value. (These small hoops had not yet been installed at the time of the data shown in Figure 4.1.) It is interesting to note that the profiles of Figures 4.6 and 4.7 obey the expected ambipolar diffusion relation[4,5] $\ell n\ I_{oi} \propto V_f$, as shown in Figure 4.8. The semilog plot is linear over the ranges from the octupole hoop to ψ_{sep}, and ψ_{sep} to the divertor hoops, with a change in slope indicating a possible change in diffusion coefficient across the separatrix. The negative slope near the octupole hoop and the vertical slope at the divertor hoops occur where field lines intersect conducting obstacles,

in which case the diffusion no longer need be ambipolar.[16] This profile is very similar to observations which have been made in the small gun plasma.[5]

Floating potential profiles were measured for a range of hoop potentials of both polarities (three hoops levitated), and these are plotted in Figure 4.9. As stated in the first section, there are three possible contributions to the net electric field: the naturally occurring ambipolar field, the field which drives a current across the magnetic field lines, and a possible contribution from a sheath near one of the boundaries. First, the ambipolar potential was removed by subtracting the profile of Figure 4.7, which represents the ambipolar potential alone, from all those of Figure 4.9. This assumes that the diffusive transport and density profile are not altered by the electric field, as is implicit in the model of Eq. (4.8), and explicit in Eq. (4.13). It has been observed with a floating double probe that ion saturation current profiles are not noticeably affected by the applied potential except at the edges, which will be omitted from later calculations for other reasons, so this seems to be a good assumption. Furthermore, it is interesting to note that this subtraction cancels any contribution to the floating potential which may be due to temperature gradients in the plasma, as long as the temperature gradient does not change with application of the hoop bias. To facilitate comparison, a constant was also subtracted from each profile to make the value at the separatrix equal to zero, which does not alter the electric field. What remains is due to the "conduction" electric field of Eq. (4.27)

(plus a possible sheath). To illustrate this, each profile was then divided by the current drawn to the hoop at that bias, leaving a profile which, outside the sheath, should be dependent only on intrinsic properties of the plasma and independent of the bias potential.

The end results are shown in Figures 4.10 and 4.11. Within each polarity, the profiles are indeed nearly independent of bias voltage. As predicted from the current characteristic of Figure 4.5, for biases of absolute value larger than 10 V any additional potential drop appears in a narrow layer near one boundary, extending about 2.5 cm from the wall when the hoop is positive and about .5 cm from the hoop when the hoop is negative. This may not be a true sheath, however; as seen in Figure 4.8, these are regions in which ambipolar diffusion does not hold, because these field lines intersect conducting obstacles. Electrons can then flow freely along field lines to the obstacles, allowing the field lines to take on whatever potential is necessary to preserve the limiting potential drop across the rest of the plasma, without violating quasineutrality.

4.B.2. Comparison to models

It is natural to inquire as to the mechanism responsible for the perpendicular conductivity. The electric field associated with the radial current has been isolated above; various functional forms for the conductivity can now be tested against the measured profiles, in the same spirit as the diffusion coefficient studies which have been

done on the octupole.[17-19] In addition to the conductivity due to neutral collisions discussed in section A, the Einstein relation ($D = \mu kT/e$) suggests candidates for the form of the mobility from the various diffusion coefficients of interest. On this hypothesis, consider diffusion and mobility coefficients proportional to n^{α}/B^{β}, where some possibilities are:

(a) $\alpha = 1, \quad \beta = 2$ Fully-ionized classical

(b) $\alpha = 0, \quad \beta = 2$ Ion-neutral classical

(c) $\alpha = 0, \quad \beta = 1$ Bohm

(d) $\alpha = -\frac{1}{2}, \quad \beta = 0$ Okuda-Dawson

(e) $\alpha = 1, \quad \beta = 0$ Kamimura-Dawson

Rather than differentiate the data, exaggerating its noise content, Eq. (4.27) is integrated, giving

$$\phi(x) = A_1 \int^{x} \frac{d\psi/dx}{n^{1+\alpha} \oint R^2 B^{1-\beta} d\ell} \, dx + A_2 \tag{4.33}$$

where A_1 and A_2 are constants. A_1 incorporates the constant factors in the mobility expression and a proportionality factor for the size of the applied potential difference, and A_2 is a constant of integration. First, the integral is calculated for the various cases, obtaining n from Figure 4.6 and using tabulated values of the field line integrals.[20] The results are plotted in Figure 4.12 with A_1 and A_2 arbitrarily selected to give all the curves the same values at the hoop and the separatrix. The shapes are distinctive, and inspection of Figures 4.10 and 4.11 seems to eliminate cases (d) and (e).

The data for 10 V were chosen as representative. The floating potential profile for -10 V on the hoop was subtracted from that for +10 V, eliminating the contribution from the ambipolar electric field. Dividing the result by 2 then gives an average value of the potential profile associated with the perpendicular current. A least-squares fit was used to determine the best values of A_1 and A_2 for each form of the conductivity. The fit was made from 0 to 9 cm from the hoop, since the 10 V profiles show no sheath but the presence of the divertor hoops makes the theory invalid beyond 9 cm. Case (b), neutral collisions, provides the best fit, with an r.m.s. error of .32 V. The r.m.s. errors of the other four cases are at least twice as large, and are too close to each other to produce a clear candidate for a second choice. The data and fitted curve are plotted in Figure 4.13.

The perpendicular conductivity evidently scales as if due to neutral collisions. However, if Eq. (4.26) is evaluated, using the fitted curve for E, 5×10^{10} cm^{-3} for the plasma density peak, a neutral density of 10^{11} cm^{-3}, a neutral collision cross-section of 5×10^{-15} cm^2, and the very optimistic estimate that $T_i = T_e = 4$ eV, then the predicted value of the current in the plasma is ~ 1 mA. There is at least a factor of 50 discrepancy, and worse if the ions are colder. However, if the inverse of the 10 μsec relaxation time found in Figure 4.2 is used in place of the neutral collision frequency, the predicted value of the current is ~70 mA, which is quite consistent.

4.B.3. Discussion

Although not analyzed in detail, the density profile (Figure 4.6) appears to show the concave slopes characteristic of diffusion coefficients with $\alpha < 0$, rather than the straight slopes of $\alpha = 0$ or convex slopes of $\alpha > 0$.[21,22] This suggests that different mechanisms are responsible for diffusion and mobility. Also, for both polarities of bias, the net electric field is observed in Figure 4.9 to go to zero near the more positive boundary at about the same hoop potentials (±10 V) where the current saturates. Given the mechanism for saturation discussed in section A, this is consistent with the ions having larger mobility than the electrons (as they would for neutral collisions), despite their smaller diffusion coefficient (evidenced by the positive ambipolar potential of the center of the plasma in Figure 4.7). In this case the ion transport is governed almost entirely by the electric field, and the perpendicular current is carried by the ions.

Similar behavior has been observed by Armentrout[23] for the small gun plasma where $T_i > T_e$, in which he finds $D_i < D_e$, but $\mu_i > \mu_e \simeq 0$, despite the Einstein relation. He concludes that the ion mobility is due to collisions with turbulence cells formed by electrons, with sizes of the order of the ion gyroradius. With such a large cross-section, the spatial density of such objects need not be large to provide a greater collision frequency than that due to neutral atoms, and they could play a similar role in the experiment.

The present observations are also consistent with those of Cavallo,[24] given a slightly different interpretation. He used biased,

levitated, hoops as giant Langmuir probes, to compare with measurements of plasma loss made with striped collectors on the hoop, and found that ion saturation current to the hoop was not always consistent with the hoop collector flux measurements. However, if $\mu_i >> \mu_e$ then the application of a large bias prevents ions from reaching the more positive boundary, while not much altering electron transport. In this case, as indicated by Eq. (4.14), the electron saturation current to a positively biased hoop measures plasma loss to the hoop, while ion saturation current to a negatively biased hoop measures plasma loss to the wall. Cavallo measured decreased electron saturation current and increased ion saturation current when the toroidal magnetic field was added, which now appears consistent with his collector observations that toroidal field inhibits transport to the hoop and enhances transport to the wall.

A direct measurement of $\sigma_\perp$ has also been made on the FM-1 spherator, in a plasma with parameters quite similar to those of the present experiment.[25] The perpendicular conductivity was found to have not only the proper scaling for classical ion-neutral collisions, but also the proper numerical coefficient. However, there were no anomalous diffusion effects such as the turbulence cells seen in the octupole, as shown by the fact that FM-1's plasma confinement time approached that due to classical charged-particle collisions.

In conclusion, the spatial distribution of electric field in this experiment is most consistent with a perpendicular conductivity that scales as if due to neutral particle collisions. However, the numerical coefficient is at least a factor of 50 too large, indicating that

some other mechanism with similar scaling may be responsible, one possibility being collisions with turbulence cells. The density profile shape seems to indicate a different scaling for the diffusion coefficient than for the mobility coefficient, suggesting that different mechanisms may dominate the two processes. As predicted in section A, some electric field does penetrate into the plasma, on the scale length of the density profile ($\gtrsim$ 1 cm), rather than on a scale of the Debye length ($\lesssim$ .1 cm). This greater penetration would be desirable for an E×B divertor.

REFERENCES - CHAPTER 4

1. F.F. Chen in Plasma Diagnostic Techniques, R.H. Huddelstone, S.L. Leonard, eds., (Academic Press, N.Y., 1965), p. 159.

2. N.A. Krall, A.W. Trivelpiece, Principles of Plasma Physics, (McGraw-Hill, N.Y., 1973), p. 629.

3. Ibid., p. 330.

4. D.J. Rose, M. Clark, Jr., Plasmas and Controlled Fusion, (MIT Press, Cambridge, 1965), p. 77.

5. C.J. Armentrout, Ph.D. Thesis, University of Wisconsin (1977), p. 129.

6. P.B. Corkum, Phys. Fluids 16, 1542 (1973).

7. L. Spitzer, Physics of Fully Ionized Gases (Wiley Interscience, N.Y., 1962), p. 38.

8. D. Montgomery and F. Tappert, Phys. Fluids 15, 683 (1972).

9. J.B. Taylor and B. McNamara, Phys. Fluids 14, 1492 (1971).

10. A.H. Boozer, Phys. Fluids 19, 149 (1976).

11. A.H. Boozer, PPPL-EPRI-2 (1976).

12. T.H. Stix, Phys. Fluids 16, 1260 (1973).

13. S.P. Hirshman, Nuclear Fusion 18, 917 (1978).

14. S.I. Braginskii in Reviews of Plasma Physics, M.A. Leontovich, ed., (Consultants Bureau, N.Y., 1965), vol. I, p. 205.

15. M.N. Rosenbluth, et.al. in Plasma Physics and Controlled Nuclear Fusion (Proc. 4th Conf., Madison, 1971), (IAEA, Vienna, 1971), vol. I, p. 495.

16. A. Simon, Phys. Rev. 98, 317 (1955).

17. J.R. Drake, J.G. Berryman, Phys. Fluids 20, 851 (1977).

18. J.R. Drake, J.R. Greenwood, G.A. Navratil, R.S. Post, Phys. Fluids 20, 148 (1977).

19. G.A. Navratil, R.S. Post, A. Butcher Ehrhardt, Phys. Fluids 20, 156 (1977).

20. A. Butcher Ehrhardt, University of Wisconsin PLP 703 (1976).

21. J.R. Drake, Phys. Fluids 16, 1554 (1973).

22. J.R. Greenwood, Ph.D. Thesis, University of Wisconsin (1975), p. 28.

23. C.J. Armentrout, Ph.D. Thesis, p. 263.

24. A.J. Cavallo, Phys. Fluids 19, 394 (1976).

25. M. Okabayaski, S. Yoshikawa, Phys. Rev. Lett. 29, 1725 (1972).

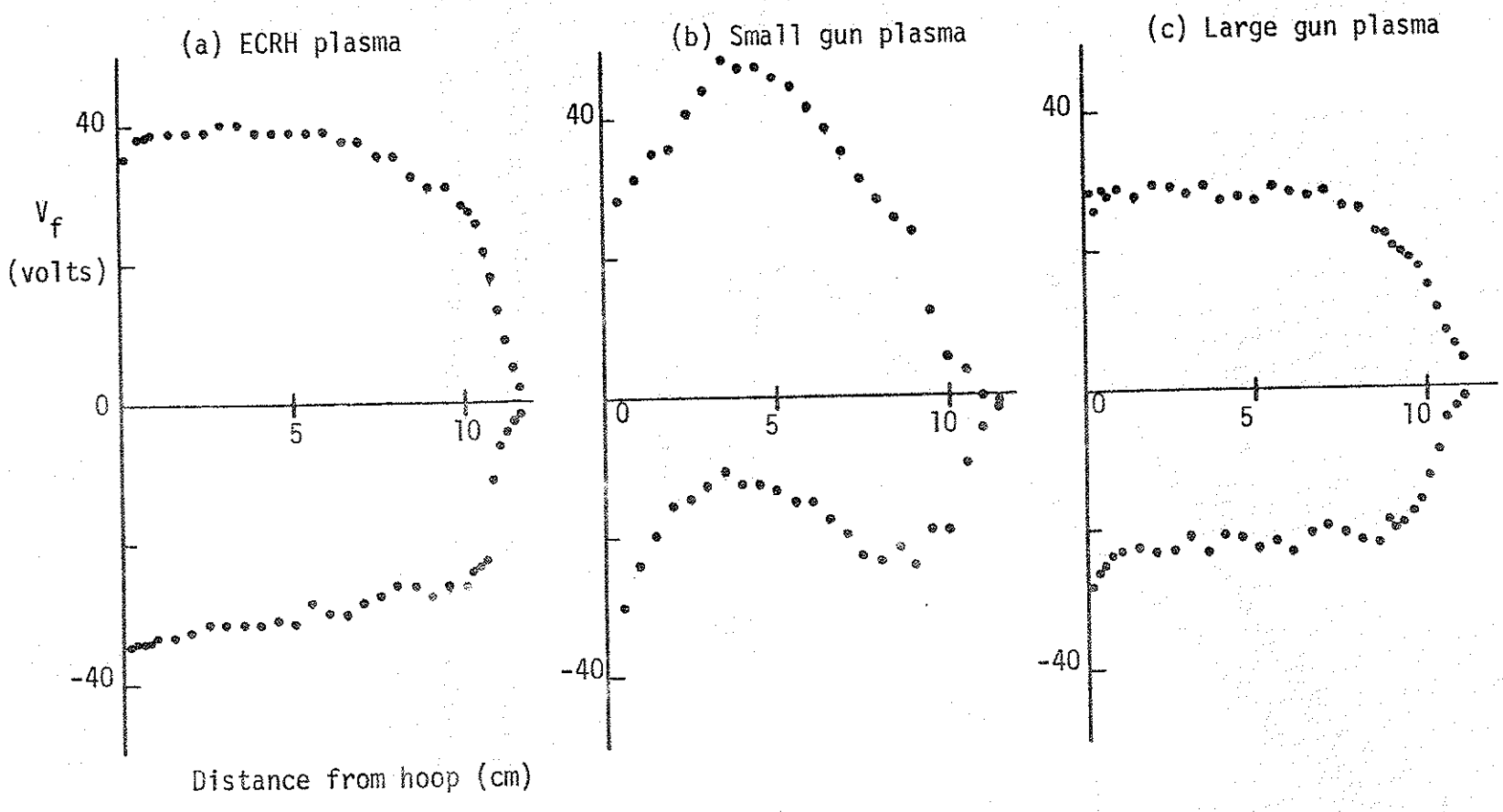

Fig. 4.1 - V_f profiles at upper outer hoop; upper outer hoop biased ±40 V with respect to tank wall. (a) ECRH plasma, (b) Small gun plasma, (c) Large gun plasma. All hoops supported.

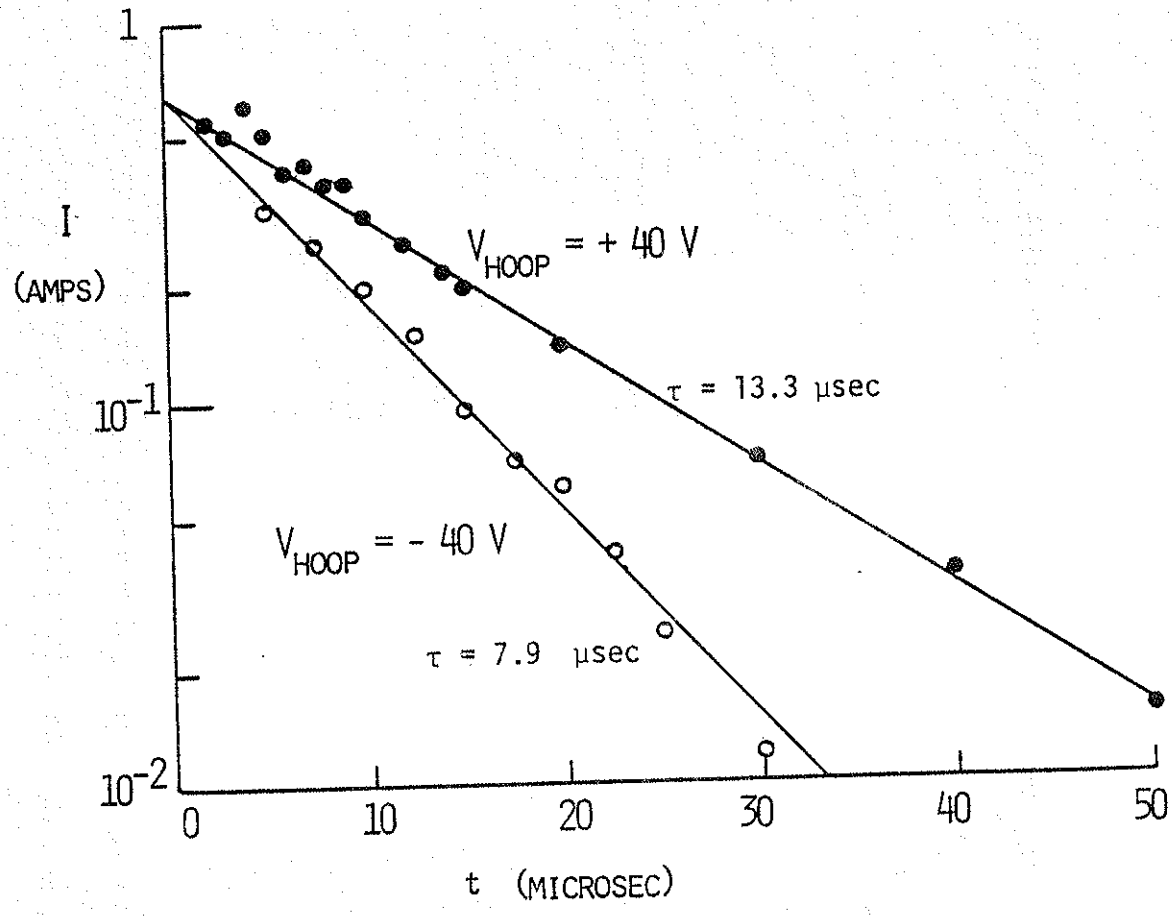

Fig. 4.2 - Relaxation of current drawn to biased hoop following switching on of bias. Plotted quantity is I_{hoop} - .20 A. (Hoops levitated).

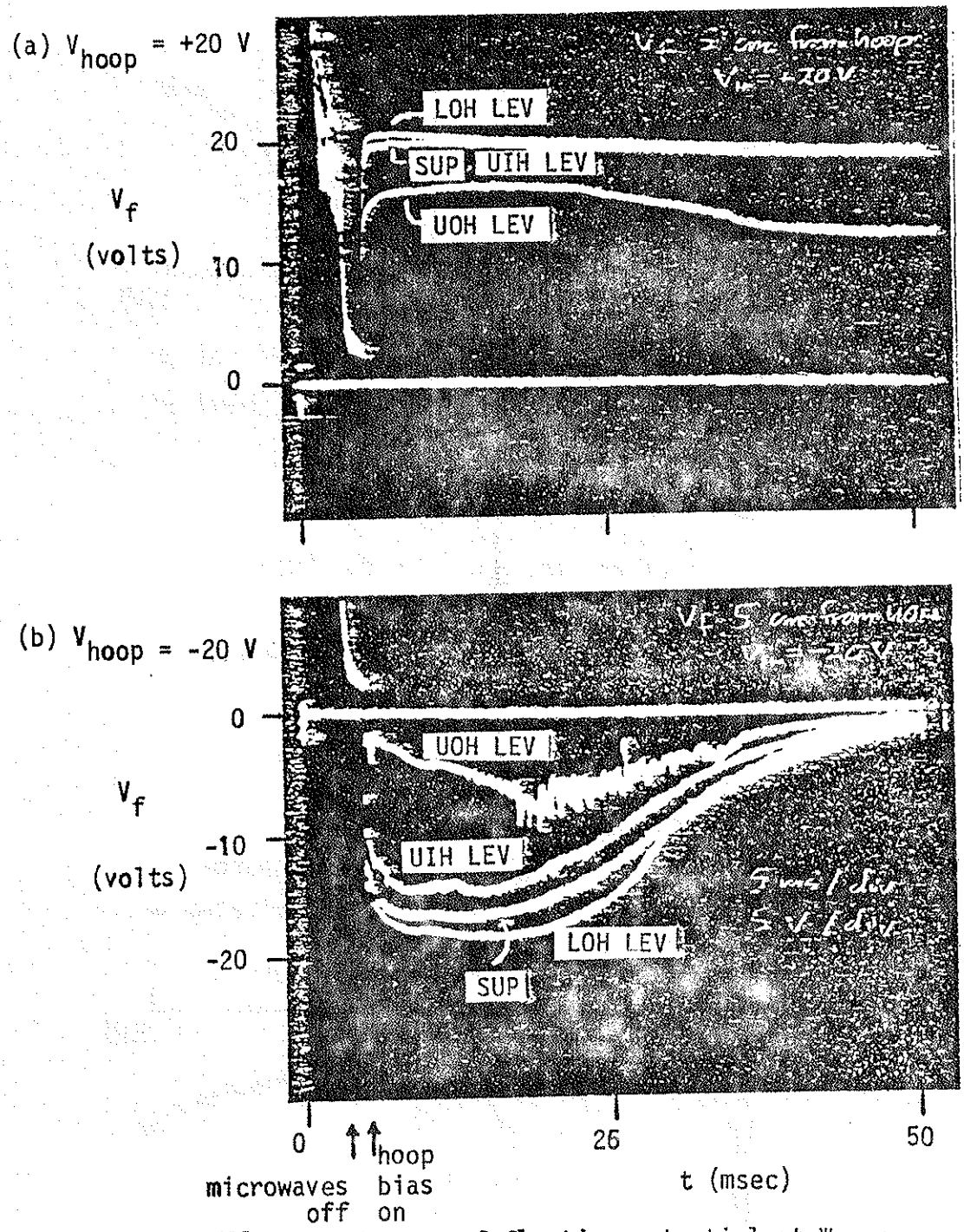

Fig. 4.3 - Oscilloscope traces of floating potential at Ψ_{sep}: upper outer hoop (UOH), lower outer hoop (LOH), and upper inner hoop (UIH) individually levitated (LEV), and all hoops supported (SUP).
UOH is biased relative to tank wall (a) + 20 V, (b) - 20 V.

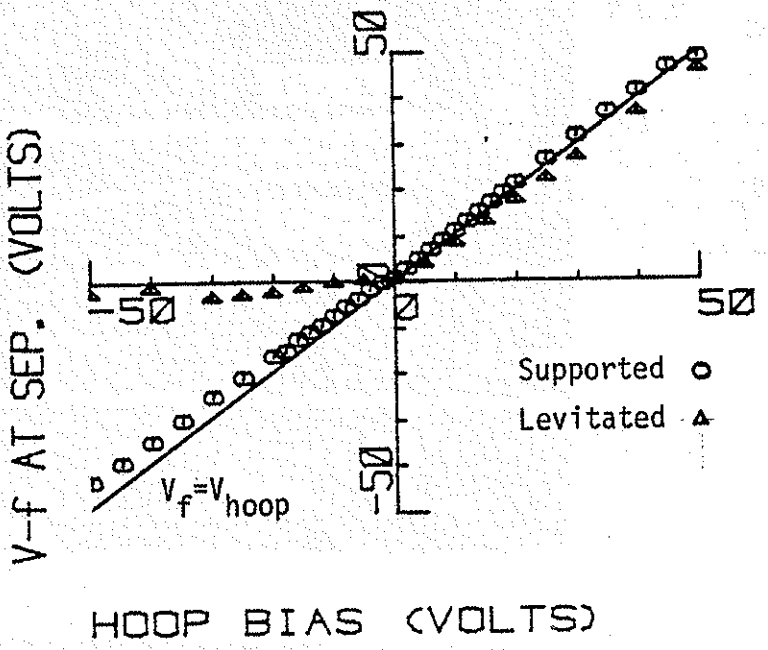

Fig. 4.4 - V_f at separatrix vs. hoop bias potential.

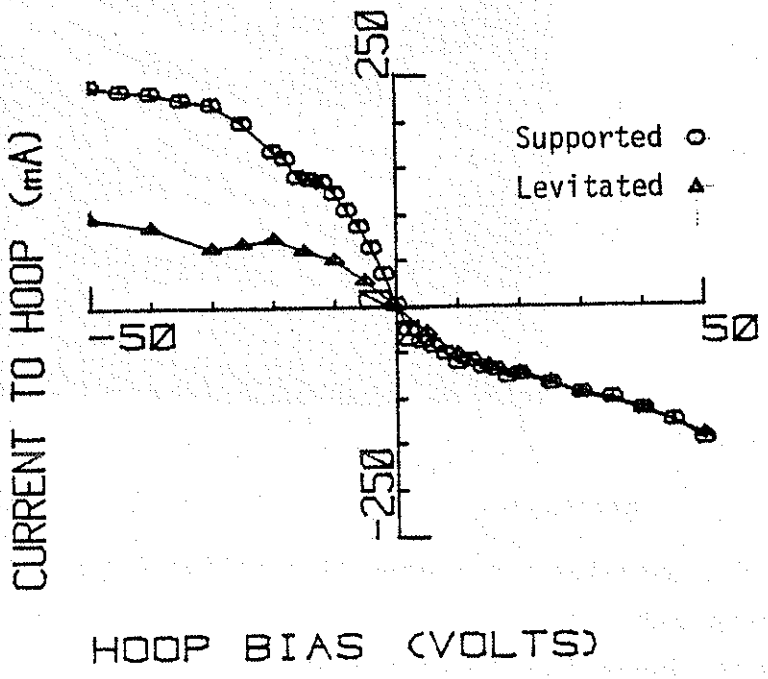

Fig. 4.5 - Current drawn to hoop vs. hoop bias potential

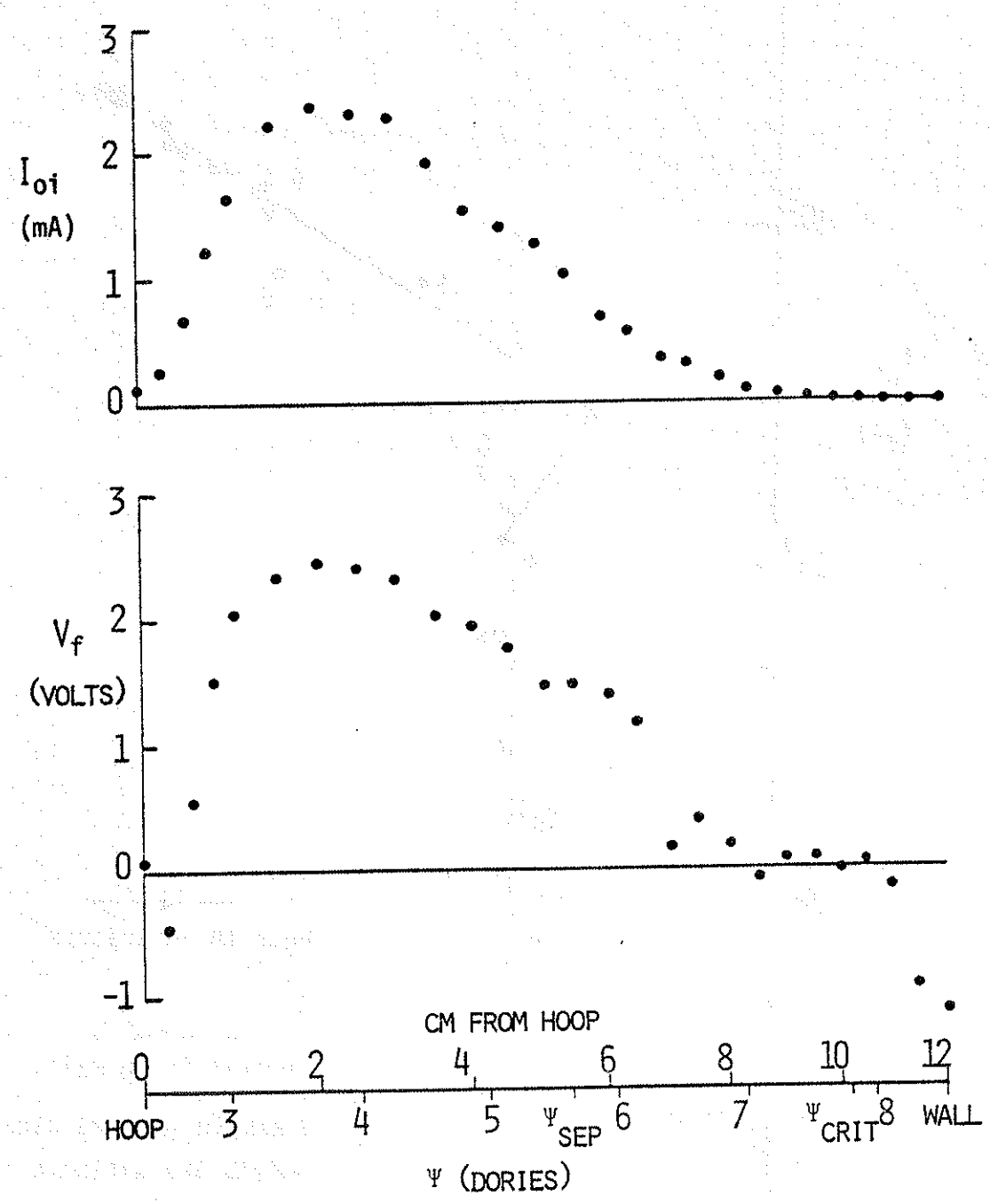

Fig. 4.6 - Ion saturation current profile.
Fig. 4.7 - Floating potential profile.
} upper outer hoop

Hoops levitated, electrically floating.

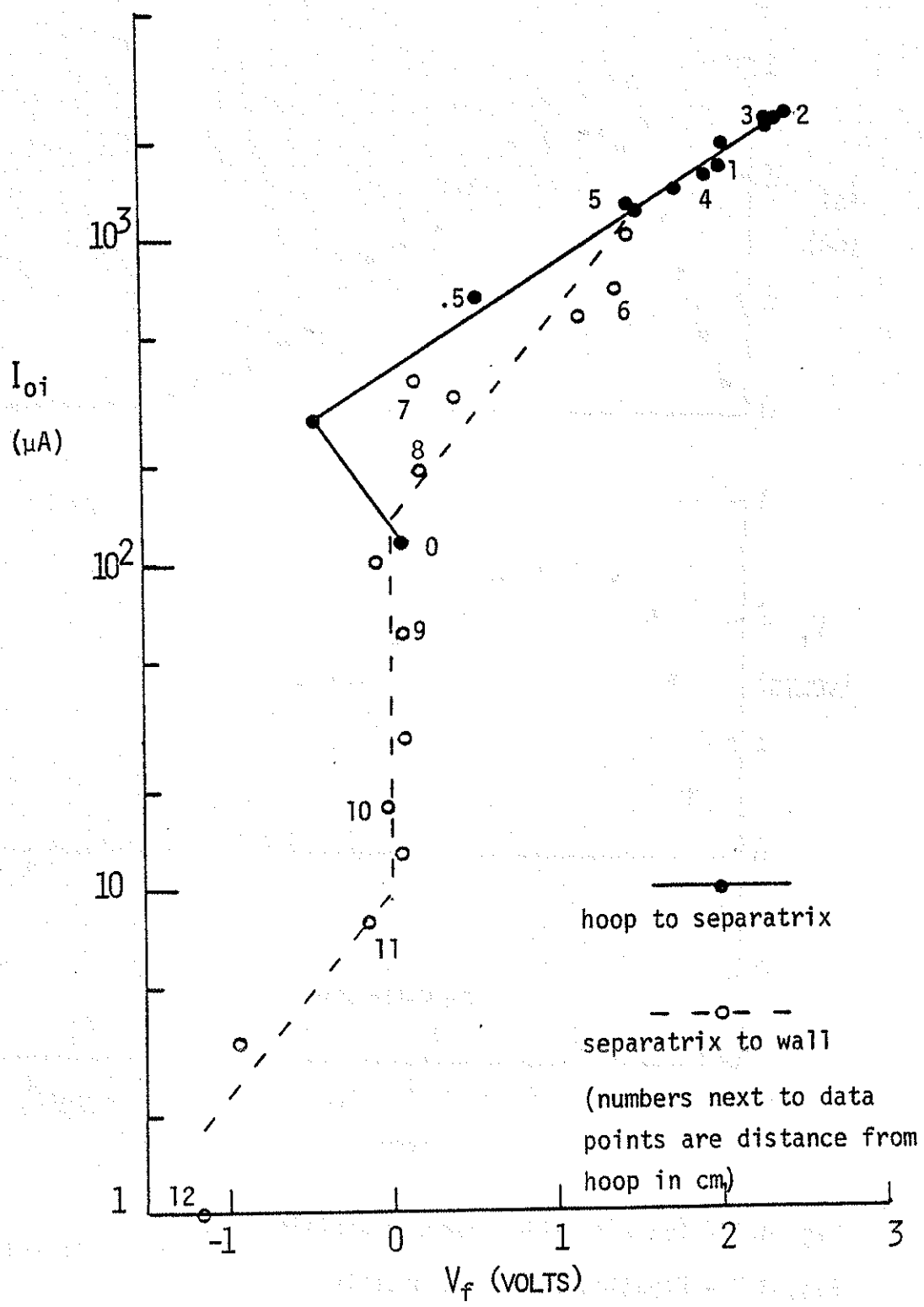

Fig. 4.8 - Parameterized plot of I_{oi} vs. V_f.

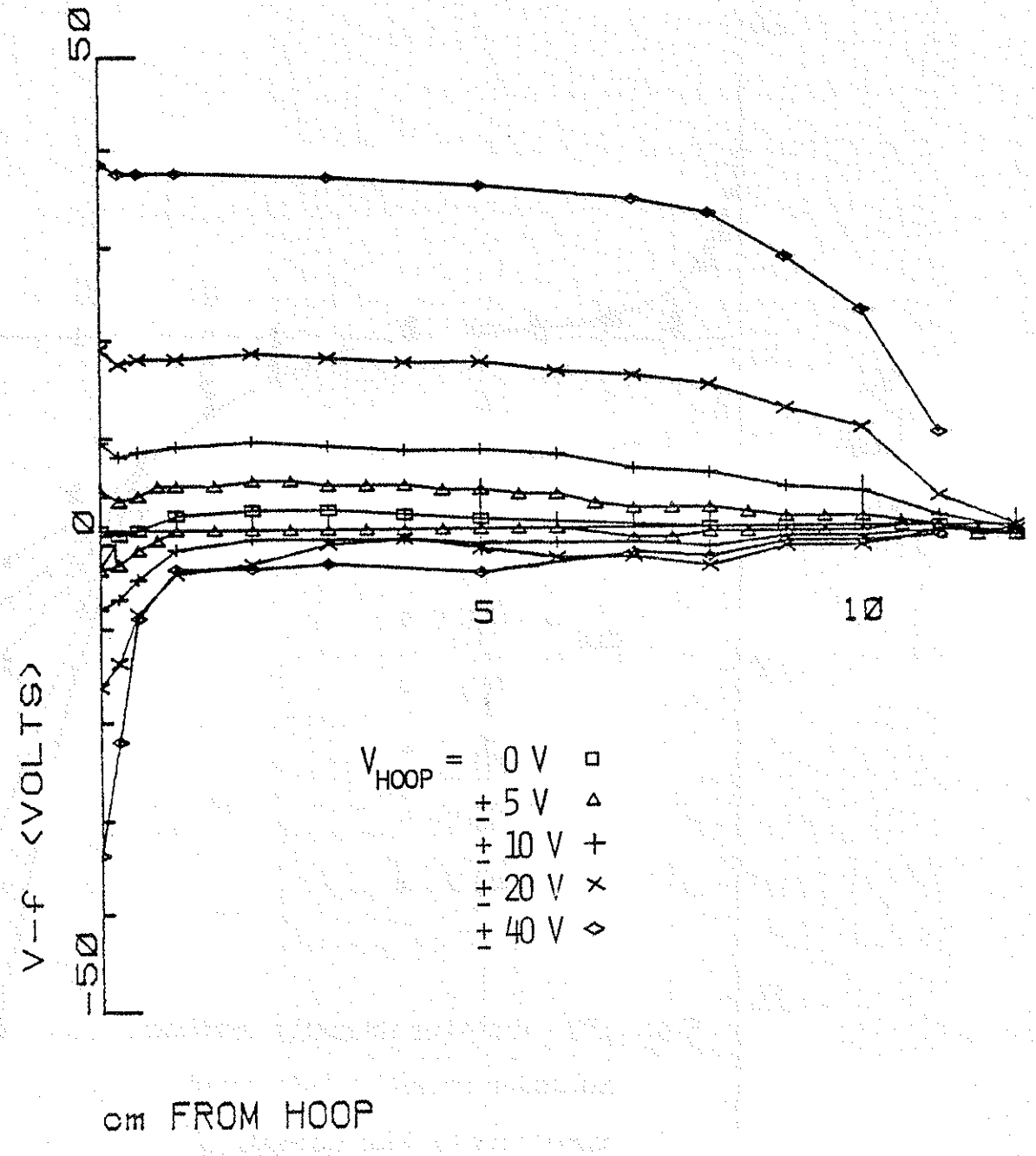

Fig. 4.9 - Floating potential profiles for various values of hoop bias.

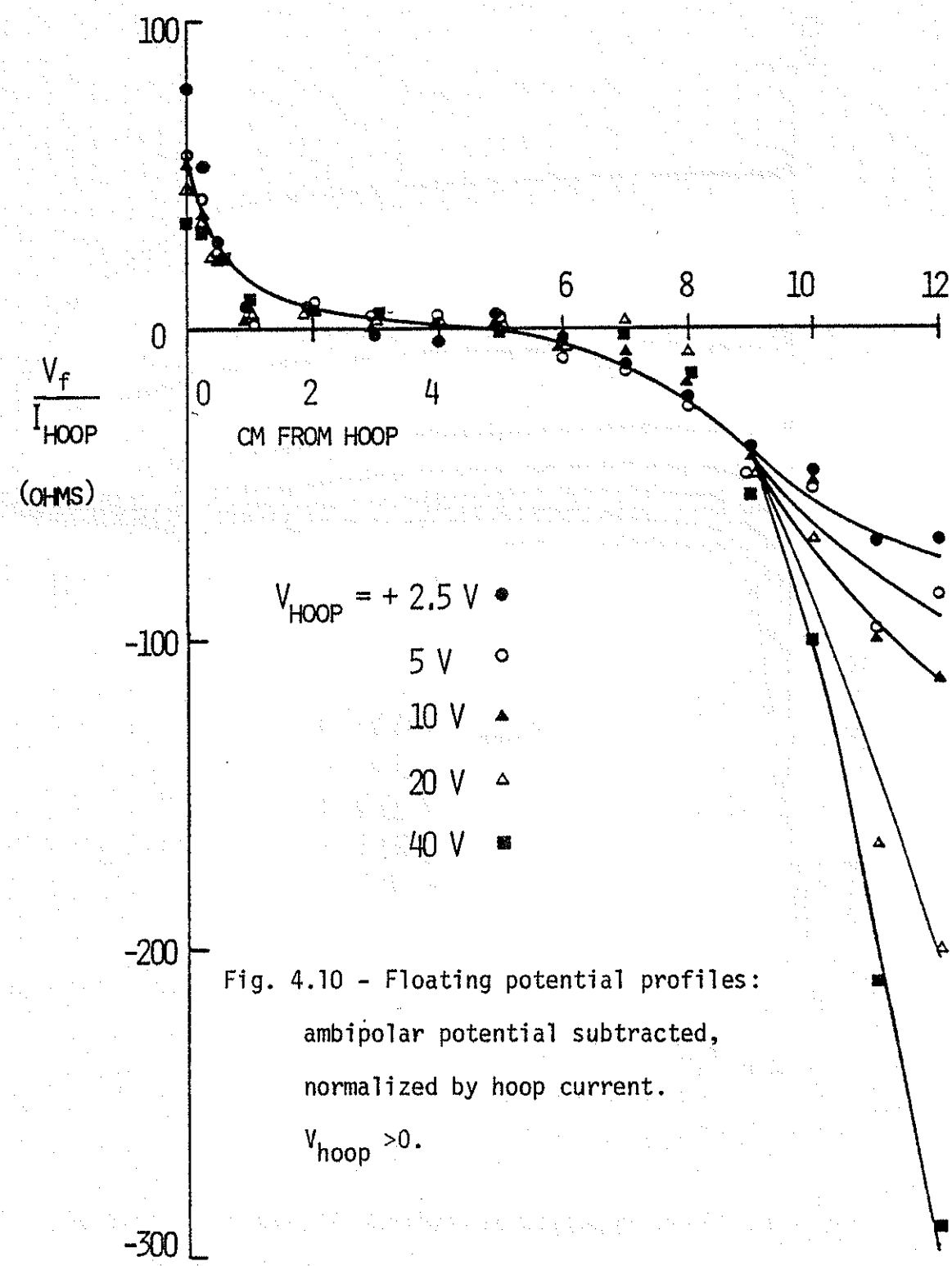

Fig. 4.10 - Floating potential profiles: ambipolar potential subtracted, normalized by hoop current. $V_{hoop} > 0$.

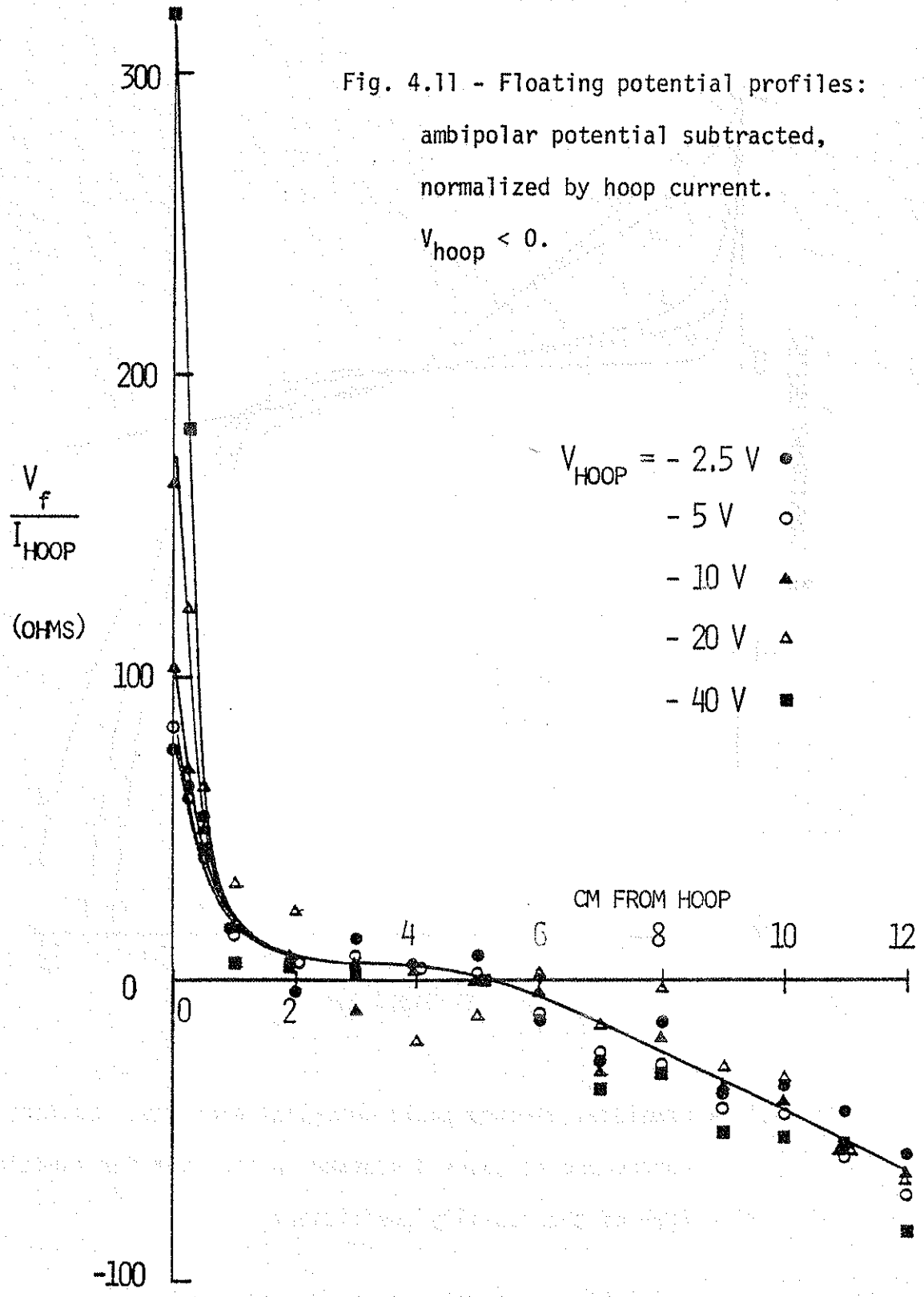

Fig. 4.11 - Floating potential profiles: ambipolar potential subtracted, normalized by hoop current. $V_{hoop} < 0$.

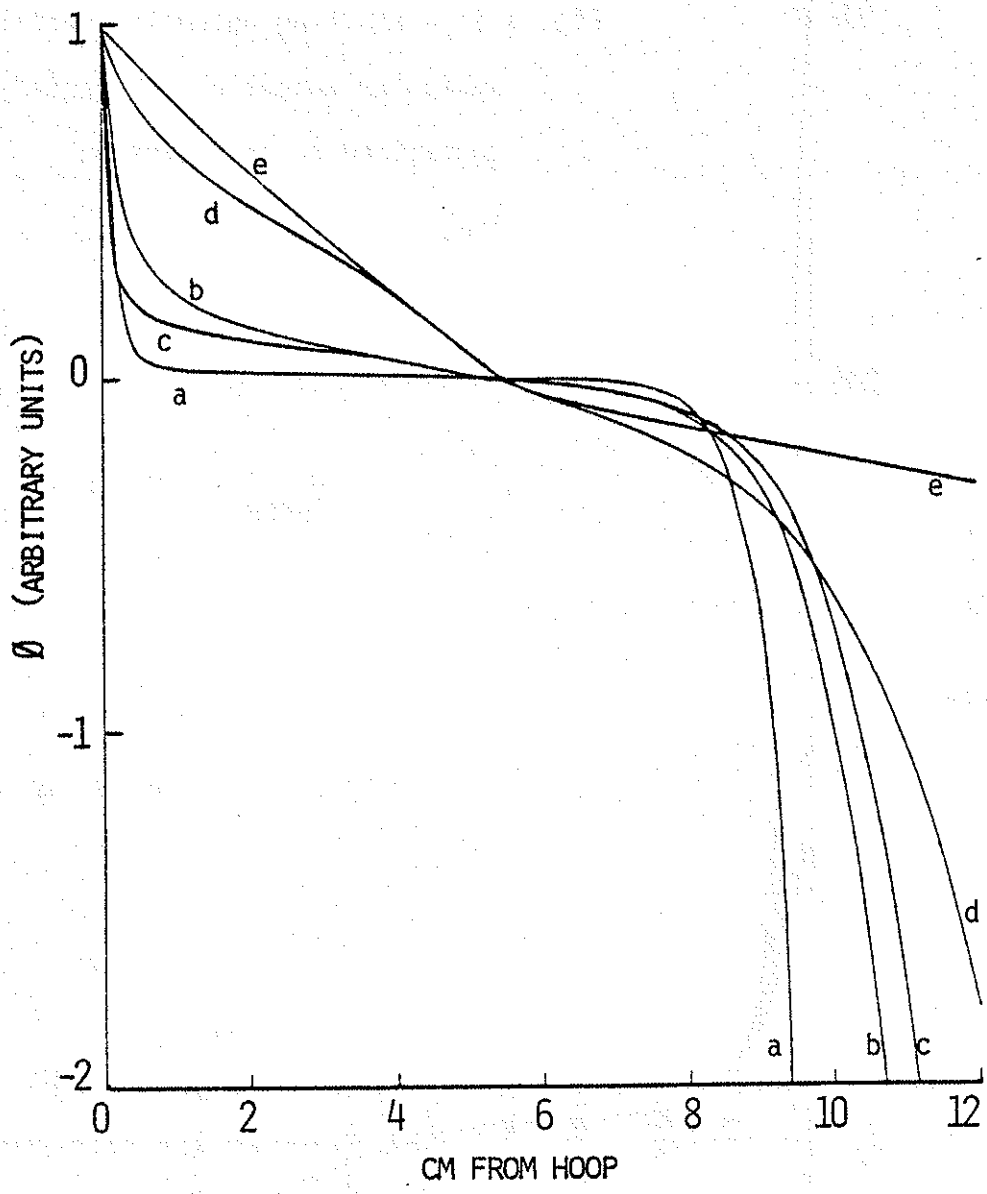

Fig. 4.12 - Predicted electrostatic potential profiles. Letters correspond to cases discussed in the text for functional form of the mobility coefficient.

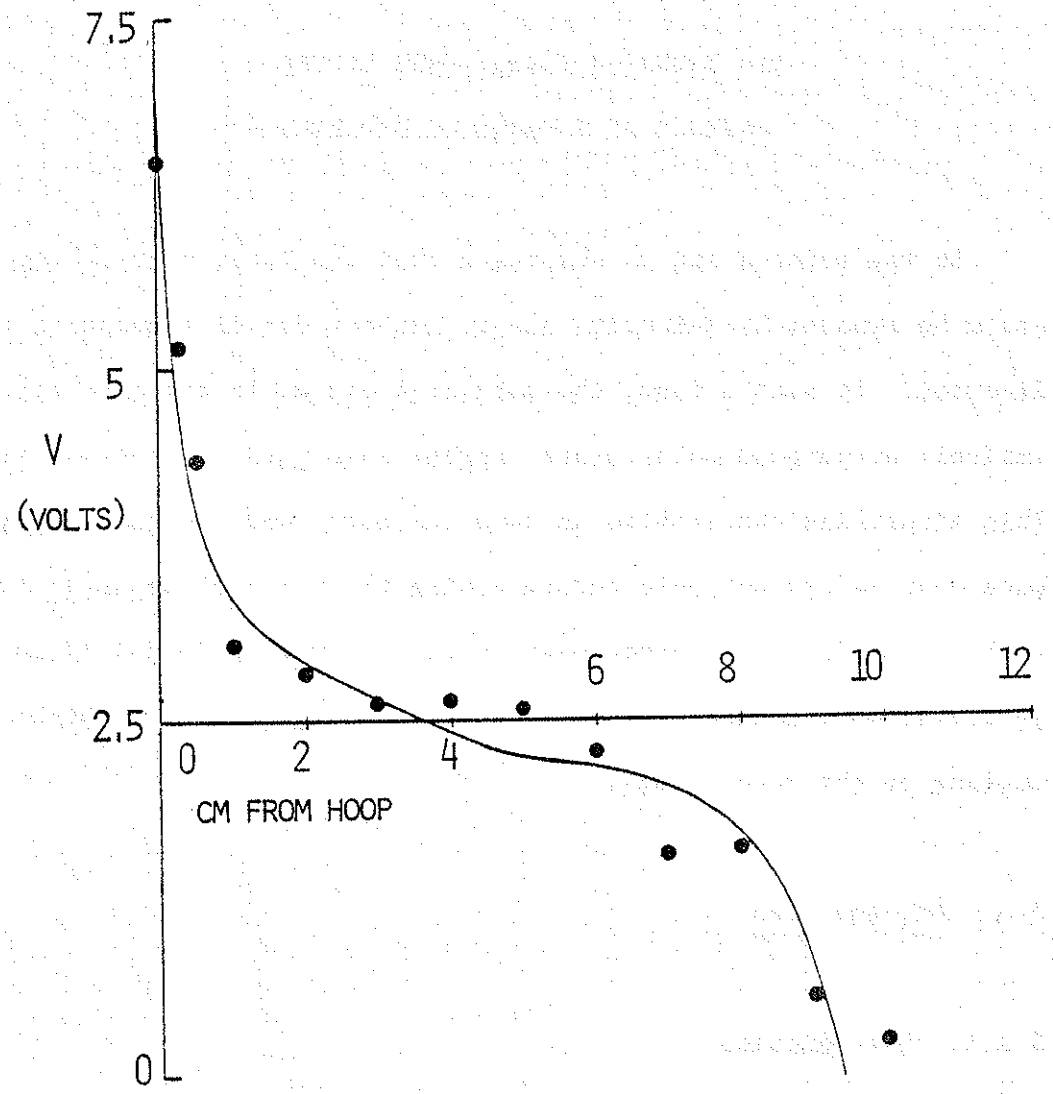

Fig. 4.13 - Electrostatic potential profiles. Experimental points are the combination of ± 10 V bias floating potential profiles (see text). Fitted theoretical curve is for case (b), ion-neutral collisions.

CHAPTER 5

E×B DIVERTOR EXPERIMENTS IN THE ABSENCE OF A MAGNETIC DIVERTOR

It was pointed out in Chapter 2 that the outer edge of the plasma could be removed by E×B drift alone, without use of a magnetic field divertor. In such a case, the motion of plasma to the divertor is entirely by perpendicular drift, rather than parallel thermal flow. This simplifies the problem in some respects, and two such experiments were done on the octupole before adding the poloidal magnetic divertor. Both of the following experiments were done with poloidal field only, at 2.5 kV on the capacitor bank, corresponding to about 2 kG at the surface of the outer rings.

5.A. Poloidal Gap

5.A.1. Introduction

An idea long familiar to experimenters using pulsed machines with conducting walls is that magnetic field lines can be thought of as entering the machine through the insulated gap in the wall on the rising half of the pulse, and departing the same way on the falling half. Plasma tends to be "frozen" to field lines, and thus as the field falls it is carried along and deposited at the wall near the gap.

Another way of saying the same thing is that the electric field associated with the time-changing magnetic field creates an E×B drift which takes plasma to the gap, and would, if possible, take it out of the machine through the gap as in a divertor. This provided the original motivation for the E×B divertor concept.[1]

The question of such inductive electric fields in the presence of a plasma was studied by Evans.[2] He has shown that, in spite of the assumption that $\vec{B}$ and consequently the magnetic vector potential $\vec{A}$ are axisymmetric, there is a non-axisymmetric scalar potential $\emptyset$, which is required to keep the tangential component of $\vec{E} = -\nabla\emptyset - \dot{\vec{A}}$ equal to zero at the conducting wall. The net electric field is such as to bring magnetic field lines into the machine through the gap and spread them out around the toroid. Treated as a dielectric surrounding the hoop, but not extending all the way to the wall, the plasma tends to shield out the $\nabla\emptyset$ part of the electric field, but not the axisymmetric $\dot{\vec{A}}$ contribution. Consequently, in the presence of plasma, field lines enter through the gap, are distributed azimuthally in the vacuum region between the plasma and the wall, and then move radially into the plasma. The process is reversed on the falling half of the pulse, so that most of the azimuthal motion toward the gap occurs in the low-density plasma near the wall, as desired for a divertor.

Other experimenters have noted these electric fields near the gap[3] and their effects on plasma flux to the wall,[4] but it was decided to repeat the observation with an emphasis on the divertor aspect.

5.A.2 Probe Cart and $\dot{\vec{A}}$ corrections

Measurements were taken using a movable cart on the floor of the octupole, constructed by Drake and described in detail by A. Butcher Ehrhardt.[5] Its location is shown in Figure 5.1, along with items associated with the second experiment which should be ignored for the present. The cart carried a probe with several tips, which could be pivoted in the poloidal plane, so that every ψ surface could be reached by at least one probe tip, and also carried a striped collector on its body. The cart could be moved azimuthally through almost the full 360° of the toroid, permitting azimuthal scans of plasma flux to the wall, and probe measurements covering the entire (ψ, θ) space. Density and potential have been shown to be constant along field lines,[6,5] so a complete map of the plasma is obtainable by this means.

A major use of the cart, in this experiment as well as others, has been to measure the electric potential structure, which determines the E×B drift in the plasma. If $\vec{E}$ can be expressed as $-\nabla\emptyset$, since $\vec{E}\times\vec{B}$ is always normal to $\nabla\emptyset$ then E×B drift surfaces must be the same as surfaces of constant $\emptyset$. In fact, it can be shown that

$$\frac{\vec{E}\times\vec{B}}{B^2} = 2\pi\left[\frac{\partial\phi}{\partial\psi}\frac{\hat{\theta}}{|\nabla\theta|} - \frac{\partial\phi}{\partial\theta}\frac{\hat{\psi}}{|\nabla\psi|}\right] \qquad (5.1)$$

so in (ψ, θ) space $2\pi\emptyset$ is a stream function for the E×B drift. In the absence of temperature gradients, when the floating potential differs from the plasma potential only by an additive constant, these statements also apply to the floating potential as measured by the cart

probe.

A certain amount of confusion has at times surrounded the question of $\vec{A}$ corrections to cart probe potential measurements; it is to be hoped that the following comments will not increase it. Evans[7] has shown that a voltmeter connected between a point P (e.g., a probe tip) and a point 0 (e.g., the grounding point at the tank wall for the measuring circuit) should measure a voltage given by

$$V = \phi_P - \phi_0 + \int_C \vec{A} \cdot \vec{d\ell} \tag{5.2}$$

where C is a path of integration from P to 0 through the measuring circuit (see Figure 5.2). (The presence of the probe locally alters the potential from the plasma potential to the floating potential; ϕ_P then denotes the floating potential.) If the circuit is grounded to the tank at a fixed point while the cart and probe are moved, then in order to obtain a measurement of the electrostatic potential ϕ_P the integral along C of $\vec{A}$ must be subtracted from V:

$$\phi_P - \phi_0 = V - \int_C \vec{A} \cdot \vec{d\ell} \tag{5.3}$$

The contribution to the integral due to wires running from the cart to the probe tip is zero, since $\vec{A}$ has only a toroidal component (and would otherwise be just an additive constant, assuming axisymmetry of $\vec{B}$). Since the wires to the cart run azimuthally along the lid, where $\vec{A}$ is well known from flux plot calculations and measurements, and depends

only on time, the integral is easily calculated.[8]

A different method which has also been used is to ground the measuring circuit at the location of the cart (point P') rather than at a fixed point.[9] Eq. (5.2) still applies, with P' substituted for O, and now the integral vanishes. To be meaningful, however, the measurements must be referred to the potential at a fixed point O:

$$\phi_P - \phi_O = V + (\phi_{P'} - \phi_O) \tag{5.4}$$

If this correction $(\phi_{P'} - \phi_O)$ is calculated by assuming $\nabla\phi$ at the tank wall is azimuthally symmetric except in the gap, as required to keep $\vec{E} = 0$ in the wall if $\vec{A}$ is azimuthally symmetric,[2] then Eq. (5.4) is equivalent to Eq. (5.3), as expected. $(\phi_{P'} - \phi_O)$ takes a jump across the gap, compensating for the disappearance of the jump in V due to moving the ground across the gap.

What results from both of these methods is a measurement of the electrostatic potential ϕ_P. The non-conservative part of V has been removed, allowing countours of ϕ measured around the full 360° of the toroid to close on themselves. What remains includes plasma effects and also a non-axisymmetric contribution due to the changing magnetic field, so this effect has not been entirely eliminated from the data.

On the other hand, the $\vec{E}\times\vec{B}/B^2$ drift of the plasma depends on the total $\vec{E}$, rather than $\nabla\phi$. If it is desired to show the total plasma E×B motion, a corrected form U (not necessarily conservative) is needed such that $\nabla U = -\vec{E} = \nabla\phi + \dot{\vec{A}}$. Due to $\vec{A}$ only having a toroidal component, it is easy to show that

$$U_P = \phi_P - \phi_O + \int_{C'} \dot{\vec{A}} \cdot \vec{d\ell}$$

$$= V_P - \int_C \dot{\vec{A}} \cdot \vec{d\ell} + \int_{C'} \dot{\vec{A}} \cdot \vec{d\ell} \qquad (5.5)$$

for the fixed ground case, where C' is a contour which goes from point O first in a poloidal plane to the ψ position of P, then azimuthally to P (see Figure 5.2). Using $A_\theta = \psi/2\pi R$,

$$U_P = V_P + (\dot{\psi}_P - \dot{\psi}_W) \frac{\Delta\theta}{2\pi} \qquad (5.6)$$

where $\Delta\theta$ is the azimuthal angle between O and P, ψ_P is the ψ value at point P, and ψ_W is the ψ value at the wall where the wires run, with ψ in Webers, and $\psi = 0$ at a perfectly conducting hoop where $\vec{A}$ must vanish.

It should be emphasized that the approximation that $\vec{A}$ is axisymmetric is a good one. Care was taken to minimize magnetic field errors in the construction of the machine, and the field errors associated with the poloidal gap have been measured as less than 1%.[10] This approximation is sometimes confused with the highly non-axisymmetric electric field at the gap, but there is no contradiction. An analogy is the case of a gas being slowly bled into a container: although the flow velocity ($\vec{E}\times\vec{B}/B^2$ of field lines) is highly non-uniform, the mass density (field line density $\vec{B}$) remains uniform to a good approximation as long as the speed at the inlet is much less than the sound speed (speed of light, or Alfvén speed if a plasma is present).

5.A.3. Observations

Measurements were made using the poloidal field with a sinusoidal waveform rather than crowbarred, in order to obtain large electric fields at the gap. The ECRH microwave pulse was turned off at 18 msec after the start of the magnetic field pulse, shortly before peak field.

Figure 5.3 shows contours of constant floating potential, with the correction of Eq. (5.6) applied, vs. ψ and θ in the vicinity of the gap, and plasma flux to the wall for the same range of θ. At 20 msec (just before peak field) the dominant feature of the potential contours is an island of -30 V near the gap, which is not well understood. This is only 2 msec after the ECRH heating pulse, so it could be caused by hot electrons leaving the confinement region along field lines, due to the field error associated with the gap; however, no negative island is seen at other possible field errors such as the 6" bung located at -30°. It may also be due to hot electrons hitting the Teflon insulator projecting from the gap and charging it negative. The plasma flux to the wall, also shown in Figure 5.3, is lower at the gap than elsewhere, since field lines are still entering through the gap at about 0.1 of the initial rate (gap voltage = 3.1 V), carrying plasma away from the gap, for example along equipotentials of -2 and -4 V. This effect is also enhanced by the circulation around the negative island.

By 30 msec the negative island has disappeared and the field is well into the falling half of the pulse (gap voltage = -8.8 V). The

potential contours show E×B drifting field lines exiting through the gap. As predicted, most of the azimuthal motion occurs near the wall and the electric field is more nearly axisymmetric and azimuthal (radial potential countours) near the separatrix. The $\dot{\vec{A}}$ contribution to the voltage difference across the θ-range of the plot at ψ_{sep} is calculated to be about 1 V, while the measured difference is about 2.5 V, so the shielding of the $\nabla\emptyset$ contribution is not complete. Evans' single rod, sharp-boundary plasma model is different enough from a real octupole plasma to make direct comparison difficult, but this measurement seems to correspond most closely to the degree of shielding in his case with a dielectric constant of 10. An average value for the dielectric constant between ψ_{sep} and the wall in this experiment is more on the order of 100, but, as pointed out in Chapter 4, the dielectric model may not be a good one when the time scale is longer than an ion collision time, as it is here. The plasma flux to the wall now has a definite peak at the gap, showing that plasma is indeed carried along and deposited there by the E×B drift.

At 40 msec, almost the end of the pulse (gap voltage = -13.4 V) the picture is similar, except for the larger electric field and the rather puzzling lack of symmetry across the plane of the gap. The plasma flux to the wall now has a sharp peak about 4° wide at the gap. If the plasma flux to the wall toward the left- and right-hand ends of the plot is representative of the other 300° of the toroid, then the flux integrated from -4° to +4° accounts for over half of the total plasma leaving the machine.

These observations demonstrate the E×B divertor-like action of the poloidal gap at late times in the magnetic field pulse. The $\nabla\emptyset$ part of the electric field is at least partially shielded by the plasma, as is desired to keep the azimuthal drift to a divertor from penetrating into the central plasma. As the electric field increases with time, the majority of the plasma loss is shifted from the wall at large to a very localized region, which could be imagined as the entrance to a divertor's pumping chamber.

5.B. Biased Fin

5.B.1. Introduction

In order to perform an experiment in which the electric fields responsible for the divertor action were independent of other parameters and easily variable by the experimenter, a retractable fin was installed on the upper lid of the toroid.[11,12,13] Made of 0.010" stainless steel sheet, in its extended position it lay in a poloidal plane, with its outer edge at ψ_{crit}. A worm gear mechanism allowed it to be folded flat against the lid when not in use. Figures 5.1 and 5.4 show the position of the fin and of the diagnostics used in the experiment.

This fin differs from a conventional limiter, which it superficically resembles, in that it lies parallel to magnetic field lines. Therefore no great amount of plasma can be lost to it by thermal flow

along field lines. However, if one of the octupole rings is given a positive DC bias potential, there results a radial electric field, causing an E×B drift in the θ direction, sweeping plasma toward the surface of the fin. In fact, as was seen in Chapter 4, the electric field is not shielded out in a Debye length, but most of it appears in a layer near the wall, conveniently where it is needed to take the outer edge of the plasma toward the fin.

Furthermore, the fin itself can be given a DC bias. This creates an E×B drift which circulates around the fin, in the nature of an artificially induced convective cell similar to, but stronger than, those which occur naturally in the octupole. This is now combined with the azimuthal E×B drift due to the biased ring. If the bias of the fin has the same sign as that of the ring, the circulation will be toward the wall on the side of the fin which is upstream relative to the main azimuthal E×B drift. Then when the azimuthally drifting plasma reaches the fin it will turn and drift toward the wall, as shown in Figure 5.5. In a true divertor there would be at the base of the fin an entrance to an external pumping chamber where the diverted plasma would be disposed of; in this experiment it simply strikes the wall and is neutralized.

As shown in Figure 5.5, there are at least two classes of E×B drift surfaces (equivalent to surfaces of constant electrostatic potential). When $V_{fin} < V_{ring}$, surfaces of potential $V < V_{fin}$ pass between the fin and the wall, and plasma drifting along them will be diverted, while surfaces of potential $V > V_{fin}$ pass the fin on the plasma side unaffected. The surface $V = V_{fin}$ then forms a separatrix

dividing these two classes, analogous to the magnetic separatrix in a conventional magnetic field divertor. When V_{fin} becomes larger than the potential anywhere in the plasma ($V_{fin} > V_{ring}$ approximately) closed potential surfaces begin to appear around the fin, introducing a third class of drift surfaces, any particles on which will also be taken to the wall. Presumably as the fin's potential is raised further, the drift surface separatrix remains near the ring potential, and more closed surfaces appear about the fin, with little additional effect on the rest of the plasma.

The experiment was carried out with the poloidal field now crowbarred in order to reduce the inductive electric field. Observations were typically made 7 msec after the end of the microwave pulse, to allow any large density or temperature gradients in the plasma to smooth out. As indicated in Figure 5.4, the fin was mounted at an azimuthal position 315° from the poloidal gap. The outer ring supports at 318°, which could have been an extraneous perturbation on the behavior of the plasma near the fin, were withdrawn manually when data were taken with the rings supported. As will be seen, most of the measurements were localized near the fin and thus were made without levitating the rings.

Figure 5.6 shows, for reference, profiles of floating potential and ion saturation current, for a typical DC bias of 40 V on the upper inner ring and the fin retracted, measured with the floating double probe indicated in Figures 5.1 and 5.4. Assuming $T_e = 4$ eV, the density at ψ_{sep} is calculated to be about 2×10^{10} cm^{-3}. The floating

potential profile is similar to those discussed in Chapter 4; the resulting E×B drift speed between ψ_{crit} and the wall is about 2×10^6 cm/s, much larger than the combined $\nabla|B|$ and curvature drifts of about 3×10^4 cm/s.

5.B.2. Variation of Bias Potentials

The diverted potential contours (E×B flow streamlines) all pass through the narrow gap between the fin and the wall. Due to the narrowness of the gap and to the potential difference across it, the plasma there will tend to be charge separated, so the current drawn by the fin provides a crude estimate of the total flux of diverted plasma. Figure 5.7(a) shows fin current vs. fin bias for a fixed value of ring bias. As V_{fin} is raised and the drift separatrix moves deeper into the plasma, the amount of diverted plasma increases, as seen by the increased fin current. The increase is not linear since layers of progressively larger plasma density are being diverted. As expected, it saturates when V_{fin} exceeds V_{ring}. The curve bears a strong resemblance to a Langmuir probe characteristic, but this illusion is dispelled by Figure 5.7(b). The fin current at a fixed fin bias is seen to rise linearly with V_{ring}, consistent with the fin collecting all the plasma carried to it by the azimuthal E×B drift, which is proportional to V_{ring}. (The location of the drift separatrix does not change much over this plot, since $V_{fin} > V_{ring}$ always.) If the positively biased fin were acting as a simple Langmuir probe drawing

electron saturation current, the current would decrease rather than increase as the plasma potential approaches the bias potential.

Next, the fin and ring biases were varied toether, with $V_{fin} = 1.5\ V_{ring}$, in order to vary the E×B drift speed while keeping the shape of the drift surfaces constant at all bias values. As shown in Figure 5.8, the current to the fin again rises approximately linearly with the drift speed. The flux to a collector mounted on the lid, just on the upstream side of the fin (collector #1) also increases linearly, showing that the plasma flow is indeed diverted toward the wall. The flux to a collector on the lid just on the downstream side (#4) decreases rapidly, as expected. Sharp density gradients leading to rapid filling-in behind the fin presumbably account for the non-zero value for collector #4 at large drift speeds.

A striped collector was also mounted on each face of the fin. Due to the large electric fields and non-ambipolar flux to the biased fin they did not give reliable measurements when used in the usual way, and showed a hysteresis effect with varying fin potential due to charging of their insulating substrates.[14] Therefore they were generally not used, and to avoid perturbing the electric field, both sets of stripes on each collector were held at the fins' potential. When the net current drawn by the collectors in this mode was measured separately, it was found to be only 1.5% of that of the entire fin, although they made up about 8% of the surface area. Since they were mounted at the edge away from the wall, this is further evidence that most of the plasma is diverted toward the wall and lost at the base

of the fin, rather than striking the fin uniformly as if it were just acting as an obstacle.

Recalling that ψ surfaces rotate as rigid bodies with E×B drift, the average rotation frequency between ψ_{crit} and the wall can be estimated from Figure 5.6(a) as (35 Hz/V) V_{ring}. The average density between ψ_{crit} and the wall can be estimated from Figure 5.6(b) as 2×10^9 cm^{-3}. Multiplying these by the circumference of the mid-cylinder, 880 cm, and the area of the fin, 460 cm^2 (one side only), gives an estimate for the total plasma flux reaching the fin by E×B drift of (4.5 mA/V) V_{ring}, which is in reasonable agreement with the measured slopes of Figures 5.7(b) and 5.8(b) of about (3.0 mA/V) V_{ring}.

Both the fin current and the flux to collector #1 are seen to saturate for V_{ring} above about 40 V. This corresponds to an azimuthal rotation period of about .7 msec. From estimates for average plasma density of 2×10^{10} cm^{-3}, plasma density lifetime of 30 msec, confinement volume of 7×10^6 cm^3, average density between ψ_{crit} and the wall of 2×10^9 cm^{-3}, wall area of 4.2×10^5 cm^2, and average distance from ψ_{crit} to the wall of 3 cm, and assuming half the plasma goes to the wall and the other half to the rings, a very rough estimate can be made for the time taken by plasma to cross from ψ_{crit} to the wall of .8 msec. Thus the saturation is probably due to the shadow of the fin wrapping all the way around the toroid.

5.B.3. Density Profiles

Ion saturation current profiles were measured with the floating

double probe at 330°, 15° or about 50 cm downstream from the fin. V_{ring} was fixed at 40 V, evidently the minimum necessary to make a modification of the density profile extending around the toroid, and V_{fin} was varied. It should be noted that the floating potential profile at the position of the probe was not noticeably altered by the presence or biasing of the fin. Due to the large range of density from ψ_{sep} to the wall, it proved most convenient to plot the ion saturation current in terms of the change from the profile measured with the fin retracted (but the ring still biased). As shown in Figure 5.9(b), although the physical edge of the fin is fixed, the point at which plasma density drops off moves deeper into the plasma as V_{fin} is raised, until V_{fin} reaches V_{ring}, which is consistent with Figure 5.5 and the earlier discussion of it.

The relationship can be made more quantitative by estimating the drift separatrix to occur at the point where the density is reduced by 20%, and reading the floating potential at this point from the profile in Figure 5.9(a). This is then plotted vs. V_{fin}. From Figure 5.5, the potential of the drift separatrix is expected to be equal to V_{fin}, for $V_{fin} \leq V_{ring}$. As seen in Figure 5.10, the relation is linear with a slope of 1, as expected. The offset of 7 V can be accounted for by noting that plasma potential should have been plotted rather than floating potential, and the correction for this has the right sign and order of magnitude.

As the plasma drifts past the fin and plasma outside the drift separatrix is removed, a large density gradient arises at the drift

separatrix. Large amplitude, high frequency ($\gtrsim$ 20 kHz) fluctuations are observed in the ion saturation current in the scrape-off zone, apparently an instability caused by the large density gradient. These probably cause enhanced transport, resulting in the non-zero density observed even a short distance downstream in the scrape-off zone. (See Figure 5.9(b), and also Figure 5.11(b) and the discussion of it below.) Figure 5.9(c) shows the relative amplitude of these fluctuations, only two representative cases being plotted for the sake of clarity. With the fin removed, the fluctuations are low in the confined plasma and rise at ψ_{crit}, where the plasma is expected to become unstable. With the fin inserted and biased to 50 V, the fluctuation level rises to 50% in the scrape-off region, and rises again to 100% at ψ_{crit}.

To eliminate the possibility that the observed reduction of ion saturation current was due to cooling of the plasma instead of a reduction of the density, full I-V characteristics of a single-tip probe at ψ_{crit} were taken for three cases: (1) fin out and grounded, ring electrically floating, (2) fin out and grounded, V_{ring} = 40 V, (3) fin in, V_{fin} = 60 V, and V_{ring} = 40 V. The electron temperature was found to be equal within experimental error for all three cases.[12] This is to be expected since the reduction of ion saturation current is seen only when biases are applied to remove plasma by E×B drift, but as mentioned in Chapter 2, this process does not cool the plasma.

5.B.4. Azimuthal Variations

Finally, for direct and graphic confirmation of some of the

foregoing, the cart was used to make detailed maps of potential and density in the vicinity of the fin, for the particular case of $V_{ring} = 40$ V, $V_{fin} = 60$ V. The probe was at its maximum elevation, with the tip used being near the inner nose as in Figure 5.1.

Figure 5.11(a) shows contours of constant floating potential near the fin, with the direction of E×B drift indicated. The drift separatrix is seen as the 36.2 V surface, which is close to the value estimated for Figure 5.10. Equipotentials of less than 36.2 V are diverted away from the main body of the plasma, while equipotentials of greater value pass by unaffected. Also visible are portions of closed contours circulating around the fin. Some indication of a standing wave is seen on the downstream side, which could develop farther downstream into the turbulence seen in Figure 5.9(c). The drift speed divided by this wavelength gives $f \sim 10^6$ cm/s/20 cm = 50 kHz, which is the right order of magnitude.

If the only plasma motion is due to $\vec{v}_E = \vec{E}\times\vec{B}/B^2$, it can be shown that in steady state, and with $\nabla\times\vec{B} = 0$, the mass continuity equation leads to

$$\frac{\nabla n}{n} \cdot \vec{v}_E = 2\,\frac{\nabla|B|}{|B|} \cdot \vec{v}_E \qquad (5.7)$$

To the extent that B is uniform in the drift direction surfaces of constant density n coincide with surfaces of constant potential Ø. Some indication of this is seen in a plot of density contours near the fin[12] (not shown here), though it is not strictly followed since there

are other contributions to the plasma motion. Figure 5.11(b) shows the results of density (ion saturation current) measurements over the same range as Figure 5.11(a), plotted in terms of the change from the case with the fin retracted. Denser plasma following diverted equipotentials toward the wall on the upstream side produces a rise in density. There is a sharp reduction of density immediately downstream, rapidly filling in to a steady but reduced profile. Though a double probe was not available on the cart, the alteration of V_f contours due to the fin is of the order of 10% of $V_{plasma} - V_{probe}$, too small to account for the observed variation in ion saturation current even if I_{oi} were proportional to $V_{plasma} - V_{probe}$ rather than saturating.

The divertor region is quite localized; these contour plots span only a small range of θ. However, the influence of the E×B divertor on plasma flux to the wall extends all the way around the toroid. Figure 5.11(c) shows plasma flux (plotted as change from the case with the fin retracted) measured by striped collectors on the inner and outer noses (see Figure 5.4). The θ range of the contour plots is indicated. The data for the contour plots were taken with the rings supported but with the outer ring supports at 318° withdrawn, so the nearest supports were on the inner rings at 292°, well out of the picture. However, since the collector data were to span the entire 360°, they were taken with the rings levitated. The graph shows an increase in plasma flux to the wall just ahead of the fin where plasma is diverted toward the wall, a sharp decrease just behind it, and a permanent decrease extending around the toroid and gradually filling in. This is consistent with the other data.

Filling-in by diffusion following an initial density distribution given by a step function, as immediately behind the fin, does not occur exponentially, but can be characterized by a time $\tau \sim \ell^2/4D$, where ℓ is a characteristic length in the direction of the density gradient.[15] In the present case τ can be replaced by d/v_θ, where d is a characteristic distance in the θ-direction for filling in behind the fin. Here the plasma flux to the wall fills in from almost 100% reduction to 30% reduction around the circumference of the toroid, and the density profile recovers almost completely, so the circumference of ~ 1000 cm seems a reasonable value for d. Using $v_\theta = 1.5 \times 10^6$ cm/sec and $\ell = 1.5$ cm, a typical density scale length in the bridge region, gives an estimate for D of 700 cm^2/sec, in reasonable agreement with more precise measurements.

5.B.5. Final Comments

This experiment, using only externally applied E×B drifts, shows behavior desired of a divertor: a decrease in density near the wall with no deleterious effects on confinement of the dense central plasma, a localized increase in plasma flux simulating removal of plasma through a narrow opening in the wall, and reduction of plasma flux to the wall everywhere away from the divertor region. These effects were not seen when either the fin or the ring was not biased, showing that they were due to the E×B drifts and not simply to the presence of the fin as a mechanical obstacle. The position of the

"divertor separatrix" could be controlled simply by varying the applied bias potentials.

Density profiles very similar to those of Figure 5.9(b) were also obtained for two other cases:[12] (1) small gun plasma, and (2) ECRH plasma, B_t = 400 G at the midcylinder. The first case shows that the E×B divertor action is not altered by the presence of hot ions, as expected. The second case shows that even when field lines intersect the fin and plasma can be lost to it by parallel flow as with a conventional limiter or magnetic field divertor, the addition of an applied E×B drift can further reduce the density near the wall.

The data available do not lend themselves to easy comparison with the prediction of Eq. (1.13) and elsewhere that the density scale length in a divertor zone is equal to $(D_\perp \tau_d)^{\frac{1}{2}}$ where $D_\perp$ is the perpendicular diffusion coefficient and τ_d is the transit time to the divertor. The semilog profile plots of Figure 5.12, however, show that for a particular bias case, both without and with B_t, the E×B divertor approximately halves the density scale length. Taking a typical value of $D_\perp$ = 1000 cm^2/s, and τ_d = 0.7 ms, the azimuthal rotation period, gives a scale length of 0.8 cm, in reasonably good agreement with the measured value of 1.1 cm. This is nearly equivalent to the filling-in calculation above.

REFERENCES - CHAPTER 5

1. D.W. Kerst, Bull. Am. Phys. Soc. 20, 1334 (1975), also University of Wisconsin PLP 613.
2. K. Evans, Jr., Phys. Fluids 16, 2330 (1973), also University of Wisconsin PLP 459 (1972) and PLP 503 (1973).
3. J.R. Drake, University of Wisconsin Ph.D. Thesis (1973), p. 93.
4. A.J. Cavallo, University of Wisconsin Ph.D. Thesis (1975), p. 96.
5. A. Butcher Ehrhardt, University of Wisconsin Ph.D. Thesis (1978), p. 15.
6. J.W. Rudmin, University of Wisconsin Ph.D. Thesis (1974), p. 100.
7. K. Evans, Jr., University of Wisconsin PLP 491 (1972).
8. M.C. Zarnstorff, University of Wisconsin PLP 571 (1974).
9. A. Butcher Ehrhardt, Thesis, p. 30.
10. J.R. Drake, University of Wisconsin PLP 537 (1973).
11. J.C. Sprott and E.J. Strait, Bull. Am. Phys. Soc. 20, 1334 (1975), also University of Wisconsin PLP 669 (1975).
12. E.J. Strait and J.C. Sprott, Bull. Am. Phys. Soc. 21, 1062 (1976), also University of Wisconsin PLP 707 (1977).
13. E.J. Strait, D.W. Kerst, J.C. Sprott, Phys. Fluids 21, 2342 (1978).
14. A.J. Cavallo, Thesis, p. 25.
15. R.L. Spencer, University of Wisconsin PLP 771 (1978).

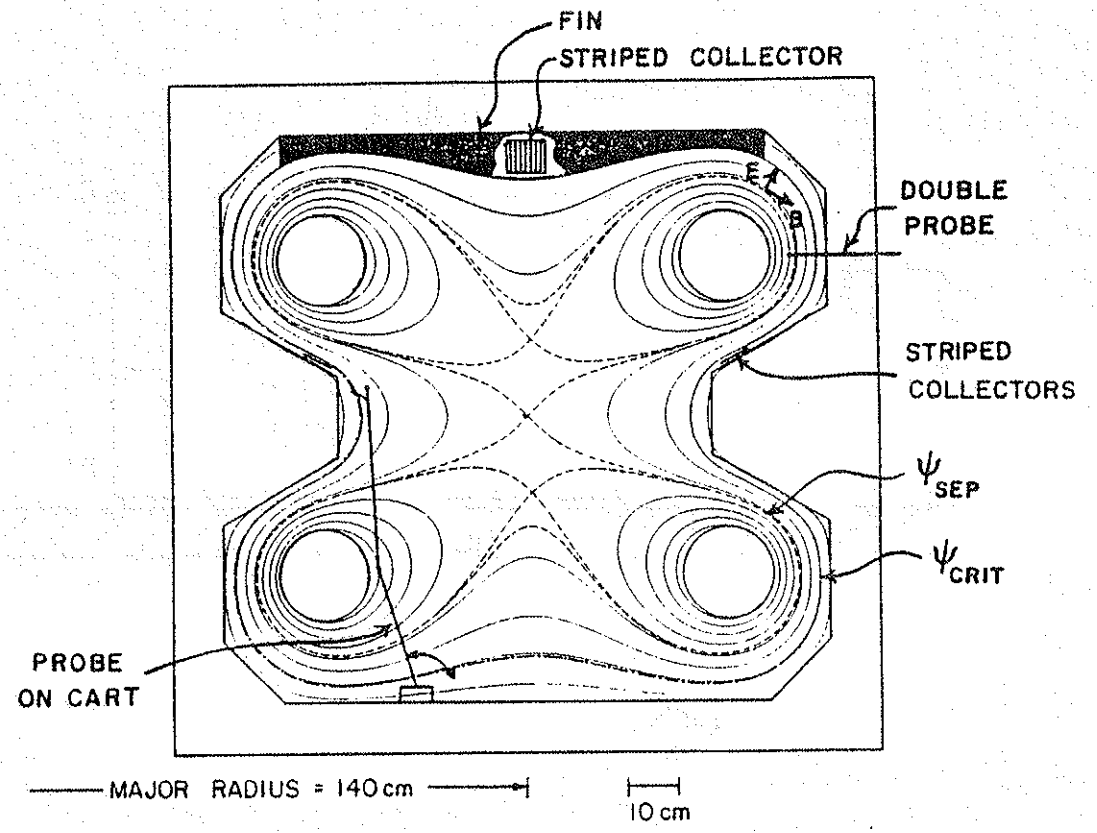

Fig. 5.1 - Minor cross-section of toroid, showing fin, probe cart, and other diagnostics (not all at the same azimuthal position).

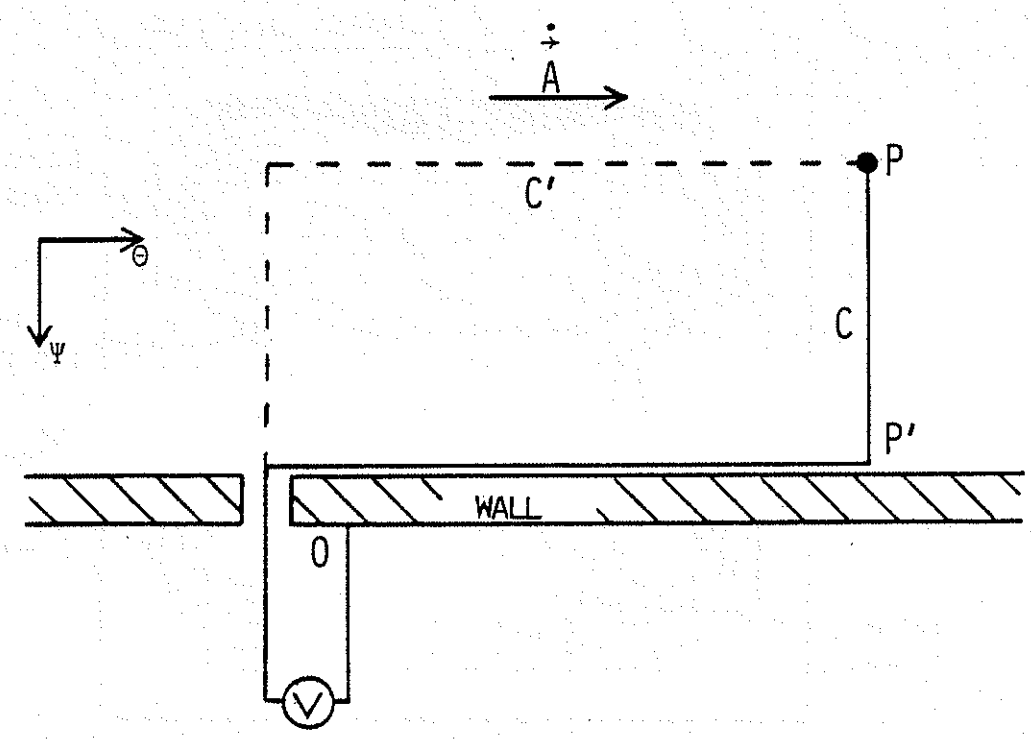

Fig. 5.2 - Contours of integration for $\dot{A}$ corrections. O = ground connection, P = probe tip, C = path of wires to probe tip. P' is location of ground connection when connection is made at the cart (not shown).

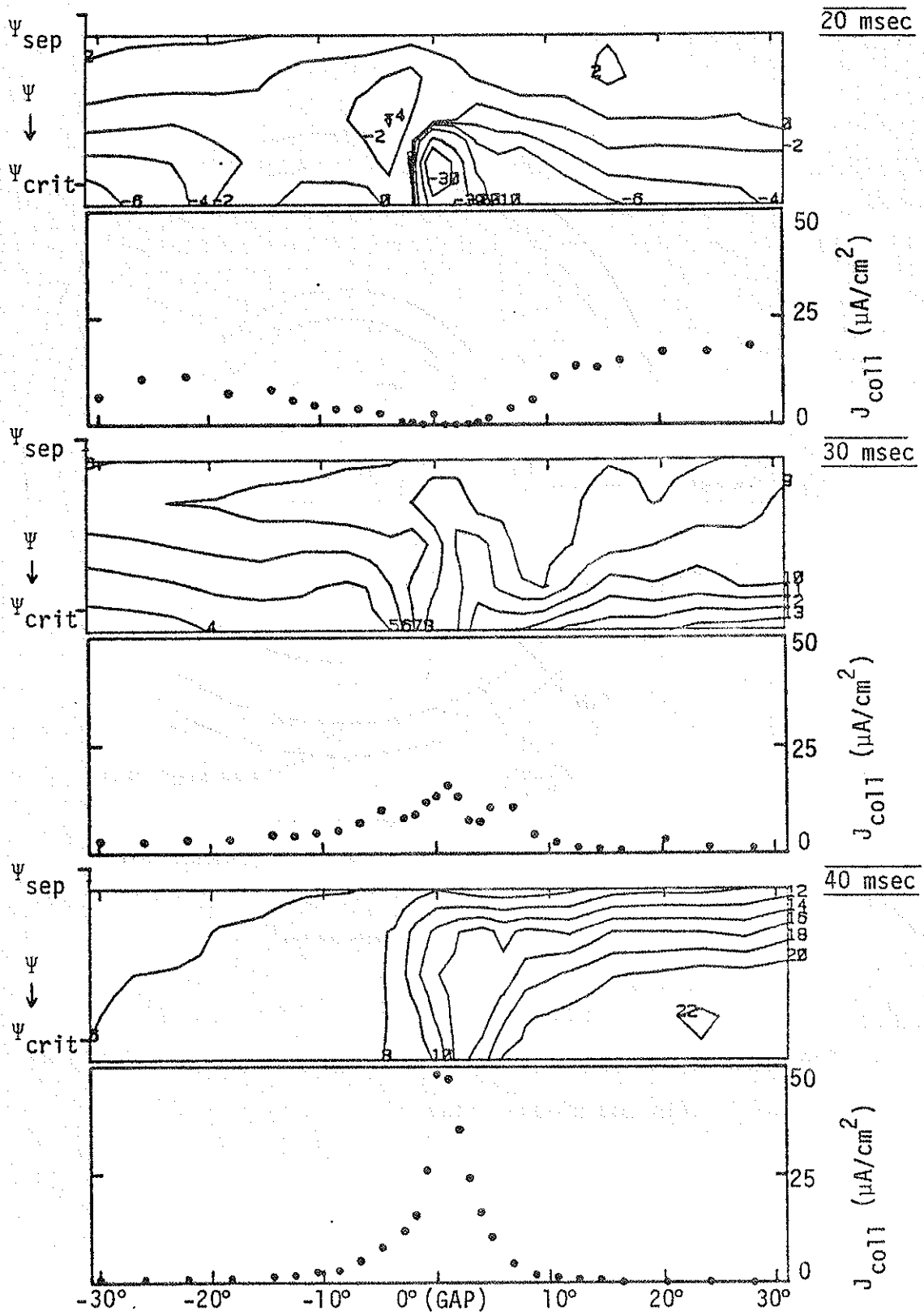

Fig. 5.3 - Equipotential contours (volts), plasma flux to wall near gap.

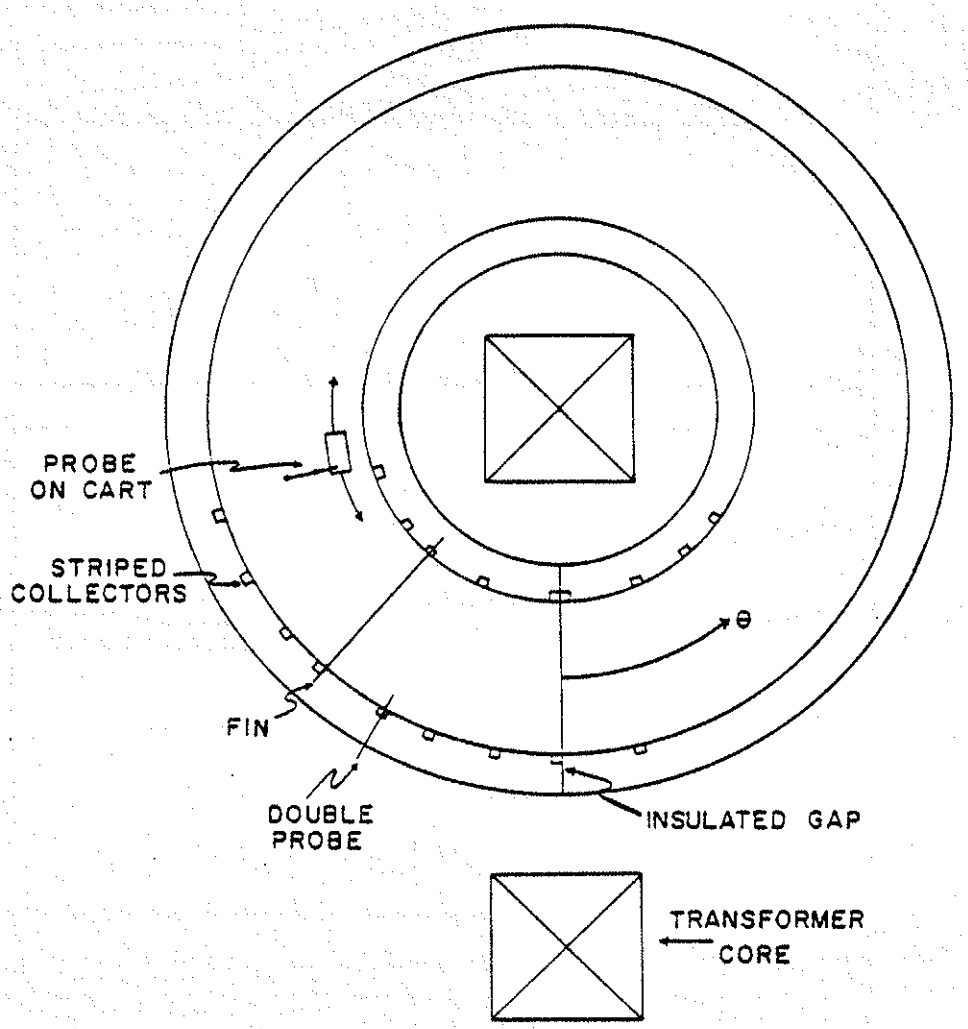

Fig. 5.4 - Top view of toroid, showing azimuthal positions of fin and diagnostics.

QUALITATIVELY, ExB DRIFT SURFACES ARE EXPECTED TO LOOK LIKE THIS :
(BROKEN LINE IS DRIFT SEPARATRIX)

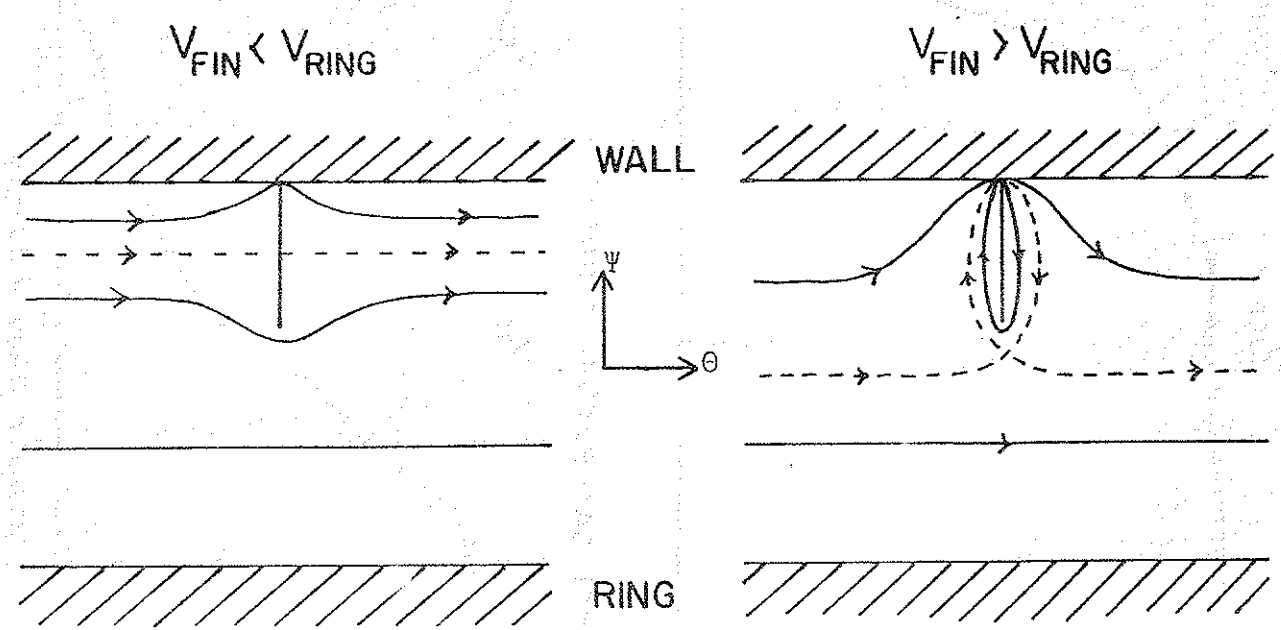

FOR $V_{FIN} < V_{RING}$, EXPECT V_{PLASMA} AT DRIFT SEPARATRIX TO EQUAL V_{FIN}.
INCREASING V_{FIN} SHOULD MOVE SEPARATRIX INTO PLASMA UNTIL $V_{FIN} \gtrsim V_{RING}$.

Fig. 5.5 - Drift surfaces near fin (schematic).

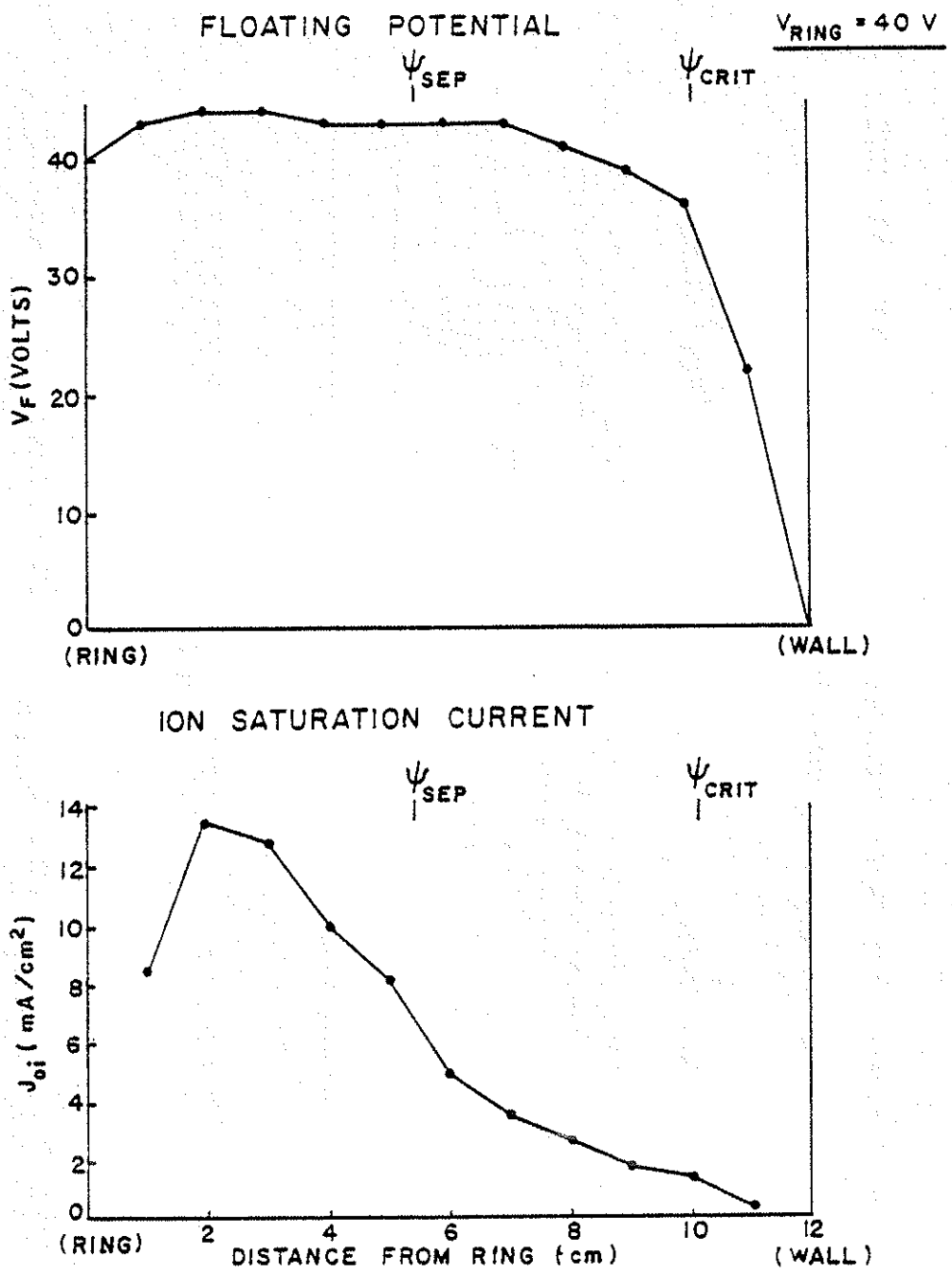

Fig. 5.6 - (a) floating potential and (b) ion saturation current profiles: V_{ring} = 40 V, fin retracted.

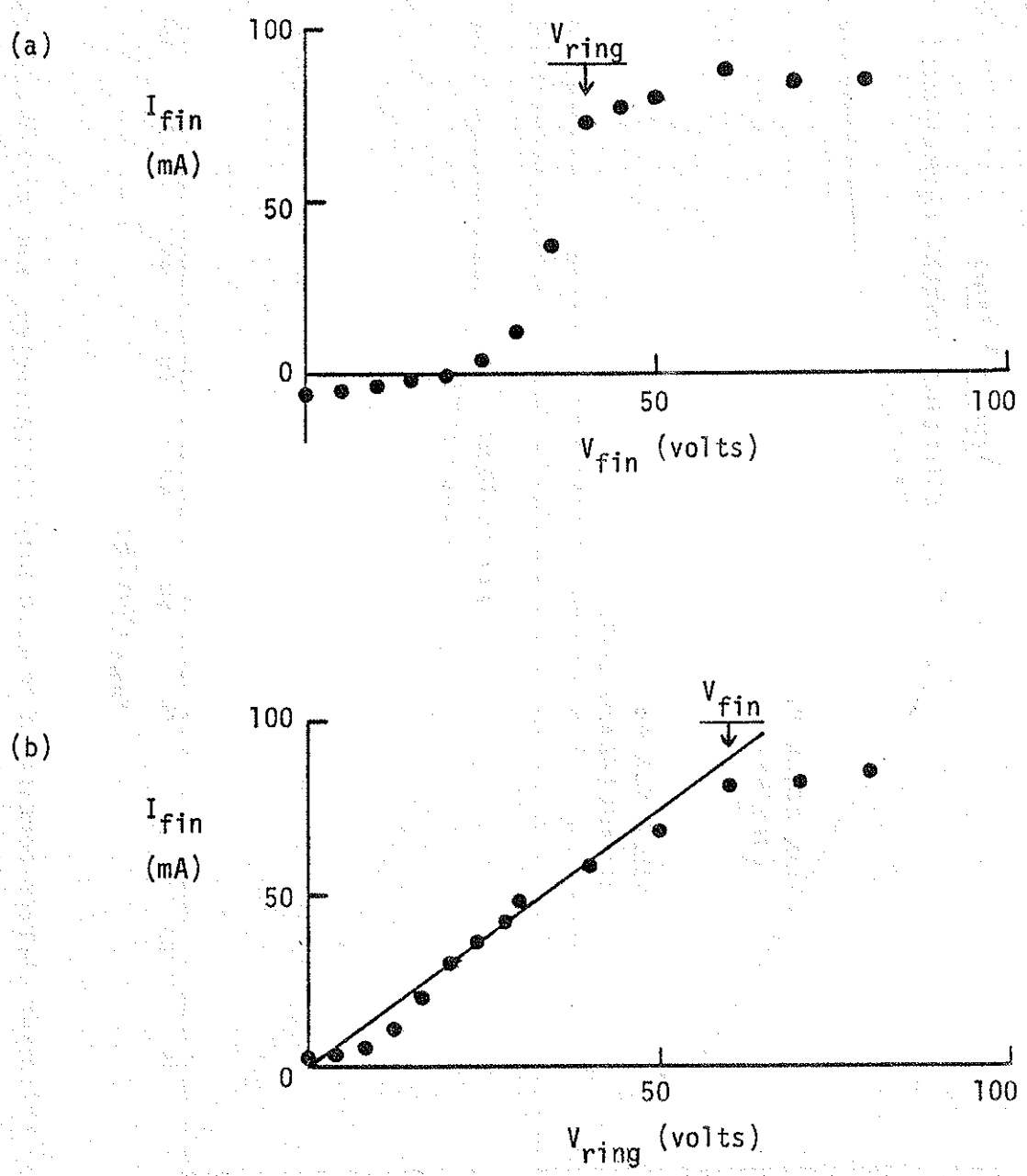

Fig. 5.7 - (a) Fin current vs. fin bias, V_{ring} = 40 V.
(b) Fin current vs. ring bias, V_{fin} = 60 V.

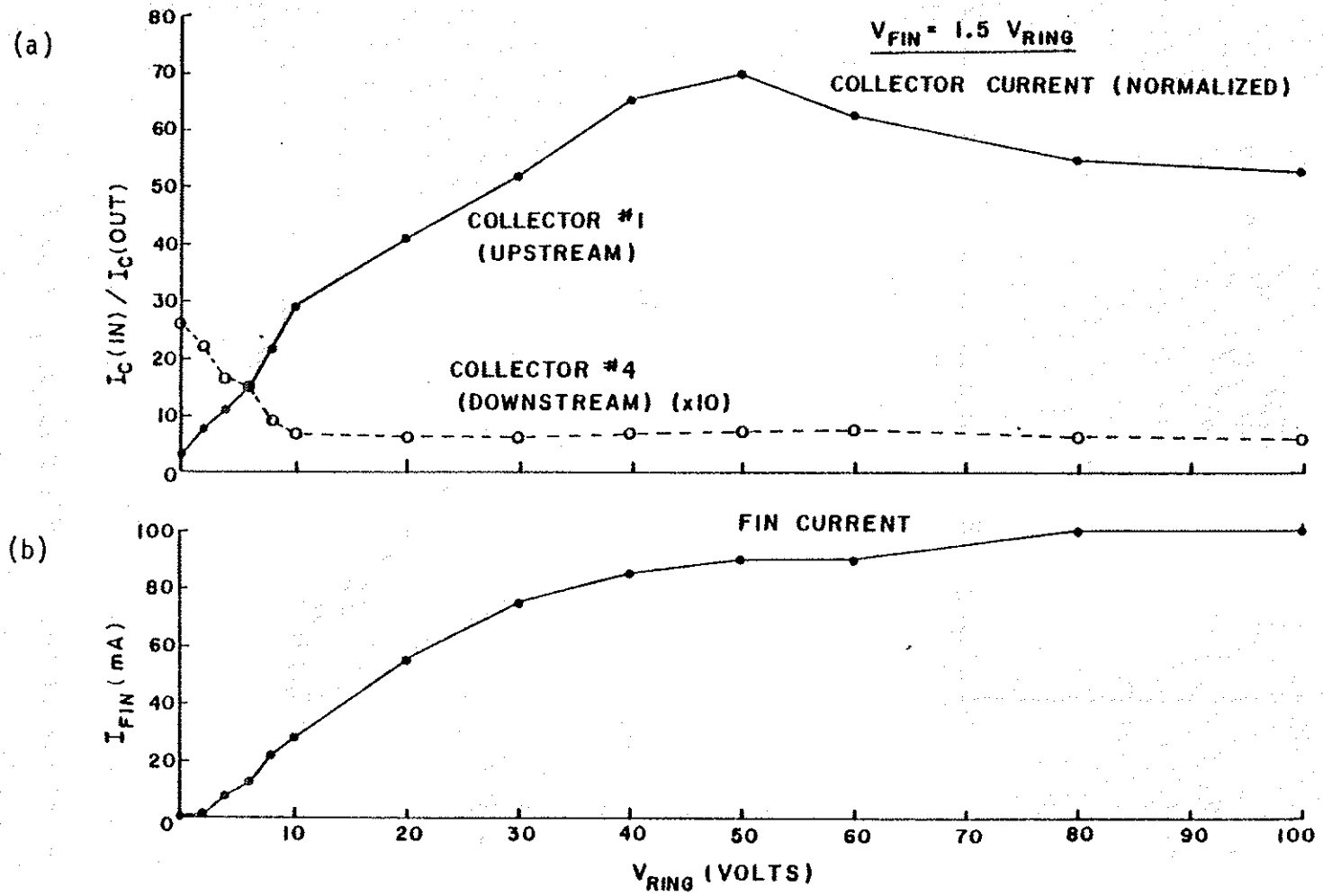

Fig. 5.8 - (a) collector current normalized to case with fin retracted, and (b) fin current, vs. ExB drift speed. $V_{fin} = 1.5\ V_{ring}$.

(a)

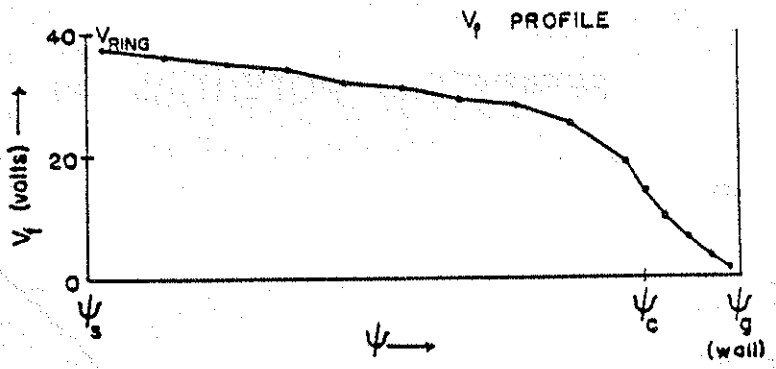

(b)

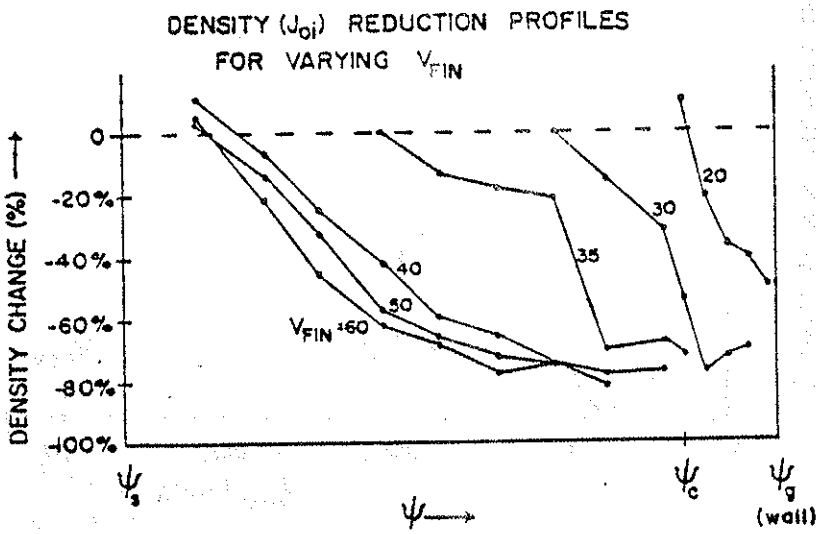

(c)

Profiles of relative amplitude of density fluctuations.

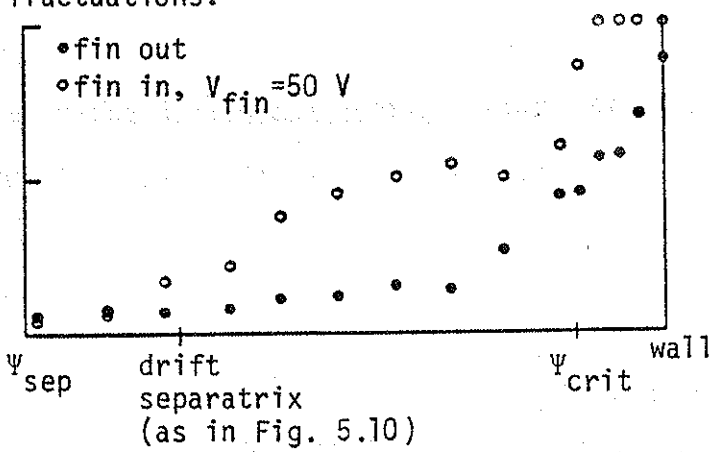

Fig. 5.9 - V_{ring}=40 V.

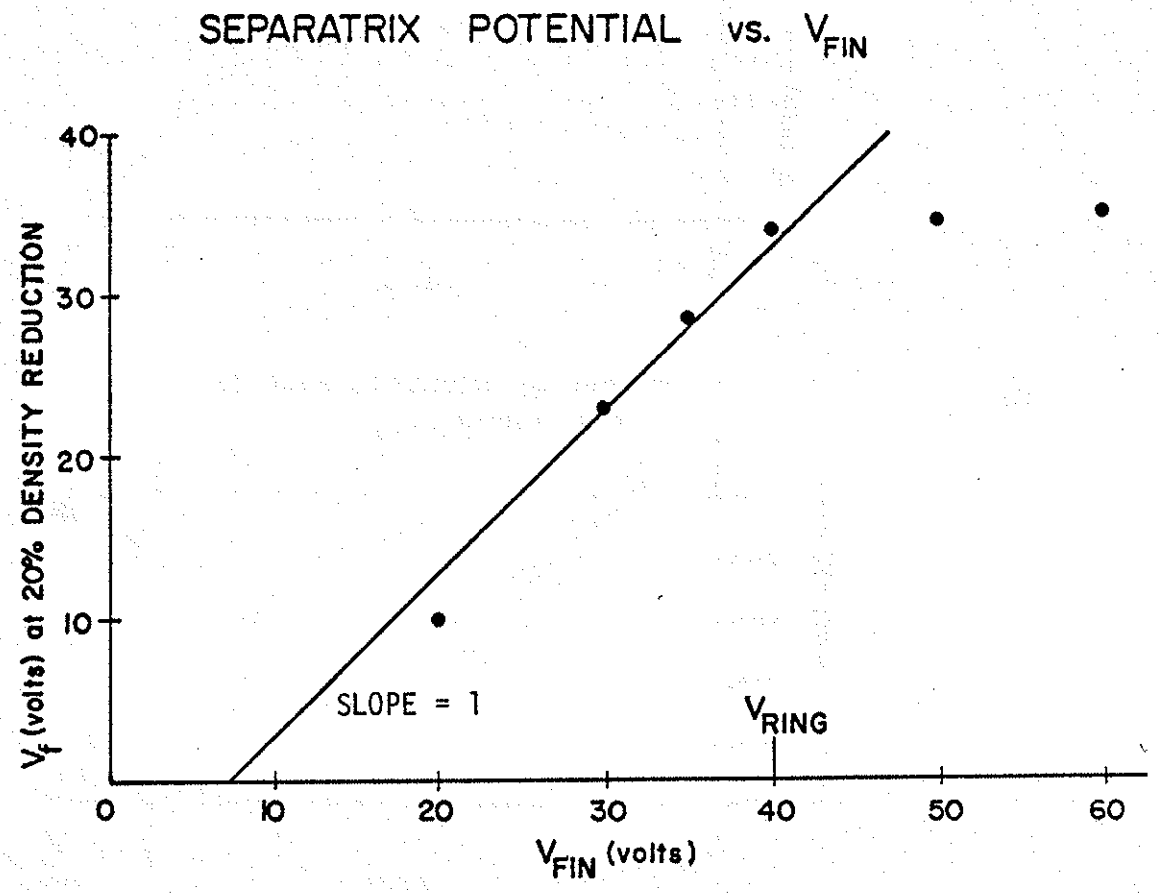

Fig. 5.10- Drift surface separatrix potential (inferred from Fig. 5.9 (a) and (b)) vs. fin bias.

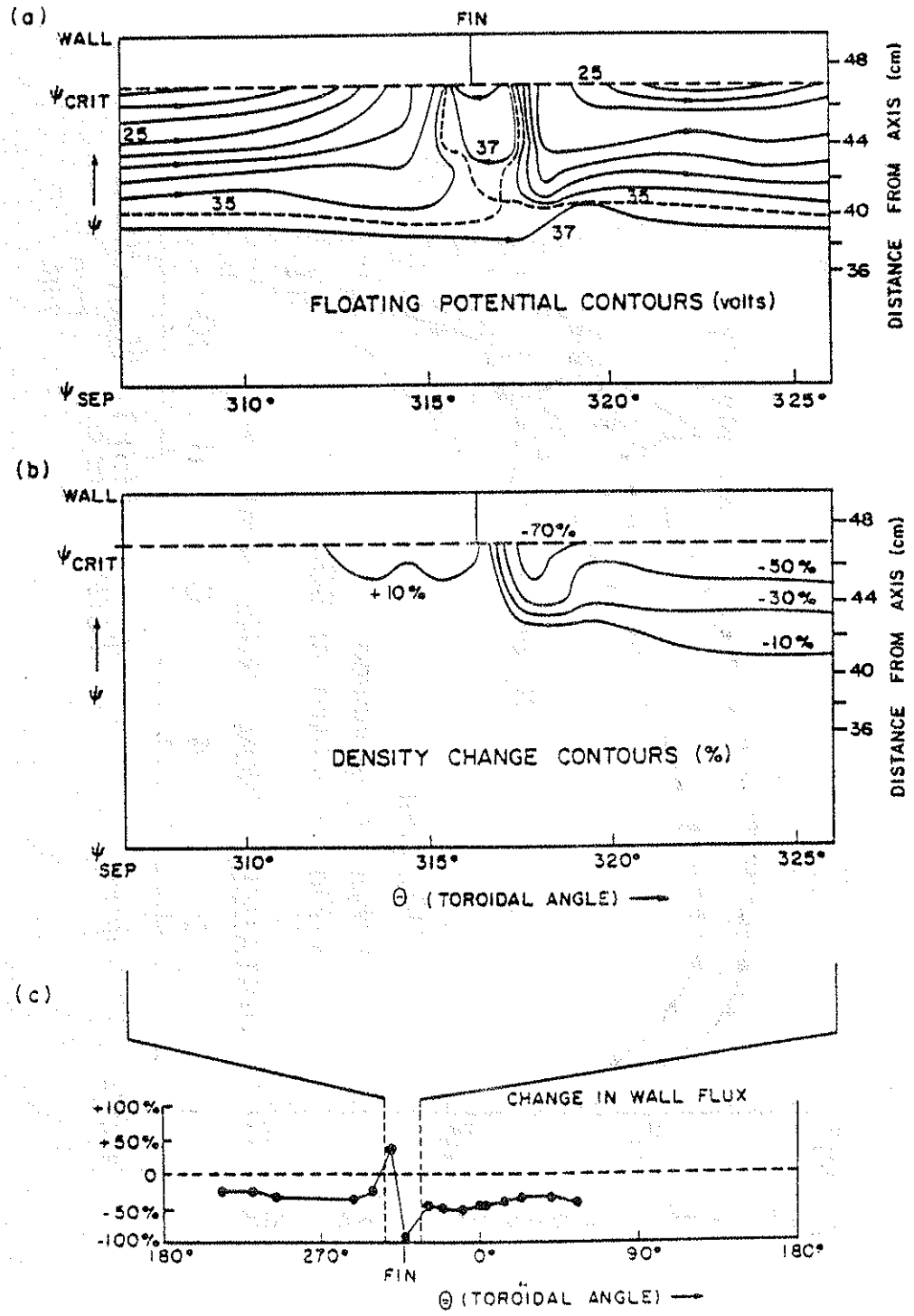

Fig. 5.11 - Azimuthal variations near fin: V(ring)=40 V, V(fin)= 60 V. (a) Floating potential contours in Ψ,Θ. Direction of ExB drift is shown. Dotted line (36.2 V contour) is drift separatrix. (b) Contours of fractional density change in Ψ,Θ. (c) Fractional change of wall flux in Θ. Vertical lines show Θ-range of (a) & (b).

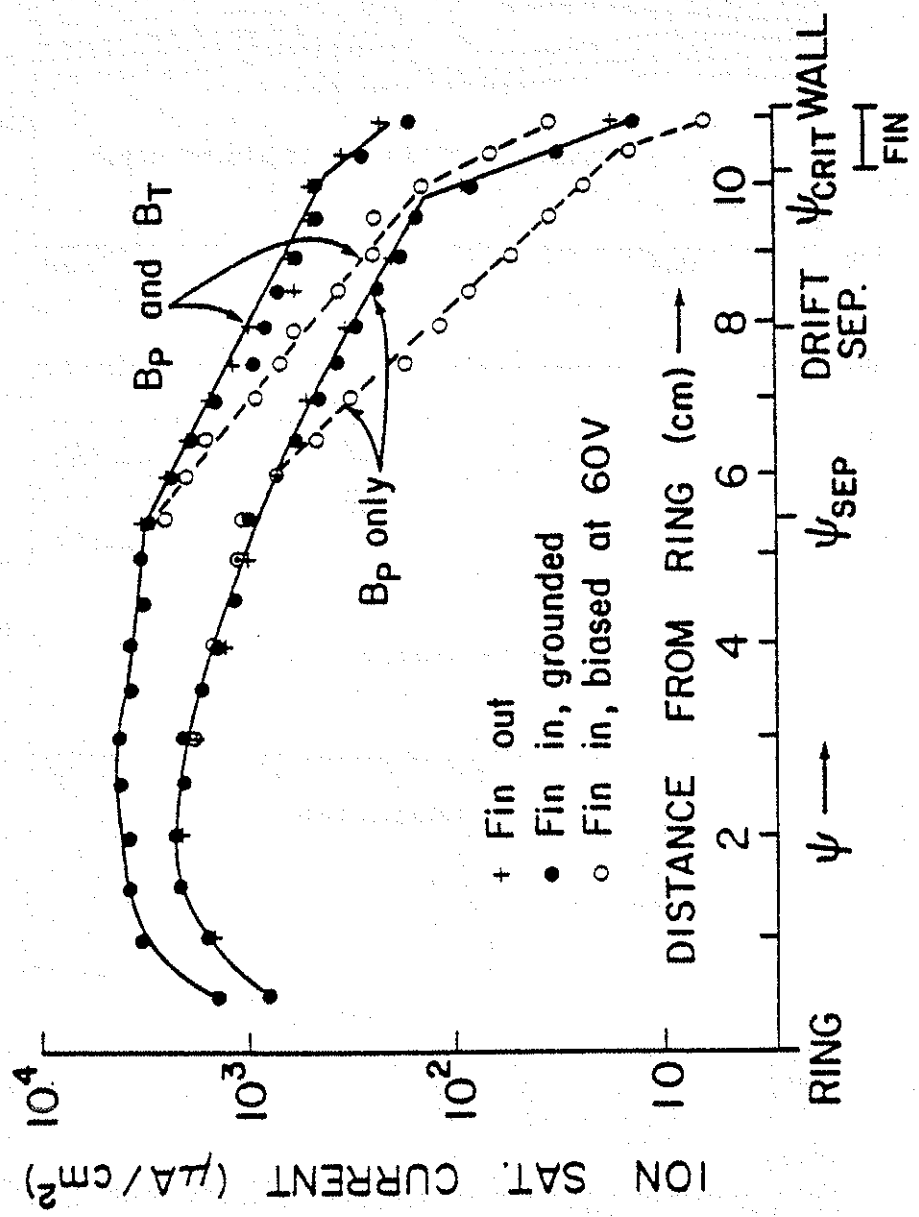

Fig. 5.12 - Semilog plots of ion saturation current profiles. V_{ring}=40 V. Location of drift separatrix with biased fin is taken from Fig. 5.11(a).

CHAPTER 6

POLOIDAL MAGNETIC DIVERTOR EXPERIMENTS

In order to test the E×B divertor under conditions closer to those of the tokamak divertor discussed in Chapters 1 and 2, a poloidal magnetic divertor was installed in the octupole, as described in Chapter 3.B. Its location is shown again in Figure 6.1, along with some of the diagnostics used in the experiment. As mentioned in Chapter 1, either "unload" or "screening" action may be required of a divertor; since it was not practical to provide pumping for permanent removal of diverted plasma and incoming impurities the emphasis in the present experiment is on the "unload" function, namely, taking outwardly diffusing plasma to the divertor before it can strike the wall.

Most of the data to be discussed below were taken in the hot-ion, collisionless plasma produced by the small gun, which is expected to approximate the collisionality of a tokamak reactor plasma. Some measurements were also made in the cold, collisional large gun plasma, since, due to their lower temperature, impurities in a tokamak divertor's scrape-off zone may be in the collisional regime. The small gun plasma will be understood if neither is specified.

The divertor in the ocutpole was first tried with the hoops in the triplet configuration. Although greatly increased plasma density was measured behind the divertor hoops when they were energized, very little effect was seen elsewhere in the plasma, either on density

outside the divertor separatrix or on plasma flux to the wall away from the divertor. One possible reason for this is the large "hill" of magnetic field strength around the hoops (see Figure 3.6), which could prevent most particles from reaching the divertor. However, the divertor also had little effect on the large gun plasma, in which particles should be quickly scattered into the loss cone by collisions, even in the absence of microinstabilities. A more likely explanation is the absence of a plate filling the space between the divertor hoops and the wall to neutralize the diverted plasma. (Such plates have been recently added.) Therefore, the data to be discussed below were taken in the single-hoop configuration, where the hoop itself serves as an obstacle to neutralize the diverted plasma.

The intent was to study a situation where plasma could go to the divertor by both parallel flow and E×B drift, as in the tokamak of Figure 2.1, so most data were taken with a relatively large ratio of toroidal to poloidal magnetic field. A standard configuration was 700 V on the B_p bank and 400 V on the B_t bank, giving a "safety factor" q of about .7, calculated midway between ψ_{sep} and ψ_{crit}. Divertor hoop currents will be expressed throughout as fractions of the current in an outer octupole hoop, for ease of comparison with the flux plots in Chapter 3. Observations shown are typically made 6 msec after gun injection, or 3 msec after peak divertor current.

6.A. Magnetic Divertor Alone

The performance of the divertor without any applied E×B drift will

be considered first, being both of interest in its own right and as a standard of comparison with the E×B drift.

6.A.1. Density Profiles

Figure 6.2 shows the effect of the divertor on the density (ion saturation current) profile in the small gun plasma, as measured at the lower outer octupole hoop, far away from the divertor. Figure 6.3 shows the corresponding profiles for the large gun plasma. In both cases, as the divertor current is raised and the divertor separatrix ψ_d moves deeper into the plasma, the profile becomes narrower, as expected.

The small gun's collisionless plasma, in the presence of a toroidal magnetic field, is governed by Kamimura-Dawson diffusion ($D \propto n^{-1}$),[1,2] while the large gun's collisional plasma is governed by classical diffusion ($D \propto n/B^2$).[3] It was shown previously in Eq. (1.12) that in a divertor scrape-off zone with constant diffusion coefficient the density scale length $[\nabla \ell n(n)]^{-1}$ is given by $\lambda = (D_\perp \tau_{11})^{\frac{1}{2}}$, and this kind of scaling can be expected to hold locally for non-constant diffusion coefficients as well. Therefore in the case of the small gun plasma the scale length is expected to increase at lower densities, while in the case of the large gun plasma it is expected to decrease at lower densities. Families of density profiles for the two cases are then expected to appear qualitatively different:

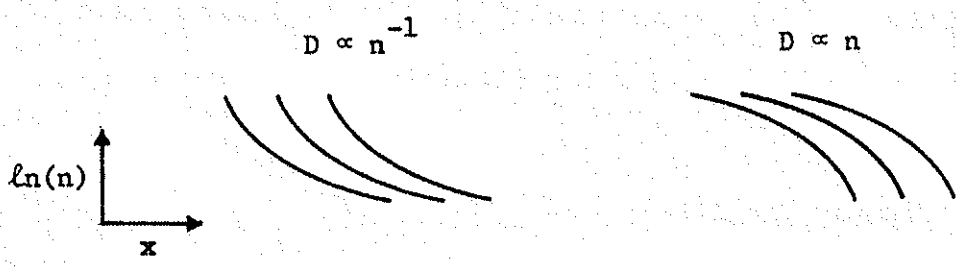

In the former case the greatest proportional change in density due to the divertor is expected to occur near the center of the plasma, while in the latter case it is expected to occur near the edge, and this is observed in Figures 6.2 and 6.3. Near the wall the density scale length in the small gun plasma becomes constant rather than increasing, however. This may indicate a different, density independent diffusion coefficient scaling in the region where field lines intersect a conducting obstacle. This would not be surprising, since the diffusion mechanism in the absence of the divertor, whether Kamimura-Dawson vortex diffusion[1] or trapped-ion instabilities,[2] depends on properties of the entire magnetic flux surface. The collisional diffusion of the large gun plasma, on the other hand, depends only on local plasma properties, and the divertor is expected to cause no qualitative change in diffusion.

A typical scale length in the scrape-off region for the small gun is 1.0 to 1.2 cm. Using $\tau_{11} = \pi Rq/v_{11} = .15$ msec, assuming $v_{11} = \frac{1}{2} c_s$ as suggested by the FM-1[4] and DIVA[5] experiments, and $T_i = 20$ eV, a value is obtained for D of 10^4 cm^2/sec, in good agreement with other measurements.[2] In the large gun plasma, the scale length at a density a factor of 10 below peak density (which turns out to fall in the scrape-off region, near ψ_{crit}) is typically .6 cm. Using $T_i = .2$ eV

then leads to a value for D of 250 cm^2/sec, which is in good agreement with the theoretical value for the classical diffusion coefficient at $n = 10^{11}\ cm^{-3}$ of 150 cm^2/sec.

These have all been qualitative arguments and consistency checks; a more realistic calculation for the normal mode shape of the profile could be carried out using the same techniques as in the diffusion coefficient studies which have been done on the octupole.[6] In particular, this could help answer the question of whether the diffusion actually changes to a Bohm-like, density-independent coefficient in the scrape-off region of the small gun plasma.

6.A.2. Floating Potential Profiles

Shown in Figure 6.4 are floating potential profiles for the cases of no divertor current, and a typical normalized divertor current of .1, giving a divertor separatrix of $\psi_d = 6.6$, about midway from the octupole separatrix ψ_{sep} to ψ_{crit}. The two profiles are qualitatively the same, the only difference being the location of the point where the slope changes sign. Though not plotted here, the potential in the central region obeys the ambipolar relationship mentioned in Chapter 3.B.1 (and references cited therein). As was mentioned there, close to the wall, where field lines intersect the conducting divertor hoops, the diffusion need no longer be ambipolar. In fact, in this region $\gtrsim$ 6 cm from the octupole hoop with the divertor and $\gtrsim$ 9 cm without, the electric field changes sign. This is consistent with the divertor

theory of Boozer[7] which, while derived under assumptions somewhat different from the present plasma, may still have some validity. He predicts that most electrons, due to their larger thermal speed, will be lost to the divertor in a narrow layer near the divertor separatrix, while the ions will be lost to the divertor over a much wider region. If this is true, since electron flow parallel to field lines is very sensitive to electrostatic potential, the electron outflow must occur at a minimum of the potential, such as is observed at the divertor separatrix here. Electrons must be present in the outer region of the divertor as well, in order to provide charge neutrality, but these are expected to be stagnant, and colder than the electrons in the main plasma, so some of the rise in floating potential seen here could also be a temperature effect. A very similar floating potential profile has been observed in the divertor experiment in the DC machine.[8]

6.A.3. Confinement Time

As the divertor separatrix moves inward with increasing divertor current, the confinement region becomes narrower and hence the confinement time becomes smaller. For both small gun and large gun plasmas, the confinement time decreases until the normalized divertor current reaches about .18. This is the point at which the divertor separatrix crosses the octupole separatrix and enters the private flux of the upper inner octupole hoop. Presumably confinement times

measured in the upper inner hoop's private flux would continue to decrease, but as far as the other three hoops are concerned, common flux is in the scrape-off region and private flux is not, so the effective divertor separatrix coincides with the octupole separatrix.

Simple dimensional analysis suggests that as the width d of the confinement region is varied, the confinement time should scale as

$$\tau \sim \frac{d^2}{D} \tag{6.1}$$

In fact, a simple slab model for normal mode decay with constant diffusion coefficient has the exact solution[9]

$$\tau = \frac{d^2}{\pi^2 D} \tag{6.2}$$

Lifetimes were measured for the small gun plasma, using the Fabry-Perot microwave interferometer to eliminate the $T^{\frac{1}{2}}$ dependence of probe measurements. Figure 6.5 shows a log-log plot of the confinement time vs. width of the confinement region, which is taken as the distance in ψ-space from the octupole hoops to the calculated position of the divertor separatrix. Only points where $\psi_d > \psi_{sep}$ are plotted.

In the case where the octupole hoops are levitated, a line of slope 2 fits the data quite well. In the supported case the dependence on d is weaker, since Eqs. (6.1-2) consider only diffusion to the boundaries of the plasma, and not losses to internal obstacles. Using Eq. (6.2) with the levitated data, with distance converted to

cm in the bridge region, gives a value for D of 10^3 cm^2/sec. This is an average value representative of the confinement region, and thus is consistent with the value of 10^4 cm^2/sec obtained earlier for the scrape-off region and a $D \propto n^{-1}$ scaling law.

6.A.4. Plasma Flux to Wall

Striped collectors were used to determine the efficacy of the divertor in reducing plasma flux to the wall. As shown previously in Eq. (1.17), in a simple slab model the plasma flux reaching the wall is expected to vary with the position of the divertor separatrix as $\Gamma_{wall} = \Gamma_o e^{-w/\lambda}$, where Γ_o is the flux crossing the divertor separatrix, w is the distance from the divertor separatrix to the wall, and λ is the density scale length in the scrape-off region. For a quantitative plot of this relationship, a collector on the edge of the outer nose was chosen as the best representative, since this is the portion of the wall which projects farthest into the plasma in ψ-space, and in the absence of the divertor most of the plasma loss to the wall is found to occur at the noses. As the divertor current is varied the flux crossing the divertor separatrix does not remain constant, but can be estimated as proportional to n_o/τ, where n_o is the density at ψ_{sep} and τ is the measured lifetime (if support losses are ignored). At each value of divertor current, if the striped collector's signal is divided by n_o/τ, a quantity proportional to the ratio of plasma reaching the wall to plasma crossing the divertor separatrix is obtained.

Figure 6.6 shows semi-log plots of the outer nose collector current divided by n_o/τ, in arbitrary units, as a function of the position of the divertor separatrix. In Figure 6.6(a), small gun data with the octupole hoops both supported and levitated are virtually identical, showing that plasma loss in the scrape-off region is indeed dominated by the divertor rather than by hoop supports, justifying the validity of taking most data in the supported mode. The value of λ obtained from the plot is .77 Dories, or about 1.5 cm in the bridge region, as compared to the value of 1.1 cm obtained from the ion saturation current profiles discussed above. Figure 6.6(b) shows similar data for the large gun plasma. The value of λ here is .46 Dories, or about .9 cm, as compared to the value of .6 cm estimated from the ion saturation current profiles near ψ_{crit}. In both cases the scale length obtained from the profiles is shorter by about the same factor; this could be due to cooling of the plasma in the scrape-off region.

As the divertor current is raised and the plasma flux to the wall is diminished, the plasma flux to the divertor region increases. Various objects intercept the plasma, including the divertor hoops, their supports, and the wall behind the hoops, since some of the diverted field lines soak into the wall, as was seen in Chapter 3.B. Figure 6.7 shows flux to a collector mounted behind the divertor hoops, plotted in the same way as in Figure 6.6 The outermost diverted field lines penetrate the wall here due to soak-in, so plasma on these field lines will reach this collector. The flux to the collector

rises by a factor of 20 before saturating when ψ_d crosses ψ_{sep}, though the rate at which it rises is not a simple function of the divertor current, since the position of the collector in ψ-space changes. Rotated about the major axis to form an axisymmetric strip, this collector would account for only about 1% of the plasma loss. Evidently most of the diverted plasma is lost by striking the divertor hoops before diffusing as far as the field lines intersecting this collector, as expected, but this measurement does show that there is a large increase in plasma flux to the divertor region while the wall flux is being reduced everywhere else.

6.A.5. Fluctuations

It would be highly undesirable if the presence of a divertor created instabilities in the plasma, leading to enhanced transport in the divertor region. No evidence of this appears in the data discussed above, but as a check, the fluctuations in the ion saturation current signal were examined. The divertor is found to actually suppress fluctuations in the region outside the octupole separatrix. This could be due to the average-minimum-B stabilizing effect of the additional magnetic separatrix, or perhaps more likely due to the short-circuiting of fluctuating electric fields on magnetic field lines which intersect the divertor hoops. Figure 6.8 shows amplitude and frequency of fluctuations at 8 cm from the lower outer octupole hoop, as a function of divertor current. The amplitude drops from

about 4% to 1%, reaching the lower value at the point where the probe begins to fall within the scrape-off zone. There appears to be no systematic change in the frequency of the fluctuations, and so probably no change in their fundamental character.

These observations indicate that the octupole poloidal magnetic divertor operates in a manner identical to that envisioned for a similar divertor in a tokamak.

6.B. Divertor with Applied E×B Drift

The divertor's performance as a conventional magnetic divertor having been characterized, a radial electric field was added to create an E×B drift with poloidal component, and its effects on the quantities discussed in the preceding section were examined. The divertor current was fixed for this part of the experiment at a normalized value of .1, providing a divertor separatrix at $\psi_d = 6.6$, about midway between ψ_{sep} and ψ_{crit}.

6.B.1. Electric Field

There are a number of possible ways to apply the electric field The simplest and "cleanest" would probably be to bias one of the octupole hoops, as in the biased fin experiment (Chapter 5.B), but with the resulting E×B drift now having a large poloidal component due to the large toroidal magnetic field. This was not done, however,

in the spirit of simulating a tokamak, which has no such electrode conveniently embedded in the plasma.

Another possibility was to bias the outer divertor hoop positive and the inner divertor hoop negative with respect to the vacuum tank wall, to try to simulate the segmented, biased walls of Figure 2.1, creating an E×B drift toward the divertor from both sides. When this was tried, however, it was found that, due to the much larger mobility of electrons parallel to magnetic field lines, the ψ surfaces in contact with the two hoops took on a potential near that of the positively biased hoop, rather than having a potential distribution antisymmetric across the minor axis of the divertor. Since the octupole hoops, which form the opposite boundary for the plasma, were electrically floating, the interior of the plasma also assumed this positive potential.

Consequently, the configuration chosen for most study was one in which the middle divertor hoop is biased positive and the two other divertor hoops are gounded. Since the divertor separatrix intersects the middle hoop, the interior of the plasma is again raised to the positive potential, and now the electric field region extends from the divertor separatrix to the wall. A typical floating potential profile for this case is shown in Figure 6.9(a), along with a profile for the case without bias. The electric field in the interior of the plasma is the same for both cases, and the large electric field in the case with the divertor hoop biased appears in the scrape-off region, as desired. This imparts a drift to the outer layer of plasma, causing

it to travel poloidally to the divertor, as shown schematically in Figure 6.9(b). This configuration then resembles most closely the segmented, biased neutralizer plate mentioned in Chapter 2.A, or Braginskii's segmented, biased limiter mentioned in Chapter 2.B.

Since the electric field does not penetrate into the central plasma, it is expected to have very little effect on confinement. Particle lifetimes measured with the Fabry-Perot microwave interferometer, as shown in Figure 6.10, have a slight downward trend as the electric field is increased. However, the change is only about 10% at a bias of 100 V, which is much larger than is required to make significant changes in the scrape-off region, as will be seen.

6.B.2. Density Profiles

The density profile, as measured by a floating double probe, shows a noticeable decrease in scale length in the scrape-off region when the electric field is applied, while remaining unchanged in the confinement region, as seen in Figure 6.11. To eliminate the possibility that this is simply due to particles being accelerated parallel to magnetic field lines by the electric field, the measurement was repeated with no toroidal field. In this case the E×B drift has no poloidal component, while effects due to parallel motion should be enhanced due to the shorter path length along field lines to the divertor. As seen in Figure 6.12, the scale length is unchanged by application of the electric field. The results are summarized in Figure 6.13, which shows the scale length (calculated between 6 and 9 cm from the hoop) as a function of time. At all times the electric field reduces the

scale length in the presence of B_t, but not when $B_t = 0$, indicating that the reduction is due to the $E \times B_t$ drift. In the absence of electric field, the smaller scale length when $B_t = 0$ is consistent with the shorter path length to the divertor. The distance particles must travel parallel to field lines to go once around poloidally (and reach the divertor) is

$$L_{11} = \oint B \frac{d\ell}{B_p} \tag{6.3}$$

where $d\ell$ is an element of distance in the poloidal direction. When $B_t = 0$, this is just

$$L_{11} = \oint d\ell = 4.8 \text{ m} \tag{6.4}$$

When $B_t = B_{to}R_o/R >> B_p$, the integral becomes

$$L_{11} \simeq B_{to}R_o \oint \frac{d\ell}{RB_p} + (2B_{to}^2R_o^2)^{-1} \oint R^2B_p^2 d\ell = 8.0 \text{ m} \tag{6.5}$$

where the integrals are evaluated at $\psi = 7$ Dories, using tabulated values[10] and the present ratio of B_t to B_p. Other things being equal, the density scale length in the scrape-off region varies as $L_{11}^{\frac{1}{2}}$, predicting a ratio of scale lengths between the two cases of 1.3, while the observed ratio varies between 1.3 and 1.6. From Eq. (6.5), if $T_i = 20$ eV and the flow is at half the ion acoustic speed, the average time for a particle to reach the divertor by parallel flow

is .18 msec.

In the presence of a toroidal magnetic field, the expression analogous to Eq. (4.24) for the poloidal rotation frequency due to E×B drift is

$$f_P = \frac{d\phi}{d\psi}\left[\frac{B_{to}R_o}{2\pi}\oint\frac{d\ell}{R^2B_p} + (2\pi B_{to}R_o)^{-1}\oint B_p d\ell\right]^{-1} = .81\,\frac{d\phi}{d\psi} \qquad (6.6)$$

evaluated at $\psi = 7$ with the present ratio of B_t to B_p. Note that when $B_t >> B_p$, an approximate expression is $f_P \approx q^{-1}d\phi/d\psi$, where q is the "safety factor." From the profile of Figure 6.9, the maximum electric field in the scrape-off region is given by $d\phi/d\psi = (70\ \text{sec}^{-1}\text{V}^{-1})\ V_{hoop}$. The time for half a poloidal rotation at $V_{hoop} = 20$ Volts is then about .44 msec. The constant electric field model of Chapter 2.D predicts a reduction of the density scale length due to the E×B drift by a factor $(1 + \tau_{11}/\tau_E)^{-\frac{1}{2}}$, as stated in Eq. (2.17). In the present case this predicts a reduction of λ by a factor of .85 for a 20 Volt bias, and .75 for a 40 V bias, which are reasonably close to the values seen in Figure 6.13.

Chapter 2.D also presented a model in which the electric field was inversely proportional to the density. This was observed to be the case in the experiment of Chapter 4 where the octupole hoop was biased, but may not hold here where field lines intersect conducting obstacles. Nevertheless, the scrape-off region of the profiles in Figure 6.11 resembles at least qualitatively those predicted by the $E \propto n^{-1}$ model (see Figure 2.5) in that the reduction in density and scale length is

much sharper near the wall than elsewhere, particularly for the larger electric field. If this model is more nearly correct, it would account for the fact that there is very little change in scale length between the 20 V and 40 V cases, especially at later times when T_i has decreased and the E×B divertor action becomes more dominant.

6.B.3. Plasma Flux to the Wall

Striped collectors were again used to measure the plasma flux reaching the wall as the electric field was varied. The constant electric field model predicts that the E×B drift will reduce the flux to the wall by a factor

$$\frac{\Gamma_w(E)}{\Gamma_w(0)} = e^{-w(\lambda'^{-1} - \lambda^{-1})} \tag{6.7}$$

where w is the distance from the divertor separatrix to the wall, λ is the density scale length without applied electric field, and $\lambda' = \lambda(1 + \tau_{11}/\tau_E)^{-\frac{1}{2}}$. In the low electric field limit, $\tau_E >> \tau_{11}$, this becomes

$$\frac{\Gamma_w(E)}{\Gamma_w(0)} \approx \exp[-\frac{w\tau_{11}}{\lambda 2\tau_E}] \approx \exp[-\frac{V_{hoop}}{25\ V}] \tag{6.8}$$

This agrees reasonably well with the semilog plot of collector current vs. hoop bias voltage shown in Fig. 6.14(a), which is linear, as predicted, with a slope of about 17 V for both supported and levitated

cases. The plasma flux to the wall decreases by about a factor of 5 to 6 before leveling off. In the constant electric field model above, in the large electric field limit, $\tau_E << \tau_{11}$, the dependence changes to

$$\frac{\Gamma_w(E)}{\Gamma_w(0)} = \exp[-\frac{w}{\lambda}(\frac{\tau_{11}}{\tau_E})^{\frac{1}{2}}] \qquad (6.9)$$

and the weaker dependence on E could account for the leveling off. The transition is expected to occur when $\tau_E \sim \tau_{11}$, at about $V_{hoop} = 40$ V in the present case, which agrees with the observation. This leveling off is predicted even more strongly by the model using $E \propto n^{-1}$ (see Figure 2.4). Collectors in other locations away from the divertor show similar behavior.[11]

To check that this result is due to E×B drift rather than acceleration by the electric field parallel to magnetic field lines, the measurement was repeated with no B_t. Again, this should eliminate the poloidal component of E×B drift while shortening the path for parallel motion. As shown in Figure 6.14(a) there is no systematic reduction of plasma flux to the collector in this case.

Plasma flux to the upper lid collector behind the divertor at first increases with the hoop bias, with a characteristic voltage comparable to that of the decrease in flux to other parts of the wall, showing that plasma is being brought to the divertor. At higher bias voltages the collector signal decreases again; presumably this is because of the fact that as λ' becomes shorter, more of the plasma is removed near the divertor separatrix, and consequently is lost to the divertor hoops

before reaching the wall surface behind the hoops.

As mentioned in Chapter 3.C.5, it was considered less perturbing to the plasma to allow the collector and its measuring circuit to float electrically rather than holding the average potential of the two sets of stripes at ground potential. The large electric fields and large flows of plasma parallel to magnetic field lines make this a much less benign environment than that in which Cavallo's testing of the collectors was done.[12] Consequently, the validity of these collector measurements in the presence of the hoop bias may be open to some question. It is observed that with the hoop bias at 20 V the outer wall collector circuit floats at +1.5 V, which could produce the results of Figure 6.14(a) by repulsion of ions if T_i were low enough at the wall. However, similar measurements made with the average potential of the collector stripes at ground show an ion current very similar in magnitude and time dependence to the current measured with the collector floating, and again show a decrease in ion current as the hoop voltage is raised. The decrease was not as great at that seen with the collector floating, but in this case it evidently cannot be attributed to repulsion of ions. As mentioned in Chapter 3.C.5, grounding the center of the collector circuit is not necessarily the correct way to make the measurement either. However, the similarity of the two measurements lends credence to the conclusion of an actual reduction of ion flux to the wall, as does the absence of the effect in the absence of B_t.

6.B.4. Plasma Flow Velocity

In order to obtain more direct evidence for the effect of the applied electric field on plasma transport to the divertor, it was desired to measure the directed flow velocity of the plasma. Localized measurements were made with a paddle probe, as described in Chapter 3.C.2. By taking data with the probe in two orientations rotated 90° with respect to each other, the two components of the velocity parallel to the wall were obtained: the θ (toroidal) component and, to the extent that field lines at the point of measurement are parallel to the wall, the χ (poloidal) component. Ion saturation current to the two sides of the probe was measured, and Eq. (3.16) was used to obtain the two components of $\vec{v}/c_s$, under the assumption that $T_i > T_e$. Spot checks made by rotating the probe through 360° at small intervals confirmed the validity of the more abbreviated measurement.

Figure 6.15 shows profiles of velocity vectors obtained in this way at the lower outer octupole hoop, for three cases. Note that the coordinate system has been rotated to make the direction of B_p upward, although in the octupole it points downward at the outer wall. Therefore the shorter poloidal distance from the probe to the divertor is upward in the machine but downward in the figure. Also shown for reference are profiles of the ion saturation current obtained by averaging the four measurement quadrants. The reductions of scale length by addition of the magnetic divertor and then addition of the E×B drift can be seen.

The case without divertor is dominated by a velocity at about 45° to $\vec{B}$, and increasing with the density gradient. The ion diamagnetic drift, which is always present when a density gradient exists, is given by $-\nabla p_i \times \vec{B}/B^2$. The perpendicular component of the observed ion fluid velocity has the right sign, and the observed magnitude (1.4×10^6 cm/sec assuming T_i = 20 eV) is consistent with the calculated magnitude of the diamagnetic drift (2×10^6 cm/sec if T_i = 20 eV). The E×B drift due to the ambipolar electric field has the same direction, but is about a factor of 5 smaller in magnitude. The parallel component of the observed fluid velocity is not as easy to explain, but as mentioned in Chapter 4.A.2, E×B drifts through regions of varying magnetic field strength give rise to parallel flows which tend to equalize pressure on a magnetic flux surface. This could be the origin of the parallel velocity component seen here, since the sign is such as to make the net flow more nearly toroidal so that it does not pass through regions of varying field strength; the magnitude of the parallel component, however, is larger than might be expected.

The effects of adding the magnetic divertor and the E×B drift are perhaps better seen in Figure 6.16, which shows the results of subtracting velocity vectors to obtain the increments due to these two changes. Also, if the random flux to the two faces of the probe results in a spurious contribution to the velocity due to asymmetries between the two faces, this subtraction removes it to first order.

The addition of the magnetic divertor results in a small velocity increment ($\lesssim .2\ c_s$) essentially parallel to $\vec{B}$ in the

scrape-off zone. The magnitude is small since this is close to the point poloidally opposite the divertor, where the parallel velocity would be expected to go to zero. Addition of the applied electric field gives rise to a large ($\lesssim c_s$) velocity increment, mainly perpendicular to $\vec{B}$, which is largest near ψ_{crit} where E is largest; the magnitude and direction are consistent with the E×B drift due to the applied electric field. There is also a parallel component to this increment which tends to keep the poloidal component smaller, as discussed above.

Figure 6.17 shows the corresponding density and ion flow velocity vector profiles between the upper inner octupole hoop and the lid; this location is about 20 cm from the divertor on the side upstream relative to the applied E×B drift. Here the density takes a sudden drop at ψ_{crit} with the divertor off and at ψ_d with the divertor on, and the density seems to be lower on diverted field lines than at the lower outer hoop. This can be compared to the one-dimensional model of a divertor in Chapter 1.B.2, which predicts the density to drop by a factor of $e^{-\frac{1}{2}} = .61$ along diverted field lines. From this figure and Figure 6.18, which shows the incremental velocity vectors, it can be seen that the flow to the magnetic divertor is mainly parallel and rises quickly outside the divertor separatrix to about .6 c_s, in reasonable agreement with the theoretical prediction of c_s and the values measured in other experiments[4,5] of .3 to .5 c_s. Addition of the electric field results in no new poloidal component of velocity (except very close to the lid). This probably occurs because, as the

perpendicular component increases with the E×B drift, the parallel component decreases due to repulsion of ions by the positively biased hoop. The repulsion of ions by the parallel component of electric field does not mean that the divertor no longer removes ions, as seen by the fact that the poloidal component of ion flow is not diminished. Although ions can no longer go to the middle divertor hoop, the E×B drift in the vicinity of the hoop tends to circulate plasma around it, bringing ions to field lines which intersect the other two divertor hoops or the lid, leading to their rapid loss. On the outermost field lines, closest to the lid, the poloidal component of ion flow is increased by the hoop bias, due to both E×B drift and the parallel component of the electric field, but the density is very low here.

It can be concluded that near the divertor, parallel flow plays an important role even in the case with applied E×B drift, due to the parallel component of the electric field. However, far away from the divertor the E×B drift is a significant factor in the rate at which plasma goes to the divertor, increasing the poloidal component of flow by a factor of 2 or more.

6.B.5. Fluctuations

In order to check that the applied electric field and accompanying velocity shear do not introduce any damaging instabilities, fluctuations in density (ion saturation current) were examined with a probe 8 cm from the lower outer octupole hoop. This position is near the middle

of the scrape-off zone, at a region of substantial E×B velocity magnitude and shear (see the potential profile of Figure 6.9 and the measured velocity profile of Figure 6.15).

As shown in Figure 6.19(a), the relative amplitude of the fluctuations is essentially constant as a function of the applied electric field. The frequency was estimated from oscilloscope traces; in all cases there was a dominant frequency component in the 10-20 kHz range, and in some cases a second component at three times the frequency could be discerned. These are plotted in Figure 6.19(b). Both frequencies increase linearly with electric field, consistent with a Doppler shift. In fact, it can be seen by comparing Figures 6.15(b) and (c) that a 20 V bias increases the fluid velocity at this point by about a factor of 1.5 over the case without bias, and the frequency of the flucutations shows the same increase, which is consistent with the phase velocity of the waves being the same as the ion fluid velocity. The electric field cannot easily be reversed, since when the hoop is biased negative the plasma tends to remain near ground potential. However, both frequency components can be extrapolated to zero frequency at a bias of about -50 V. From the profile of Figure 6.9(a), the extrapolated E×B drift speed at -50 V is about -10 V/cm/500 G = -2×10^6 cm/sec, so the phase velocity of the waves with no applied electric field must be 2×10^6 cm/sec. As noted before, this is the calculated magnitude and direction of the ion diamagnetic drift. This gives wavelengths perpendicular to B of about 250 cm and 80 cm for the two frequency components. All these

observations are consistent with the mode identified by Drake as a collisionless trapped ion instability.[2]

Since the amplitude of the fluctuations does not increase, and the change in frequency is consistent with a Doppler shift of existing waves, it seems safe to conclude that application of the electric field does not give rise to any new instabilities.

6.B.6. Temperature

It was predicted in Chapters 1.B.2 and 2.A that a magnetic divertor should have a cooling effect on the electrons, while an E×B divertor should not. To check this, the electron temperature was determined from I-V characteristics of two single-tip probes, one at the octupole separatrix (5 cm from the lower outer octupole hoop) and the other in the middle of the scrape-off region (8 cm from the lower outer hoop), for three cases.

The scrape-off zone (8 cm) measurements are shown in Figure 6.20. T_e at the separatrix is not plotted, being the same for all three cases and about the same as the 8 cm data without the divertor shown here. After an initial decay, T_e in the scrape-off zone flattens out at about 4 eV with the divertor off, but at about 2 eV with the divertor on. If the electrons leaving the central plasma have an average energy of $(3/2)kT_{eo}$ each and electrons lost to the divertor carry an average energy of $6kT_{el}$ each (see Chapter 2.A) then a simple energy balance dictates $T_{el} = T_{eo}/4$, as compared to the observed

values $T_{el} = T_{eo}/2$.

When the electric field is applied T_e returns almost to its original value. In Chapter 2.A it was pointed out that if plasma is taken to the divertor only by E×B drift there will be no cooling effect. However, in the present case the lack of cooling is more likely due to the positive bias on the divertor hoops which results in parallel acceleration of electrons rather than retardation, and hence no cooling.

Ion temperature was measured at the octupole separatrix with a skimmer probe, but the low density in the scrape-off region prevented a reliable measurement there. Figure 6.21 shows T_i at the octupole separatrix for the same three cases. The magnetic divertor causes no cooling, but there may be some cooling in the case with applied electric field. With a positive bias on the divertor hoop, the cooling could be due to the same mechanism which cools the electrons in a conventional divertor.

6.C. Summary

Operated without applied electric field, the divertor behaves as expected. The plasma density and density scale length are reduced in the scrape-off region due to the flow of plasma to the divertor, by an amount consistent with theory. Floating potential profiles suggest a non-ambipolar nature for the transport in the scrape-off zone. Although the divertor hoops act as a limiter even when not energized and

thus account for the loss of most of the plasma diffusing toward the wall, the plasma flux to the wall is further reduced by a factor of 5 to 10 when a current in the divertor widens the scrape-off zone, and the amount of reduction is consistent with theory. This is the desired "unload" function of the divertor, but a price is paid in decreased confinement time due to the narrowing of the confinement region. The fact that all the foregoing effects occur in a manner consistent with simple divertor theory indicates that there is no anomalous increase of perpendicular transport in the divertor's scrape-off zone, which would be undesirable; this is also supported by the observation that fluctuations are suppressed rather than enhanced in the scrape-off zone.

It proved possible to apply a radial electric field across the scrape-off zone, and restricted to it, thereby producing no deleterious effects on confinement of the central plasma. When the electric field is applied, the density and density scale length in the scrape-off zone are further reduced, by an amount consistent with theory. The plasma flux to the wall is also further reduced by a factor of 5, in reasonable agreement with theory. That these effects are due to E×B drift is demonstrated in two ways: by the absence of the effects in the absence of a poloidal component of E×B drift, and by direct measurements of ion flow velocity. The latter show that parallel flow and parallel electric fields are important in the vicinity of the divertor, but far away the E×B drift dominates. No new instabilities are introduced by the application of the electric field. Cooling of electrons in the scrape-off zone of a conventional divertor is

predicted and observed, but does not occur when the electric field is applied, in agreement with prediction.

REFERENCES - CHAPTER 6

1. J.R. Drake, D.W. Kerst, G.A. Navratil, R.S. Post, S. Ejima, R. LaHaye, C. Moeller, T. Ohkawa, P.I. Petersen, R. Prater, S.K. Wong, in Plasma Physics and Controlled Nuclear Fusion Research (Proc. 6th Conf., Berchtesgaden, 1976),(IAEA, Vienna, 1977), Vol. II, p. 333. Also University of Wisconsin PLP 688 (1976) and PLP 696 (1976).

2. J.R. Drake, University of Wisconsin PLP 697 (1976).

3. G.A. Navratil, R.S. Post, A. Butcher Ehrhardt, Phys. Fluids 22, 241 (1979).

4. H. Hsuan, M. Okabayaski, S. Ejima, Nuclear Fusion 15, 191 (1975).

5. H. Ohtsuka, et al., Plasma Phys. 20, 749 (1978).

6. J.R. Drake, J.G. Berryman, Phys. Fluids 20, 851 (1977).

7. A.H. Boozer, Phys. Fluids 19, 1210 (1976).

8. C.M. Strawitch, G.A. Emmert, Bull. Am. Phys. Soc. 23, 896 (1978). Also University of Wisconsin PLP 795 (1979).

9. F.F. Chen, Intro. to Plasma Physics (Plenum Press, N.Y., 1974), p. 142.

10. A. Butcher Ehrhardt, University of Wisconsin PLP 703 (1976).

11. E.J. Strait, Bull. Am. Phys. Soc. 23, 895 (1978). Also University of Wisconsin PLP 773 (1978).

12. A.J. Cavallo, University of Wisconsin Ph.D. Thesis (1975).

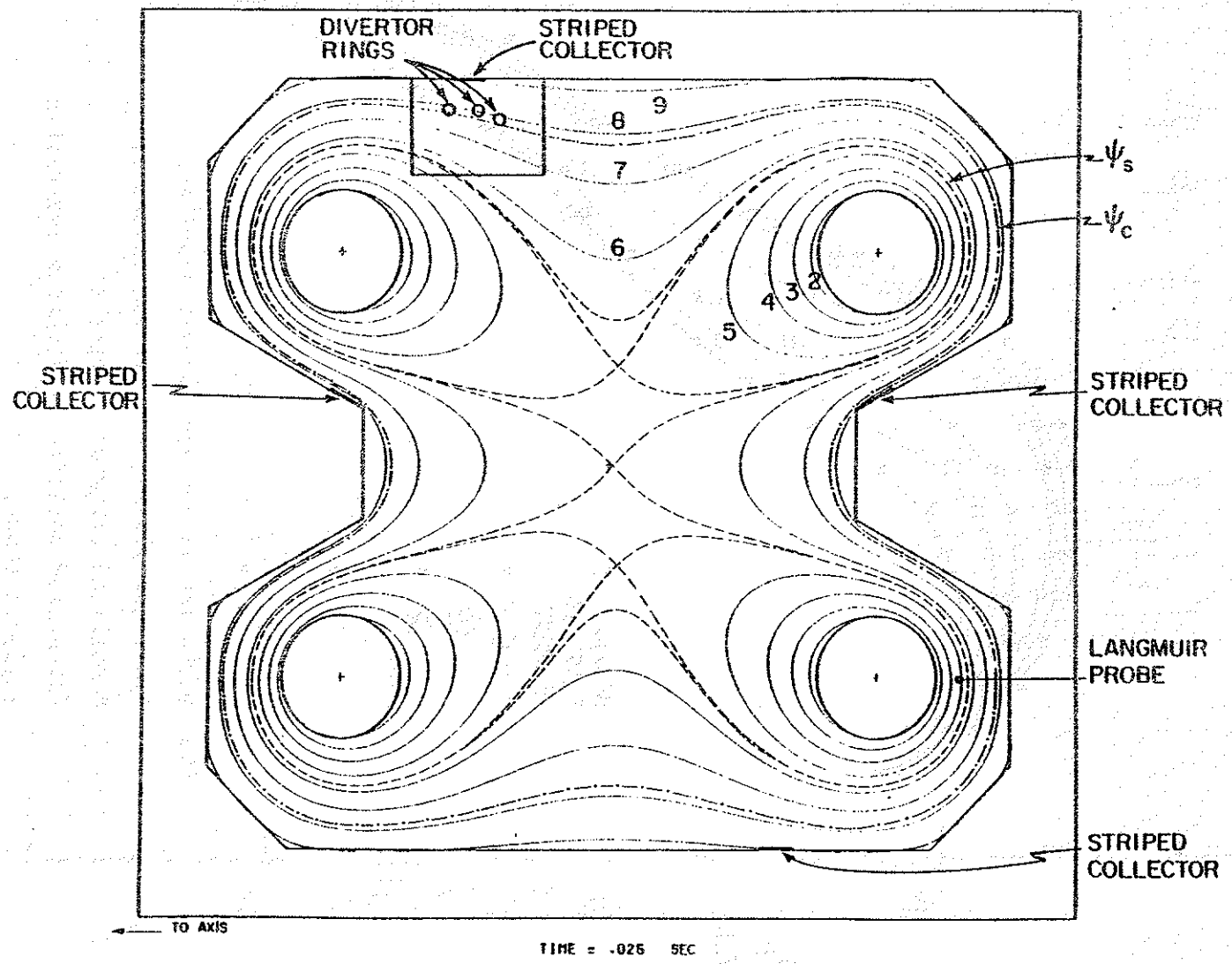

Fig. 6.1 - Minor cross-section of toroid, showing location of divertor hoops and diagnostics.

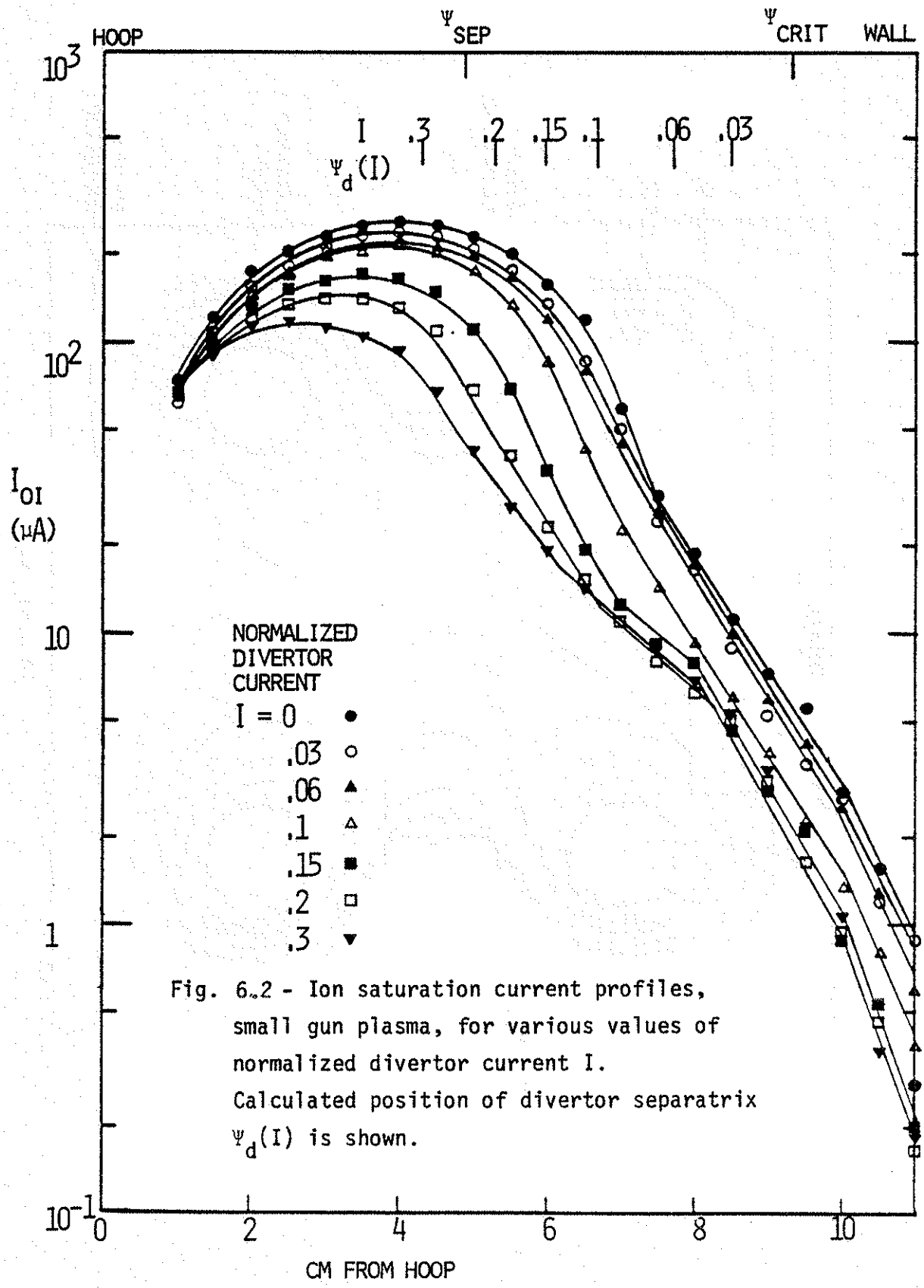

Fig. 6.2 - Ion saturation current profiles, small gun plasma, for various values of normalized divertor current I. Calculated position of divertor separatrix $\Psi_d(I)$ is shown.

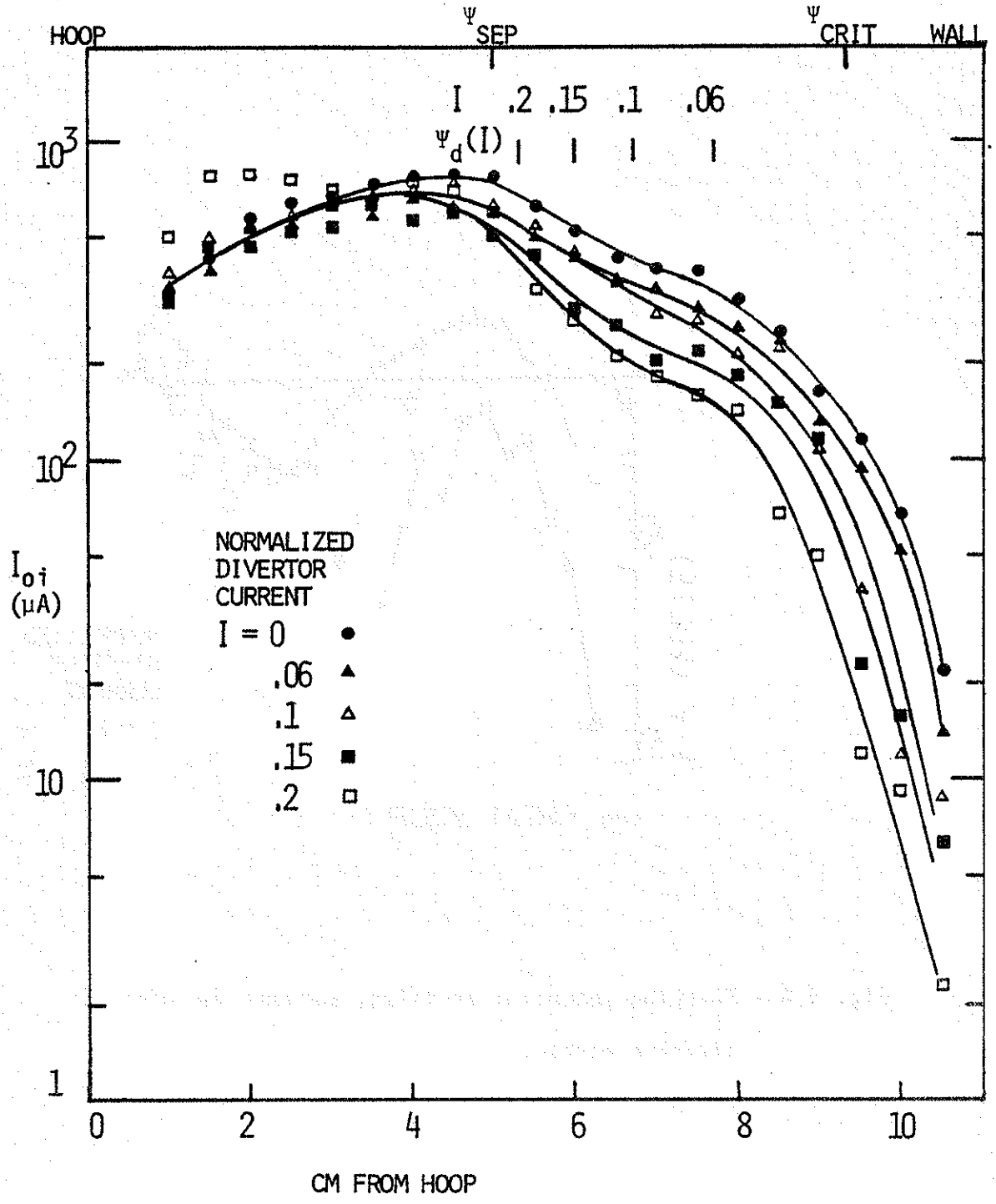

Fig. 6.3 - Ion saturation current profiles, large gun plasma, for various values of normalized divertor current I. Calculated position of divertor separatrix $\Psi_d(I)$ is shown.

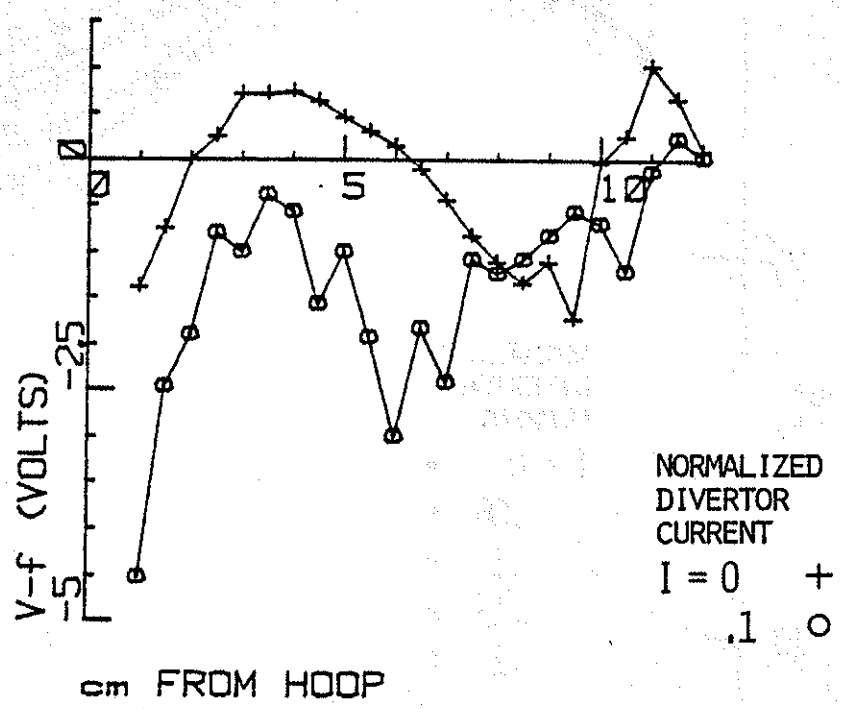

Fig. 6.4 - Floating potential profiles, without and with divertor current.

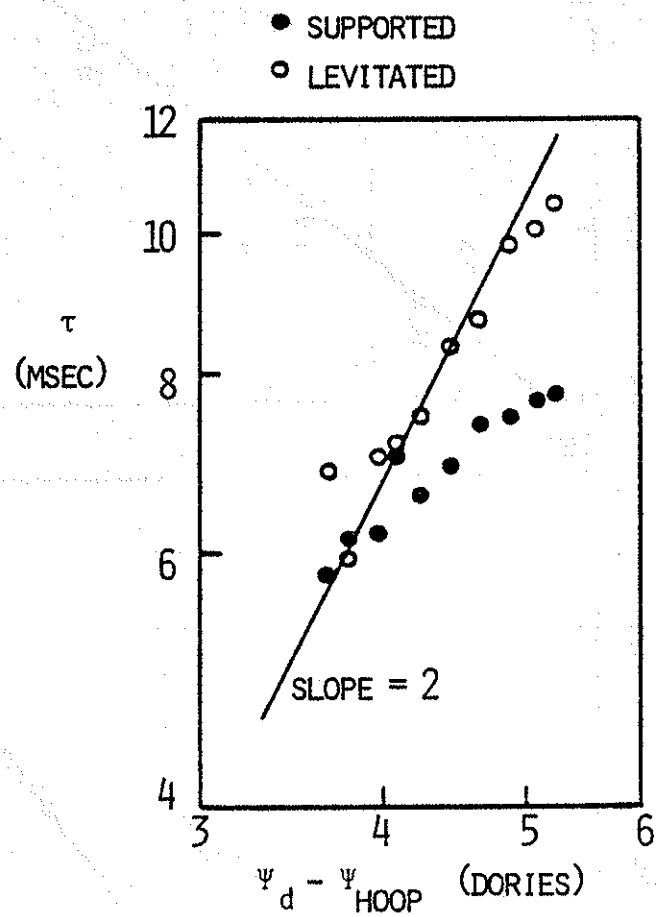

Fig. 6.5 - Particle confinement time (from Fabry-Perot microwave interferometer) vs. width of confinement region. (log-log plot)

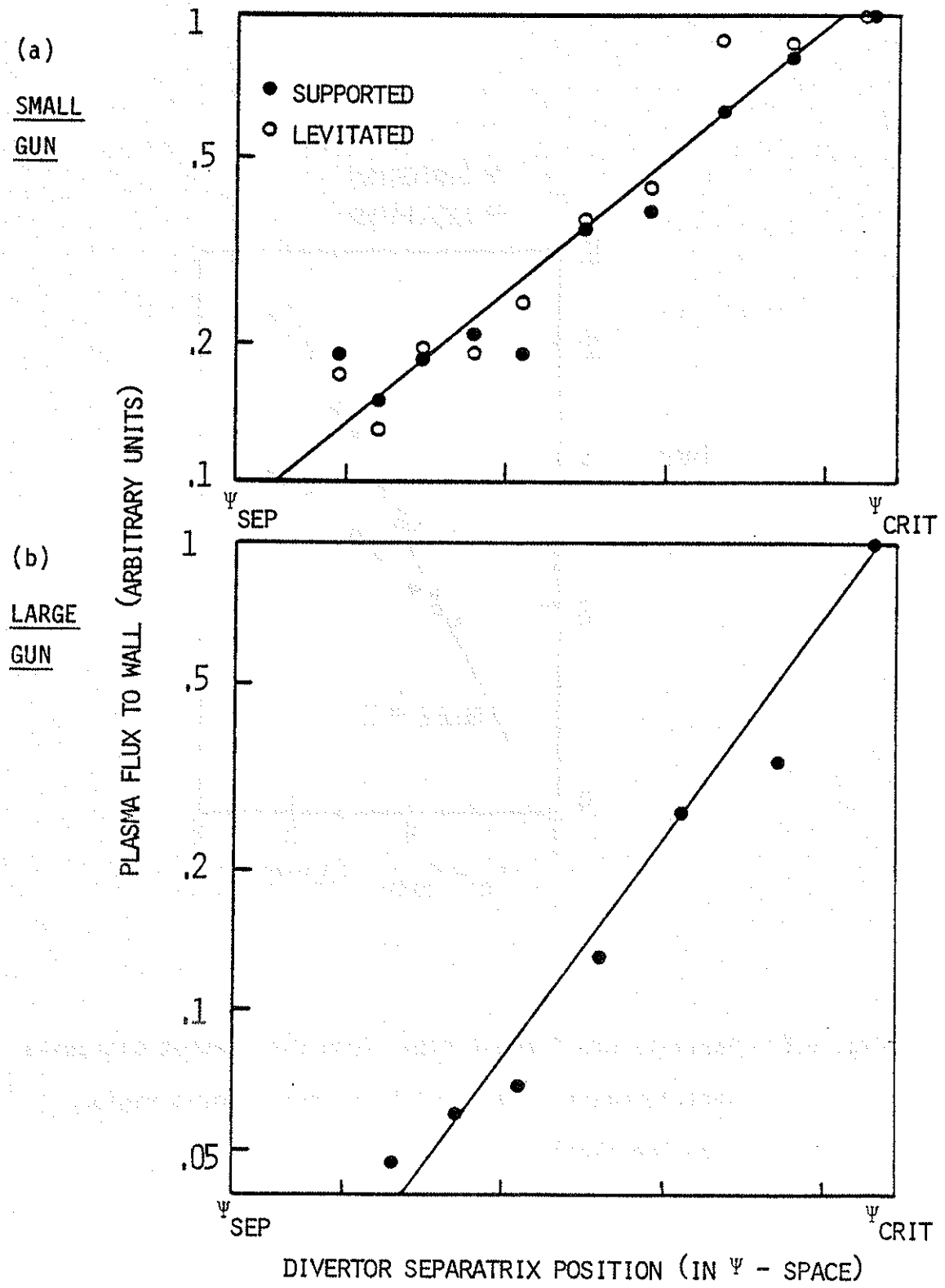

Fig. 6.6 - Plasma flux to wall vs. divertor scrape-off zone width.

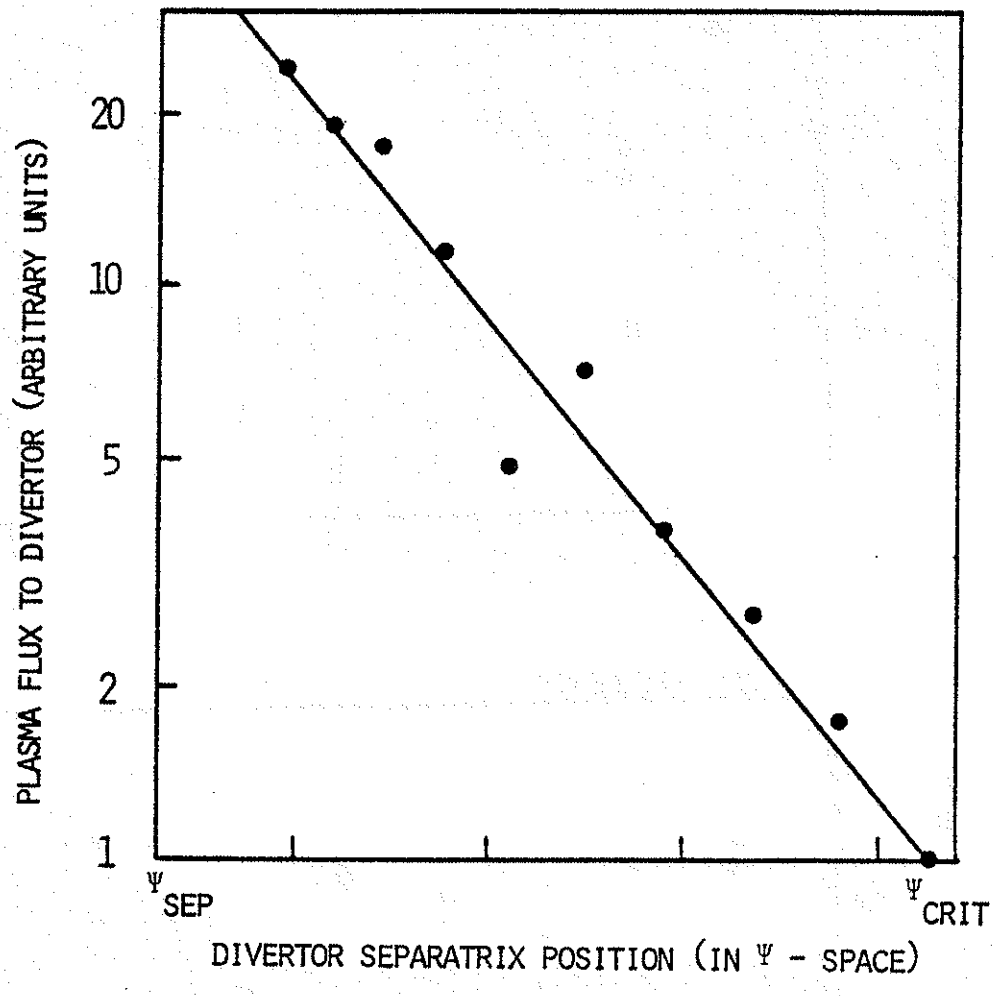

Fig. 6.7 - Plasma flux to divertor vs. width of divertor scrape-off zone.

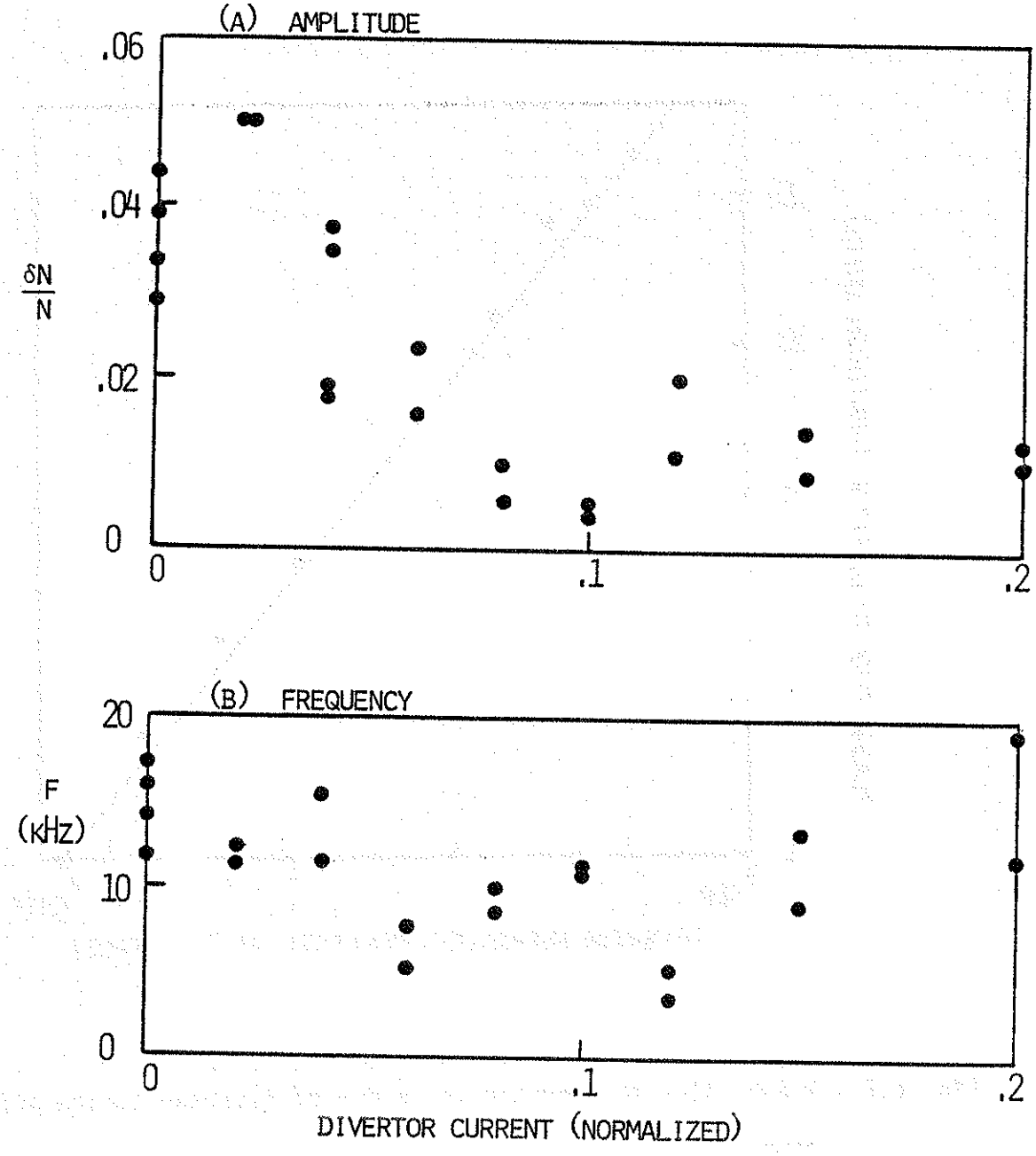

Fig. 6.8 - Ion saturation current fluctuations 8 cm from octupole hoop, vs. normalized divertor current: (a) relative amplitude, (b) frequency.

(a)

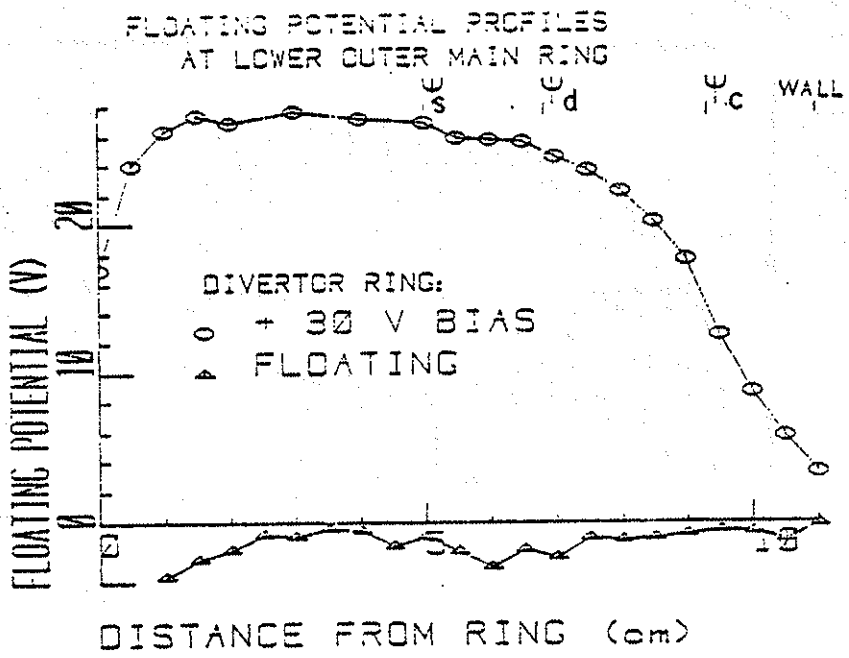

(b)

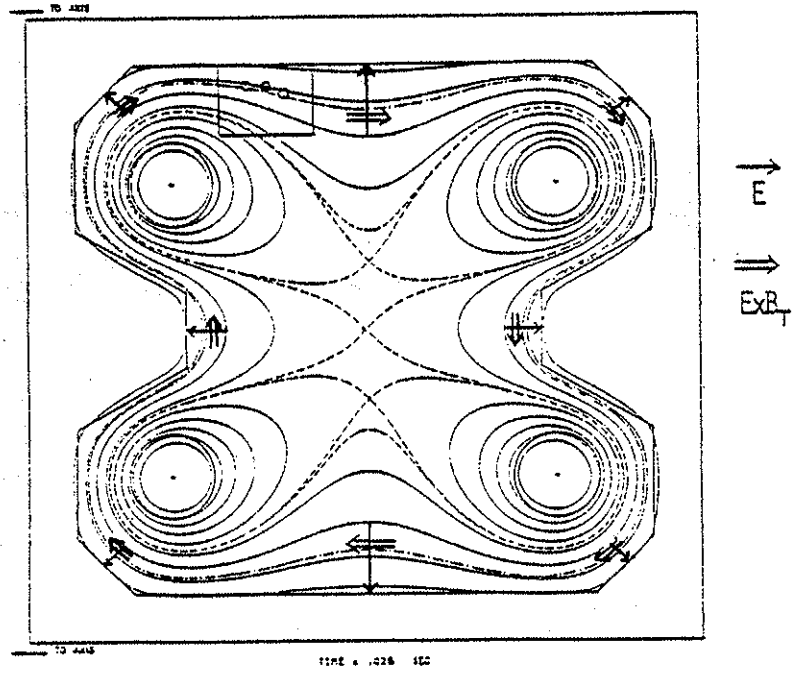

Fig. 6.9 - (a) Floating potential profiles without and with applied bias. (b) Radial electric field and resulting poloidal ExB drift in case with bias (schematic). Divertor current = 0.1

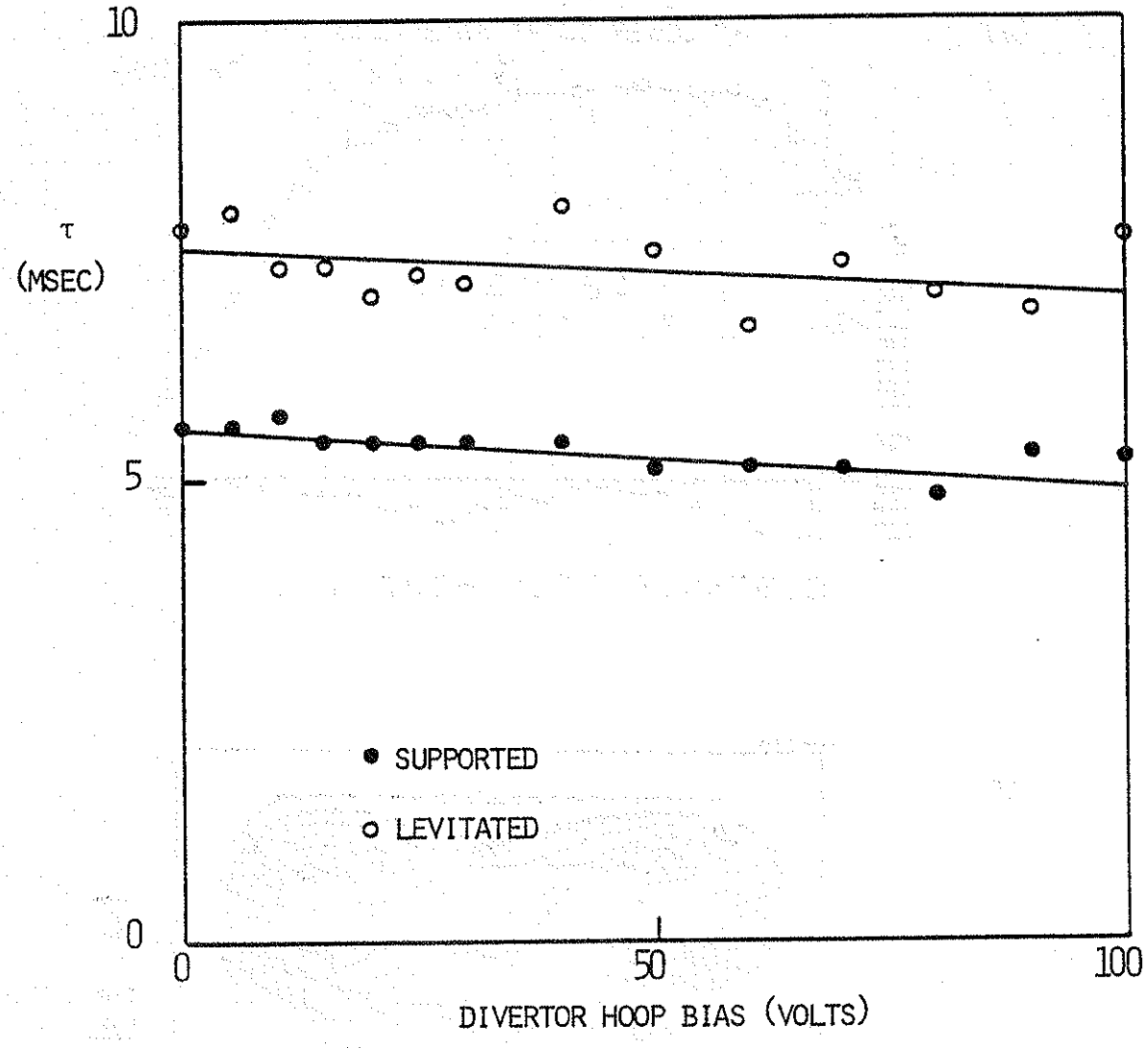

Fig. 6.10 - Particle confinement time (from Fabry-Perot microwave interferometer) vs. applied electric field.
Normalized divertor current = .1.

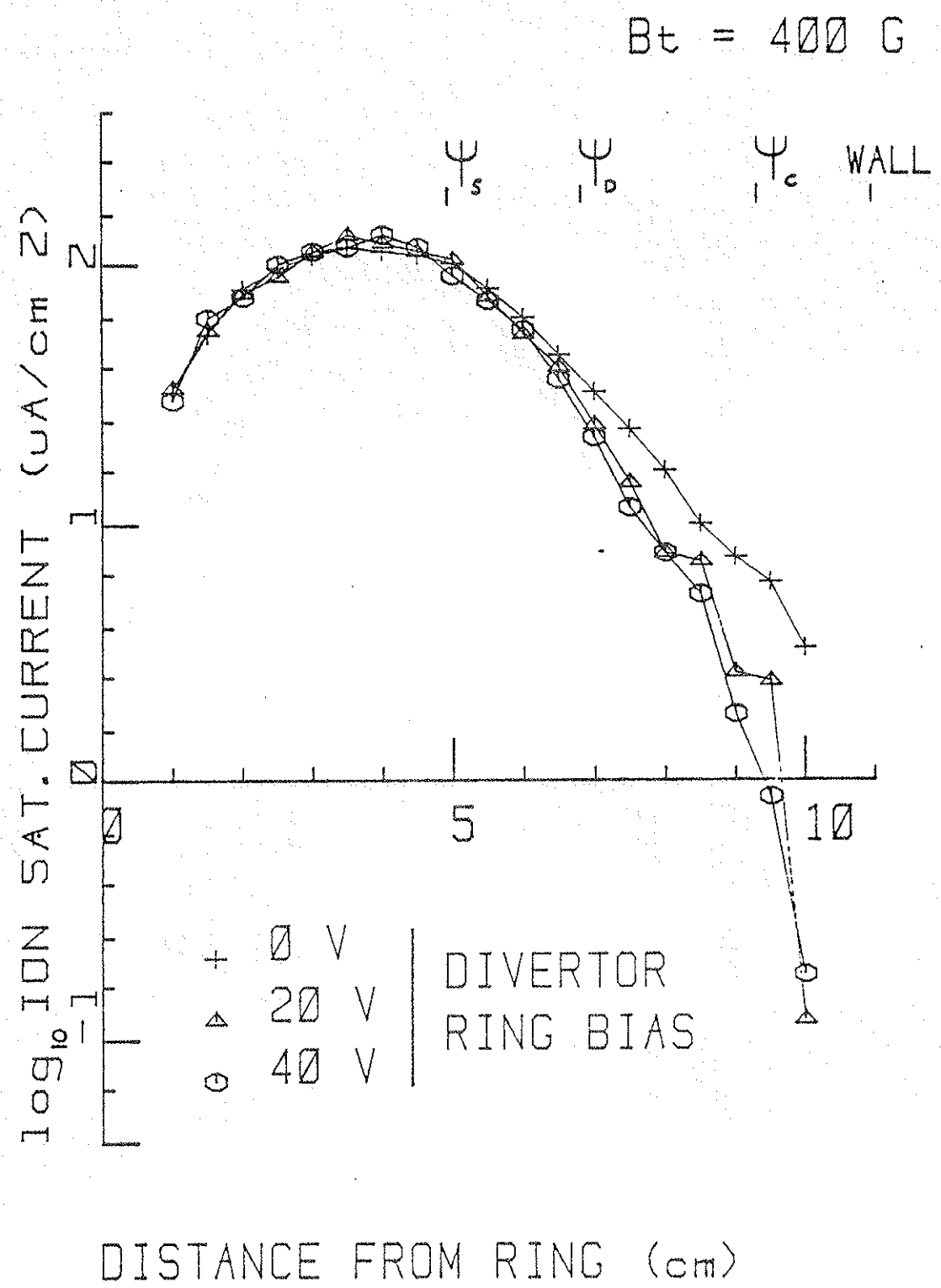

Fig. 6.11 - Ion saturation current profiles at lower outer octupole hoop, for various values of applied electric field. B_t = 400 G.

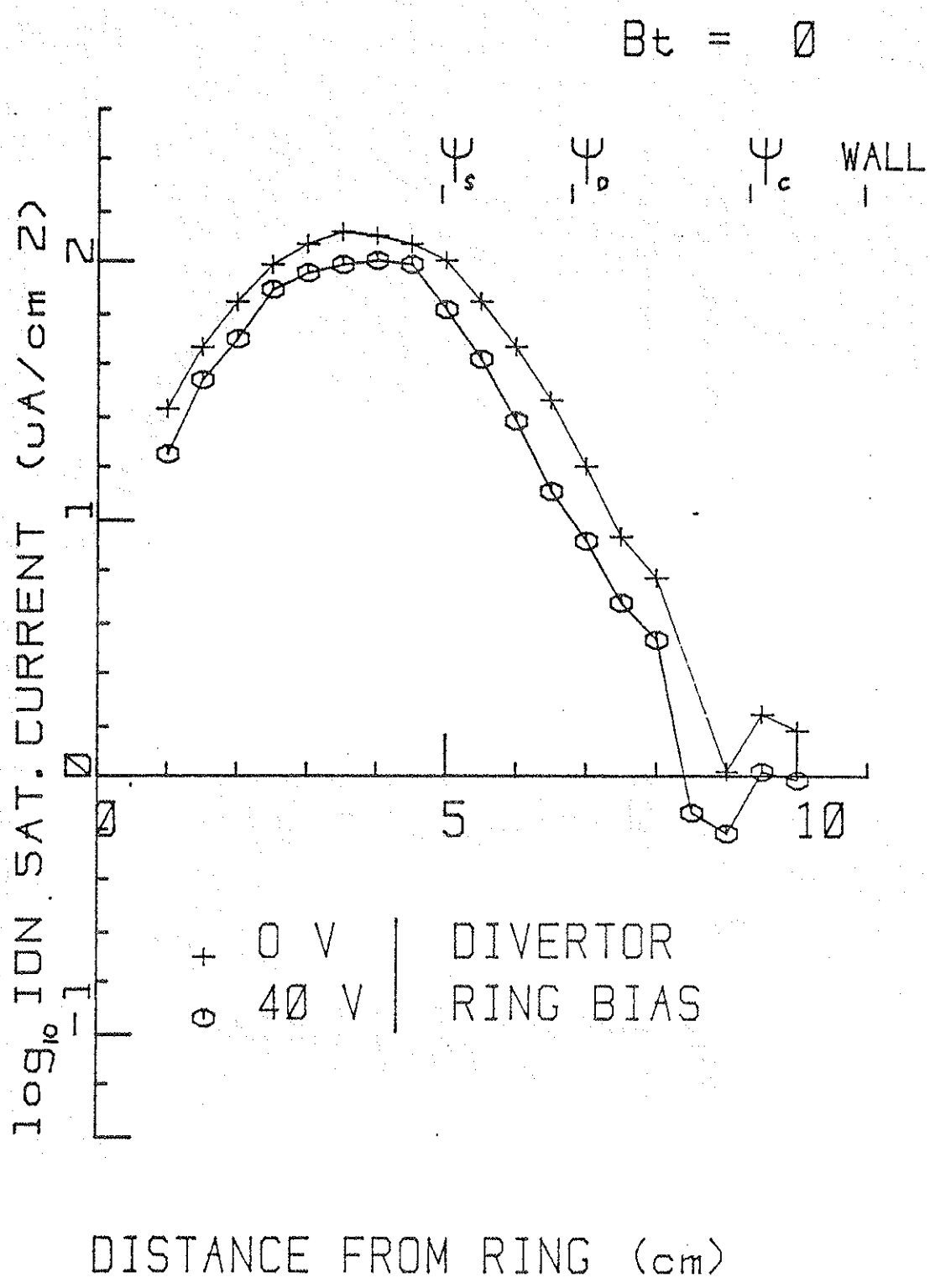

Fig. 6.12 - Ion saturation current profiles at lower outer octupole hoop, without and with applied electric field. $B_t = 0$

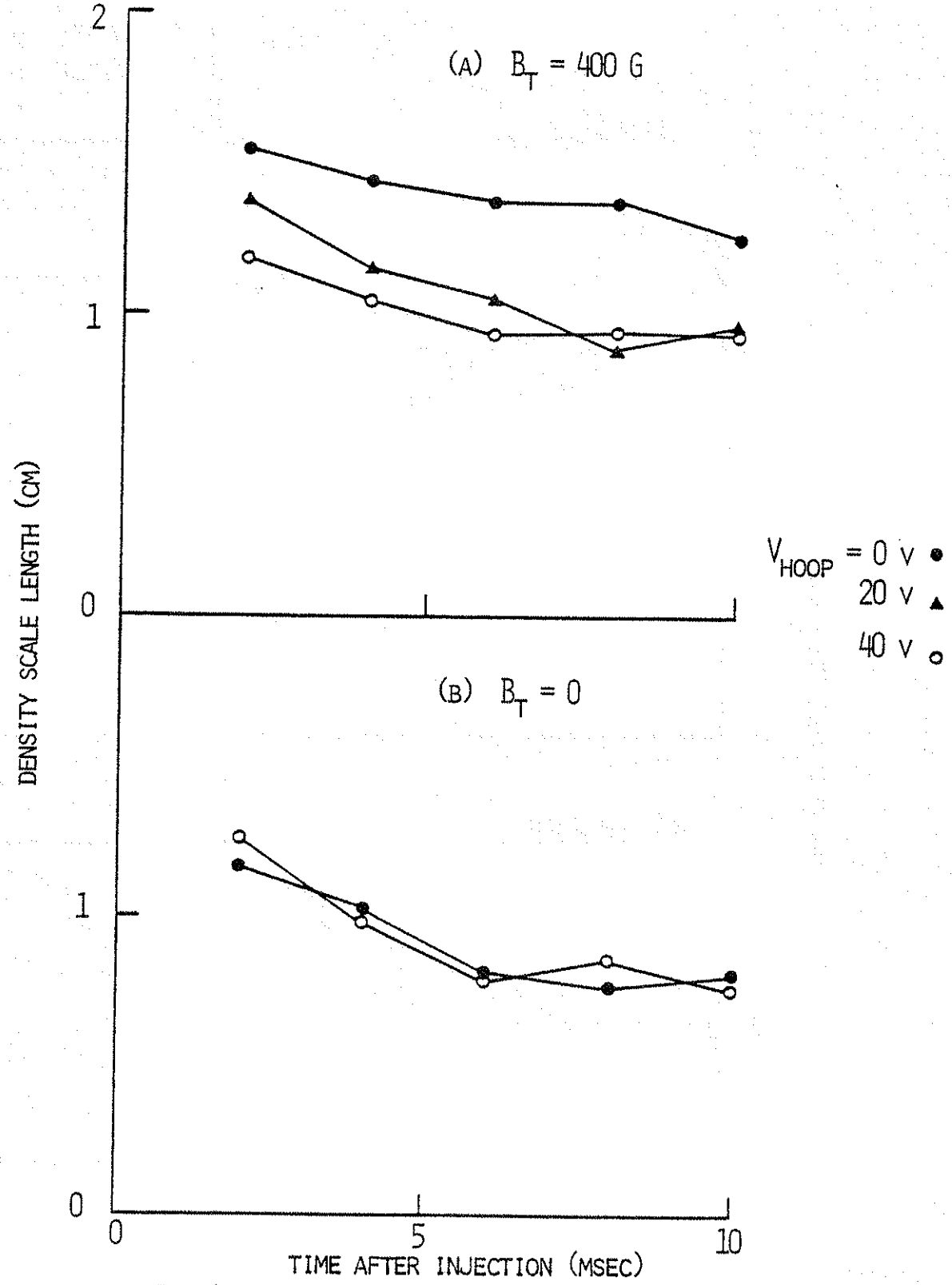

Fig. 6.13 - Density scale length in scrape-off zone vs. time.

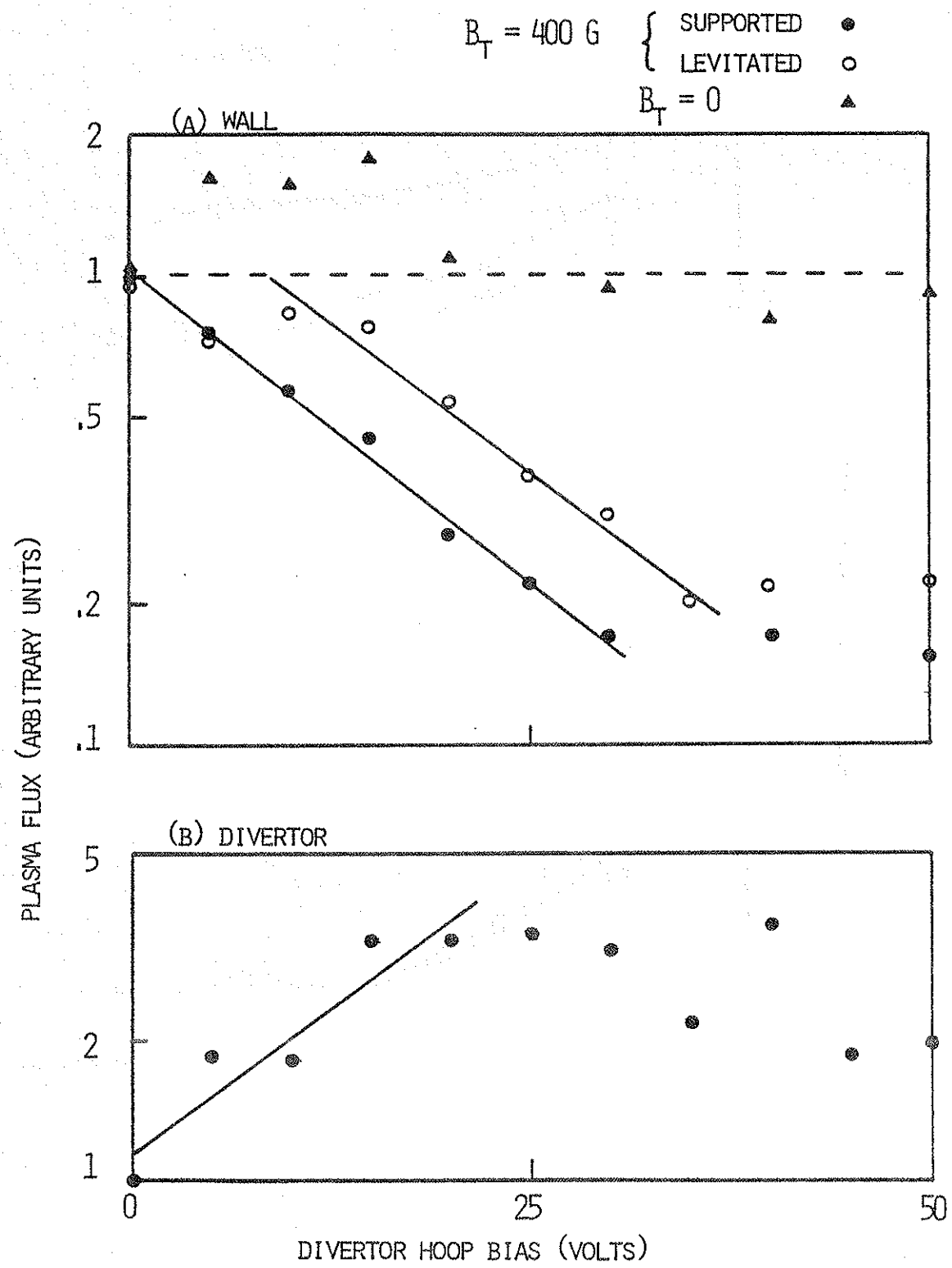

Fig. 6.14 - Plasma flux vs. applied electric field
(a) outer wall, (b) lid behind divertor hoops.

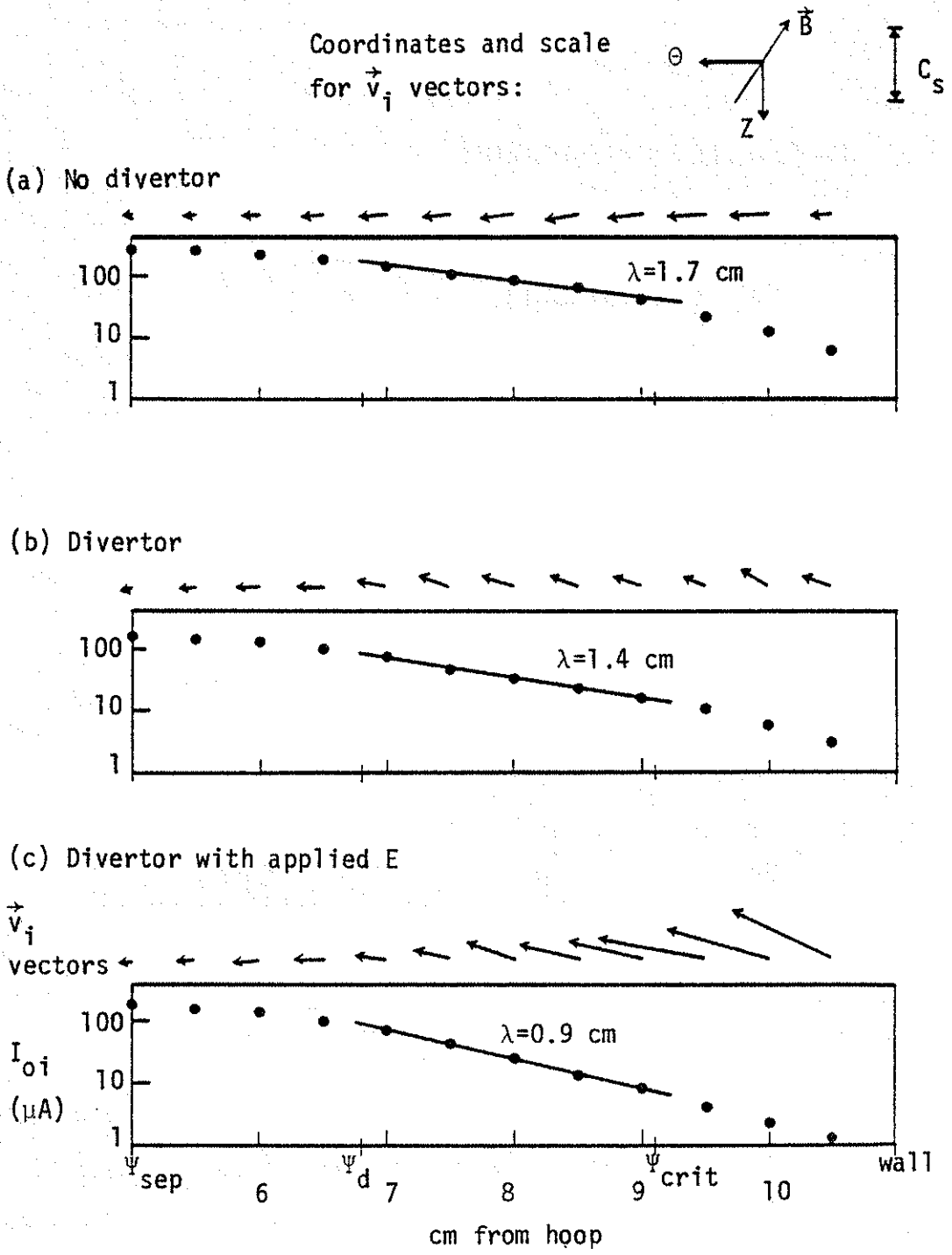

Fig. 6.15 - Profiles of ion flow velocity vectors and density (measured with paddle probe) at lower outer octupole hoop. (a) Divertor current = 0. (b) Divertor current = .1 (c) Divertor current = .1, and divertor hoop bias = 20 V.

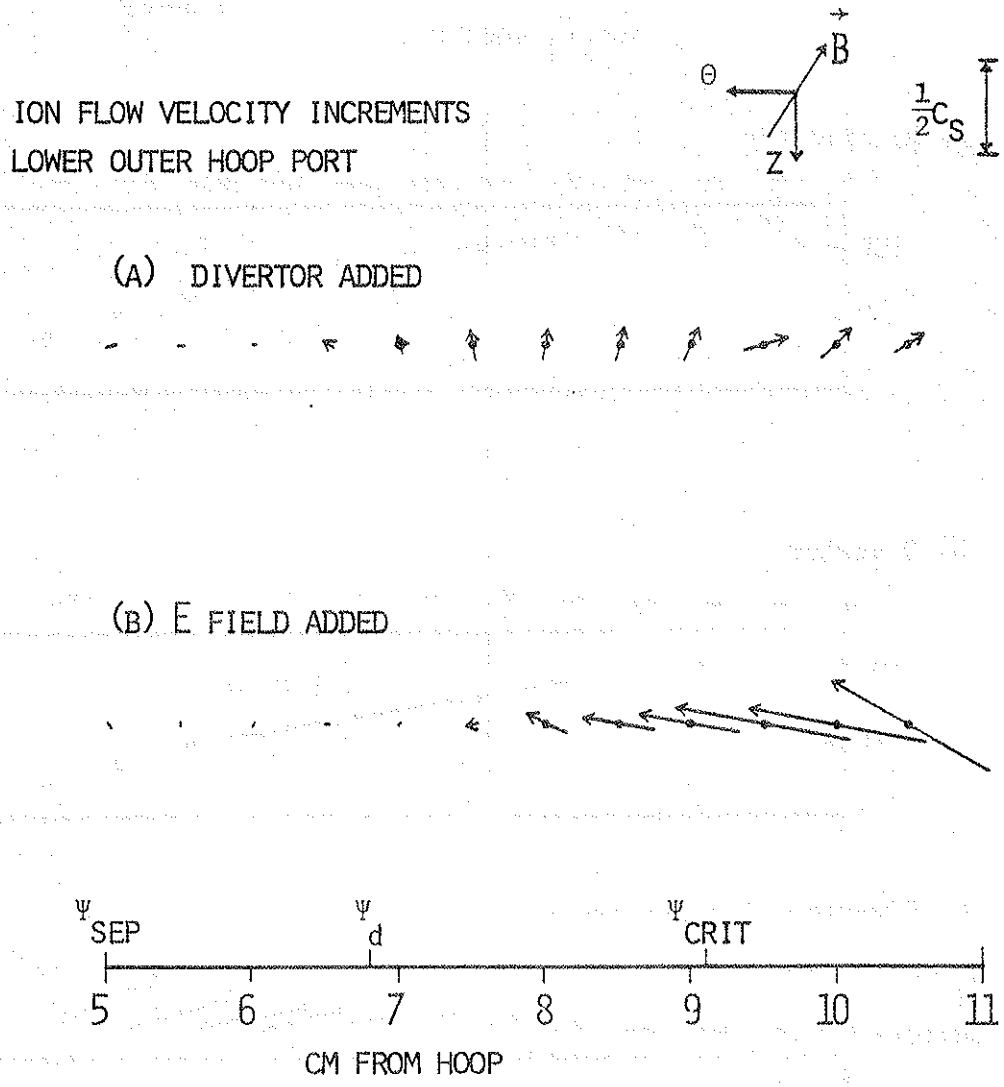

Fig. 6.16 - Profiles of changes in ion flow velocity vectors at lower outer octupole hoop, due to (a) addition of divertor current, (b) addition of applied electric field.

(Obtained by subtracting velocity vector profiles of Fig. 6.15)

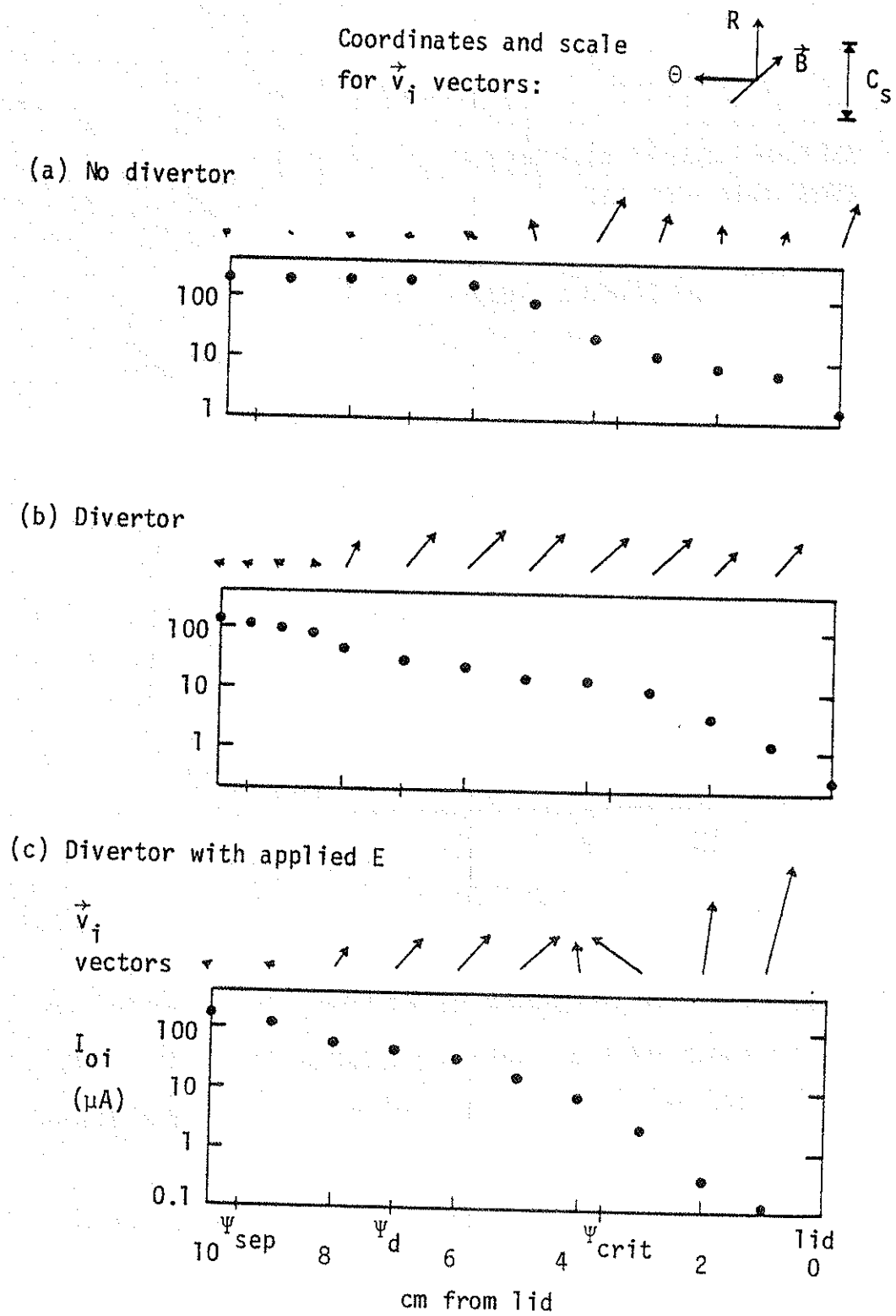

Fig. 6.17 - Profiles of ion flow velocity vectors and density at upper inner octupole hoop. (similar to Fig. 6.15)

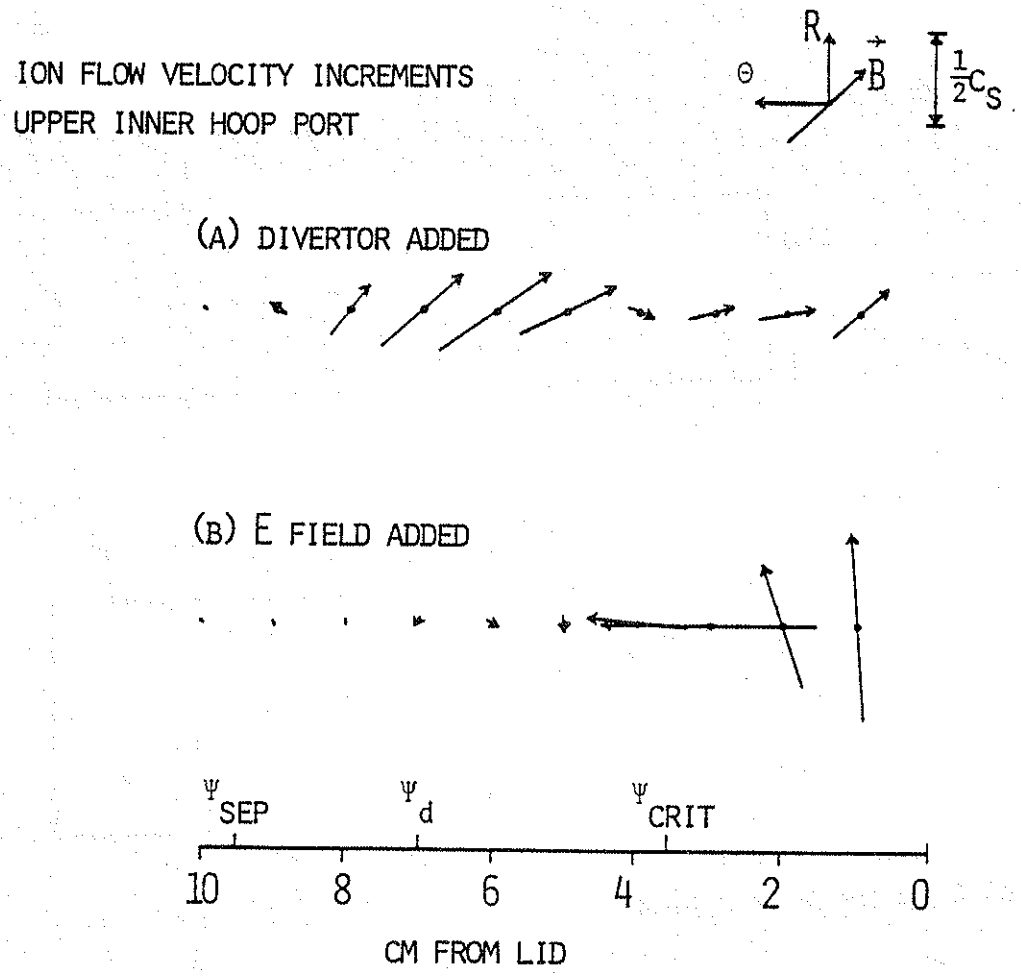

Fig. 6.18 - Profiles of changes in ion flow velocity vectors at upper inner octupole hoop, due to (a) addition of divertor current, (b) addition of applied electric field.

(Obtained by subtracting velocity vector profiles of Fig. 6.17)

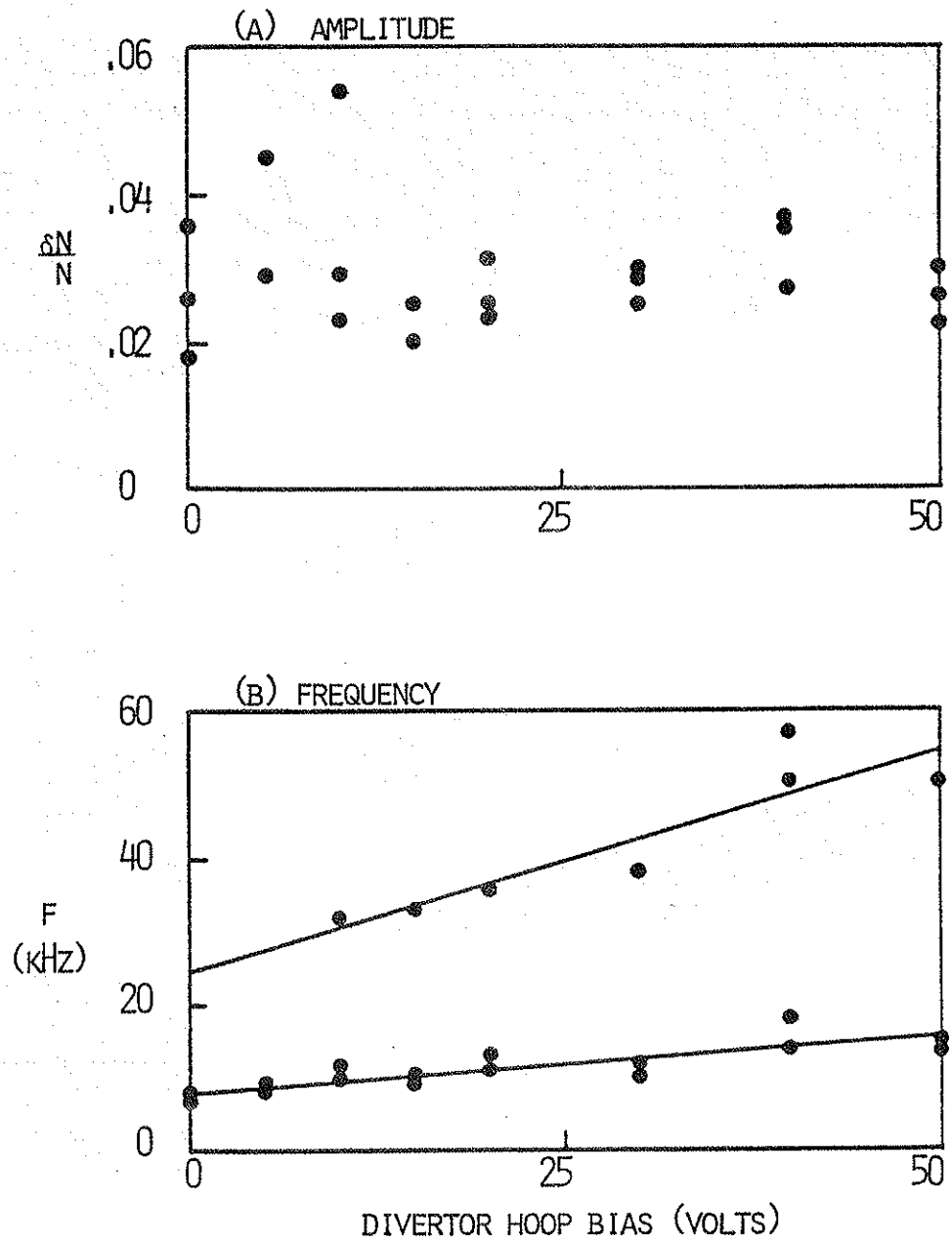

Fig. 6.19 - Ion saturation current fluctuations 8 cm from lower outer octupole hoop, vs. applied electric field:
(a) relative amplitude, (b) frequency.

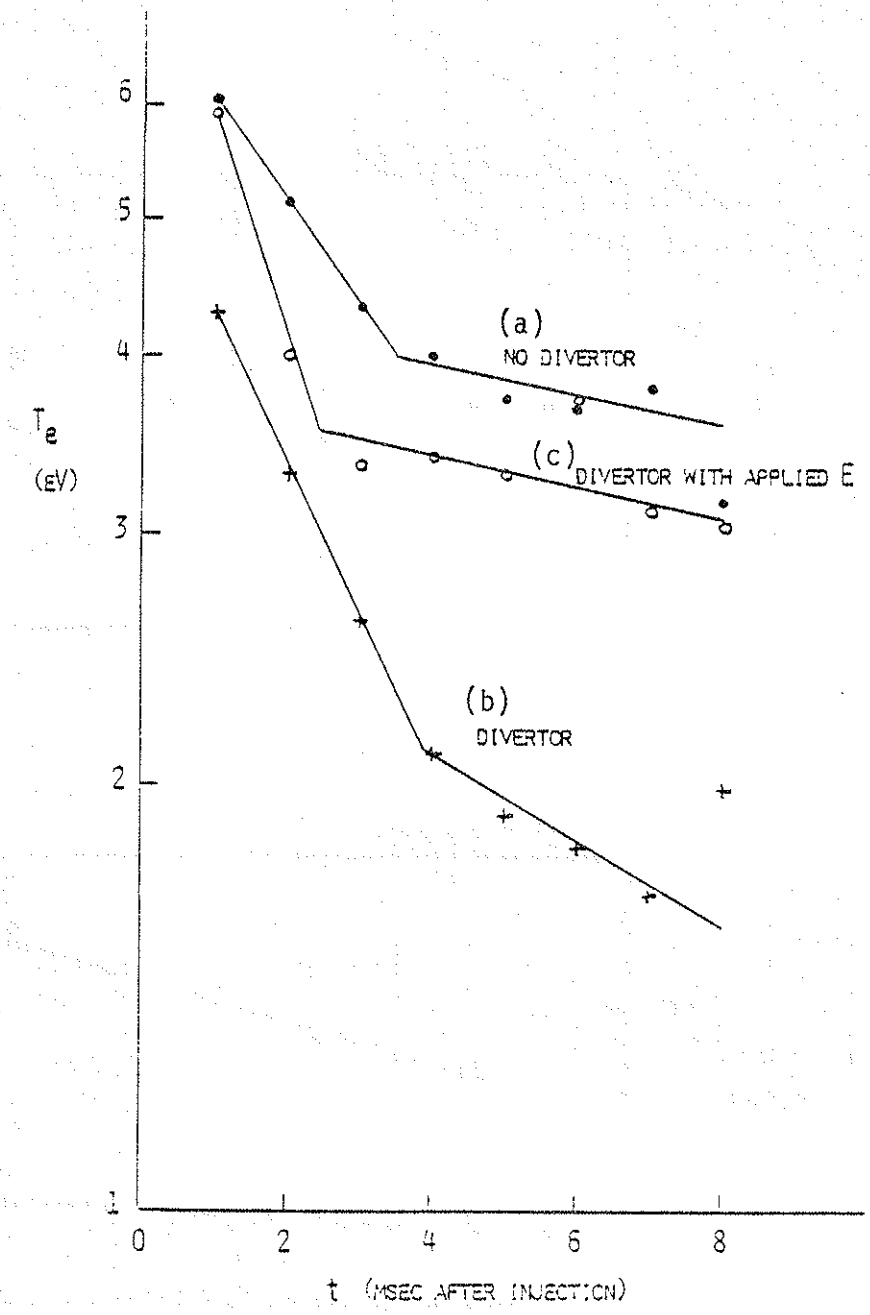

Fig. 6.20 - Electron temperature 8 cm from lower outer octupole hoop vs. time. (a) Divertor current = 0
(b) Divertor current = .1
(c) Divertor current = .1, divertor hoop bias = 20 V.

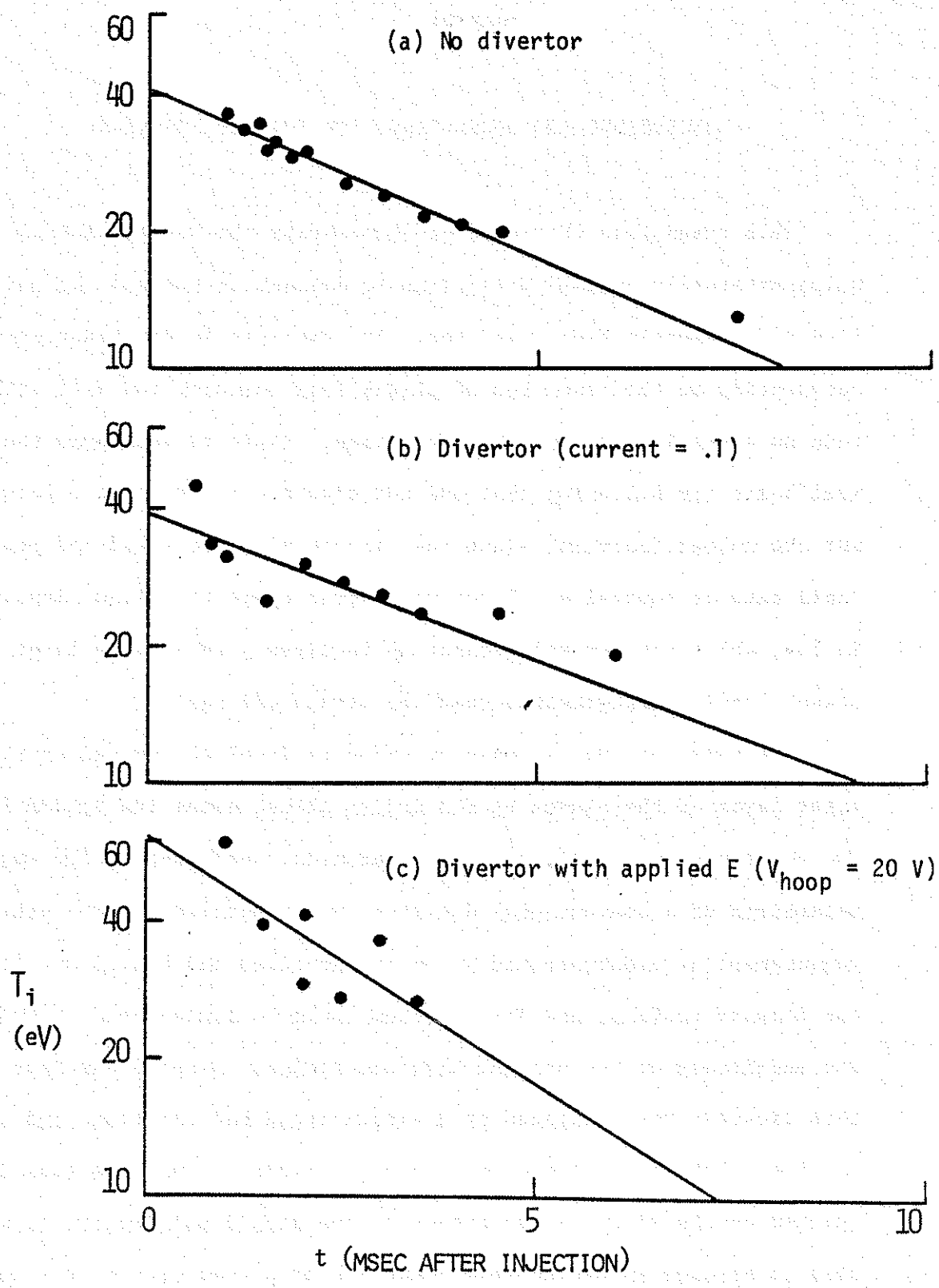

Fig. 6.21 - Ion temperature at Ψ_{sep} vs. time

CHAPTER 7

CONCLUSIONS AND SUGGESTIONS FOR FURTHER RESEARCH

This thesis has attempted to demonstrate the feasibility of using externally applied E×B drifts to augment or replace the parallel flow of a magnetic field divertor. The emphasis in the experiments is necessarily on the reduction of plasma flux reaching the wall rather than on screening of incoming impurities. There is also some theoretical basis for believing that the E×B divertor may be more effective for the unload function, since the largest electric field and most rapid rate of removal of plasma will occur where the plasma density is low, while the screening function requires a relatively large plasma density integrated across the scrape-off region.

The first of the two main experiments involved removal of the outer layer of the plasma by E×B drifts alone, using the biased fin. The existence of a drift surface separatrix, analogous to the magnetic separatrix of a conventional divertor, was confirmed both by direct measurement of electrostatic potential contours and by its effect on the density profile, and its position could be manipulated through the magnitudes of the applied electric fields. Despite the fact that this divertor was localized at a single azimuthal position, and the physical obstacle extended only to ψ_{crit} radially and less than a quarter of the minor circumference of the toroid poloidally, it was able to produce an appreciable reduction of plasma flux to the wall

everywhere in the machine. The amount of diverted plasma collected by the fin was consistent with the calculated value. As expected, it had no cooling effect on the plasma. This experiment, then, showed that externally applied E×B drifts could indeed be used to skim off the outer layer of plasma at a specified location, reducing the density near the wall and the plasma flux to the wall elsewhere, with no deleterious effect on confinement of the central plasma, as desired for an "unload" divertor.

That the reduction of plasma flux to the wall was not greater was undoubtedly due to the localized nature of the divertor and the rapid filling-in of the density profile behind it. This filling-in process is one question which could have been given further study; the evolution of the density profile downstream from the fin could have been measured over a wider variety of circumstances and compared with either a two-dimensional, steady-state calculation or a one-dimensional, time-dependent calculation. This would likely provide insights not only about the behavior of a localized E×B divertor of this type, but also about diffusion processes in the octupole.

Although demonstrating the general principle, the biased fin experiment differed in many respects from the E×B divertor envisioned for a tokamak, lacking axisymmetry and a competing process of plasma removal by parallel flow. The latter difference was addressed briefly by the addition of a weak toroidal magnetic field with results very similar to the case with poloidal field only, which was encouraging. Rather than pursue this aspect, however, the

full-fledged poloidal divertor was constructed.

The second of the two main experiments, then, concerned the poloidal magnetic divertor. The octupole was now operated with a relatively large ratio of toroidal to poloidal magnetic field ($q = .7$), in order to simulate more closely a tokamak's magnetic field configuration. This experiment was subdivided into studies of the divertor's behavior as a conventional magnetic divertor, and of the effects of an externally applied E×B drift. The addition of the poloidal divertor was almost equivalent to building a new machine in the large number of questions and possible lines of research which were opened, many of which had to be left unexplored.

Operated as a conventional divertor, without any applied E×B drift, the divertor's effect on confinement in the central region seemed to agree with the prediction of a simple slab model, decreasing the confinement time as the width of the confinement region was decreased. The divertor reduced plasma flux to the wall by an order of magnitude or more, with a simultaneous increase in plasma flux to the immediate vicinity of the divertor, as expected and desired. The observed reduction of flux to the wall was in agreement with a simple model using a constant diffusion coefficient, as seemed to be the case with the observed density profile and its constant scale length (at least for the small gun plasma) in the scrape-off region. It should be noted that even when not energized the divertor hoops acted as a limiter, already collecting most of the plasma leaving the confinement region. If they were located

outside the main chamber as in a real divertor, the reduction of plasma flux to the wall for the divertor separatrix at a given position would be much greater.

Rather than the simple slab models used here, it would be an interesting extension of the diffusion coefficient studies which have been done in the octupole to repeat those calculations with a variable boundary location, corresponding to the divertor separatrix, and attempt to predict the exact density profile shape and confinement time. Transport in the divertor's scrape-off zone is likely to differ from that in the confined plasma; in fact, it need not even be ambipolar. The study of such transport under various plasma conditions, for example by comparison with calculated density profiles, is a topic for investigation in its own right, and in fact such studies are being made on the single ring DC machine.

When E×B drifts were created by an externally applied electric field, the plasma flux to the wall was reduced by a further factor of 5 or more, with a simultaneous increase in plasma flux to the immediate vicinity of the divertor. The more rapid removal of plasma also reduced the density scale length in the scrape-off zone. These effects were consistent at low electric fields with the predictions of a simple model using a spatially constant electric field, but seemed to saturate at higher electric fields. As expected, no new instabilities were introduced. Electron cooling caused by the conventional magnetic divertor vanished when the electric field was

applied. The E×B divertor, then behaved as anticipated, reducing plasma flux to the wall with essentially no deleterious effect on confinement of the main plasma, but with the following reservations.

Two possible limitations of the E×B divertor can be seen here. First, the tendency of the E×B drift to "dig a hole" in the density profile, lowering it most near the wall where it is already lowest, was predicted in the theoretical model and could evidently be seen in the measured density profiles; this is probably the reason for the saturation of its unload efficiency at large electric fields mentioned above. More detailed profile measurements would be required for complete confirmation. This effect may or may not be a drawback, depending on what is desired of the divertor. Second, the flow velocity measurements showed that the poloidal component of flow was enhanced by the E×B drift far away from the divertor but was not much changed by it near the divertor itself, evidently due to parallel electric fields. This could be confirmed if the electric field could be applied in such a way as to avoid a parallel component, perhaps by biasing one of the octupole hoops as in the fin experiment (although such a thing could not be done in a tokamak). The parallel electric field also resulted in a large current being drawn from the plasma, which it would be preferable to avoid.

Other obvious extensions of the poloidal divertor experiments would be to repeat the measurements presented here with different plasma parameters, and with the divertor in the triplet configuration, making use of the new baffles behind the divertor hoops.

It is clear that a major question connected with the E×B divertor is whether the electric field can be applied as desired. It was predicted that either a non-zero perpendicular conductivity, or the perpendicular dielectric constant in the case of zero perpendicular conductivity, leads to the possibility of a perpendicular electric field whose scale length is that of the density profile rather than the Debye length. This was seen to occur in a supporting experiment where the electric field was applied by biasing an octupole hoop. The conductivity had the spatial dependence for collisions with neutral particles, but the magnitude was almost two orders of magnitude larger, indicating some anomalous process. The diffusion coefficient appeared to have a different spatial dependence, and the relationship of the two, and the role of the Einstein relation, are not completely clear. Nevertheless, the plasma does sustain an appreciable electric field, though the details of applying such a field in a tokamak without drawing prohibitively large currents to the electrodes may be more difficult. A detailed study of the perpendicular conductivity in the octupole and its relation to the diffusion coefficient under various plasma conditions, paralleling the diffusion coefficient studies, would be an interesting basic plasma physics project in its own right.

APPENDIX: MAGNETIC COORDINATES AND UNITS

Magnetic coordinates have been described elsewhere[1,2,3] and will be only briefly summarized here. It is desired to have three orthogonal coordinates which are oriented in a natural way with respect to the poloidal magnetic field at every point (see Figure A.1).

$\underline{\chi}$ If $\nabla \times \vec{B} = 0$ then the poloidal coordinate can be taken as the magnetic scalar potential χ, where

$$\vec{B} = \nabla\chi \tag{A.1}$$

This has the property that surfaces of constant χ are perpendicular to $\vec{B}$. If $d\ell$ is a small element of length along a poloidal field line then

$$d\chi = Bd\ell \tag{A.2}$$

$\underline{\theta}$ In an axisymmetric machine it is convenient to take as one coordinate the angle θ about the symmetry axis.

$\underline{\psi}$ This is the magnetic flux coordinate, such that if a point labeled by (ψ, θ, χ) is rotated about the symmetry axis, the resulting circle links a total magnetic flux of ψ. This definition, together with $\nabla \cdot \vec{B} = 0$, guarantees that ψ is constant along a magnetic field line, and thus serves to label the field lines. It is easy to show that

$$|\nabla\psi| = 2\pi RB \tag{A.3}$$

and

$$\psi = 2\pi RA_\theta \tag{A.4}$$

Where R is major radius and $\vec{A}$ is the magnetic vector potential. (An alternative definition often used is $\psi = RA_\theta$, giving the mathematically more pleasing result that $\nabla\chi = \nabla\psi \times \nabla\theta$.)

Units of ψ. The MKS units for ψ are, of course, Webers, but it is often convenient to use a normalized unit known as Dory.[4] The definition generally used on the large octupole is that 10 Dories are equal to the total flux in the iron transformer core at peak field, and field lines are then labeled from 0 Dories deep in the hoops to 10 Dories deep in the wall, independent of the amplitude of the magnetic field pulse, but with a given field line retaining the same label as it moves in and out of the machine during the pulse.[5] The conversion factor to MKS units is then

$$\psi_{\text{Webers}} = \psi_{\text{Dories}} \left(\frac{.72 \text{ Webers}}{10 \text{ Dories}}\right)\left(\frac{V_{\text{bank}}}{5000 \text{ V}}\right) \tag{A.5}$$

where V_{bank} is the charging voltage of the poloidal field capacitor bank. The reader should be aware, however, that other definitions of the Dory have been used by other authors, including one in which ψ runs from -5 in the hoops to +5 in the walls, and one in which the total flux in the core is defined to be 10 Dories at all times. In the latter case, the field line labeled by a given numerical value of ψ

is not constant with time, though the spatial location of that value of ψ is approximately constant.

Non-zero B_t. In the presence of a toroidal magnetic field the magnetic coordinates remain the same. B, χ, and ψ in the equations above are understood to refer only to the poloidal component of the magnetic field.

REFERENCES FOR APPENDIX

1. J.W. Rudmin, University of Wisconsin PLP 349 (1970).

2. C.J. Armentrout, J.C. Sprott, University of Wisconsin PLP 470 (1973).

3. C.J. Armentrout, University of Wisconsin PLP 667 (1976).

4. R.A. Dory, University of Wisconsin PLP 15 (1963).

5. R.L. Willig, University of Wisconsin PLP 418 (1971).

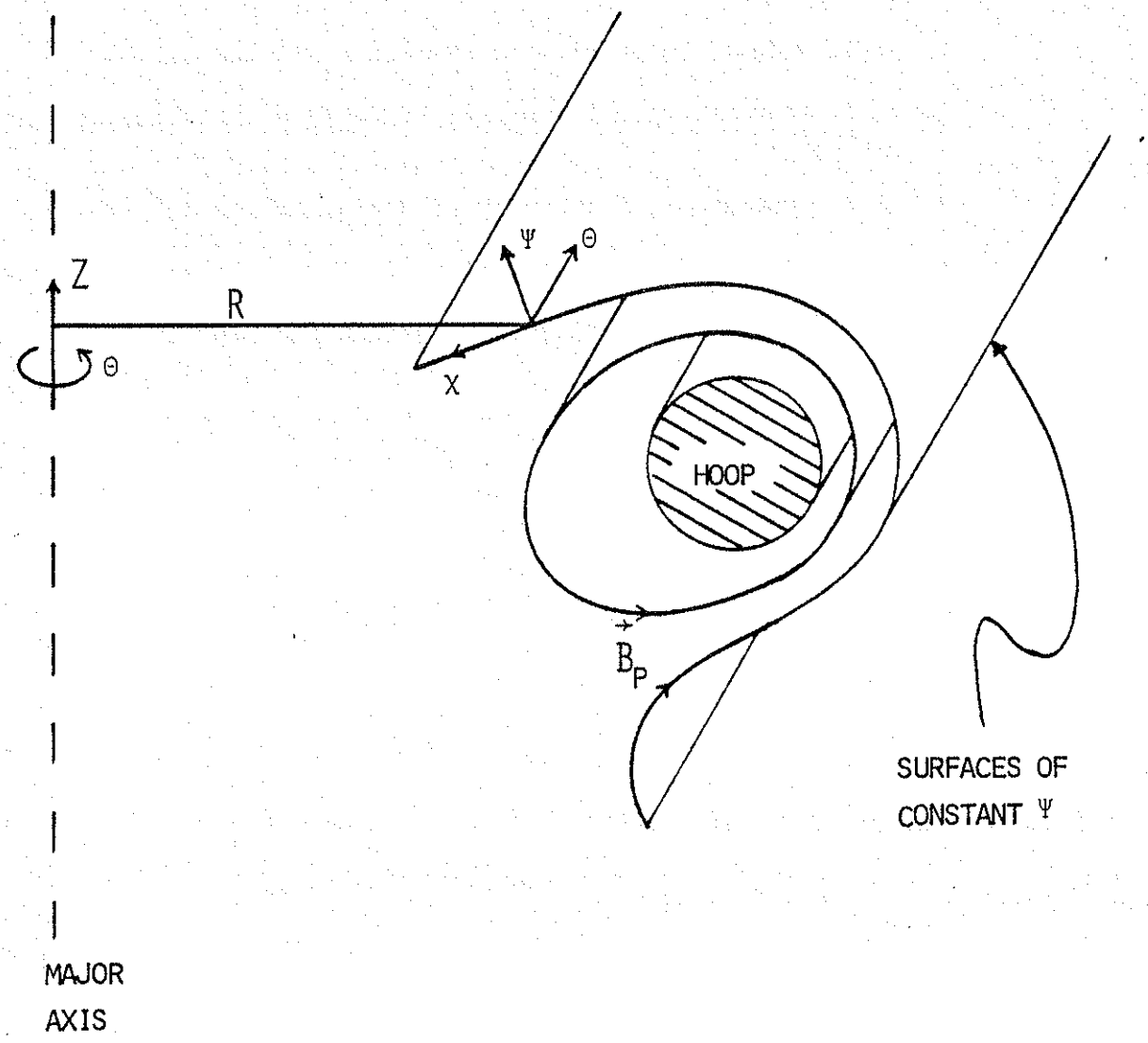

Fig. A.1 - Octupole coordinate systems.

Cylindrical coordinates (R,Θ,z): R = major radius,

Θ = toroidal angle, z = vertical.

Magnetic coordinates (Ψ,Θ,χ): Ψ = poloidal flux,

Θ = toroidal angle, χ = magnetic scalar potential

PLP REPORTS

In this thesis, several references are made to the internal reports of the University of Wisconsin plasma physics group. These reports, which are identified by PLP numbers, are available upon request from:

Plasma Physics Office
University of Wisconsin
1150 University Avenus
Madison, Wis. 53706